

Planning of CT-guided Accurate Extra-fine  
Needle Insertion in Lower-abdomen

下腹部を対象とした極細針による  
CT ガイド下高正確度穿刺プランニング

February 2019

Ryosuke TSUMURA

津村 遼介

Planning of CT-guided Accurate Extra-fine  
Needle Insertion in Lower-abdomen

下腹部を対象とした極細針による  
CT ガイド下高正確度穿刺プランニング

February 2019

Waseda University  
Graduate School of Creative Science and Engineering,  
Department of Modern Mechanical Engineering,  
Research on Neuro-Robotics

Ryosuke TSUMURA

津村 遼介

# Abstract

The number of patients and deceased people due to cancers has been increased worldwide amid aging of population. In various types of cancers, lymphatic malignancy is one of the blood-tumors that most of Japanese disease. The lymphatic malignancy occurs at mainly lymph nodes and lymph tissues of spleen and tonsil, and at possibly gastrointestinal tracts, thyroid, lung, liver, skin, bone marrow and brain. In order to diagnose the types of lymphatic malignancies through pathology examinations, doctors usually conduct biopsies and observed the sampled tissues with microscopes. The therapeutic principle for lymphatic malignancy is decided considering patient's body conditions based on the appropriate pathology examination and stage classification. The standard therapies are chemotherapy and radiation therapy. Meanwhile, those therapies often cause a side effect due to injure normal cells. Recently, immune therapies are expected to be new approaches as the fourth cancer treatment all over the world, in addition to three major cancer treatments.

Percutaneous needle insertion is used for various purposes of the cancer diagnosis and therapy in addition to the HITV cancer therapy. Meanwhile, the percutaneous needle insertion is constrained and complex procedure because of target visibility, tool maneuverability and physiological interaction. Especially, the needle deflection is a key issue to affect the misplacement of needle tip. The needle deflection occurs generally due to needle tip shape and needle diameter. The needle used in usual therapies are bevel-tip type, which is contributed to needle deflection because the asymmetric reaction forces are generated between needle tip and tissues during insertion into tissues. Moreover, the diameter of needle is a serious factor for causing needle deflection. The needle is easily deflected if the diameter is small because second moment of area of the needle become small. Meanwhile, tissue damages for patients can be decreased with using fine needles since the amount of cutting tissue is small. Serious tissue damages may lead to not only patient's trauma due to pain but also swelling and complications. Therefore, the fine needle insertion is preferred for patients although it is difficult for doctors to manipulate the fine needle to reach the target accurately.

In this paper, the author focused on a lymphatic malignancy located on para-aortic lymph nodes in lower-abdomen as the insertion target. The para-aortic lymph node in lower-abdomen is one of the most difficult targets because the target is located at a deep part in a body (about 100 mm from skin). Then, the needle has to pass through several tissues and organs in order to reach the target so that the needle deflection occur complexly. In addition, it is necessary to use the extra-fine needle (around 25 gauge) since the needle is inserted into bowels, thereby peritonitis from perforation of bowels need to be avoided. In case of the lower abdominal insertion, CT is

usually used as the medical image modality. However, patients are exposed to X-ray every time of scanning with CT. If the needle is inserted repeatedly once the needle deflection occurs, the amount of radiation exposure for patients is increased. Therefore, in case of the lower abdominal insertion, it is necessary to insert the extra-fine needle into the target with minimum CT scanning. Although there have been many interventional robotic systems for assisting needle insertion in the past, there has been limited development of the CT-guided needle insertion robot systems focusing on the lower-abdominal insertion.

Then, in order to develop the robotic-assisted technologies for achieving an accurate insertion, the purpose of this study is to develop the planning method of CT-guided lower-abdominal needle Insertion. In particular, in order to minimize the needle deflection, the author addressed three technological challenges following; (i) a planning of needle insertion control, (ii) a planning of needle insertion path, and (iii) a CT-guided needle insertion robot system for performing the proposed planning. This thesis is composed of seven chapters. Overviews of each chapter are described following.

In chapter 1, regarding the lymphatic malignancy which is the targeted disease in this study, the author summarized the number of diseased patients, diagnosis method and treatment method, and described the necessity of percutaneous needle insertion. Moreover, by summarizing the research trends of needle insertion robots and methods for achieving the accurate insertion, the author showed the difficulty of lower-abdominal insertion and technological challenges, and described the purpose of this study.

In chapter 2, regarding the mechanical phenomena during needle insertion into each tissue and organ composing lower abdomen (layered tissue including skin, fat and muscle, and bowel), the author summarized the mechanical properties needed to be considered in order to decrease the needle deflection through experimental analysis. At first, the needle insertion was performed in *ex vivo* experiment with porcine rib and bowel in order to observe the behavior of needle deflection and insertion force depending on the tissue properties. Next, the needle is inserted at various angle to the same tissues in order to observe the needle deflection and insertion force depending on tissue geometries.

In chapter 3, based on the experimental analysis of chapter 2, the author proposed insertion control planning to the layered tissue and bowel, respectively. As the requirements of insertion control, it is necessary to consider the equalization of needle tip forces, the reduce of friction force around the needle shaft and the avoidance of winding-up tissues. Then, regarding the insertion for layered tissue, the author proposed the insertion control method with combination of high frequency vibration along insertion direction and bidirectional axial spinning to insertion direction. Regarding the insertion for bowels, the author proposed the combination of the vibration and the rotation of needle tip angle every time at puncturing bowel walls to cancel the



needle deflection.

In chapter 4, the author proposed the preoperative insertion path planning method for determining appropriate needle insertion position and angle to achieve a straight path from skin to tumor. In the chapter 2, it was confirmed that the insertion angle at tissue boundary is key issue to affect the needle deflection. Then, the author made a hypothesis that the amount of needle deflection can be minimized by selecting the path that the sum of insertion angles with respect to each tissue boundary that the needle passes through is minimized. In addition, the effect of insertion angle for the needle deflection varies due to the tissue properties and the tissue boundary positions. Then, weight factors of each insertion angle in the path planning were implemented. As the design of weight factor, the author developed the probability that the needle deflection is within acceptable amount. Moreover, in order to implement the path planning method on CT images, the author developed the image processing method to detect the tissue boundary from CT images and to calculate the insertion angle in each boundary.

In chapter 5, the author described the CT-guided needle insertion robotic systems for implementing the proposed insertion control planning in chapter 3 and insertion path planning in chapter 4. This robotic system is composed of needle insertion unit which enable to implement the insertion with vibration and rotation; robot arm which move the needle insertion unit to appropriate position and angle based on the path planning; and registration marker for conducting coordinate transform between the robot arm and CT image.

In chapter 6, the availability of the proposed insertion control and path planning with the robotic system was evaluated through *in vivo* experiment with micro pig. As the results, by applying the proposed insertion control planning, the needle deflection could be decreased up to 1.0 mm at an insertion point obtained from the proposed insertion path planning. In addition, the limitation of this study was mentioned in terms of insertion control planning, insertion path planning and CT-guided needle insertion robot systems.

In chapter 7, summary of the achievement and remaining tasks of this study were described in this chapter. As the future work, the author described the issues for achieving the robotic system to clinical application.

Thus, in order to minimize the needle deflection for achieving straight insertion path in CT-guided lower-abdominal needle insertion, this thesis proposed novel planning methods of insertion control and insertion path. As the insertion control planning, insertion with the combination of vibration and rotation was proposed. As the insertion path planning, the optimization-based planning model based on the insertion angle was proposed. The effectiveness and validity of the proposed methods were evaluated through *ex vivo* and *in vivo* experiments.

The contribution of this thesis is to address the technological challenges regarding the CT-guided lower-abdominal insertion with the extra-fine needle. The proposed methods for

minimizing the needle deflection will contribute the other target application such as lung, liver and bone, which needs the preoperative insertion planning. In addition, the concept of proposed approaches will be applied to other medical and surgical instruments and robotic systems, not only needle insertion applications.

# Acknowledgement

This study was conducted at the Graduate School of Creative Science and Engineering, Waseda University. This research was supported by Hasumi International Research Foundation (HIRF), Leading Graduate Program in Embodiment Informatics, Waseda University from MEXT, Japan and Research Fellowships for Young Scientists, Japan Society for the Promotion of Science.

First of all, I would like to gratefully appreciate to my supervisor Prof. Hiroyasu Iwata. Over the last seven years, including bachelor's and master's degrees, his insightful, strict, kind and variable suggestions on my research enhanced my abilities as not only a researcher but a person. I would also like to appreciate to my examiners, Prof. Mitsuo Umezu, Prof. Atsuo Takanishi, Prof. Shigeki Sugano, and Prof. Ken Masamune, for providing me appropriate and helpful comments on my presentation and thesis.

I would also like to appreciate to my collaborative advisers, Dr. Kenichiro Hasumi and the members in the hospital. They would give me opportunities of developing the needle insertion robot and a lot of clinical advices. Thanks to them it has become possible to realize this study. I would also like to thank my collaborative researchers, Prof. Iulian Iordachita, Prof. Jin Kim Seob, and the members in the Laboratory for Computational Sensing + Robotics (LCSR), Johns Hopkins University, USA, as an oversea research practicum for six months in 2017.

I would like to appreciate to Dr. Kazuhiro Yasuda, Dr. Makiko Ishikawa (Denso Co.), Dr. Takabumi Watanabe (Canon Inc.), Dr. Takao Watanabe (Bosch Co.) and Dr. Yuta Fukushima (Attraction Inc.) for assisting my research. I would also like to appreciate to the graduate and undergraduate students belonging to "Cancer therapy" group, Mr. Kai Shitashima (DeNA Co., Ltd.), Mr. Tomoya Suzuki, Mr. Shota Sawada (Olympus Co.), Mr. Yusuke Takishita (JFE Steel Co.), Mr. Shun Inoue, Mr. Ryutaro Matsumoto and Mr. Koki Izumi. They made my life as a doctoral student enjoyable and variable. I am also thankful to the other Iwata Laboratory members and community members that I belong such as Leading Graduate Program, Waseda University and young researchers in Global Robot Academia, Waseda University for their comments their encouragement, and their interest in my research. I would like to thank the secretaries in Iwata Laboratory and the all staff related to the Leading Graduate Program in Embodiment Informatics, Waseda University for their continued research support.

I would also like to especially thank my friends and family for their enriching my life. I am able to have a great time during student life.

*Tokyo, February 2019*

Ryosuke Tsumura



# Table of contents

Chapter 1: Introduction .....	1
1.1 Chapter introduction .....	1
1.2 Background of cancer treatment.....	1
1.2.1 Cancer trend and lymphatic malignancy .....	1
1.2.2 Treatment for lymphatic malignancy .....	5
1.2.2.1 Standard therapies .....	5
1.2.2.2 Immune therapy.....	6
1.2.2.3 HITV cancer therapy .....	7
1.2.3 Percutaneous needle insertion .....	8
1.2.3.1 Type of needle insertion application.....	8
1.2.3.2 Medical image modality .....	9
1.2.4 Challenges for accurate percutaneous needle insertion.....	11
1.3 Purpose of this study .....	12
1.4 Related studies.....	13
1.4.1 Interventional needle insertion robots .....	13
1.4.2 Needle steering techniques.....	16
1.5 Objective of this study .....	17
1.5.1 Setting the theme .....	17
1.5.2 Objective .....	18
1.5.3 Contribution .....	19
1.6 Overview .....	21
Chapter 2: Experimental analysis of needle deflection.....	23
2.1 Chapter introduction .....	23
2.2 Mechanism of needle deflection.....	23
2.2.1 General needle insertion flow.....	23
2.2.2 Needle deflection model.....	24
2.2.2 Composition of lower abdomen .....	25
2.3 Experimental analysis of needle deflection .....	27
2.3.1 Experimental setup .....	27
2.3.2 Effect of target properties .....	28

2.3.3 Effect of insertion angle .....	32
2.4 Approach for decreasing needle deflection .....	34
2.5 Summary.....	34
<b>Chapter 3: Insertion control planning .....</b>	<b>35</b>
3.1 Chapter introduction.....	35
3.2 Approach.....	35
3.2.1 Requirements of planning .....	35
3.2.2 Rotation .....	36
3.2.3 Vibration.....	38
3.2.4 Combination of rotation and vibration .....	39
3.3 Control method for layered tissue .....	39
3.3.1 Bidirectional rotation.....	39
3.3.2 Evaluation of deflection and tissue damage .....	40
3.3.2.1 Tissue damage analysis .....	40
3.3.2.2 Experimental protocol .....	41
3.3.2.3 Results of deflection.....	42
3.3.2.4 Results of tissue damage .....	43
3.3.2.5 Discussion .....	46
3.3.3 Evaluation of control paramters .....	48
3.3.3.1 Experimental protocol .....	48
3.3.3.2 Results .....	49
3.3.3.3 Discussion .....	49
3.4 Control method for bowel .....	53
3.4.1 Rotation of needle tip direction.....	53
3.4.2 Evaluation of insertion control method.....	54
3.4.2.1 Experimental protocol .....	54
3.4.2.2 Results .....	54
3.4.2.3 Discussion .....	55
3.4.3 Evaluation due to insertion positions .....	57
3.4.3.1 Experimental protocol .....	57
3.4.3.2 Results .....	57
3.4.3.3 Discussion .....	59
3.5 Summary.....	59

<b>Chapter 4: Insertion path planning</b> .....	<b>61</b>
4.1 Chapter introduction .....	61
4.2 Insertion path planning .....	62
4.2.1 Concept of insertion path planning .....	62
4.2.2 Tissue boundary distance .....	63
4.2.3 Deflection probability .....	64
4.2.4 Evaluation.....	66
4.2.4.1 Experimental setup.....	66
4.2.4.2 Fitting deflection probability.....	67
4.2.4.2 Verification .....	71
4.2.5 Discussion .....	75
4.3 Path planning system based on CT images .....	77
4.3.1 System overview .....	77
4.3.2 Boundary detection .....	78
4.3.3 Insertion angle calculation.....	79
4.3.4 Verification .....	80
4.3.4.1 Experimental setup.....	80
4.3.4.2 Tissue boudary detection.....	80
4.3.4.3 Insertion angle calculation.....	81
4.3.5 Discussion .....	82
4.4 Summary.....	84
<b>Chapter 5: CT-guided needle insertion robot</b> .....	<b>85</b>
5.1 Chapter introduction .....	85
5.2 Requirements .....	85
5.2.1 Usage of the robot system .....	85
5.2.2 CT scan.....	86
5.2.3 Requirements for the needle insertion robot .....	87
5.3 Overall design.....	89
5.3.1 Total configration .....	89
5.3.2 Positioning arm .....	90
5.4 Needle insertion unit.....	92
5.4.1 Overall design .....	92
5.4.2 Mechanism of insertion with rotation and vibration .....	94

5.4.3 Material and size for CT compatibility .....	96
5.5 Registration method.....	99
5.5.1 Registration concept.....	99
5.5.1.1 System overview .....	99
5.5.1.2 Procedure.....	100
5.5.1.3 Requirements of registration marker .....	100
5.5.2 Registration marker design.....	101
5.5.2.1 Property of the oblique prism.....	102
5.5.2.2 Caluculation procuedure of yaw and pitch angle .....	104
5.5.2.3 Caluculation procuedure of cranio-caudal distance .....	105
5.5.2.4 Calculation flow .....	107
5.5.3 Verification of registration marker .....	109
5.5.3.1 Experimental setup.....	109
5.5.3.2 Results .....	110
5.5.3.3 Discussion .....	112
5.6 Summary.....	113
Chapter 6: Evaluation.....	115
6.1 Chapter introduction.....	115
6.2 <i>In vivo</i> experiment .....	115
6.2.1 Experimental setup.....	115
6.2.2 Insertion path planning.....	120
6.2.3 Results .....	123
6.2.4 Discussion .....	125
6.3 Originarity and limitation .....	128
6.3.1 Insertion control planning .....	128
6.2.2 Insertion path planning.....	129
6.2.3 CT-guided needle insertion robot .....	130
6.4 Summary.....	131



Chapter 7: Conclusion.....	133
7.1 Conclusion.....	133
7.2 Future works.....	135
References .....	137



# List of figures

Chapter 1: Introduction .....	1
Fig. 1.1 The number of deceased people due to cancers .....	2
Fig. 1.2 The number of deceased people by types of cancer .....	3
Fig. 1.3 Classification of stem cell types .....	3
Fig. 1.4 Areas of lymph malignancy occurred .....	4
Fig. 1.5 Roll of dendritic cells .....	7
Fig. 1.6 Overview of brachytherapy .....	9
Fig. 1.7 Sample of metal artifacts on CT image .....	11
Fig. 1.8 Types of needle steering methods .....	17
Fig. 1.9 The concept of proposed CT-guided needle insertion robot system .....	19
Fig. 1.10 Overview of this paper .....	22
Chapter 2: Experimental analysis of needle deflection .....	23
Fig. 2.1 General flow of needle insertion into soft tissue .....	24
Fig. 2.2 Mechanical model of needle deflection .....	25
Fig. 2.3 Anatomical structure of lower abdomen .....	27
Fig. 2.4 Overview of needle insertion robot used in this experiment .....	28
Fig. 2.5 Experimental conditions of insertion targets: (a) pork rib, (b) porcine small bowel .....	30
Fig. 2.6 The result of needle deflection due to tissue properties .....	30
Fig. 2.7 The result of time-series of insertion force of (a) layered tissue and (b) bowel .....	31
Fig. 2.8 Experimental condition changing insertion angles of (a) layered tissue and (b) bowel .....	32
Fig. 2.9 The result of needle deflection due to the insertion angle .....	33
Fig. 2.10 The needle deflection in phase1 caused by the tissue deformation due to insertion angle .....	33
Fig. 2.11 The distribution of interaction forces due to insertion angle .....	33

Chapter 3: Insertion control planning .....	35
Fig. 3.1 Rotational insertion model with cantilever beams in each time step .....	37
Fig. 3.2 Tissue deformation model during insertion with the modified Kelvin model .....	39
Fig. 3.3 Friction force model with viscous friction and Kelvin-Voigt model .....	39
Fig. 3.4 Continuous rotation method .....	40
Fig. 3.5 Sliced tissue sections with a microtome into 10- $\mu$ m-thick sections along the radial direction of the needle .....	41
Fig. 3.6 Comparison of rotation and vibration with respect to deflection.....	42
Fig. 3.7 A piece of tissue was attached to the needle tip when winding up of the tissue occurred .....	42
Fig. 3.8 Comparison of rotation and vibration with respect to (a) insertion force and (b) insertion torque .....	43
Fig. 3.9 Samples of time series data of insertion force.....	44
Fig. 3.10 Samples of time series data of insertion torque.....	45
Fig. 3.11 Comparison of rotation and vibration with respect to the hole area created by the needle.....	46
Fig. 3.12 Samples of tissue section images .....	48
Fig. 3.13 Results of needle deflection due to vibration and rotation parameters ...	50
Fig. 3.14 Results of the average of (a) maximum insertion force and (b) maximum torque force during insertion into the layered tissue varying at the vibration and rotation parameters .....	51
Fig. 3.15 Result of needle deflection due to insertion angles.....	52
Fig. 3.16 The rotation of needle tip direction when breaching the bowel surface .	53
Fig. 3.17 Insertion path types .....	54
Fig. 3.18 The result of needle deflection due to the insertion control methods .....	55
Fig. 3.19 Results of the average of (a) maximum insertion force and (b) maximum torque force during insertion into the bowel varying at the vibration and rotation parameters.....	56
Fig. 3.20 Bowel insertion situation.....	57
Fig. 3.21 Results of the deflection due to (a) insertion positions and (b) insertion angle .....	58

Chapter 4: Insertion path planning .....	62
Fig. 4.1 (a) Ideal insertion case of multi-layered tissue (b) complex insertion case of multi-layered tissue (c) definition of insertion angle .....	63
Fig. 4.2 The effect for deflection due to boundary distance: (a) the long distance causing large deflection, and (b) the short distance causing small deflection.....	64
Fig. 4.3 (a) Illustration of the probability that the deflection occurrence due to the insertion angle is within the acceptable deflection (blue area) (b) Example of calculated deflection probability (orange line) and deflection probability distribution (blue line) to deflection slope $\varphi_i$ in an insertion angle at $\theta_i$ .....	66
Fig. 4.4 Experimental setup is composed of 2-DOF needle driver (insertion and rotation axes), Cartesian stage and tissue phantom .....	67
Fig. 4.5 Needle insertion overview: (a) PVC experiment (b) biological tissue (chicken) experiment, (c) definition of deflection-slope .....	69
Fig. 4.6 Experimental result of deflection-slope due to insertion angles .....	69
Fig. 4.7 Results of fitting experimental deflection data to Gaussian model: (a) PVC50%, (b) PVC75% and (c) chicken.....	70
Fig. 4.8 Results of fitting parameters $\mu$ (upper row) and $\sigma$ (bottom row) of Gaussian model to polynomial regression model:.....	70
Fig. 4.9 Experimental scenario overview .....	73
Fig. 4.10 Comparison of scores calculated with the objective function and needle tip deflections in all needle entry positions .....	73
Fig. 4.11 Flow overview of the insertion angle calculation .....	77
Fig. 4.12 Region of interest (ROI) setting overview .....	78
Fig. 4.13 Candidates for needle insertion path in region of interest (ROI).....	78
Fig. 4.14 Boundary detection system flow .....	79
Fig. 4.15 Graphs of brightness value and amount of brightness change along the insertion path .....	79
Fig. 4.16 Angle calculation system flow chart .....	80
Fig. 4.17 Result of boundary detection with dynamic time warping Insertion path types.....	81
Fig. 4.18 Result of insertion angle error with respect to distance $L$ from the target .....	82
Fig. 4.19 Unsuccessful situations causing divided boundaries .....	83
Fig. 4.20 Adhesion of muscle and bowel .....	83
Fig. 4.21 Higher order of a polynomial (left) ideal separation (right).....	83

Chapter 5: CT-guided needle insertion robot .....	85
Fig. 5.1 CT scan used to needle insertion robot: Aquilion LB .....	86
Fig. 5.2 Clearances between CT gantry and patient body .....	88
Fig. 5.3 Sample of metal artifacts on CT images .....	88
Fig. 5.4 General layout of the needle insertion robot system .....	89
Fig. 5.5 Overview of needle insertion robot composed of 1) needle insertion robot, 2) positioning arm and 3) registration marker .....	90
Fig. 5.6 Setting positions of the positioning arm.....	91
Fig. 5.7 6-DoF robot arm used in this study (VS-068).....	91
Fig. 5.8 Overview of needle insertion unit .....	92
Fig. 5.9 Detailed design of mounting base attached to piezo actuator and stepping motor.....	95
Fig. 5.10 Cross section of components for applying rotation and vibration .....	95
Fig. 5.11 The shape of shaft and gear for accepting the rotation and vibration .....	96
Fig. 5.12 The needle guidance for decreasing needle deflection before punctuation .....	96
Fig. 5.13 Results of FEA experiments of the shaft.....	97
Fig. 5.14 Size of the needle insertion unit designed for avoiding to interfere the gantry and body .....	98
Fig. 5.15 The overview of each coordinate in the CT guided-needle insertion robot system .....	99
Fig. 5.16 Definition of coordinate of robot to CT image .....	101
Fig. 5.17 Overview of registration marker .....	101
Fig. 5.18 A parallelogram with sides of length of $a'$ and $b'$ appears when a rectangular prism is cut by an inclined cross section .....	103
Fig. 5.19 The gradient of the ratio $\zeta$ of side length change depending on the angle cut by an inclined cross section to a rectangular .....	103
Fig. 5.20 The shape of oblique prism inclined by an angle defined with $\zeta$ .....	104
Fig. 5.21 Calculation of angle of oblique prism .....	105
Fig. 5.22 The cross section's appearance depending on the cut position changes in the Cranio-Caudal distance.....	106
Fig. 5.23 Paris of oblique disposed oppositely.....	106
Fig. 5.24 Registration steps with the proposed marker .....	107
Fig. 5.25 The sample of the cross-section of the marker after image processing by	

varying the yaw/pitch angle.....	108
Fig. 5.26 The sample of the cross-section of the marker after image processing by varying the z-axis position after adjusting the yaw and pitch angles .....	108
Fig. 5.27 The definition of the central coordinate of the registration marker .....	109
Fig. 5.28 Experimental setup for verifying the registration marker .....	110
Fig. 5.29 The result of errors of (a) yaw angle, (b) pitch angle and (c) the craniocaudal distance.....	111
Chapter 6: Evaluation.....	115
Fig. 6.1 Experiment setup overview .....	117
Fig. 6.2 Insertion paths selected in this experiment .....	118
Fig. 6.3 Experimental result of deflection-slope due to insertion angles .....	121
Fig. 6.4 The comparison of needle deflection between without and with insertion control planning .....	123
Fig. 6.5 The result of score calculated by objective function of insertion path planning .....	123
Fig. 6.6 The sequential transversal CT images tracking the needle in No. 10 insertion path .....	125
Fig. 6.7 The sequential transversal CT images tracking the needle in No. 1 insertion path .....	125
Fig. 6.8 The sequential sagittal CT images tracking the needle in No. 1 insertion path .....	126
Fig. 6.9 The sequential CT images tracking the needle in No. 7 insertion path...	126





# List of tables

Chapter 1: Introduction .....	1
Table 1.1 Classification of types of non- Hodgkin’s lymphoma by clinical grades.	4
Table 1.2 Classification of interventional robotic system for assisting needle insertion .....	15
Table 1.3 Comparison of previous researches of CT-guided needle insertion robot and this study .....	20
Chapter 4: Insertion path planning .....	61
Table 4.1 Gaussian distribution parameters.....	68
Table 4.2 Polynomial regression model coefficient .....	68
Table 4.3 Order of deflection and score in all entry position .....	72
Chapter 5: CT-guided needle insertion robot .....	83
Table 5.1 Specification of CT scan.....	84
Table 5.2 Specifications of robot arm.....	89
Table 5.3 Specifications of actuator and sensors in needle insertion unit .....	91
Table 5.4 Specification of CT scan.....	95
Table 5.5 Conditions of CT scan.....	108
Chapter 6: Evaluation.....	117
Table 6.1 Tissue boundary positions on the selected insertion path .....	119
Table 6.2 Insertion angles on each tissue boundary on the selected insertion path .....	119
Table 6.3 Gaussian distribution parameters.....	123
Table 6.4 Polynomial regression model coefficient .....	123
Table 6.5 The result of needle deflection.....	124



# Chapter 1: Introduction

## 1.1 Chapter introduction

Percutaneous needle insertion has become standard procedure for treating cancers in place of open surgery in those days. Using fine needles contributes to decrease tissue damages and complication risks. Meanwhile, the accuracy of needle insertion may be decreased due to the needle deflection. This work describes the development of planning for achieving accurate needle insertion using interventional robotic systems.

This chapter introduces the background of this study that includes trends of recent cancer treatments focusing on lymphatic malignancy, importance of percutaneous needle insertion skills and clarification of our target in this study, and related works regarding modeling for needle insertion, approaches for accurate needle insertion and robotics systems.

## 1.2 Background of Cancer Treatment

### 1.2.1 Cancer trend and lymphatic malignancy

The number of patients and deceased people due to cancers has been increased worldwide amid aging of population. As described in World Health Organization (WHO) report, 8.8 million people all over the world died from cancer in 2015, which is nearly 1 in 6 of all global deaths [1.1]. As same in Japan, cancers are also leading the top cause of death and affect about 300,000 people per year as shown in Fig. 1.1 [1.2]. Cancers become immediate diseases and be called “National affliction”. The number of deceased people due to cancers between 1960 and 2014 in Japan is shown in Fig. 1.2, which is classified for specific major types of cancers [1.2]. The number of cancer patients will be increased obviously considering progress in aging of population in developed countries.

In those many types of cancers, lymphatic malignancy is one of the blood-tumors that most of Japanese disease [1.3]. Lymphatic malignancy is a disease that lymphocytes in blood vessels, which is a type of white blood cells, become cancerous. The lymphocyte is differentiating cells of blood-forming stem cells in blood vessels as same as other types of white blood cells. The differentiating lymphoid stem cells are classified in terms of immune functions such as T

lymphocyte (T-cells) and B lymphocyte (B-cells) as shown in Fig. 1.3 [1.4-1.5]. The cause of lymphatic malignancy has not been entirely cleared, although it is considered that cancer genes are activated because the genes mutate [1.5]. The lymphatic malignancy occurs at mainly lymph nodes and lymph tissues of spleen and tonsil as shown in Fig. 1.4, and at possibly gastrointestinal tracts, thyroid, lung, liver, skin, bone marrow and brain.

As the first symptoms of lymphatic malignancy, some lumps occur at areas where there are many lymph nodes without pain [1.5]. If the disease condition progresses for several weeks or months continually, the lumps are spread as tumors to the entire bodies and cause systemic symptoms such as a fever, losing weight and nocturnal sweating. In addition, it is possible to lead airflow obstructions, paralysis and blood flow disturbances when the organs are compressed by the tumors. In those cases, it is often necessary to do urgent surgical operation.

The lymphatic malignancy is divided into Hodgkin's lymphoma and non-Hodgkin's lymphoma [1.5]. The feature of Hodgkin's lymphoma is that there are less necrosis and fibrosis of lymph tissues. The non-Hodgkin's lymphoma is more divided in terms of lymphocyte types, morphological features, immune characteristics and clinical grades (Table 1.1). The type of lymphatic malignancies that most of Japanese disease are the non-Hodgkin's lymphoma.

In order to diagnose the types of lymphatic malignancies through pathology examinations, doctors usually conduct biopsies that a part of tumor, which cut by surgical procedures such as percutaneous needle insertion, is observed with microscopes [1.6]. In addition, for evaluating the tumor size and how spread the tumor is in the entire body, image inspections with computer tomography (CT), magnetic resonance (MR) or ultrasound (US), pancreatic endocrine tumor (PET) inspection and bone-marrow inspection are implemented [1.6].

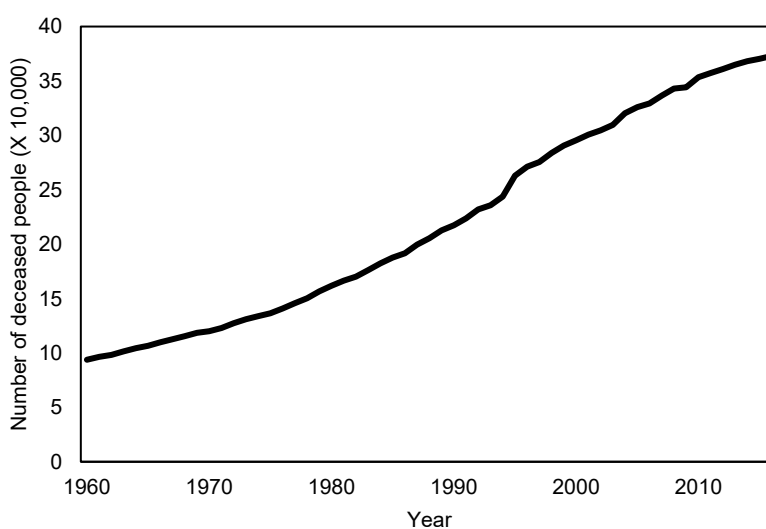


Fig. 1.1 The number of deceased people due to cancers

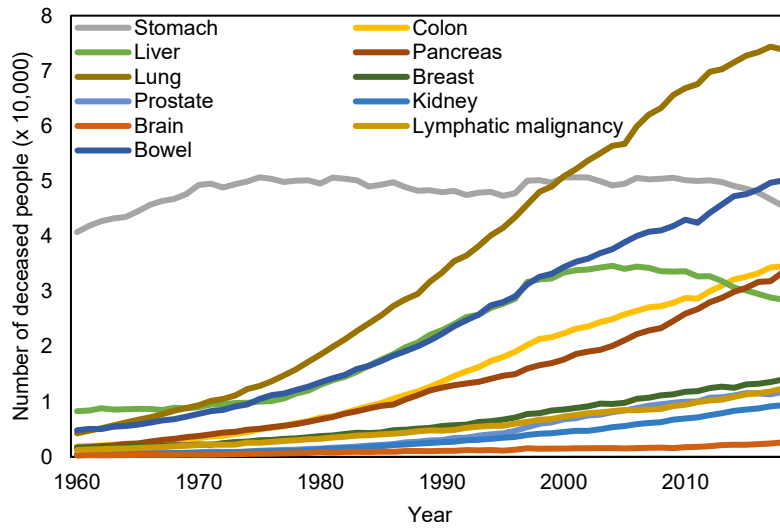


Fig. 1.2 The number of deceased people by types of cancer

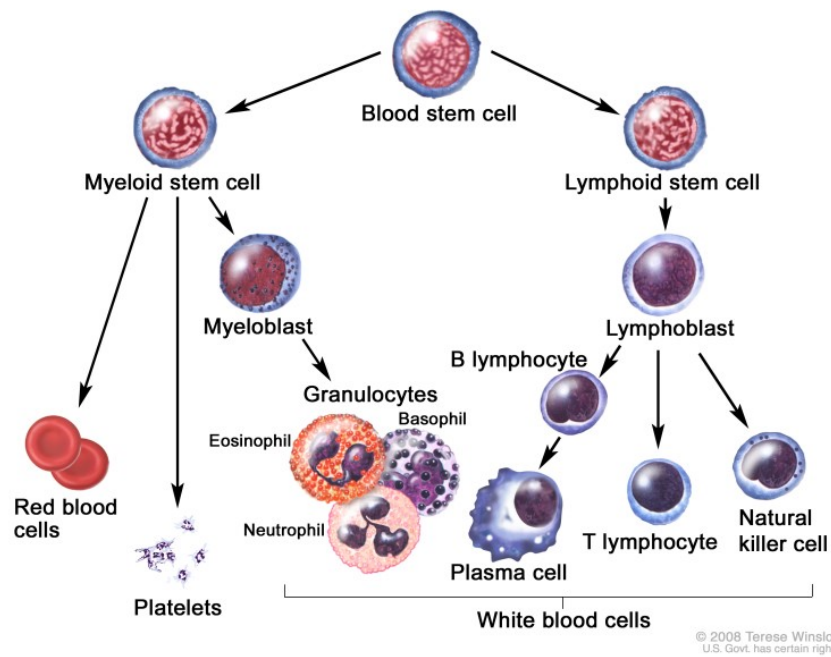


Fig. 1.3 Classification of stem cell types [1.4]

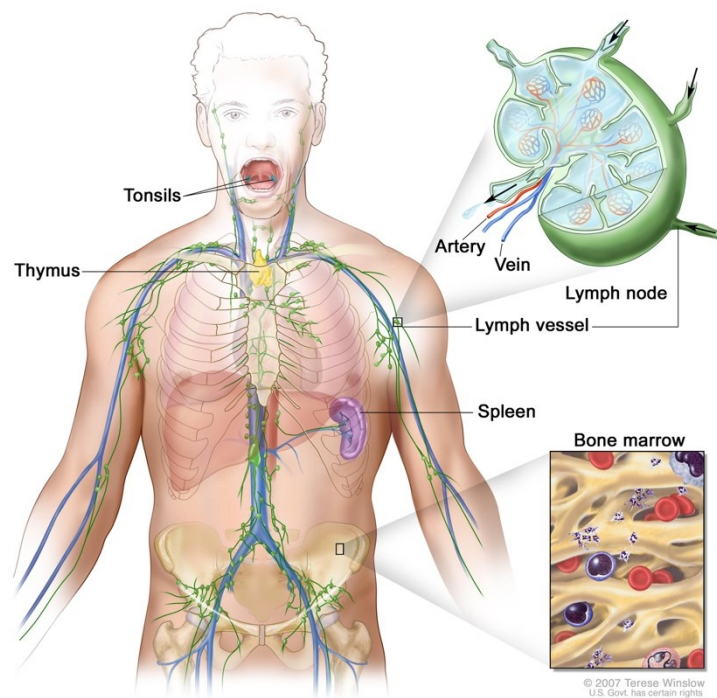


Fig. 1.4 Areas of lymph malignancy occurred [1.7]

Table 1.1 Classification of types of non- Hodgkin’s lymphoma by clinical grades

Clinical grades	Types of non- Hodgkin’s lymphoma
Low-grade malignancy (Progress in years)	<ul style="list-style-type: none"> <li>● Follicular lymphoma (stage I, II)</li> <li>● Mucosa-associated lymphatic tissue lymphoma</li> <li>● Lymphoplasmacytic lymphoma</li> <li>● Mycosis fungoides</li> <li>● Sezary syndrome</li> </ul>
Middle-grade malignancy (Progress in months)	<ul style="list-style-type: none"> <li>● Follicular lymphoma (stage III)</li> <li>● Mantle cell lymphoma</li> <li>● Diffuse large B-cell lymphoma</li> <li>● Peripheral T-cell lymphoma</li> <li>● Extranodal NK-T-cell lymphoma</li> </ul>
High-grade malignancy (Progress in weeks)	<ul style="list-style-type: none"> <li>● Burkitt's lymphoma</li> </ul>

## 1.2.2 Treatment for lymphatic malignancy

### 1.2.2.1 Standard therapies

The therapeutic principle for lymphatic malignancy is decided considering patient's body conditions based on the appropriate pathology examination and stage classification. The standard therapies are chemotherapy and radiation therapy [1.3], [1.8]. In case that those therapies have low effect, intensive chemotherapies or hematopoietic stem cell transportation are implemented.

Main standard therapy is chemotherapy to take or inject cancer drugs or molecular target drugs for eliminating the tumor's size. Cancer drugs can decrease the number of cancer cells but normal cells are also damaged, which may lead various side effects such as bone-marrow suppression, nausea, vomiting, diarrhea, canker sore, hair loss and fever [1.9]. Although there are many types of cancer drugs, multidrug therapies combining four or five types of cancer drug are usually provided as standard approaches [1.8]. Combinations of several cancer drugs usually work better than only single drugs because different types of drug can kill cancers in different ways. ABVD chemotherapy, which is combined with Adriamycin, Bleomycin, Vinblastine and Dacarbazine, is widely provided for the Hodgkin's lymphoma [1.10]. To most of the non-Hodgkin's lymphoma, Composition of R-CHOP chemotherapy, which is combined with Rituximab, Cyclophosphamide, Doxorubicin Hydrochloride, Oncovin and Prednisone, and monoclonal antibody is used as standard approaches [1.11]. Molecular target drugs can block the cancer cell's growth by hindering with specific targeted molecules associated with carcinogenesis and tumor growth [1.12]. The molecular target drugs are often injected with ordinal cancer drugs. Representative molecular target drug is Rituximab which can kill malignant B-cells that have CD20 on their surface as a characteristic protein of cancer cells [1.12].

Radiation therapy can eliminate the cancer by exposing high-energy X-ray to the targeted tumors from the outside body [1.13]. In case that the focus is in one place and early stage lymphatic malignancy, the radiation therapy is provided alone or with short-term chemotherapies. As side effects of radiation therapy, dermatitis and mucositis occur at the exposure part. In additions, nausea, vomiting, lassitude, loss of appetite and reduction of white blood cells appear as systemic symptoms of side effects.

In case that both the chemotherapies and radiation therapies don't even exert a curative influence or the possibility of recurrent cancer is high, hematopoietic stem cell transportation is conducted [1.14]. Hematopoietic stem cell transportation can recover the function of bone marrow by injecting hematopoietic stem cell obtained previously from patients.

### 1.2.2.2 Immune therapy

Recently, immune therapies are expected to be new approaches as the fourth cancer treatment all over the world, in addition to three major cancer treatments (surgeon, radiation therapy and cancer drug) [1.15-1.18]. Our body eliminates generated cancer cells by using our immune system. The immune system can prevent foreign substances such as bacteria and virus from invading. In the immune system, white blood cell plays the main roll of immunity and dendritic cell (DC) has a roll of conveying the information about the foreign substances to the white blood cell [1.19-1.22]. Immunity is divided into mainly two types; natural immunity which we have by nature; acquired immunity which we can acquire by contacting various foreign substances thorough our life. In the natural immunity, there are natural killer (NK) cells which can attack the foreign substance, and macrophage and neutrophil cell which have an ability of phagocytosis. In the acquired immunity, T-cell and B-cell have important rolls. T-cell is composed of killer T-cell, helper T-cell and suppressor T-cell. The killer T-cell can attack the foreign substance following the information obtained from the helper T-cell which has a roll of command of immune system.

The patients cannot control the cancer growth because the patient have weak immune systems due to damages of cancer genes or tumor-suppressor genes. Especially, the ability for recognizing the foreign substances such as a cancer with DC is decreased, which may lead the cancer growth.

Immune therapies are a type of cancer treatment that improves the immune system to attack the cancer directly or to stimulate the immune system [1.23]. Representative types of immune therapy to attack the cancer directly are checkpoint inhibitors, adaptive cell transfer, monoclonal antibodies and cancer vaccines. The author describes the overview of each representative immune therapy following.

- (a) Check point inhibitor [1.24]: Check point inhibitors are drugs that can enhance the immune system to respond more strongly to tumors by releasing “brakes” of T-cells to attack cancer cells. Then, the drug can interfere with the ability of cancer cells to avoid immune system attack.
- (b) Adaptive cell transfer [1.25]: Adaptive cell transfer can boost the natural ability of the T-cells to attack cancer. In the treatment, the T-cells are collected from a patient’s tumor and grown in the laboratory. By increasing the number of T-cells outside and returning its inside the body via needles, the immune system to fight cancers can be improved.
- (c) Monoclonal antibody [1.26]: Monoclonal antibodies are immune system proteins produced in the laboratory and called therapeutic antibody. The antibody is designed to attach targets found on cancer cells. Monoclonal antibodies are divided into two types. Some monoclonal antibodies can mark cancer cells in order to be detected easily and destroyed by the immune system. Other monoclonal antibodies can prevent cancer cells



from growing or cause them to self-destruct.

- (d) Cancer vaccine [1.27-1.28]: Cancer vaccine can work against cancer by boosting immune system's responses to cancer cells. Types of cancer vaccine are divided into peptide vaccine and DC vaccine. The peptide vaccine is the treatment that, by injecting the cancer specific antigen synthesized from various peptide artificially, the immune system recognizes the antigen and attack the cancer tumor. While, the DC vaccine is the treatment that by injecting DCs after culturing DCs extracted from body and training the DCs to recognize the cancer antigen, the response to the cancer is caused effectively.

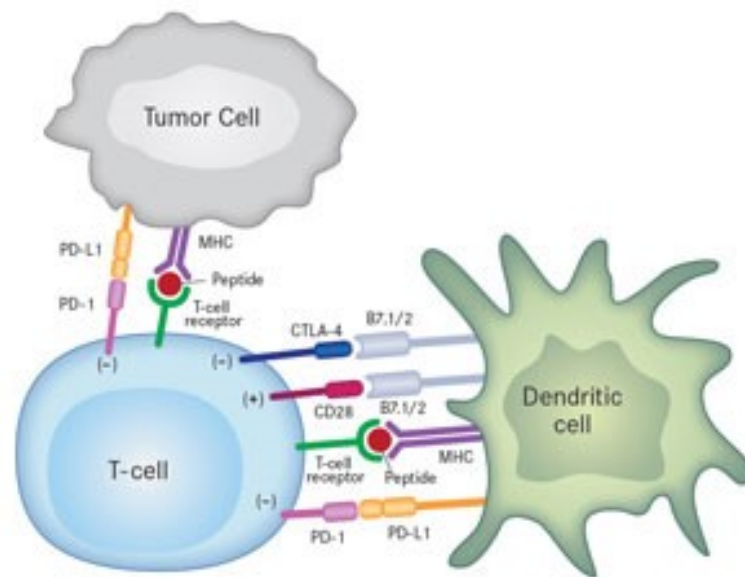


Fig. 1.5 Roll of dendritic cells [1.19]

### 1.2.2.3 HITV cancer therapy

As a new approach of immune therapy, HITV (Hasumi Immuno- Therapeutic Vaccine) cancer therapy has been developed by Dr. Kenichiro Hasumi [1.29-1.31]. The protocol involves injection of immature autologous DCs into tumor directly combined with Tomotherapy. As I mentioned, dendritic cells have the ability for enabling selective and effective attack against tumor cells by T-cells. Meanwhile, ordinal dendritic cells based anti-cancer therapy had not performed to initial expectations. As one of the reasons, since many dendritic cells injected intravenously may be trapped in the pulmonary circulation, enough dendritic cells are not able to reach the targeted tumor site. By injecting DC into the tumors, DC can be reached to the tumors certainly. The number of DCs reaching the tumor is obviously effective to introduce T-cells. Therefore, it is necessary to inject the vaccine into the targeted tumor accurately through percutaneous needle insertions in order to perform the therapy effectively. Especially, the HITV cancer therapy was a proven therapy for lymphatic malignancies and adenoma [1.29].

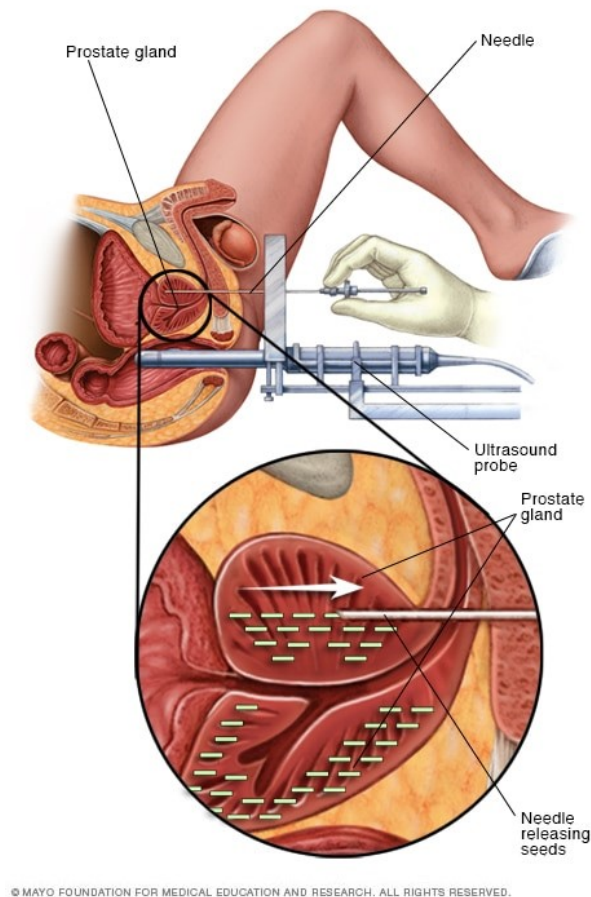
## 1.2.3 Percutaneous needle insertion

### 1.2.3.1 Types of needle insertion application

Percutaneous needle insertion is used for various purposes of the cancer diagnosis and therapy in addition to the HITV cancer therapy, and be necessary to be placed into tumors accurately. I categorize the major applications of percutaneous needle insertions in terms of diagnosis and therapy in this section.

- (a) Biopsy [1.32]: Biopsy is a sample of tissue taken from the suspected parts in the patient's body. As we mentioned, percutaneous biopsy is often needed to obtain a definite diagnosis of cancer. Therapy plan and procedure are basically established based on the firm diagnosis with biopsy. The biopsy also can categorize the localized region spread, lymph node involvement and metastasis. For patients taking treatments, repeat biopsies are necessary in order to evaluate the treatments are effective for the patient or to check the occurrence of recurrent cancer. Moreover, the demand for biopsy has been increased drastically in those days because of the emergence of targeted therapies aiming at specific molecular defects. The types of biopsy are divided into three common techniques: fine-needle aspiration biopsy (FNAB), core-needle biopsy (CNB) and vacuum-assisted biopsy (VAB) [19]. FNAB and CNB have been compared in terms of the sensitivity, specificity and other aspects, and chosen depending on the lesion of biopsy.
- (b) Percutaneous ethanol injection [1.33]: Percutaneous ethanol injection therapy (PEIT) is an injection of ethanol through the skin directly into the tumor. Ethanol has a chemical action of clotting proteins composing cancers. This therapy is basically applied for liver tumor and thyroid cancers. As side effects of PEIT, transient aching pain, a feeling of drunkenness and fever occur although the specific treatment to each symptom is not necessary.
- (c) Radio frequency ablation [1.34]: radio frequency ablation (RFA) is a treatment to insert a needle thorough the skin into a liver tumor under image guidance such as ultrasound image. RFA can heat the tumor by passing high-frequency electrical currents through an electrode in the needle.
- (d) Cryosurgery [1.35]: Cryosurgery is to destroy tumors by being frozen with an extreme cold liquid nitrogen or argon gas. The cryosurgery is used to treat external tumors such as skin tumors and apply the liquid nitrogen directly to the tumors. For internal tumors, liquid nitrogen or argon gas are injected through a hollow instrument such as a needle under image guidance.

- (e) Brachytherapy [1.36]: Brachytherapy is to destroy tumors by placing a small radioactive source directly into the tumor through a needle. This therapy is performed to prostate cancers. The needle is inserted with transrectal ultrasound probe as shown in Fig. 1.6.



© MAYO FOUNDATION FOR MEDICAL EDUCATION AND RESEARCH. ALL RIGHTS RESERVED.

Fig. 1.6 Overview of brachytherapy [1.36]

### 1.2.3.2 Medical image modality

Percutaneous needle insertion is required to obtain target positions and needle tip positions with medical image modalities for showing information of internal body [1.37]. As the representative medical image modalities in the percutaneous needle insertion, physicians ordinarily use computer tomography (CT), magnetic resonance imaging (MRI), ultrasound (US) as the guidance. The feature of each modality is described below briefly.

- (a) CT scan [1.38][1.39]: CT images can be produced by computing X-ray absorption values which is measured by exposing X-ray as fan-beam to targeted parts in spirals. The CT scan is used in various cases because the image clarity and resolution are high compared to other modalities. It is also the convenient modality as the time of imaging takes only about

ten seconds. As the difference of X-ray absorption is calculated for generating CT images, CT scan are mainly used in areas including bone and air where X-ray are less to transmit, such as head, lung and abdomen. As the disadvantage, patients must be exposed to 5-30mSv of X-ray with every CT scans. In case of needle insertion therapies, doctor also be often exposed to holding and keeping needles to the body. In addition, some artifacts are generated on the images if metal materials are included in the scan area as shown in Fig. 1.7 [1.40].

- (b) MRI [1.38][1.41]: MRI can generate hydrogen atom image with proton nuclear magnetic resonance symptom. Then, it is suitable to image soft tissue and organ including much moisture, and vessel. The MRI can also provide high clarity and resolution images as same as CT scan. As the significant difference between CT and MRI, the MRI can generate images without radiation exposures. However, the scanning time of MRI takes about 30-60 minutes and MRI generate loud noises during scanning. Then, the claustrophobia patient and children are difficult to use MRI since they must wait inside MRI gantry for long time. Moreover, as much magnetism are generated during the scan, magnetic material is prohibited to take near and inside the MRI gantry. Then, patients who implant a pacemaker cannot use MRI.
- (c) US [1.38][1.42]: US can generate images of internal body structure with the difference of tissue conduction (acoustic impedance) by sending and receiving ultrasound pulses from the US probe. Although the image clarity of US is inferior as compared with CT and MRI, high frequency ultrasound can generate high resolution images because of increasing distance resolutions. The feature of US compared to both CT and MRI is to obtain images real-time without any stresses for patients during scan such as noise and radiation exposure. However, as biological tissues absorb the signal of ultrasound, it is difficult to obtain the clear image at the deep part of body. Especially, in case of the abdomen including thick fat, it is difficult to observe the deep part as the ultrasound is reflected or scatter. In addition, it is not suitable for the area including air such as lung and lower-abdomen because the ultrasound decay significantly.

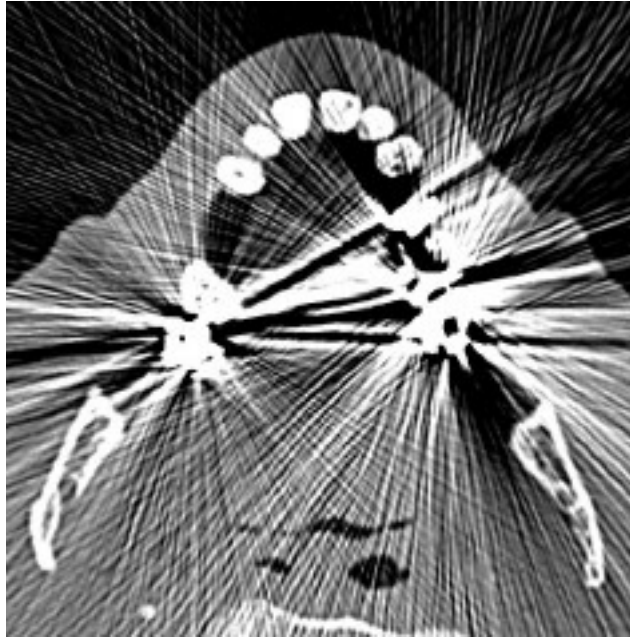


Fig. 1.7 Sample of metal artifacts on CT image [1.40]

## 1.2.4 Challenges for accurate fine-needle insertion

As the author described above, the accurate percutaneous needle insertion into tumors is required in various diagnosis and therapies. Meanwhile, the percutaneous needle insertion is constrained and complex procedure because of target visibility, tool maneuverability and physiological interaction [1.43]. Doctors conventionally manipulate needles based on haptic feedback from the needle and their imagination of anatomical structure obtained through experiences. For improving the visibility during the procedure, it is important to select the appropriate image modality to check the position of needle and target during insertion depending on the targeted part, although there are still several problems such as modality cost, image resolution, material compatibility and stress/tissue damage for patients [1.37]. In addition to the imaging limitation, there are several causes to decrease the needle insertion accuracy such as needle deflection, tissue deformation, target uncertainty and human errors [1.43-1.45].

Especially, the needle deflection is a key issue to affect the needle tip misplacement. The dominant factors to cause the needle deflection are the needle tip shape and needle diameter [1.46-1.49]. The needle used in usual therapies are bevel-tip type, which is contributed to needle deflection because the asymmetric reaction forces are generated between needle tip and tissues during insertion into tissues. Moreover, the diameter of needle is a serious factor for causing needle deflection. The needle with small diameters is easily deflected because a second moment

of area of the needle become small when the needle is assumed as a cantilever beam.

Meanwhile, tissue damages for patients can be decreased with using fine needles since the amount of cutting tissue is small [1.50-1.51]. Serious tissue damages may lead to not only patient's trauma due to pain but also swelling and complications [1.52-1.55]. According to a previous research, in biopsies of lung lesions, the number of cases with severe complications such as air embolism were increased by using a core biopsy needle of 18-20 gauge, compared to use fine aspiration needles [1.56]. In another research regarding lung biopsy, the complication rate of pneumothorax was drastically decreased by using extra-fine needle of 25 gauge [1.57]. Also, in the survey of liver biopsy, procedures of 16 gauge needles had a higher percentage of complication occurrence compared with 18 and 20 gauges [1.58]. In additions, regarding a risk fine-needle abdominal biopsy, the rate of major complications such as peritonitis, tumor seeding and hematoma was 0.05% in 11,700 patients by using fine needles of 20-23 gauges [1.54]. Therefore, the fine needle insertion is preferred for patients although it is difficult for doctors to manipulate the fine needle to be inserted into the target accurately.

The tissue deformation which occurs during the needle insertion into tissue may also cause the needle deflection [1.44][1.59-1.60]. The amount of tissue deformation varies depending on interaction forces between needle and tissue, which is related to mechanical properties such as elasticity and needle insertion conditions such as the insertion speed.

## 1.3 Purpose of this study

The purpose is to explore new ways to improve the procedure of percutaneous needle insertion with medical image guided interventional robotic systems. The goal is to develop the system for achieving accurate insertion to arbitrary tumors with an extra-fine needle (under 25 gauge) under ensuring the patient's safety.

In this paper, the author focused on a lymphatic malignancy located on para-aortic lymph nodes in lower-abdomen as the insertion target [1.61]. The para-aortic lymph node in lower-abdomen is one of the most difficult targets because the target is located at a deep part in a body (about 100 mm from skin). Then, the needle has to pass through several lower-abdominal tissues and organs for reaching into the target, and thereby the needle deflection occurs complexly. The size of lymph nodes diagnosed as lymphatic malignancy is more than  $\phi 10$  mm [1.62]. As the feature of lymphatic malignancy, the lymph node is rubbery compared with swollen lymph nodes due to usual infections. Then, it is required to insert the needle at the center of tumor as possible, thereby the target accuracy is set at 2 mm in this study.

In addition, it is necessary to use the extra-fine needle since the needle is inserted into bowels,

thereby peritonitis from perforation of bowels need to be avoided for decreasing the crack generated by needle tips [1.63]. As mentioned above, extra-fine needle insertions can contribute the decrease of complications and painful. While, the length of commercial extra-fine needle is limited. In anthesis and hypodermic needles, extra-fine needles of 25-33 gauge have already gained clinical acceptance and been commercialized [1.64-1.65]. However, the commercial needles which satisfy both the diameter of thinner than 25 gauge and the length over 100 mm for reaching the para-aortic lymph node in lower-abdomen are very rare when the author surveyed. Therefore, in this study, the author uses the extra-fine needle of 25 gauge which satisfy the length of 100 mm and be used in clinical site.

In case of the lower abdominal needle insertion, CT is usually used as the medical image modality. As lower abdomen includes bowel, airs such as bowel gas may be included in the imaging area [1.66]. CT can provide high resolution images at deep parts in the body, even including airs in the imaging area, compared to US and MRI. However, patients are exposed to X-ray every time of scanning with CT. If the needle is inserted repeatedly once the needle deflection occurs, the amount of radiation exposure for patients is increased. The typical radiation dose in CT abdomen is about 10 mSv per scan [1.67]. While, high-level radiation exposure greater than 100 mSv to the body in short period of time may cause potential health risks. Therefore, it is not desirable to obtain the needle tip position real-time as same as US imaging and be necessary to realize the accurate insertion with the extra-fine needle with minimum abdominal CT scan.

In this study, the author aims to develop the system for achieving accurate insertion with the extra-fine needle (under  $\pm 2$  mm) with minimum CT scan in lower abdomen.

## 1.4 Related works

In the past, a number of researchers has been explored approaches to achieve accurate needle insertion from various standpoints. The author divides the related researches into two categories; interventional needle insertion robots and state of arts of insertion methods: needle steering techniques.

### 1.4.1 Interventional needle insertion robots

Many interventional needle insertion robotic systems have been developed in the past. Those robotic systems can be classified by the type of medical image modalities. Table 1.2 shows a list of all the CT-, MRI- and US-guided robotic systems targeting thorax and abdomen, which the

author could survey from the recent science literatures and review articles [1.68-1.109].

In the table 1.2, we can see that the previous interventional systems vary significantly in terms of architectures, degree of freedom and so on. Those systems can be further categorized based on the mounting types: patient-mount type and table-mount type including a gantry and floor, and the insertion types: manual insertion (just holding and placing needle) and robotic insertion, in addition to the image guidance types.

The design of CT- and MRI-guided robots is especially limited since the robots locate and move in the limited space inside the scanner gantry (typically 60-90 cm). In addition, it is necessary to consider the material compatibility of robots. As mentioned above, the artifact occurs on CT images if the metallic material is included in the field of view of CT images. In MRI, ferromagnetic materials cannot be used as parts of the robots due to the strong magnetic field generated from the MRI gantry. Most of the CT- and MRI-guided robots are designed for conducting the biopsy in thoracic and abdominal areas and RFA in liver. While, US-guided robots are focused on the brachytherapy in prostate and RFA in liver due to the restriction of US image resolutions.

Focusing on the CT-guided needle insertion robot systems, the author could not find the research using extra-fine needles under 25 gauge. As the robots were basically designed to the procedure of biopsy, the needle thicker than 20 gauge was used. Therefore, the accuracy of needle placement using the thick needle could be under 5 mm, although the certain needle deflections still remain. In addition, there is no research regarding the lower-abdominal insertion, even including other types of interventional robots.



Table 1.2 Classification of interventional robotic system for assisting needle insertion

University	Project/robot name	Modality	Actuator types	Mounting types	DOF	Needle condition		Accuracy mm	Evaluation Depth mm	Test phantom	Target	Therapy Type	Project status	Ref.
						Motion	Gauge							
University of Freiburg	-	CT	Motor	Table	2	Manual	-	1.6	75	Pig organs	Liver, lung	-	P	[1.68]
University of Twente	RICIBION	CT	Motor	Table	5	Robotic	23G	<2	100	Gelatin phantom	Lung	Biopsy	P	[1.69-1.70]
Okayama university	-	CT	Motor	Table	6	Robotic	16-19G	3.2	50-90	In vivo pig	Liver, lung etc.	Biopsy, RFA etc.	C	[1.71-1.73]
LSIIT	CT-Bot	CT	Piezo motor	Patient	5	Manual	16G	<5	65	Artificial phantom	-	Biopsy	A	[1.74-1.75]
University of Tokyo	-	CT/MRI	Ultrasonic motor	Table	6	Robotic	-	<3	-	Watermelon	Brain	Neurosurgery	P	[1.76]
MIT	Robopsy	CT/MRI	Motor/ Piezo motor	Patient	3	Robotic	18G	-	-80	In vivo pig	-	Biopsy	A	[1.77-1.78]
TIMC Laboratory MIT	LPR	CT/MRI	Pneumatic	Patient	5	Robotic	15-22G	<2	100	Foam phantom	-	Biopsy	A	[1.79-1.83]
Harvard Univ.	-	CT/MRI	Piezo motor	Patient	3	Robotic	17G	-	125	-	-	-	P	[1.84-1.85]
Johns Hopkins University	PAKY/RCM /AcuBot	CT/US	Motor	Table	6	Robotic	22G	1.2	-	Agar phantom	Lumbar spine Prostate	Nerve/facet block Brachytherapy	C	[1.86-1.90]
Johns Hopkins University	B-ROB/iSYS	CT/MRI /US	Motor	Table	4-6	Manual	15-20G	1.1	85	Foam phantom	Prostate	Biopsy Brachytherapy	C	[1.91-1.93]
Innomedic	Innmotion	MRI/CT	Pneumatic	Table	5	Manual	15G	1	40-70	In vivo pig	General	Biopsy	C	[1.94-1.95]
Johns Hopkins University	MR Safe Robot	MRI/CT	Motor	Table	1	Manual	18G	<3	70	Beagle dog	Prostate	Biopsy	A	[1.96]
Johns Hopkins University	Arthrobot	MRI	Piezo motor	Patient	4	Manual	20G	3.4	45	Gelatin phantom	Shoulder	Biopsy	P	[1.97-1.98]
KIOS Research Center	-	MRI	Manual	Table	6	Manual	20G	<5	-40	Butter phantom	-	-	P	[1.99]
Washington University	-	MRI	Pizeo motor	Table	7	Manual	-	1.6	-	-	-	-	P	[1.100-1.101]
Worcester Polytechnic Institute	-	MRI	Piezo motor	Table	6	Manual	-	-	-	-	Brain, prostate	Biopsy Brachytherapy	A	[1.102-1.104]
University of Twente	-	US	Motor	Table	2	Robotic	0.5mm (Nitinol)	<2	100	Gelatin phantom	Prostate	Brachytherapy	P	[1.105]
University of Alberta	-	US	Motor	Handy	2	Manual	18G	<1	140	PVC phantom	Prostate	Brachytherapy	P	[1.106]
Stanford University	-	US	Motor	Table	2	Robotic	0.5mm (Nitinol)	<2	30	ex vivo bovine liver	Liver	RFA	A	[1.107]
Waseda University	-	US	Motor	Handy	2	Robotic	18G	-	80	Pig liver	Liver	RFA	A	[1.108]

Noted that the status of (P), (A) and (C) in the table shows to conduct a phantom test, animal test and clinical test, respectively.

## 1.4.2 Needle steering techniques

Recently, novel approaches to control a needle path trajectory, calling *needle steering*, have been developed [1.110-1.114]. The types of needle steering methods can be divided into tip-based steering, base control, and tissue control as shown in Fig. 1.8 [1.110]. According to the recent literatures regarding the needle steering, the main stream is based on the tip-based steering because other two methods have been still challenging [1.115-1.118]. Inserting a bevel-tip (asymmetric tip) needle used most commonly in clinical procedures into a soft tissue, the needle is deflected following a circular arc due to the interaction forces between the needle and tissue applied to the needle tip. Thus, the needle tip can be placed at arbitrary positions if the needle deflection is modeled and controlled.

As the first versatile model, Webster et al. proposed a kinematic-based nonholonomic model for controlling the trajectory of a flexible needle with the bevel-tip [1.119]. As the direction of needle deflection can be controlled by rotating the bevel-tip direction, it is able to generate a trajectory avoiding anatomical interferences such as bones and sensitive areas concentrating blood vessels and nerves. Therefore, for achieving the accurate needle steering, it is necessary to model the arbitrary needle deflection.

As the limitation of the kinematic-based model, the interaction between the needle and tissue is not taken into account the model [1.120-1.121]. For estimating the needle deflection accurately, mechanical properties of needle and tissue are required to implement the needle deflection model. In the past, several researches focused on a mechanic-based needle deflection model [1.46], [1.47], [1.49], [1.122-1.125]. The model can estimate the needle deflection with an interaction force between the needle and surrounding tissue, which require mechanical properties of the tissue and needle as input data of the model. Representative tissue parameters are Young's modulus, tissue cutting forces, and viscosity coefficients. The parameters are needed to be approximated or obtained from direct measurements accurately since the error of the measured parameters may cause a drastic effect for the accuracy. However, in most of the developed models, the parameters are obtained through material tests such a compression test under assuming that the tissue is a homogeneous. It is challenging for obtaining the accurate parameters preoperatively in clinical situations because the parameters vary depending on individuals.

In order to adjust the parameters of the deflection models and compensate errors of needle trajectory, it is necessary to measure the needle tip position and posture real-time for inserting the needle under closed-loop control [1.111]. In most of researches, the needle is steered with US image as shown in Fig. 1.8 [1.105-1.107], [1.122], [1.126-1.136]. The radius of curvature of needle deflection in a kinematic model can be fitted adaptively with filters (i.e. a particle filter

and a linear Kalman filter) based on needle tip position tracked by 2D axial ultrasound images [1.136]. Meanwhile, there are still many challenges of tracking needle tip clearly. Especially, the noise or artifact are often contained in the image depending on the targets.

As an alternative approach for tracking the needle tip, fiber Bragg grating (FBG) sensors and electromagnetic (EM) sensors have been researched. The FBG sensors which are embedded into the needle can measure axial strains inside the needle by using a reflection of light through the fiber, thereby can estimate and visualize the needle deflection directly [1.137-1.141]. The EM sensors which are also embedded into the needle can obtain three-dimensional positions by detecting the varying electromagnetic field that the field generator emits [1.69-1.70], [1.143-1.144].

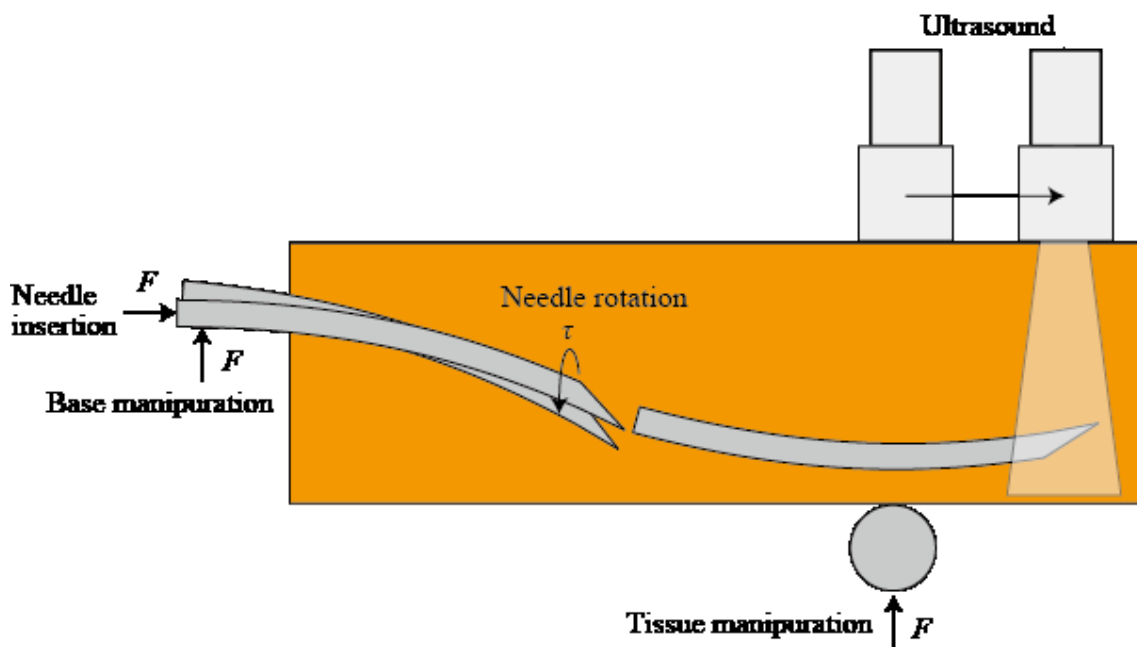


Fig. 1.8 Types of needle steering methods

## 1.5 Objective of this study

### 1.5.1 Setting the theme

As introduced in the previous sections, a number of interventional robotic systems for percutaneous needle insertion has been developed. However, there are few studies for assisting the lower abdominal needle insertion. Most of previous studies aimed to assist for targeting the prostate and liver. Since those targets are solid organs/tissues and can be reached without several tissues or organs the needle has to penetrate, the modeling of needle deflection can be developed accurately. In addition, those targets can be applied to US imaging, which enable to obtain real-time feedback of needle tip and target positions. Consequently, a closed-loop control of needle path such as the needle steering technique can be applied to those targets. Meanwhile, in case of the lower abdominal insertion, applying the needle steering is still challenging for two issues. First, as the lower abdomen is composed of several characteristic tissues, which may cause complex needle-tissue interactions, the accurate modeling of needle deflection is difficult. Especially, modeling the behavior of bowels may not be realistic due to uncertain boundary conditions. As another issue, there is less feedback information with CT imaging. As I mentioned in previous section, CT is usually used as medical imaging modality in case of the lower abdominal insertion because of obtaining clear images even including airs. Then, applying the real-time closed-loop control such as the needle steering with CT imaging is not desirable for patient's damages in terms of much radiation exposures.

In short, in case of the lower abdominal insertion, it is ideal to plan an optimal trajectory that the fine needle can be reached into the target accurately only with preoperative CT imaging. Meanwhile, it is difficult to estimate the accurate path trajectory under the complex situation. Then, the author considered that it is realistic to generate a straight insertion path by minimizing the needle deflection robustly. If the method for generating the straight insertion path robustly under such the complex case can be developed, the number of CT scan time can be minimized (ideally, before insertion and after completed insertion). Therefore, in this study, the author aims to develop needle insertion planning for minimizing the needle deflection targeting lower abdomen.

## 1.5.2 Objective

The objective is the development of a CT-guided needle insertion robotic system for implementing needle insertion plan for minimizing the needle deflection targeting around para-aortic lymph node in lower-abdomen.

In order to achieve the objective, the author approached from two perspectives mainly; insertion control planning and insertion path planning. The insertion control planning determines how to insert the needle into each tissue for minimizing the needle deflection. While, the insertion path planning determines where to insert the needle from the body surface for minimizing the needle deflection. Moreover, it is also required to develop the robotic system for implementing those approaches to clinical sites. The concept of the proposed system is shown in Fig. 1.9.

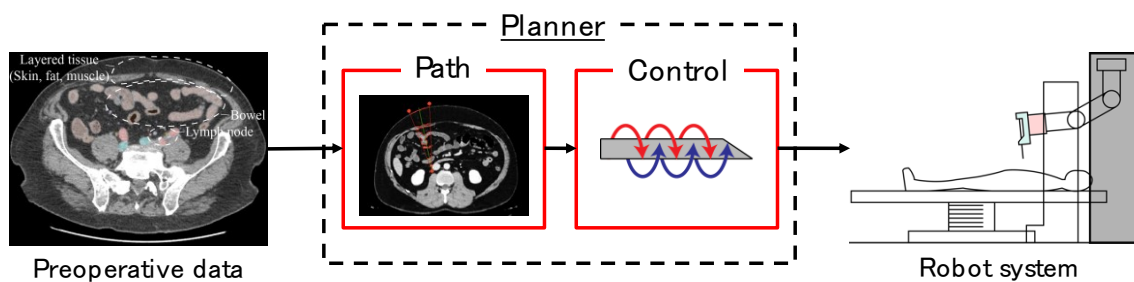


Fig. 1.9 The concept of proposed CT-guided needle insertion robot system

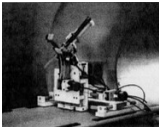




## 1.5.3 Contribution

As described previously, there has been few developments of the interventional robotic system assisting the lower abdominal insertion with the extra-fine needle. Table 1.3 shows a difference between previous studies and this study. Through the comparison to previous studies, the author can describe the major contributions of this study as follows.

- The interventional robotic system with an extra-fine needle (under 25 gauge) focusing on the lower abdominal insertion was developed.
- The author developed new preoperative planning methods for minimizing the needle deflection in terms of insertion control and insertion path.
- The author designed a CT-guided interventional robotic system for implementing the insertion control and path planning.
- The availability of the insertion control planning, insertion path planning and robotic

systems are quantitatively evaluated through *ex vivo* and *in vivo* experiments.

Table 1.3 Comparison of previous researches of CT-guided needle insertion robot and this study

	 (1991)	 (AcuBot, 2010)	 (Innomotion, 2008)	 (LPR, 2016)	 (Zerobot, 2017)	This study
Institution	U. Tokyo TWMU	Johns Hopkins Univ.	Innomedic	TIMC- IMAG	Okayama Univ.	Waseda Univ.
Target	Brain	Lumbar spine	Prostate	General	Liver, lung, kidney	Lower abdomen
Depth	-	-	40-70mm	100mm	50-90mm	80-120mm
Needle diameter	(Φ3mm)	22G	15G	15-22G	16-19G	25G
Accuracy	<2mm	<3mm	1mm	<5mm	3.2mm	<2mm
Therapy type	Neuro surgery	Nerve/facet block	Biopsy	Biopsy	Biopsy RFA	Drug injection

## 1.6 Overview

This thesis is composed of seven chapters. Overviews of each chapter are described following.

- Chapter 2 (Experimental analysis of needle deflection)

Regarding the mechanical phenomena during needle insertion into each tissue and organ composing lower abdomen (layered tissue including skin, fat and muscle, and bowel), the author summarized the mechanical properties needed to be considered for decreasing the needle deflection through experimental analysis. At first, the needle insertion was conducted into *ex vivo* tissues with porcine loin and bowel in order to observe the behavior of needle deflection and insertion force depending on the tissue characteristic. Next, the needle is inserted at various angle to the same tissues for observing the needle deflection and insertion force depending on tissue geometries.

- Chapter 3 (Insertion control planning)

Based on the experimental analysis of chapter 2, the author proposed insertion control planning to multi-layered tissue and bowel, respectively. As the requirements of insertion control, it is required to equalize the direction of needle tip forces and to reduce stiffness force, cutting force and friction force during needle insertion under satisfying the safety for patient. Then, regarding the insertion for multi-layered tissue, the author proposed the insertion control method with combination of high frequency vibration along insertion direction and bidirectional axial spinning to insertion direction. Regarding the insertion for bowels, the author proposed the combination of the vibration and the rotation of needle tip angle every time at puncturing bowel walls to cancel the needle deflection.

- Chapter 4 (Insertion path planning)

The author proposed the preoperative insertion path planning method for determining appropriate needle insertion position and angle to achieve a straight path from skin to tumor. In the chapter 2, it was confirmed that the insertion angle at tissue boundary is key issue to affect the needle deflection. Then, the author made a hypothesis that the total needle deflection can be minimized by performing the insertion path that the sum of insertion angles at each tissue surface and boundary on the path is minimized. In addition, the effect of insertion angle causing the needle deflection varies due to the tissue properties and the tissue boundary positions. Then, weight factors of each insertion angle in the path planning were implemented. As the design of weight factor, the author developed the probability that the needle deflection is within acceptable amount. Moreover, in order to implement the path planning method on CT images, the author developed the image processing method to detect the tissue boundary from CT images and to calculate the insertion angle in each boundary.

- Chapter 5 (CT-guided needle insertion robotic systems)  
The author described the CT-guided needle insertion robotic systems for implementing the proposed insertion control planning in chapter 3 and insertion path planning in chapter 4. This robotic system is composed of needle insertion unit which enable to implement the insertion with vibration and rotation; robot arm which move the needle insertion unit to appropriate position and angle based on the path planning; and registration marker for conducting coordinate transform between the robot arm and CT image.
- Chapter 6 (Evaluation)  
The availability of the proposed insertion control and path planning with the robotic system was evaluated through *in vivo* experiment with micro pig. In addition, the limitation of this study was mentioned.
- Chapter 7 (Conclusion)  
Summary of the achievement and remaining tasks of this study were described in this chapter. As the future work, the author described the issues for achieving the robotic system to clinical application.

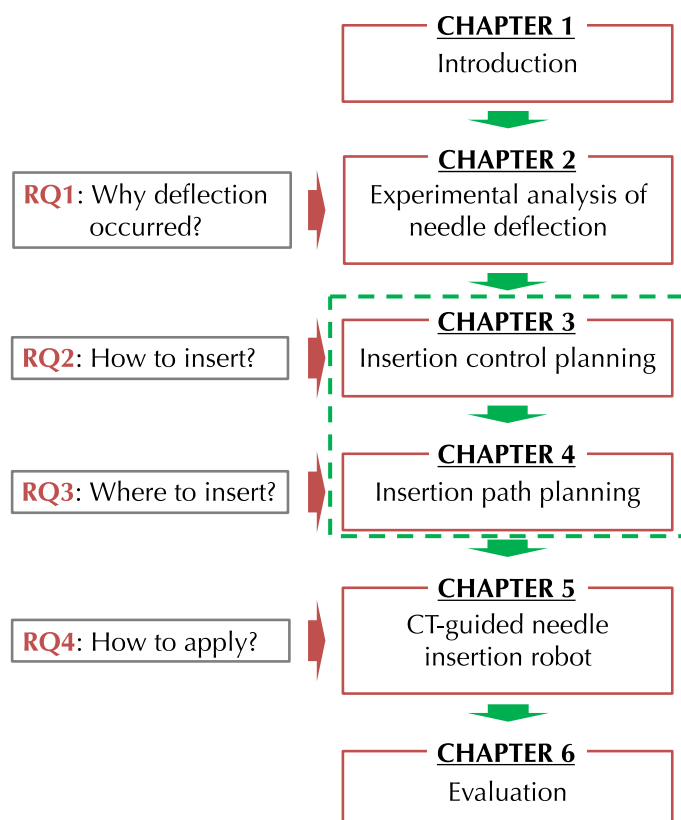


Fig. 1.10 Overview of this paper



# Chapter 2: Experimental analysis of needle deflection

## 2.1 Chapter introduction

Experimental analysis of the needle deflection is described in this chapter. The needle deflection occurs complexly due to several factors such as the tissue properties, interaction forces, amount of tissue deformation, boundary conditions and other uncertain phenomena. Then, it is important to investigate the tendency of the needle deflection and the needle-tissue interaction in each tissue composing lower abdomen through experimental analysis in order to develop the insertion control and path planning method to decrease the needle deflection. This chapter shows the experimental analysis with biological tissues dividing the lower abdomen into layered tissue and bowel in terms of tissue properties.

The author uses figures and sentences by referring the author's published papers in this chapter.

## 2.2 Mechanism of needle deflection

### 2.2.1 General needle insertion flow

When inserting the needle into soft tissue, the relative behavior of needle and surrounding tissue must be considered. By observing the position of the needle relative to tissue surface or boundary, needle insertion flow can be divided into two phases in terms of interaction between the needle and tissue mainly, as shown in Fig. 2.1 [2.1-2.2]. Phase 1 is a term that the needle comes into contact with the tissue surface or boundary, and phase 2 begins after puncturing the tissue surface or boundary. The needle cuts and be inserted inside the tissue during phase 2, which ends when the needle passes through the tissue or contacts an internal tissue boundary. These phases may be repeated during the needle insertion into multilayered tissues or organs.

While, focusing on forces applied to the needle during insertion into the tissue (needle insertion force), the behavior of the needle insertion force varies depending on each the insertion phase. According to previous works, the needle insertion force can be divided into stiffness force, friction force and cutting force [2.2-2.3]. To model the needle insertion force considering needle-tissue

interactions, the total loaded force of needle can be expressed following [2.2]:

$$f_{total}(x) = f_{stiffness}(x) + f_{friction}(x) + f_{cutting}(x) \quad (2.1)$$

where  $z$  represents needle tip position,  $f_{total}$  is the total loaded force during insertion, and  $f_{stiffness}$ ,  $f_{friction}$ , and  $f_{cutting}$  are the stiffness force, friction force, and cutting force applied on the needle, respectively. The stiffness force occurs when the needle is breaching the membrane. The friction force loaded around the needle shaft occurs due to the tissue adhesion and damping. The cutting force occurs when the needle tip slices the contact tissue during passing through the tissue. In the phase 1, the tissue surface or boundary deforms until the stiffness force exceeds a certain value. The stiffness force increases nonlinearly until breaching the boundary and drops significantly after the breach. Some researchers modeled the stiffness force [2.2-2.5]. The amount of tissue deformation differs due to tissue properties such as the elasticity and the direction of the deformation, which further changes depending on the tissue shape and fiber type inside the tissue [2.6-2.7]. In addition, the breach event differs due to the needle insertion speed [2.8-2.9]. During the second phase, the cutting force loaded at the needle tip and the friction force load around the needle shaft occur. The sum of cutting force and friction force often increases linearly according to the insertion distance [2.10-2.11]. The cutting force is approximately constant depending on the tissue characteristics [2.12-2.14]. While, the friction force differs due to the insertion distance and insertion speed, and be modeled by some researches [2.12], [2.14-2.17].

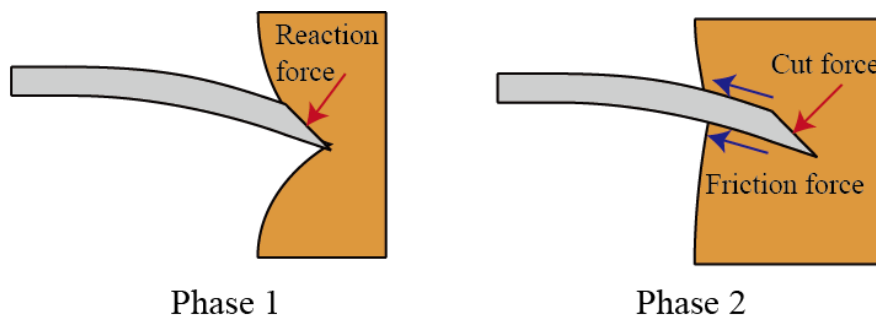


Fig. 2.1 General flow of needle insertion into soft tissue

## 2.2.2 Mechanical model of needle deflection

Several research groups have developed the needle deflection model with kinematic and mechanical based approaches as introduced in chapter 1. As referring the mechanics-based deflection model, the needle-tissue interaction forces in phase 1 and 2 can be represented as shown

in Fig. 2.2. The main factors of needle deflection are the stiffness/cutting force loaded at a needle tip ( $F_{stiffness}/F_{cutting}$ ) and the friction force loaded around a needle shaft ( $F_{friction}$ ). To support the vertical direction forces, the virtual spring which represents reaction forces from tissues is located along the needle.

The needle-tissue interaction force varies due to needle insertion conditions such as insertion speeds and tissue properties such as stiffness, viscous elasticity, non-homogeneity and boundary conditions [2.3]. Some studies showed that the needle insertion speed affected the needle-tissue interaction forces in phase 1 since the amount of tissue deformation until breaching tissue surface changes [2.1], [2.9], [2.11], [2.18-2.20]. Thus, the stiffness force in phase 1 can be reduced as the insertion speed is increased. While, the friction force in phase 2 also varies due to the insertion speed [2.3]. As the soft tissue has viscoelasticity, the relative velocity between the needle shaft and surrounded tissues causes the friction force. Thus, fast needle insertions cause to increase the friction forces. Moreover, the author assumed that relative insertion angles between the needle insertion direction and tissue surface/boundary which change due to the tissue shape cause the needle deflection. Misra *et al.* described that the tissue deformation direction pushed by the needle tip differs depending on the tissue shape [2.6]. Thus, the relative angle between the needle insertion direction and tissue surface/boundary may affect the direction of tissue deformation. As the tissue deformation occurs in phase 1 significantly, the change of deformation direction due to the insertion angle may cause misplacements of needle tip in phase 1, thereby causes large deflections.

In short, the author consider that it is necessary to investigate the behavior of needle deflection in lower-abdomen because the interaction force varies due to needle insertion conditions and tissue properties.

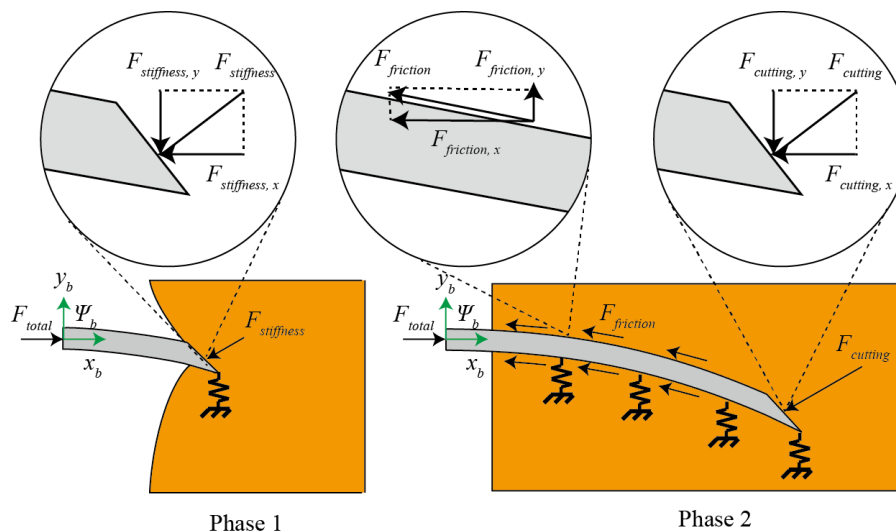


Fig. 2.2 Mechanical model of needle deflection

## 2.2.3 Composition of lower-abdomen

As introduced in the previous section, the needle deflection can be modeled generally. Based on the needle deflection model, the author investigates the behavior of needle deflection in lower abdomen. In order to insert the needle into para-aortic lymph node in lower abdomen from body surface, the needle needs to pass through several tissues which have different features respectively as shown in Fig. 2.3. The features of main tissues composing lower abdomen are described below.

- (a) Skin with fat [2.21]: the structure of human skin is divided into epithelium, dermis and hypodermal tissue. Although the thickness of epithelium is about 2 mm, the large force is required to breach it with needle as the stiffness of epithelium is high. Hypodermal tissue includes fats so that the tissue is easily deformed. The thickness of hypodermal tissue in lower abdomen varies between different individuals including age, sex and body-mass index.
- (b) Muscle [2.22]: muscle is located under skin with connective tissues. Respective muscles in lower abdomen are abdominal rectus muscle and abdominal external oblique muscle. In contrast to skin, as the muscle is fibered tissue, the stiffness of muscle varies due to the thickness, density and direction of the muscle fiber.
- (c) Bowel [2.23]: abdominal cavity is under the muscle and includes many organs inside. In this case, the needle can pass through large and small bowels. The bowel is a tube shape and composed of several membranes. The bowel often generates bowel-gas in decomposing residual dross of food with bowel bacteria. In addition, the bowel performs peristaltic motion for digestion.

In terms of tissue properties, it is considered that the feature of bowel is totally different from skin and muscle. Therefore, the author investigates the needle deflection during insertion into the lower abdomen, which is separately divided into (I) layered tissues including skin, fat and muscle, and (II) bowels.

In additions, when the path planning of the needle is performed on preoperative CT images, the insertion angles at each tissues surface and boundary vary depending on selected needle paths. In usual clinical case, physicians determine a target and entry point on the patient's skin avoiding large blood vessels and obstacles such as ribs [2.24]. Since the insertion angle may cause the large deflection as mentioned above, the author investigates the needle deflection due to the insertion angle in both the layered tissue and bowel.

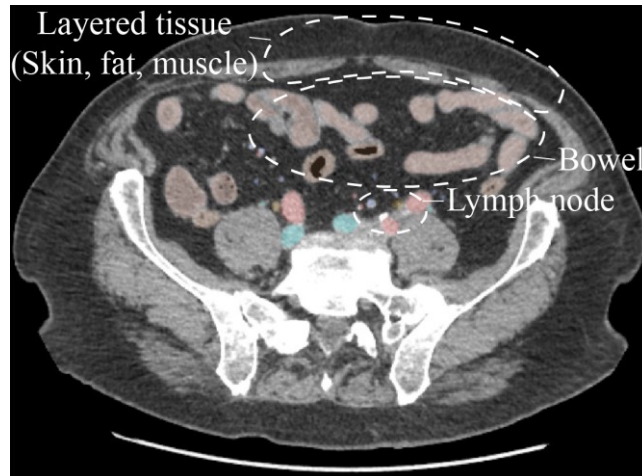


Fig. 2.3 Anatomical structure of lower abdomen

## 2.3 Experimental analysis of needle deflection

### 2.3.1 Experimental setup

In this section, the author investigates the needle deflection in layered tissues composed of skin and muscle, and bowels through needle insertion experiments. As introduced in the previous section, the interaction forces causing the needle deflection may be changed due to tissue properties and relative angle between the tissue surface (or boundary) and insertion direction. Then, the needle deflection is measured under several conditions of insertion angle to the layered tissue and bowel. As the target of layered tissue and bowel, a pork rib including a fat layer and porcine small bowel are used in this experiment, respectively.

A needle insertion robot system used in this experiment has 3-DOF; a ball screw actuator for needle insertion, a stepping motor for rotation around insertion axis and a piezo actuator for vibration along insertion direction as shown in Fig. 2.4. The insertion motion is achieved by positioning the mounting base attached to the needle. The force/torque sensor (Nano 17 force/torque sensor; ATI Industrial Automation, USA) is attached to the needle hold part for measuring the needle insertion force loaded at needle base. The detailed specification of the needle insertion robot is described in chapter 5. The needle specifications were following: diameter, 25 gauge; length, 100 mm; Young's modulus, 197 GPa; and tip type, bevel tip at 20°. The needle deflection was measured from front and side direction on camera images captured by a high-definition camera (FCB-EV7500; Sony, Tokyo, Japan). The deflection was calculated with the Pythagorean theorem with pixel numbers of transverse direction length between the initial and

the final needle tip positions on both front and side images. The image resolution was 1920 pixel  $\times$  1080 pixel.

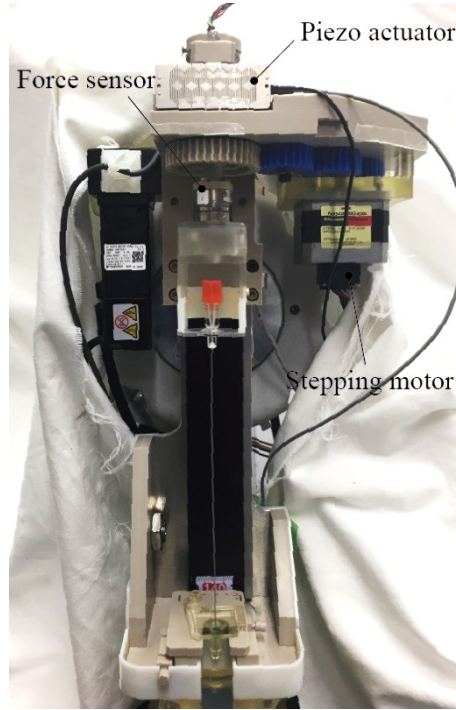


Fig. 2.4 Overview of needle insertion robot used in this experiment

### 2.3.2 Effect of target properties

In the first experiment, the needle deflection due to target properties is measured with a pork rib and bowel. The pork rib is cut to be rectangular solid at  $50 \times 50 \times 40 \text{ mm}^3$ . The bottom of pork rib is fixed at a base and both sides are free end as shown in Fig. 2.5 (a). The bowel is cut to be a cylinder at  $\varnothing 25 \times 100 \text{ mm}$  and fixed by clamping both side edges of bowel with glues to cylinder bases as shown in Fig. 2.5 (b). Four insertion speed is set at 5 mm/s in both targets. The insertion distance and angle are fixed at 60 mm and  $0^\circ$ , respectively. Twelve insertions were conducted in each condition. The results were analyzed statically with one-way analysis of variance (multiple comparison method: Bonferroni correction).

The result of the needle deflection of layered tissue and bowel is shown in Fig. 2.6. The time series of the insertion force of layered tissue and bowel is shown in Fig. 2.7 (a) and (b), respectively. The needle deflection of the layered tissue was higher than of the bowel, although the thicknesses of the targets are different. Focusing on the time-series of the insertion force data, the behaviors of insertion force between layered tissue and bowel are different.

Focusing on Fig. 2.7 (a), the insertion force was increase nonlinearly and drastically up to 2 sec from starting at the insertion. This behavior shows that the needle was pushing the skin surface, thereby the tissue deformation occurred. Thus,  $f_{stiffness}$  in Eq. (2.1) was loaded at the needle tip dominantly. Between 2 and 3.5 sec, the insertion force was repeatedly increased and decreased after the drastic decrease of insertion force at 2 sec. The behavior shows that the needle cut internal tissues (fat) under the skin after a puncture of the skin due to the certain force applied to the skin surface, and be pulled with stick-slip frictions by surrounding fats. Thus,  $f_{cutting}$  and  $f_{friction}$  in Eq. (2.1) were loaded at the needle tip and shaft, respectively. After that, the insertion force was increased drastically again around 4 sec. The behavior shows that the needle was pushing a boundary tissue (connective tissue) between the fat and muscle. As same as the behavior during the insertion into the skin, the drastic decrease of insertion force occurred around 4 sec. The similar tissue deformation when puncturing the boundary may occur inside although the current setup could not observe the phenomena. The insertion force was composed of  $f_{stiffness}$  due to the connective tissue and muscle, and  $f_{friction}$  of the fat. From 4 sec up to 9 sec, the insertion force was repeatedly increased and decreased as same as the insertion into fat. The behavior also shows that the needle cut internal fibers repeatedly in the muscle and be pulled with the stick-slip friction of the fat and muscle. After 9 sec, as the needle passed through the layered tissue, only the friction force of fat and muscle loaded at the needle shaft remained.

Focusing on Fig. 2.7 (b), the insertion force was increase nonlinearly and drastically up to 2.5 sec from starting at the insertion. As same as the behavior of puncturing the skin, this behavior shows that the needle was pushing the upper surface of bowel, thereby  $f_{stiffness}$  in Eq. (2.1) was loaded at the needle tip dominantly. After puncturing the upper surface, the insertion force was decreased up to near zero. This is because the bowel is hollow organ, thereby cutting force don't occur as there is no internal tissue and the friction force is low as the contact area between the needle and bowel is so small. Around 3 sec, the insertion force was increased drastically again. This also shows that the needle was pushing the lower surface of bowel and  $f_{stiffness}$  was loaded at the needle tip again. After puncturing the lower surface at 4.5 sec, the insertion force was decreased up to 0.05 N. Between 4.5 and 9 sec, the insertion force was increased slightly after puncture of lower surface. This may occur because the bowel attached the needle with the friction force is deformed and generate the restoring force to the insertion force. Although the restoring force was relaxed around 10 sec, the force was increased slightly again.

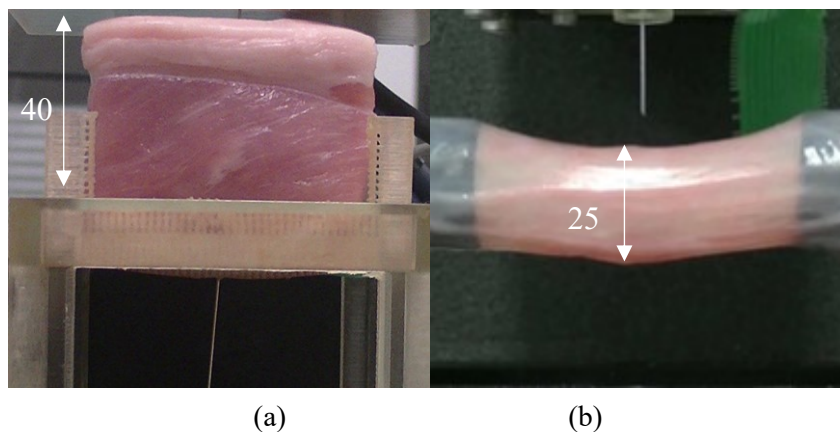


Fig. 2.5 Experimental conditions of insertion targets: (a) pork rib, (b) porcine small bowel

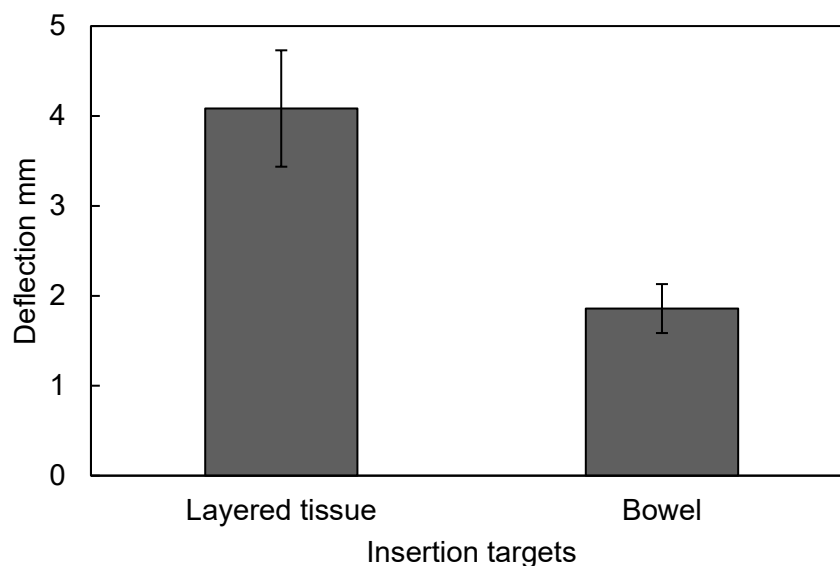
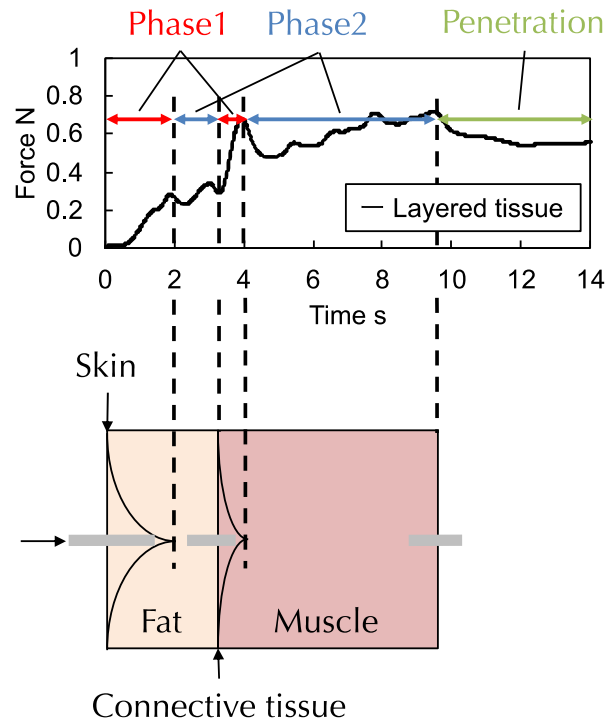
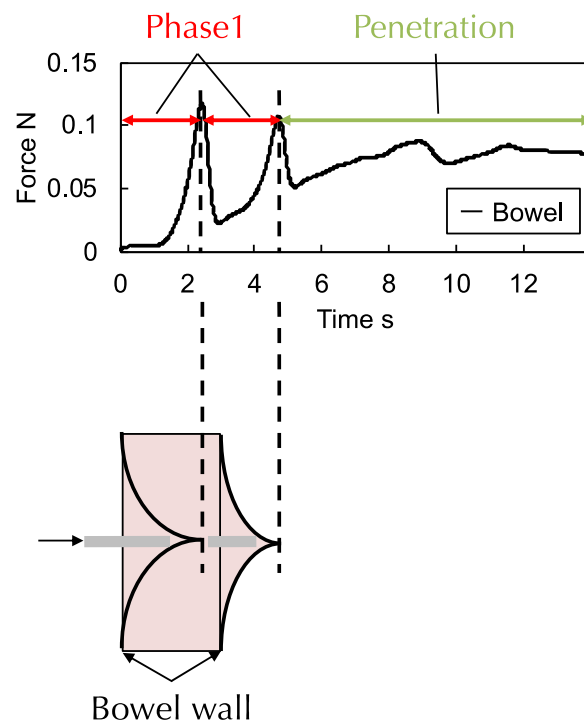


Fig. 2.6 The result of needle deflection due to tissue properties





(a)



(b)

Fig. 2.7 The result of time-series of insertion force of (a) layered tissue and (b) bowel

### 2.3.3 Effect of insertion angle

In the second experiment, the pork loin is cut to be rectangular solid at  $150 \times 200 \times 40 \text{ mm}^3$ . The bottom of pork loin is fixed at a base and both sides are free end as shown in Fig. 2.8 (a). The bowel is cut to be square membrane at  $10 \times 10 \text{ mm}^2$  and fixed by clamping the edge of membrane as shown in Fig. 2.8 (b). Four-way insertion angles were conducted ( $0, 15, 30$  and  $45^\circ$ ) in both targets. The insertion distance and speed are fixed at  $60 \text{ mm}$  and  $5 \text{ mm/s}$ , respectively. Twelve insertions were conducted in each insertion angle.

The result of the needle deflection of layered tissue and bowel is shown in Fig. 2.9. In both targets, the deflection was significantly increased due to the increase of the insertion angle. We assumed that the reason why the insertion angle affected the deflection is that the tissue deformation until puncturing the surface or boundary (in phase 1) causes the increase of deflection as shown in Fig. 2.10. The tissue surface or boundary continue to be deformed until the stiffness force loaded at needle tip exceeds a certain value. As the author mentioned, the amount of tissue deformation differs due to the tissue property and insertion condition, and the direction of the deformation varies due to the tissue geometry and fiber type [2.2]. Thus, the interaction forces in phase 1 may vary due to the amount and direction of tissue deformation, which leads further consequence deflections possibly. In case of inserting needle into the tissue surface or boundary perpendicularly, the interaction force between the needle tip and tissue is roughly even distributed as shown in Fig. 2.11. Meanwhile, in case of inserting at an angle, the distribution of the interaction force may be unequal. It is considerable that an additional load at the needle tip for the transverse direction arises for causing further deflections. In additions, the needle tip position may be slipped slightly on the tissue surface or boundary by the tissue deformation. It can be assumed that the needle tip position error until puncturing the surface had a large effect on the final deflection because the error affects the final deflection depending on the insertion depth linearly.

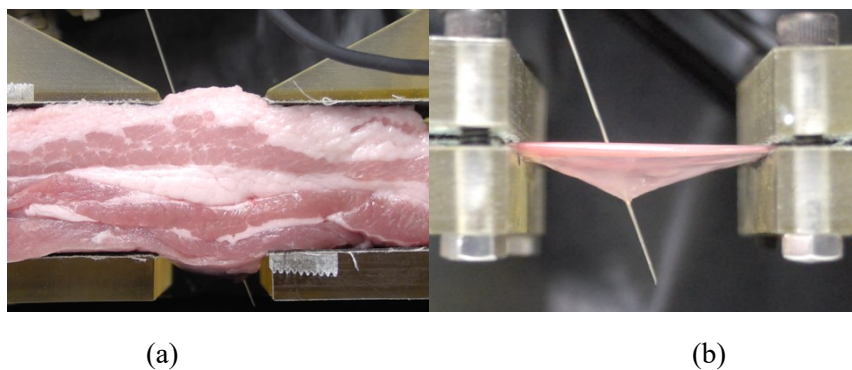


Fig. 2.8 Experimental condition changing insertion angles of (a) layered tissue and (b) bowel

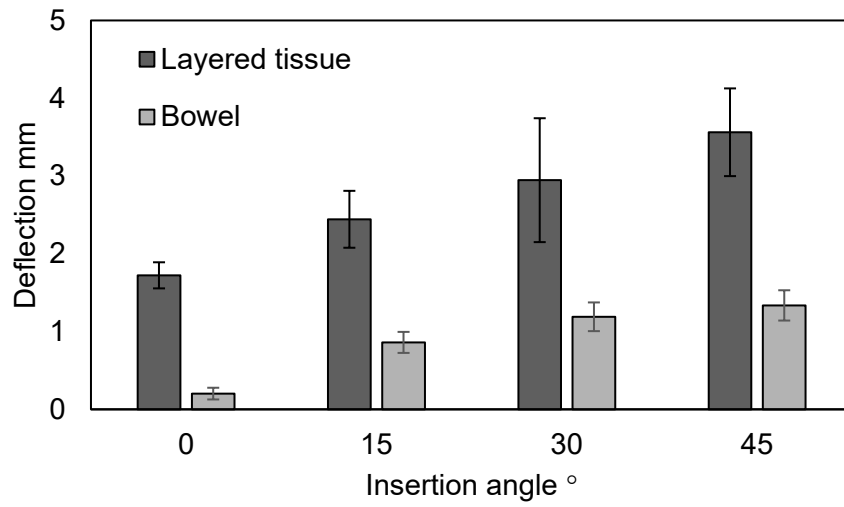


Fig. 2.9 The result of needle deflection due to the insertion angle

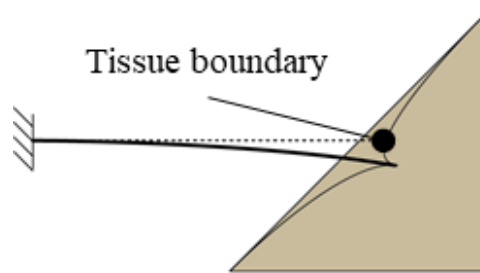


Fig. 2.10 The needle deflection in phase1 caused by the tissue deformation due to insertion angle

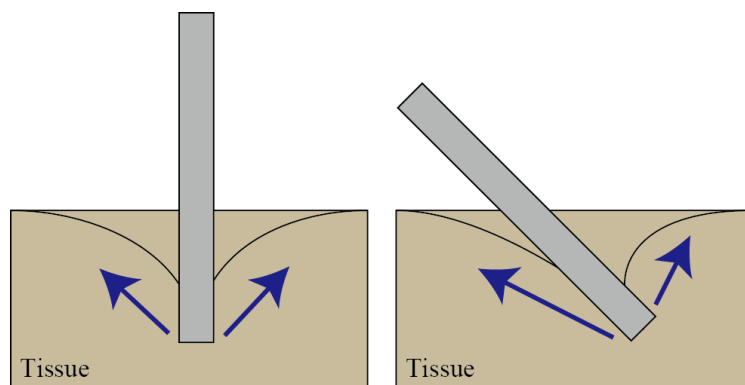


Fig. 2.11 The distribution of interaction forces due to insertion angle

## 2.4 Approach for decreasing needle deflection

The author observed that the behavior of insertion force between the layered tissue and bowel varied due to target properties. In the layered tissue, as the factors causing the needle deflection, there were the stiffness forces when puncturing the skin and boundary connective tissue (in phase 1), and the cutting and friction forces when inserted into the fat and muscle (in phase 2). While, in the bowel, the stiffness force when puncturing the upper and lower surfaces of bowel (in phase 1) may be the dominant factor for causing the needle deflection. Therefore, in order to decrease the needle deflection in each target, each insertion force in respective insertion phase need to be decreased or cancelled appropriately.

While, regarding the effect of insertion angles, the needle deflection was increased due to the increase of insertion angles definitely. Then, it is desired to insert the needle into the target surface and boundary perpendicularly, when the insertion path is planned with CT images. Meanwhile, as the structure of lower-abdomen is really complexed, it is impossible to search the desire insertion path in a clinical case. Therefore, it is required to develop the planning method to determine an optimum insertion path in an obtained CT image.

## 2.5 Summary

In this chapter, the author showed the mechanism of needle deflection referring previous mechanical models, and analyzed the needle deflection due to the target properties and insertion angles through *ex vivo* experiments in order to extract requirements of insertion control planning and insertion path planning. The author performed the needle insertion into the layered tissue and bowel that those targets compose the lower-abdomen mainly, and measured the needle deflection and insertion forces. In addition, the needle insertion is performed from various insertion angle into those targets. The results showed the behavior of insertion force varied due to the target properties and the needle deflection was increased due to the increase of insertion angle.

Therefore, for minimizing the deflection in each target, each insertion force in respective insertion phase need to be decreased or cancelled appropriately as insertion control planning, while, it is required to develop the planning method to determine an optimum insertion path taken into account of insertion angles.

# Chapter 3: Insertion control planning

## 3.1 Introduction

This chapter describes various insertion control planning methods for decreasing needle deflection. As introduced in the previous chapter, the interaction forces between the needle and tissue during needle insertion may cause excessive needle deflection. It can thus be assumed that needle deflection can be decreased by controlling the interaction forces.

The objective of this chapter is to describe methods for decreasing needle deflection by controlling the needle insertion motion based on the experimental analysis presented in the previous chapter. The methods were designed for use with layered tissue and bowel, respectively, and were verified through *ex vivo* experimentation.

This chapter details the requirements for insertion control and an approach that can be applied to significantly decrease needle deflection. In addition, the approach was optimized in terms of both accuracy and safety with respect to layered tissue and bowel. As a basic requirement for insertion control, the interaction forces loaded on the needle tip and shaft during the whole insertion procedure must be minimized. Consequently, a combination of high-frequency vibration along the direction of insertion and axial rotation around the insertion axis was applied to the insertion procedure. The vibration decreased the puncture/cutting force loaded on the needle tip along with the frictional forces around the needle shaft. The rotation equalized the asymmetric forces loaded on the beveled needle tip. The control method for the rotation was modified for each target in terms of both accuracy and safety.

The author has used figures and excerpts from the author's published papers in this chapter [3.1]–[3.3].

## 3.2 Approach

### 3.2.1 Planning requirements

As introduced in Chapter 2, the interaction forces between the needle and tissue during insertion may cause excessive needle deflection. The interaction forces were divided into forces loaded on the needle tip and forces loaded on the needle shaft in each insertion phase as shown in 2.2.1. In

phase 1, when the needle tip was pushing on the surface/boundary, the stiffness force, represented by  $F_{stiffness}$  in (2.1) and loaded on the needle tip increased until it overcame a certain value to breach the surface/boundary of tissue, which was defined as the puncture force. In phase 2 when the needle tip and shaft were inserted into tissue after breaching the surface/boundary, the cutting force was loaded on the needle tip and the frictional force was loaded on the needle shaft, represented by  $F_{cutting}$  and  $F_{friction}$  in (2.1), respectively. Minimization of these needle-tissue interaction forces is thus the desired outcome achieved by controlling needle insertion motion to minimize needle deflection.

Although there are some needle tip types that are designed to produce leading symmetric forces at the needle tip, such as the conical tip, it is difficult and costly to manufacture an extra-fine and long needle with that type of tip [3.4]. It is thus necessary to find a solution for reducing needle deflection by controlling the insertion motion with a typical beveled tip needle used in commercial products. Moreover, the previously discussed insertion forces may cause unnecessary pain to patients [3.5], [3.6]. Especially when the needle passes through an area that contains a number of sensory nerves and applies too much force to them. Trauma and body motion may occur in response to the pain, leading to the misplacement of the needle.

Therefore, it is proposed that the needle deflection can be decreased by controlling the insertion motion as a means of decreasing the interaction forces. As a method for controlling insertion motion, a combination of high-frequency vibration along the direction of insertion and axial rotation around the insertion axis is proposed. The details are described in the following sections.

### 3.2.2 Rotation

When using a bevel-tipped needle, the needle deflection depends on the direction in which the tip faces because an asymmetric cutting force is loaded on the needle tip during insertion into tissue. As mentioned in Chapter 2, the needle deflection can be modeled using cantilever beams and occurs predominantly due to the action of needle tip forces. Needle deflection can then be minimized by applying axial rotation because the asymmetric forces can be canceled by equalizing the vertical direction of the cutting force loaded on the needle tip as shown in Fig. 3.1.

Previous studies have also shown that insertion with rotation can decrease the needle deflection and targeting errors. Minhas et al. developed a duty-cycled rotation technique to control the needle's path [3.7]. By applying a high duty-cycle spinning motion, a straight insertion path could be ensured. Likewise, Abolhassani et al. developed a method to compensate for the needle deflection using rotation by estimating force/moment measurements online at the needle's base [3.8]. From the insertion force analysis perspective, a high-speed continuous rotation, like drilling

(spinning), was effective at reducing interaction forces as well as tissue deformation [3.9]. While, applying a low frequency rotation was reported to reduce tissue indentation and frictional forces [3.10].

However, the application of continuous axial rotation can lead to some tissue damage. Torsional frictional forces between the tissue and needle shaft occurring due to the rotation are especially harmful in this regard. This torsional friction may cause a discrepancy between the needle base and the tip angle, increasing the lateral force on the needle shaft [3.11]. Some researchers have stated that tissue damage may be mitigated by applying rotation. Observation of the needle path under axial rotational insertion into a gel substrate showed that high rotation speeds tended to increase tissue damage [3.12]. In addition, it was observed that connective tissue was wound up during rotational needle insertion into rats, and the force was increased during needle withdrawal [3.13].

Therefore, rotational insertion is expected to contribute to the reduction of needle deflection, but it is necessary to consider safety, because tissue damage may occur when applying continuous rotation to lower abdominal needle insertion.

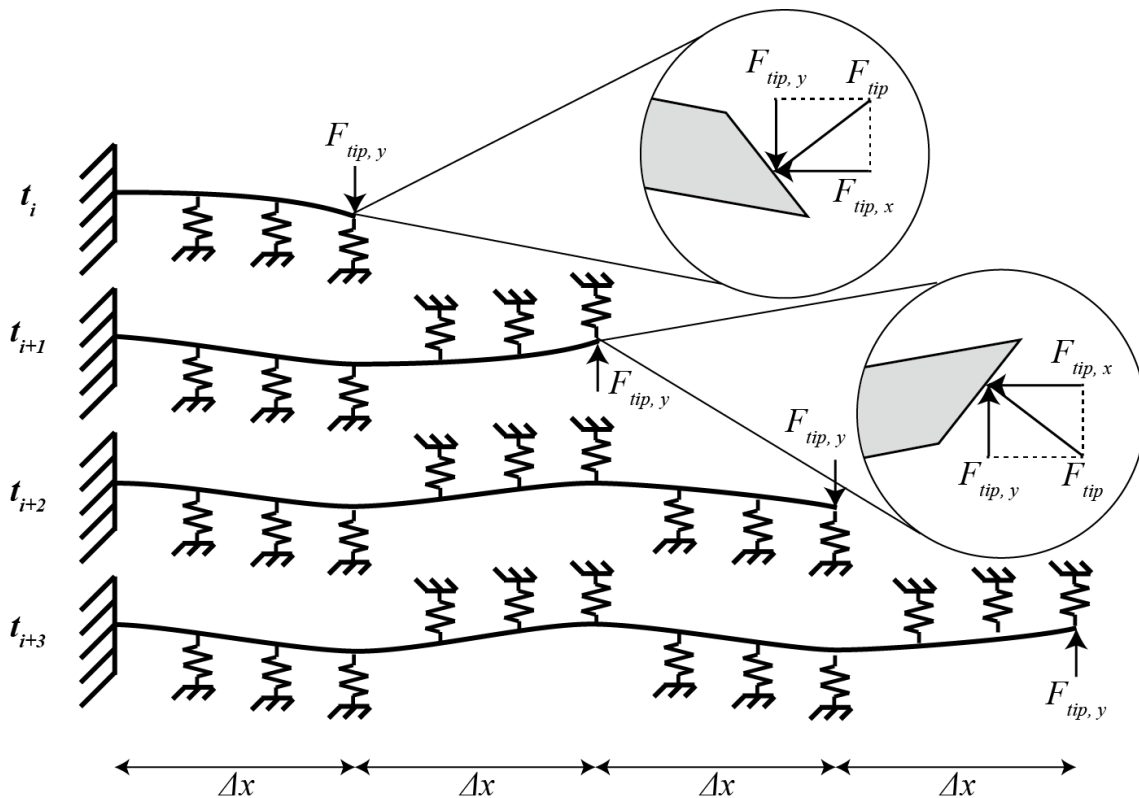


Fig. 3.1 Rotational insertion model with cantilever beams in each time step

### 3.2.3 Vibration

As mentioned above, fast needle insertion can decrease tissue deformation and the puncture forces in phase 1, thereby contributing to decreasing the needle deflection. Mahvash et al. modeled the interaction between the needle and tissue deformation using a modified Kelvin model as shown in Fig. 3.2, and showed that fast insertion contributed to decreased puncture force [3.14]. The author concluded that fast insertion also contributed to decreasing the cutting force, because internal tissue is composed of many layered components that possess viscoelasticity, such as fibers in muscle, and it may be easier to puncture each of the layers using fast insertion as shown in Fig. 3.2. However, fast insertion caused an increase in frictional forces loaded around the needle shaft due to the viscoelasticity of tissue mentioned above. Reed et al. noted that the needle-tissue interaction could be modeled as viscous friction, and tissue deformation could be modeled using the Kelvin-Voigt model, as shown in Fig. 3.3 [3.11]. In addition, the safety of the fast insertion procedure for practical cases involving living tissue is questionable. Actually, needle insertion speeds in clinical procedures typically range between 0.4–10 mm/s according to previous reports [3.15]. Speeds above this range may cause damage to surrounding organs and blood vessels. Thus, there are pros and cons to fast needle insertion.

It is proposed that the insertion speed of the needle tip can be increased locally by applying a vibrating motion along the direction of needle insertion, thereby contributing to decreasing the puncture and cutting forces. Moreover, by vibrating the needle shaft, the needle-tissue interaction in terms of viscous friction is expected to reduce. There are many reports in various fields of manufacture that indicate that ultrasonic vibration is effective at reducing frictional forces.

Previous research has been conducted related to vibration-assisted needle insertion. Shinei *et al.* reported the reduction of needle insertion forces by applying mechanical vibration to a needle [3.16]. Through the use of multilayered piezoelectric actuators, it was possible to apply vibrational motion at frequencies of up to 10 kHz to the needle. Through experimentation with insertion into swine muscle tissue, it was shown that the maximum reduction in frictional forces was 69%. A detailed explanation of the effect of the vibration amplitudes and insertion speeds used in the experiment was not described and there was no statistical analysis provided. Khalaji *et al.* developed a mathematical model of needle-tissue friction and showed that vibration-assisted needle insertion was effective for the reduction of friction [3.17]. However, as the experiment was performed in limited conditions using only a chicken breast as the insertion target, it is necessary to further investigate the effectiveness of vibration in lower abdominal needle insertions.

Another consideration is that, inspired by the mechanism associated with the insertion motion of a mosquito bite, the use of vibration-assisted needle insertion could reduce pain. As the



insertion force is related to the amount of pain experienced by the patient, as shown in other studies, it is expected that vibration-assisted needle insertion may contribute to improvements in accuracy and safety [3.5, 3.6].

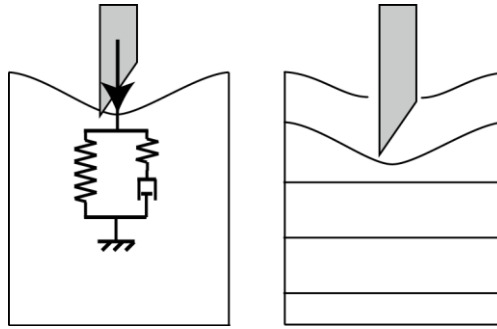


Fig. 3.2 Tissue deformation model during insertion with the modified Kelvin model [3.14]

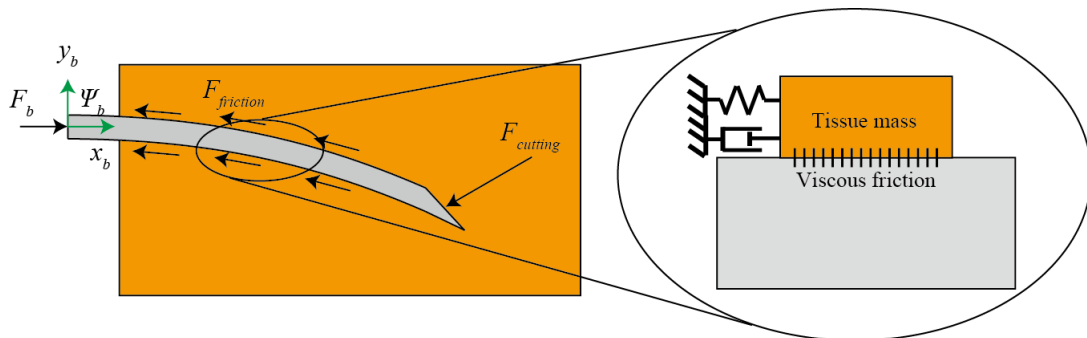


Fig. 3.3 Friction force model with viscous friction and Kelvin-Voigt model [3.11]

### 3.2.3 Combination of rotation and vibration

As mentioned above, rotational insertion can minimize needle deflection. Nevertheless, a potential disadvantage is that the interaction forces generated during rotational insertion may cause some pain, tissue damage, and winding-up of tissues. Vibration-assisted insertion, on the other hand, is expected to reduce the interaction forces. Thus it is believed that a combination of rotational motion and vibrational motion would be effective at reducing needle deflection and torsional friction forces due to the rotational motion, thereby improving safety.

Layered tissue and bowel are the main components and insertion targets of the lower abdomen and possess different biological properties as mentioned above. The thickness of layered tissue is significantly different to that of bowel tissue. It is thus important to apply the appropriate rotation in order to avoid unnecessary tissue damage. The following sections describe the method of rotational control within each target.

## 3.3 Control method for layered tissue

As introduced in the previous section, needle deflection can be minimized by combining rotational and vibrational movement. In this section, an appropriate insertion control method for layered tissue is described in terms of accuracy and safety, and is evaluated using *ex vivo* experimentation.

### 3.3.1 Bidirectional rotation

As mentioned above, rotational insertion can minimize needle deflection by equalizing the direction of needle tip forces. Continuous rotation is especially effective in terms of layered tissue due to the tissue's thickness in comparison with bowel tissue. A potential disadvantage is the possibility of interaction forces during rotational insertion causing some tissue damage including pain, tissue cuts, and tissues being wound up. In particular, the phenomena of tissues being wound up may occur frequently due to the rotation, because the layered tissue includes a number of muscle fibers and connective tissues such as fascia.

It was proposed that a bidirectional rotation, that involved switching the rotational direction clockwise and counterclockwise (CW/CCW) once every full 360° rotation as shown in Fig. 3.4, could decrease both the needle deflection and tissue damage such as wound-up tissue.

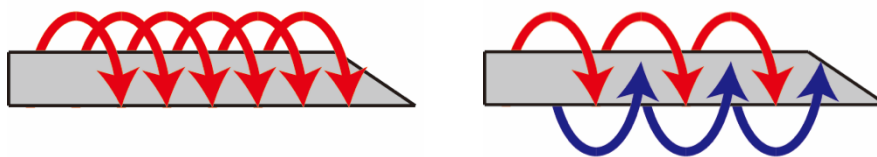


Fig. 3.4 Continuous rotation method: left) unidirectional rotation, right) bidirectional rotation

## 3.3.2 Evaluation of deflection and tissue damage

### 3.3.2.1 Tissue damage analysis

As mentioned above, insertion with continuous rotation may cause tissue damage. Therefore, in order to satisfy the requirements for patient safety during insertion using bidirectional rotation,

the tissue damage was quantitatively evaluated. Tissue damage was evaluated with respect to the insertion force and area of the hole through which the needle passed. In the present study, both the insertion force and area of the hole when applying rotation and vibration were evaluated. It was proposed that the safety of needle insertion could be insured for patients by quantitatively evaluating tissue damage using several approaches.

To evaluate the area of the insertion hole, previous researchers have histologically observed tissue sections after fixing them in formalin with the needle still inserted. In this experiment, a histological observation was used to evaluate the area of the hole created inside the tissue after needle insertion using rotation and vibration. The tissue was dehydrated using a tissue processor (ASP300; Leica Microsystems, Wetzlar, Germany) and then embedded in paraffin (EG1160; Leica Microsystems). The tissues embedded in paraffin were sliced with a microtome into 10  $\mu\text{m}$  thick sections along the radial direction of the needle as shown in Fig. 3.5. The tissue sections were stained with hematoxylin and eosin and observed under an optical microscope (ECLPSE E600; Nikon, Tokyo, Japan). The stained tissue sections were imaged with a camera (DP70 Digital Camera; Olympus, Tokyo, Japan) attached to the microscope.

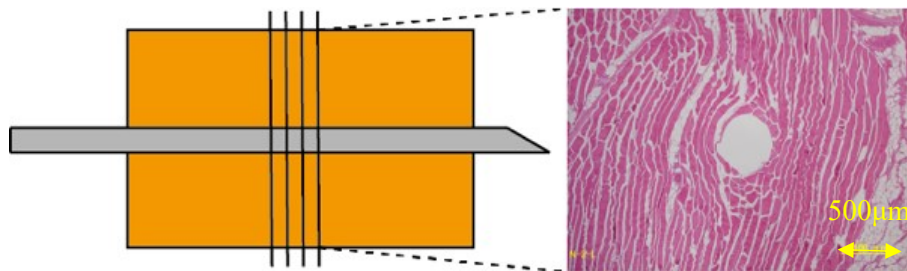


Fig. 3.5 Sliced tissue sections with a microtome into 10- $\mu\text{m}$ -thick sections along the radial direction of the needle

### 3.3.2.2 Experimental protocol

In order to confirm the viability of bidirectional spinning compared to unidirectional spinning, the needle insertion was performed using three rotational speeds (0 rpm, 100 rpm unidirectionally, and 100 rpm bidirectionally). Two vibrational frequencies (0 and 100 Hz) were also applied with the amplitude fixed at 0.2 mm. The insertion length was set at 50 mm. The insertion speed was set at 1 mm/s. Pork back ribs were used as the targets for this experiment because of their layered tissue. The size of the pork back ribs specimen was  $50 \times 50 \times 20$  mm. The tissues were set in a case with many small holes to aid formalin penetration. The specifications for the needle insertion robot and needle used in this experiment were identical to the equipment used in Chapter 2. After complete insertion of the needle, the base of the needle was cut and the case containing the tissue

with the needle still inserted was placed into a tank of formalin. After creating tissue sections, the areas of the holes were calculated with an image processing method as proposed by Chan and Vese [3.18] to detect the contours. Nine trials were performed for each insertion condition. The results were statistically analyzed using two-way analysis of the variance (Bonferroni correction).

### 3.3.2.3 Results of deflection

Fig. 3.6 shows the results for the needle tip deflection measurement. In some of the trials using unidirectional rotation, winding up of tissues occurred, and a piece of tissue became attached to the needle tip as shown in Fig. 3.7. In comparing the different rotational conditions, a significant difference was noted between the zero rotation and the bidirectional rotation conditions ( $p < 0.01$ ). When winding up of tissues occurred under unidirectional rotation, a large deflection was caused. In comparing insertion with and without vibration, although the deflection was slightly decreased with vibration, there were no significant differences between the rotational conditions.

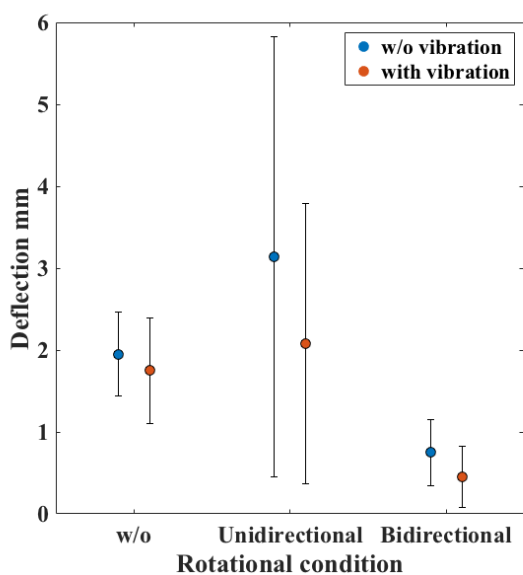


Fig. 3.6 Comparison of rotation and vibration with respect to deflection

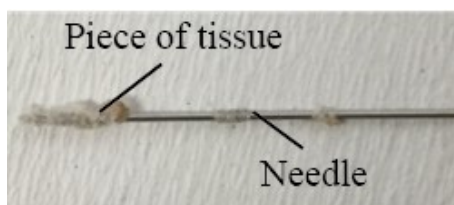


Fig. 3.7 A piece of tissue was attached to the needle tip when winding up of the tissue occurred

### 3.3.2.4 Results of tissue damage

Fig. 3.8 (a) and (b) show the average insertion force and torque for each rotational and vibrational condition. Figs. 3.9 and 3.10 show a time series of the insertion force and torque data for each condition. The average insertion force was larger under unidirectional rotation than under zero rotation and bidirectional rotation. In comparing insertion with and without vibration, significant differences were observed between zero rotation and unidirectional rotation ( $p < 0.01$ ). Under bidirectional rotation, although the force decreased slightly when vibration was applied, the difference was not significant. A larger average insertion torque was observed under bidirectional rotation. There was a significant difference between zero rotation and unidirectional rotation, and between zero rotation and bidirectional rotation ( $p < 0.01$ ). In comparing insertion with and without vibration, there were significant differences between the zero rotation and bidirectional rotation conditions ( $p < 0.01$ ).

Fig. 3.11 shows the results of the hole area measurement. Fig. 3.12 shows examples of tissue section images under each condition. In comparing the rotational conditions, there was a significant difference noted between zero rotation and bidirectional rotation, and between unidirectional rotation and bidirectional rotation ( $p < 0.05$ ). In comparing insertion with and without vibration, although deflection was slightly decreased, there were no significant differences between the rotational conditions.

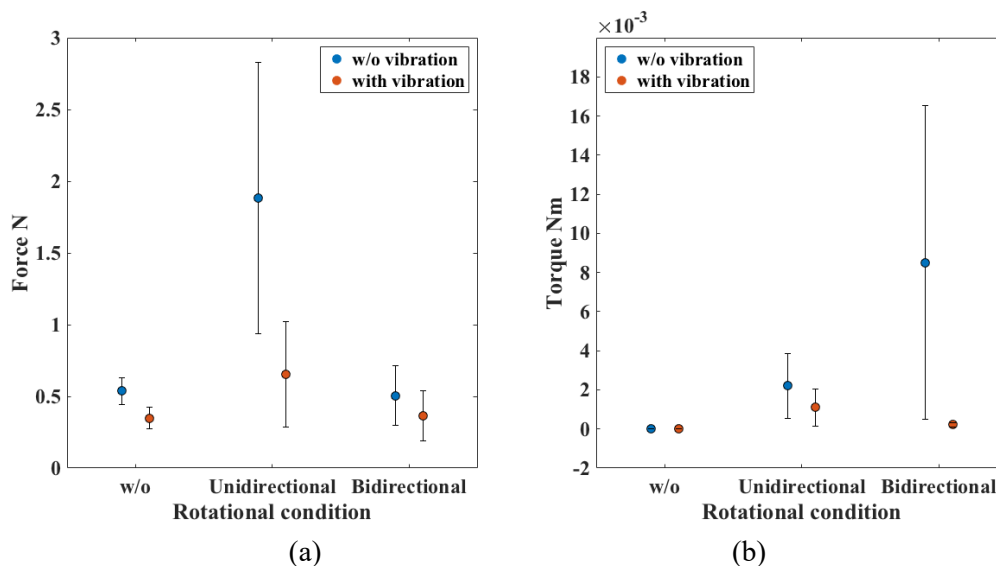


Fig. 3.8 Comparison of rotation and vibration with respect to (a) insertion force and (b) insertion torque.

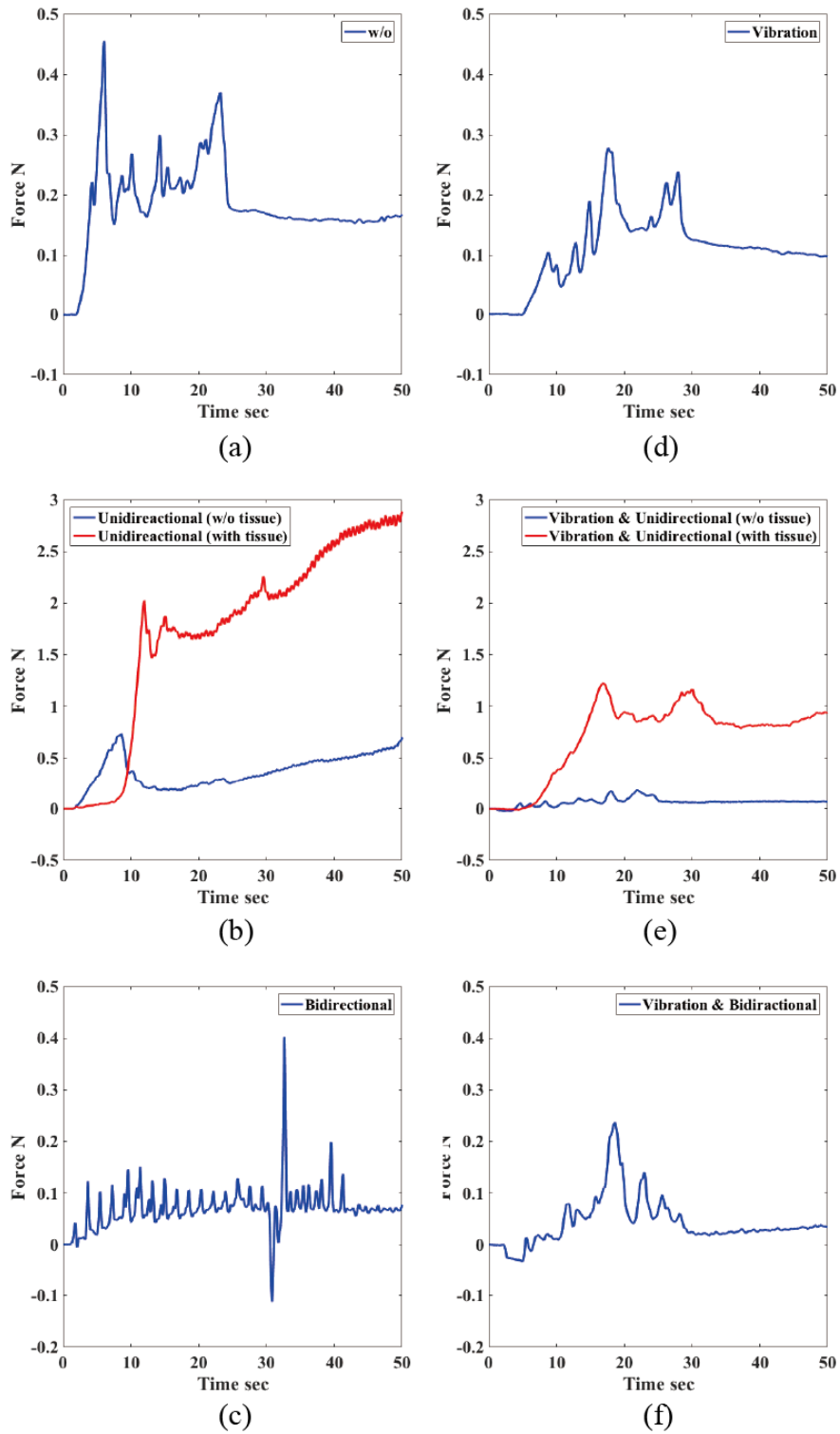


Fig. 3.9 Samples of time series data of insertion force (a) without rotation or vibration, (b) with unidirectional rotation (red line shows tissue attached data), (c) with bidirectional rotation, (d) with vibration, (e) with unidirectional rotation and vibration (red line shows tissue attached data),

and (f) with bidirectional rotation and vibration.

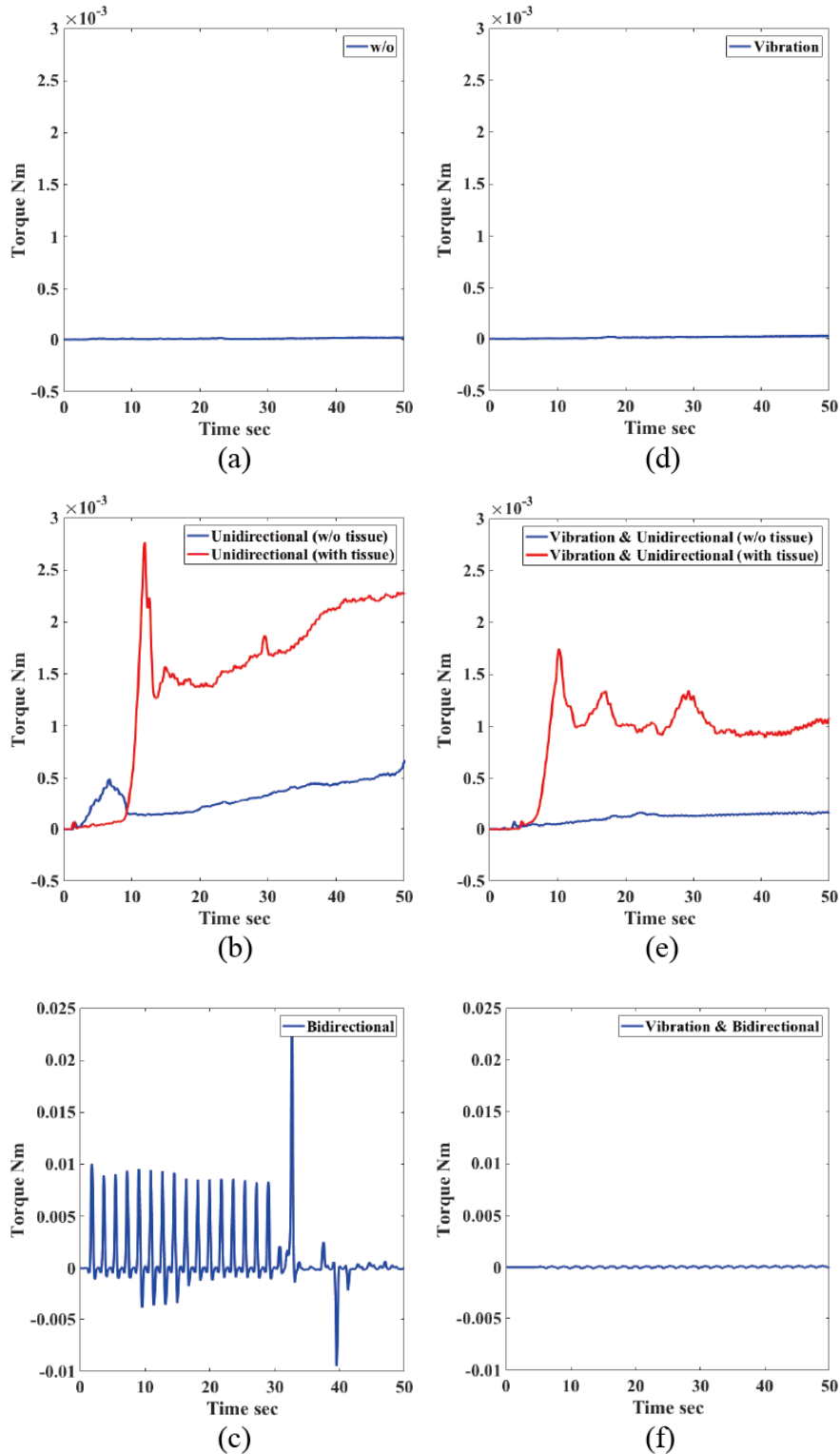


Fig. 3.10 Samples of time series data of insertion torque (a) without rotation or vibration, (b) with unidirectional rotation (red line shows tissue attached data), (c) with bidirectional rotation, (d) with vibration, (e) with unidirectional rotation and vibration (red line shows tissue attached

data), and (f) with bidirectional rotation and vibration.

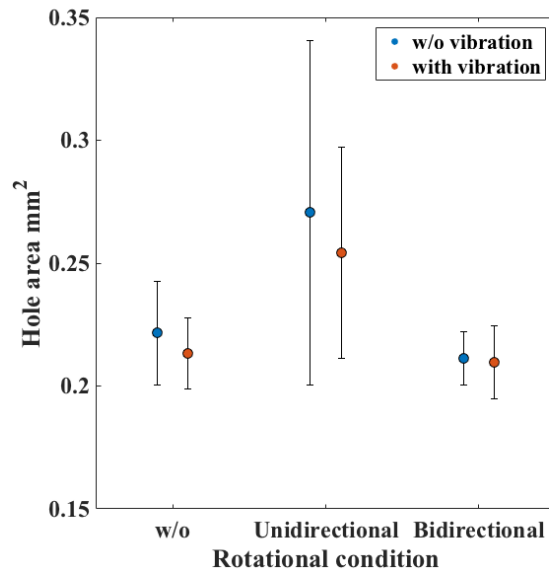


Fig. 3.11 Comparison of rotation and vibration with respect to the hole area created by the needle.

### 3.3.2.5 Discussion

The dominant reason for increased deflection when unidirectional rotation was applied is believed to be tissues being wound up. The time series data for the insertion force under the condition of unidirectional rotation (Fig. 3.9 (b)) shows that the insertion force drastically increased when a piece of tissue became attached to the needle tip. The attached piece of tissue may have produced additional resistance, which increased the deflection. Additionally, the time series data of torque under unidirectional rotation (Fig. 3.10 (b)) shows that the torque drastically increased and decreased at approximately 10 s. This may indicate that the needle tip started to wind up the tissue at 10 s and tore the surrounding tissue immediately after this. The attached tissue may have been connective tissue between the fat and muscle layers as noted in previous work [3.19]. Examination of the hole area (Fig. 3.11) showed that the area was larger under unidirectional rotation than under zero rotation. This may have been caused by tearing of the tissues after attachment to the needle as mentioned above. Differences in the hole area could be observed in the tissue section images (Fig. 3.12(b)). Needle insertion with unidirectional rotation may be considered risky in terms of both accuracy and tissue damage. The characteristics and structure of the target tissue, such as whether it contains connective tissues and fibers that may become wound up on the needle, must be considered. Additionally, the relationship between the rotational speed and insertion speed must be investigated.

No reports have described tissue attachment under bidirectional rotational conditions, and the



measured deflection was also significantly decreased. The time series of insertion force data (Fig. 3.9(c)) shows that the insertion force with bidirectional rotation was lower than that under zero rotation, although a drastic peak force was observed at approximately 30 s. No significant difference in the hole area was noted between zero rotation and bidirectional rotation when examining the tissue section images (Fig. 3.11(c)). However, the torque data (Fig. 3.10(b)) indicated that the torque was much greater under bidirectional rotation than under the other conditions. The time series data for torque (Fig. 3.10(c)) showed that a drastic peak appeared intermittently each time the rotational direction was switched. This may be an indicator that patient stress may be increased due to these torque peaks, although both deflection and the hole area decreased. Thus, in order to decrease peak torque, the rotational speed must be controlled when switching direction.

With respect to the effect of vibration, the deflection decreased slightly for each condition. It is believed that this occurred because the cutting and frictional forces were decreased by the vibration, as indicated in previous studies [3.17][3.20]. The insertion force data (Fig. 3.9(a)) showed that the forces were decreased under each rotational condition. However, because there was no significant difference in deflection between insertion with and without vibration, more comprehensive trials are needed to determine the effect of vibration on deflection. On the other hand, the torque data (Fig. 3.10(b)) showed a significant difference between insertion with and without vibration under the condition of bidirectional rotational. It is believed that the torsional frictional forces during rotation can be minimized by vibration in the same way that the lateral frictional forces can be minimized. To further decrease the torque, the rotational speed will be modified when switching direction as mentioned above. It was observed that there was no remarkable difference in the hole area with application of vibration. The phenomenon of tissue burning while applying high-frequency vibration may need to be verified using other histological techniques.

Overall, it was shown that needle insertion with a combination of bidirectional rotation and vibration can minimize needle deflection and tissue damage (i.e., the insertion force, torque, and the area of the hole that the needle creates could be decreased). Although applying only bidirectional rotation could decrease the needle deflection and avoid a larger hole area, peak torque occurs due to torsional friction between the needle and tissue. Adding vibration to bidirectional rotation can significantly decrease the peak torque when compared with zero vibration. This may lead to a decrease in patient stress.

This experiment's limitations included the fact that the rotational and vibrational parameters used in the experiments were limited because of the experimental setup and the cost of creating tissue sections. Because no significant difference was noted in the hole area in the comparison between tests involving the presence and absence of vibration and bidirectional rotation, an

investigation into the optimal parameters, based on force and torque data, was undertaken.

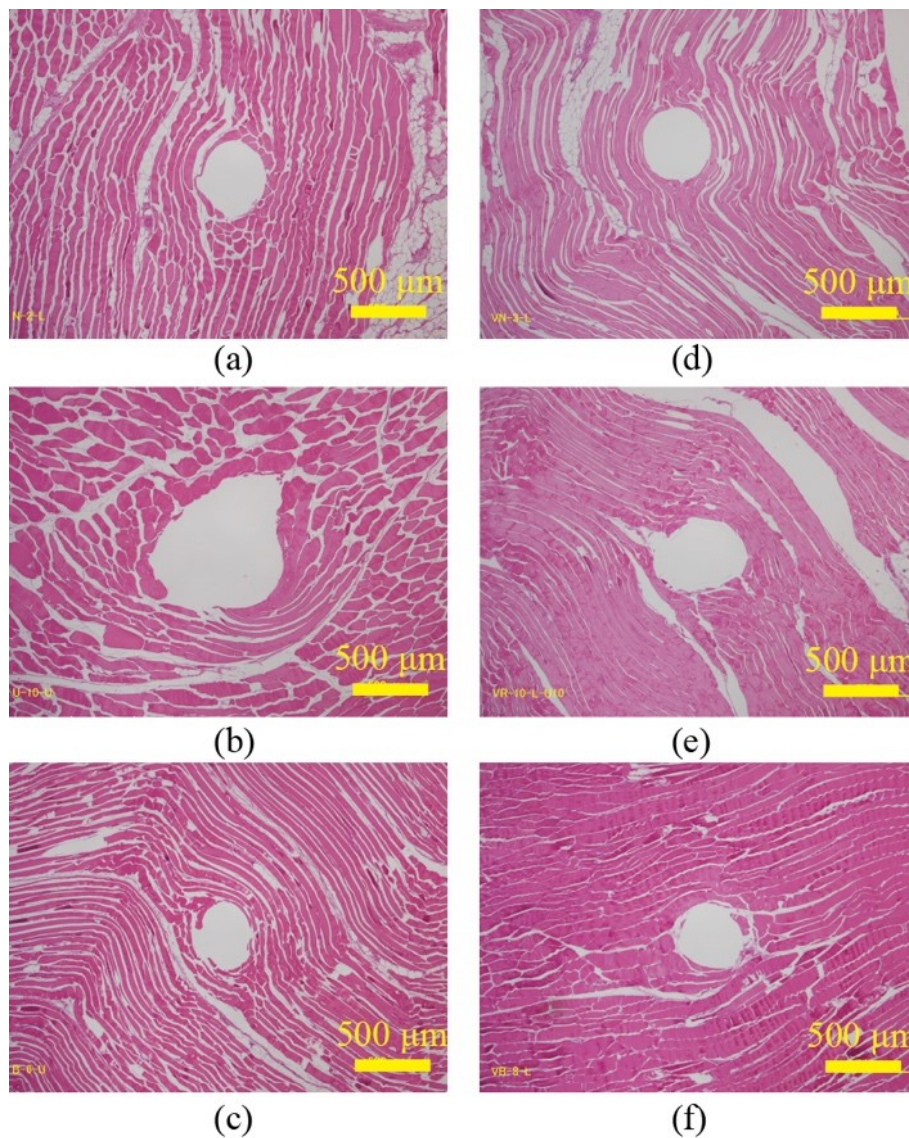


Fig. 3.12 Samples of tissue section images (a) without rotation or vibration, (b) with unidirectional rotation, (c) with bidirectional rotation, (d) with vibration, (e) with unidirectional rotation and vibration, and (f) with bidirectional rotation and vibration.

### 3.3.3 Evaluation of control parameters

#### 3.3.3.1 Experimental protocol

In the previous experiment, it was confirmed that needle insertion with a combination of applied bidirectional rotation and vibration could minimize needle deflection and tissue damage. An investigation into the optimal insertion control conditions was then undertaken by experimentally changing rotation and vibration parameters. In addition, insertion angle is one of the factors that can cause large deflection as mentioned in Chapter 2. The effectiveness of the proposed insertion control method at minimizing deflection for angular insertion was thus investigated. The following was investigated: i) The effects of the control parameter. ii) The needle deflection insertion angle. At first, needle insertion was performed under four bidirectional rotation speeds (0, 10, 100, and 1000 rpm) and three vibrational frequencies (0, 10, and 100 Hz), with a fixed amplitude of 0.1 mm. The deflection and insertion force/torque were then measured using the same method described in Section 3.3.2. Needle insertion was then performed for four insertion angles (0, 15, 30, and 45°), in each case comparing the insertion with and without the application of rotation and vibration. The rotation and vibration parameters were fixed at 100 rpm and a frequency of 100 Hz, respectively.

The dimensions of the pork rib used in this experiment was  $50 \times 50 \times 40$  mm. The insertion speed was set at 5 mm/s and the insertion distance was 60 mm in all cases. Twelve trials were conducted for each condition. The results were statistically analyzed using two-way analysis of variance (Bonferroni correction). The remainder of the experimental setup and the needle insertion robot used were identical to those used in Section 2.3.

#### 3.3.3.2 Results

Figs. 3.13 shows the results for the average needle deflection in layered tissue. In comparison between the various rotational and vibrational conditions, there was a significant difference between 0 and 10 rpm ( $p < 0.01$ ), between 0 and 100 Hz ( $p < 0.01$ ), and between 0 and 1000 Hz ( $p < 0.01$ ), respectively. Figs. 3.14 (a) and (b) show the average of the maximum insertion force and torque, respectively. Focusing on the insertion force results, there was a significant difference between the results for 0 and 100 Hz ( $p < 0.05$ ) in comparison with the results under vibrational conditions. On the other hand, the results associated with insertion torque in comparison with the rotational conditions demonstrated a significant difference between 0 and 10 rpm ( $p < 0.01$ ), between 10 and 100 rpm ( $p < 0.01$ ), and between 100 and 1000 rpm ( $p < 0.01$ ). In comparison

with the vibrational conditions, there was a significant difference between 0 and 100 Hz ( $p < 0.05$ ). Fig. 3.15 shows the average needle deflection with respect to the insertion angle. A comparison of the insertion angle showed a significant difference between 0 and 15° ( $p < 0.01$ ), between 0 and 30° ( $p < 0.01$ ), and between 0 and 45° ( $p < 0.01$ ), respectively. There was also a significant difference in comparison with the results obtained under application of the insertion control ( $p < 0.01$ ).

### 3.3.3.3 Discussion

The results show a decrease in needle deflection under application of bidirectional rotation and vibration, in accordance with the original assumption. The application of bidirectional rotation could significantly decrease the needle deflection when compared with the application of vibration. Moreover, applying vibration contributed to a decrease in the insertion force and torque in all rotational conditions. However, an increase in rotational speed caused an increase in torque, although the torque could be decreased by applying vibration. Focusing on needle deflection results, there was little difference between the tests carried out at 10 rpm and 100 rpm and between 100 rpm and 1000 rpm. Thus, there may not be a significant increase in effectiveness associated with applying rotation speeds greater than 10 rpm to needle insertion in layered tissue. Setting a minimum rotation speed enabled the minimization of needle deflection and avoided an increase in torque and lead to a reduction in tissue damage. The needle deflection could not effectively be minimized as the insertion angle continued to increase even with application of bidirectional rotation and vibration. Therefore, in order to address the remaining deflection due to insertion angle, it was necessary to determine the optimal insertion path for minimizing the insertion angle at each tissue boundary.

A limitation of the proposed insertion control method is that theoretical models for estimating needle deflection when under a combination of bidirectional rotation and vibration were not developed. Moreover, the effect of insertion angle was not taken into account within the control parameters. In order to apply the control method to real procedures, it will be necessary to model the appropriate parameters of rotation, vibration, insertion speeds, and insertion angles with respect to individual tissue characteristics such as tissue stiffness. In addition, the parameters used in this experiment were limited. The rotational speeds and vibration frequencies were limited to only three and four conditions, respectively, and the insertion speed was fixed at 5 mm/s. Thus, it will be necessary to investigate the trend of deflection and insertion forces further by setting parameters in detailed ranges. Further experimental analysis will contribute to the development of theoretical models.

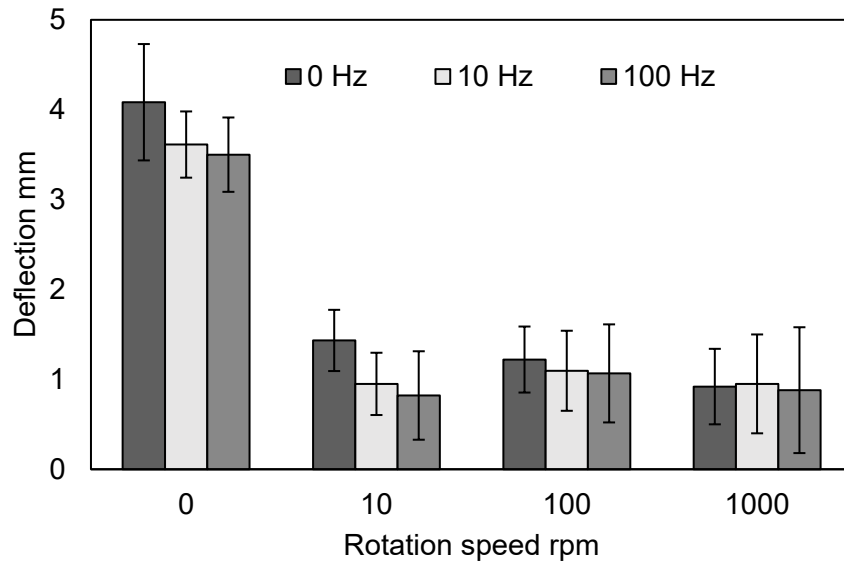
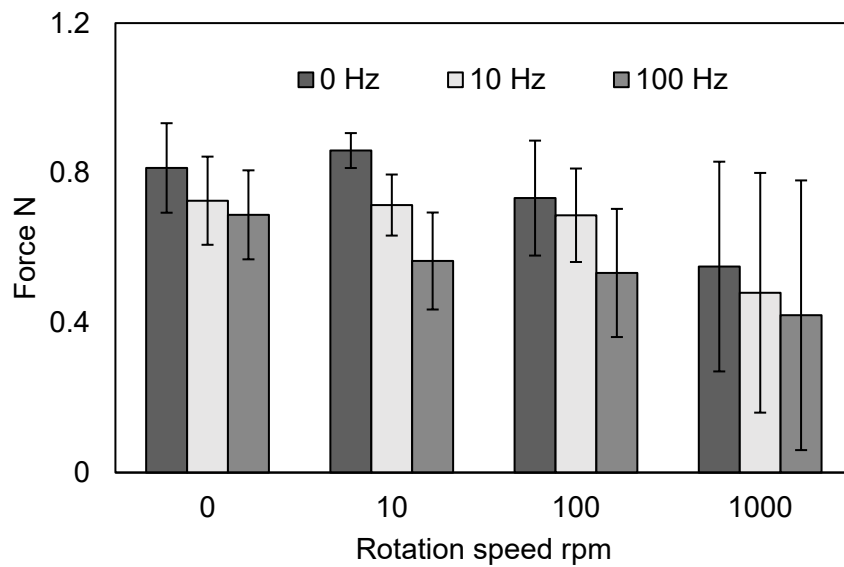
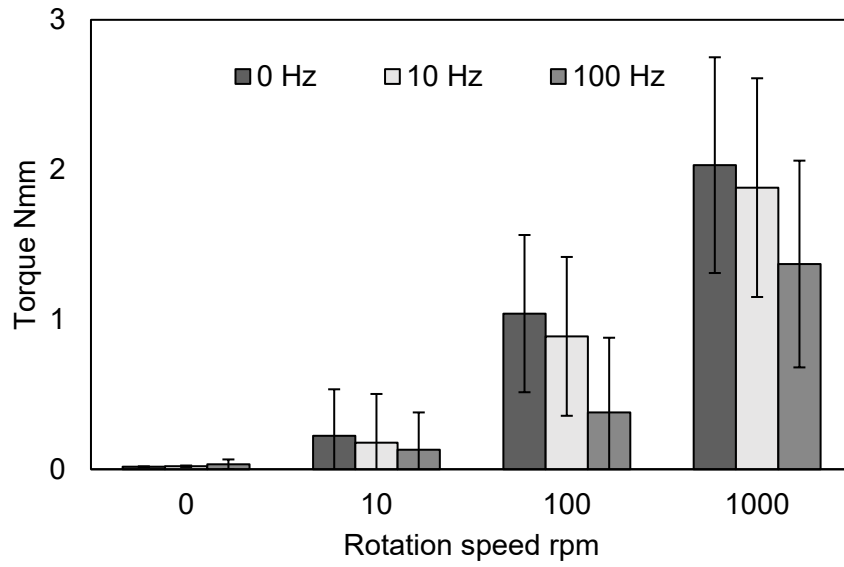


Fig. 3.13 Results of needle deflection due to vibration and rotation parameters



(a)

Fig. 3.14 Results of the average of (a) maximum insertion force and (b) maximum torque force during insertion into the layered tissue varying at the vibration and rotation parameters



(b)

Fig. 3.14 (continue) Results of the average of (a) maximum insertion force and (b) maximum torque force during insertion into the layered tissue varying at the vibration and rotation parameters

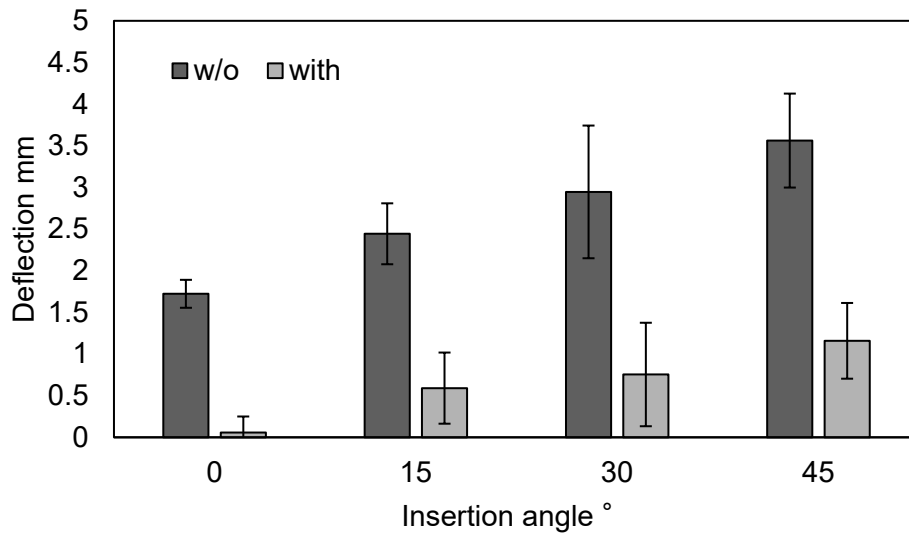


Fig. 3.15 Result of needle deflection due to insertion angles

## 3.4 Bowel insertion control method

### 3.4.1 Rotation of needle tip direction

In the previous section, it was shown that continuous rotation could minimize needle deflection in layered tissue. The anatomical shape of segmented bowel is hollow, possibly causing the slip of the needle tip on the bowel wall due to the needle's spinning motion when being inserted at an angle. As mentioned in Chapter 2, the insertion angle needs to be perpendicular, once breaching each the bowel wall to minimize the needle deflection. Actually, the needle must pass through a number of bowel sections in order to reach at the targeted tumor. Then, it is ideal to select the insertion path in which the needle can pass through each bowel wall in a direction perpendicular. Meanwhile, the ideal path cannot be always selected due to the arrangement of the bowel loops in actual situations. Thus, it is required to develop an insertion control method for decreasing the needle deflection, instead of the continuous rotation during insertion.

It is proposed that the effect of needle deflection at each bowel wall can be cancelled by rotating the needle tip direction at every breach of a bowel wall, thereby minimizing total deflections. As shown in Fig. 3.16, the total deflection in the segmented bowel may be cancelled by adjusting the needle tip direction to the left ( $0^\circ$ ) when puncturing the upper wall of the bowel, and to the right ( $180^\circ$ ) when puncturing into the lower wall. Moreover, to cancel the total deflection, it is required to select an insertion path in which the sum of the insertion angles in the upper and lower bowel walls is minimized (Fig. 3.17). When selecting no cancellable path in which the sum of each insertion angle is not zero, the deflection may still remain after the cancellation process has been completed.

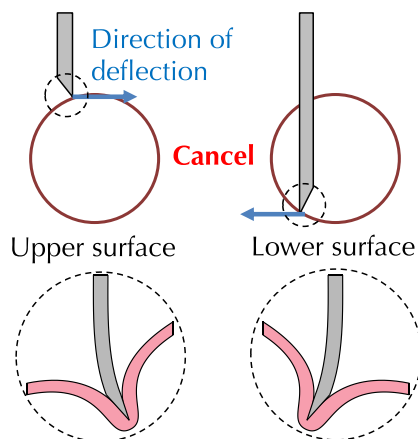


Fig. 3.16 The rotation of needle tip direction when breaching the bowel surface

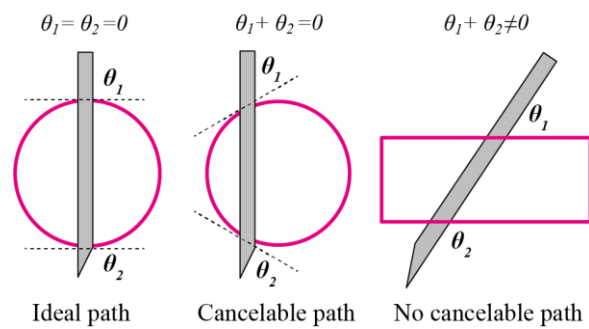


Fig. 3.17 Insertion path types; ideal path is that both insertion angles at upper and lower walls are zero; cancelable path is that the sum of each insertion angles is zero; no cancelable path is that the sum of each insertion angles is not zero.

## 3.4.2 Insertion control method evaluation

### 3.4.2.1 Experimental protocol

To evaluate the proposed insertion method, the needle insertion was performed under several conditions. The experimental setup including the needle insertion robot, needle conditions, and the measurement way of deflection was identical to those used in Section 2.3.2. The needle insertion was performed under three vibrational frequency parameters (0, 10, and 100 Hz at a fixed amplitude of 0.1 mm), and two rotational methods. These rotational methods were as follows: 1) without rotation (fixed at  $0^\circ$ ), 2) with rotation at  $0^\circ$  in the upper wall and at  $180^\circ$  in the lower wall.

Twelve insertions were performed for each condition. The results were statistically analyzed using two-way analysis of variance (Bonferroni correction).

### 3.4.2.2 Results

Fig. 3.18 shows the results for the average needle deflection. A significant difference was noted between tests performed with and without using the tip direction control ( $p < 0.01$ ), and between 0 Hz and 100 Hz ( $p < 0.05$ ) when comparing tests performed at various vibrational frequencies, respectively. Fig. 3.19 (a) and (b) show the average of the maximum insertion force and torque during insertion, respectively. Focusing on the insertion force, there was a significant difference between 0 Hz and 100 Hz ( $p < 0.05$ ) when comparing tests performed at various vibrational frequencies. While focusing on the insertion torque, a significant difference was noted between tests performed with and without the tip direction control ( $p < 0.01$ ).



### 3.4.2.3 Discussion

The results showed that needle deflection could be decreased by applying needle tip direction control and vibration. In particular, by changing the needle tip direction when puncturing each bowel surface, the needle deflection could be significantly decreased. It is considerable that the effect of needle deflection on each surface may be cancelled following the author's assumption. However, some deflection remained despite the application of needle tip direction control. It was found that the effect of needle deflection on each surface could not be totally cancelled. As needle deflection occurred slightly after puncturing the upper surface, the insertion angle when reaching the lower surface differed from the pre-insertion planned insertion angle. In addition, consideration was given to the fact that the effect of each surface on final needle deflection differs depending on the distance between the surface position and final needle tip position. Thus, the needle deflection observed for penetration of a bowel in a shallow position may yield a large error.

Applying vibration contributed to decreasing the insertion force, which resulted in a decrease in needle deflection. This meant that the puncture force required for breaching the bowel surface could be decreased by applying vibration. In this experiment, although the frequency was set to 100 Hz because of actuator limitations, higher frequencies over 100 Hz are expected to further decrease the puncture force. Although applying tip direction control causes an increase in torque, the value of the torque associated with the insertion was really low compared to the torque observed when applying bidirectional rotation in the layered tissue experiment. It may be considered negligible with respect to this higher value.

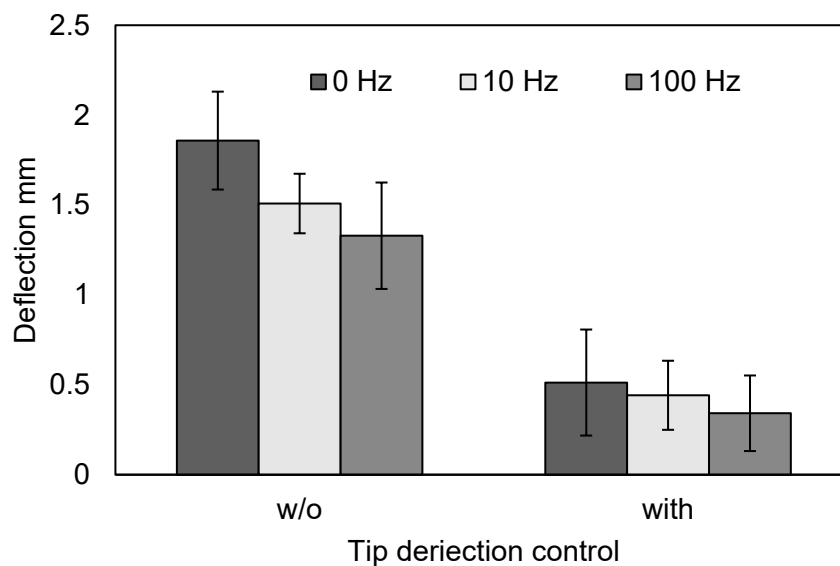
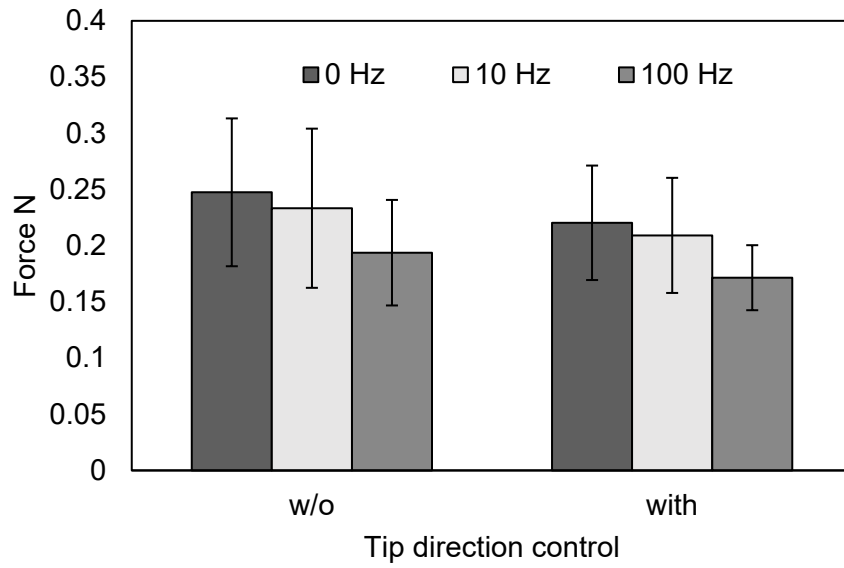
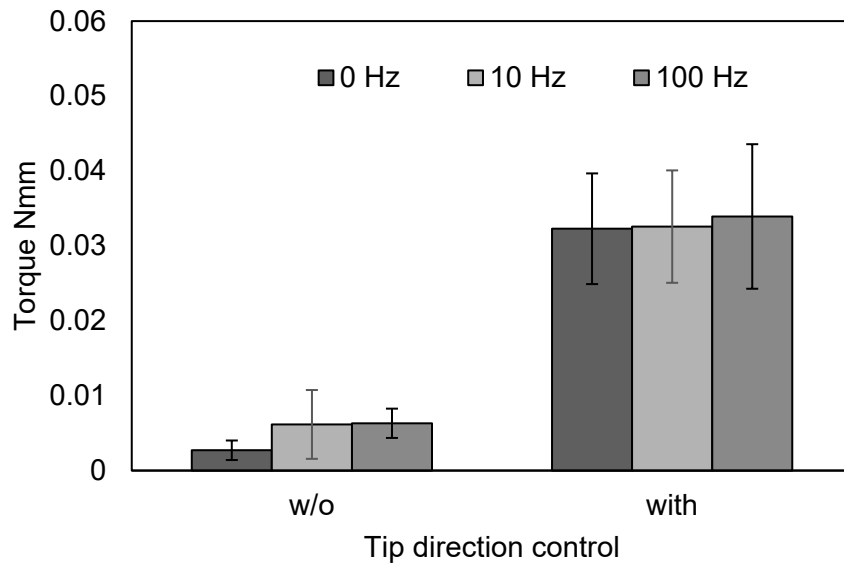


Fig. 3.18 The result of needle deflection due to the insertion control methods



(a)



(b)

Fig. 3.19 Results of the average of (a) maximum insertion force and (b) maximum torque force during insertion into the bowel varying at the vibration and rotation parameters

### 3.4.3 Insertion position and angle evaluation

#### 3.4.3.1 Experimental protocol

In this experiment, the proposed insertion method was investigated for several insertion situations as the relative position between the needle and bowel can vary depending on the insertion position. Needle insertion was performed for two situations as follows: 1) three conditions for the insertion position (0, 4, and 8 mm from the center of the bowel) as seen in the front view of the bowel shown in Fig. 3.20(a). 2) three conditions for the insertion angle (0, 20, and 40° from the vertical) as seen in the side view shown in Fig. 3.20(b). Insertion methods used in this experiment were as follows: 1) Without rotation (fixed at 0°). 2) With rotation at 0° for penetration of the upper surface and at 180° for penetration of the lower surface.

The vibration frequency and amplitude were fixed at 100 Hz and 0.1 mm, respectively, for all conditions. Twelve trials were performed for each condition. The results were statistically analyzed using one-way analysis of variance (Bonferroni correction).

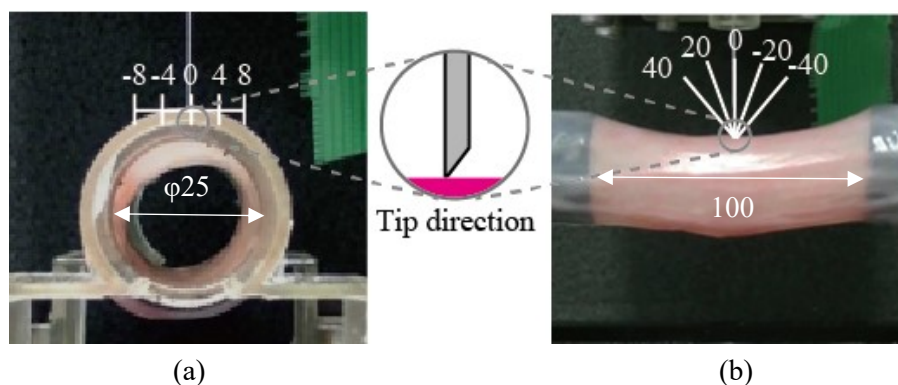
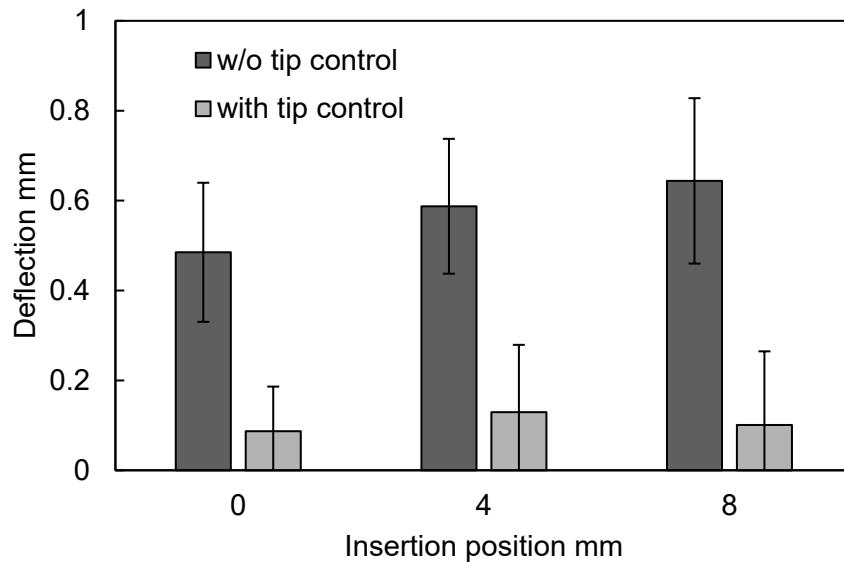


Fig. 3.20 Bowel insertion situations; (a) insertion positions looking at front view axis and (b) insertion angles looking at the side view

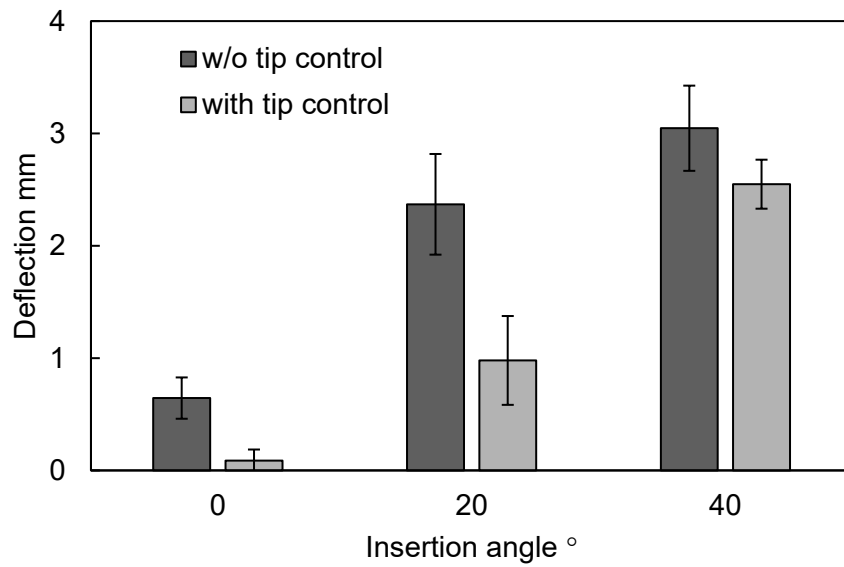
#### 3.4.3.2 Results

Fig. 3.21 (a) and (b) show the results of the needle deflection with respect to the insertion position and insertion angle, respectively. Focusing on the result of insertion position, needle deflection was significantly decreased when applying the tip direction control for all conditions ( $p < 0.01$ ). Focusing on the result of insertion angle, although the needle deflection was decreased when applying the tip direction control for all conditions, needle deflection remained slightly. There was a significant difference in needle deflection between the conditions at 0° and 20° ( $p <$

0.01), while there was no significant difference between 20° and 40°.



(a)



(b)

Fig. 3.21 Results of the deflection due to (a) insertion positions, (b) insertion angle. Black data show the condition without needle tip direction control, gray data show the condition with needle tip direction control.

### 3.4.3.3 Discussion

Focusing on the result of the insertion position, insertion method for applying the needle tip direction control proved effectiveness. The condition in which the insertion position was at 0 mm was equivalent to the ideal path shown in Fig. 3.17, and the condition of the insertion positions at 4 and 8 mm were equivalent to the cancelable path shown in Fig. 3.17. Thus, the effect of each surface on total deflection could be almost perfectly canceled in those cases. Focusing on the insertion angle, a deflection remained slightly during insertion with varying needle tip directions. This is also in agreement with the proposed assumptions, because the insertion angles of 20 and 40° were equivalent to the non-cancelable path, which means that the deflection effect of each surface could not be completely canceled. Therefore, it was required to determine the insertion path, taking into account the insertion angle at each surface for canceling the deflection effect.

Whether the implications of this assumption are acceptable in a real situation is still unknown. In actuality, the bowel used in this experiment was an ideal cylinder shape due to being clamped strictly to keep its shape. The boundary conditions of this bowel sample may be different from bowel present within a real abdominal situation. In additions, as the bowel is a continuous, stacked tube, the needle must potentially pass through multiple bowels. It is challenged to imitate real bowel conditions because the boundary conditions include a lot of factors such as internal and external air pressure, fixing way, bowel motion and so on. It is therefore necessary to verify the proposal in *in vivo* experiments, but it is needed to develop a model imitating bowel condition.

## 3.5 Summary

In this chapter, the author proposed insertion control methods for targeting both layered and bowel tissue. As an approach to developing an insertion control method, the author hypothesized that needle deflection could be significantly minimized by combining both vibration and rotation and examining the effect through the use of the experimental analysis introduced in Chapter 2. Moreover, the rotational method was optimized for the target tissue properties and for improved patient safety for each target composed of lower abdominal tissue. Bidirectional rotation, that switches the rotational direction CW and CCW every 360°, was proposed for layered tissue. While needle tip direction control, that rotates the needle bevel direction from 0 to 180° when puncturing the bowel surface in order to cancel the effects of needle deflection on each boundary, was proposed for the bowel tissue. A limitation to this method was encountered under conditions associated with some insertion angles in that needle deflection could not be effectively minimized even with application of both rotation and vibration.



# Chapter 4: Insertion path planning

## 4.1 Chapter introduction

The insertion path planning for decreasing needle deflection is described in this chapter. As introduced in chapter 2, the insertion angle between the insertion direction and tissue surface/boundary may be one major factor causing needle deflection. Therefore, needle deflection can be minimized by inserting the needle into the tissue surface perpendicularly. Meanwhile, when selecting a needle insertion path on CT images, the insertion angles on the tissue surface and boundary that the needle passes through are changed, depending on the shape of tissues composing the lower abdomen. Consequently, an ideal insertion path through which all the insertion angles on tissue boundaries are perpendicular cannot always be selected. Hence, it is believed that it is important to find an optimal insertion path, which enables minimization of the needle deflection in obtaining CT images from patients.

The objective of this chapter is to describe methods of needle insertion path planning for finding the insertion path that minimizes needle deflection. The method is designed for multi-layered tissue and organs, such as the lower abdomen, and verified through *in vitro* and *ex vivo* experiments.

This chapter shows a methodology for improving the accuracy of insertion path planning. The model of insertion path planning can determine the optimal insertion path based on the sum of insertion angles at each tissue boundary that the needle passes through. In order to improve the accuracy of the insertion path planning, the author implemented the effect of distances between tissue boundaries and insertion target, and the probability that deflection is acceptable by implementing weighting factors into the model. In addition, as an application of insertion path planning, the system for finding the optimal insertion path from the CT image is described. In order to apply the model of path planning to the clinical setting, a system needs to be developed to automatically calculate the insertion angle and determine the optimal insertion path on CT images. The author presents a method for multilayered tissue boundary detection in the lower abdomen and insertion angle calculation along the insertion path based on the boundary detection. Since this detection method does not depend on the tissue shape, the boundary points showing peak brightness change along each insertion path are detected and connected.

In this chapter, the author uses figures and sentences by referring to the author's published paper [4.1].

## 4.2 Insertion path planning

### 4.2.1 Concept of insertion path planning

In this section, the author describes the path planning for determining an optimal needle insertion positions and angles, which can minimize needle deflection. As the author described, the insertion angle at each tissue boundary may cause substantial deflections. For an ideal multiple layered tissue where each tissue is aligned parallel to the target, as shown in Fig. 4.1 (a), it is easy to determine the optimal insertion path to pass through each tissue boundary vertically. However, in the case of a real multiple-layered tissue that is aligned randomly, as shown in Fig. 4.1 (b), it is essential to take into account the effect of each angle between the insertion path direction and the tissue boundaries in order to decide the optimal insertion path.

As the optimal insertion path in such a complex situation, the author hypothesizes that the deflection can be minimized when the sum of each insertion angle at each tissue surface or boundary on a selected path is minimized. The hypothesis is expected to cancel out the effect of deflection at each tissue layer during insertion by minimizing the sum of each insertion angle. Moreover, there are some factors causing deflection, such as tissue characteristic and insertion distance. In order to account for effects of those factors to insertion angles, a weighting factor is assigned to each insertion angle. Then, the objective function score  $s$  for determining the optimal insertion path is defined as follows:

$$s = \sum_{i=1}^n w_i \theta_i \quad (4.1)$$

$\theta_i$  represents the angle between the normal vector to the tissue boundary and the insertion direction vector at the  $i$ -th tissue boundary where the needle will pass thorough, shown in Fig. 4.1 (c);  $w_i$  represents the weighting factor at that time; and  $n$  is the total number of layers composing the multi-layered tissue. For example, in the case of the three-layered tissue shown in Fig. 4.1 (b),  $\theta_1$ ,  $\theta_2$ , and  $\theta_3$  represent the insertion angles at the surface of tissue A, the boundary between tissue A and B, and the boundary between tissue B and C, respectively. Those insertion angles vary due to the selected initial position and angle. The optimal insertion path can be determined by selecting an insertion path with minimum objective function score. The author will describe the weighting factors for increasing accuracy in following section.



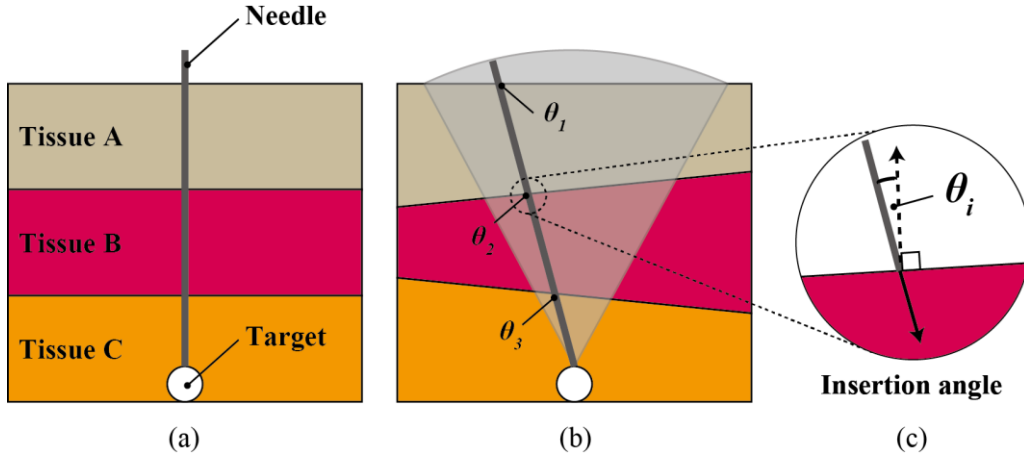


Fig. 4.1 (a) Ideal multi-layered tissue (b) Real multi-layered tissue (c) Insertion angle definition

## 4.2.2 Tissue boundary distance

The effect of the tissue boundary distance which causes a large deflection needs to be accounted for in the weighting factor. The amount of deflection was affected almost linearly due to the insertion distance according to previous research [4.2]. Then, once there are minute needle tip errors at the tissue boundary, it is considerable that the final deflection is increased due to the insertion distance between the tissue boundary and the target. For example, two cases of two-layered tissues with different boundary distances ( $L_i$ ) are compared. Noted that the layered tissues are composed of tissues with the same angles and properties shown in Fig. 4.2 and both deflection slopes in Fig. 4.2 can be approximated as almost equal. The final deflection is linearly decreased as the difference between  $L_i$  and the total insertion distance from an initial position to the target ( $L_{tar}$ ) is decreased. Thus, the author defines the effect for deflection due to boundary distance as the following weight factor:

$$w_i^{Dist} = \frac{L_{tar} - L_i}{L_{tar}} \quad (4.2)$$

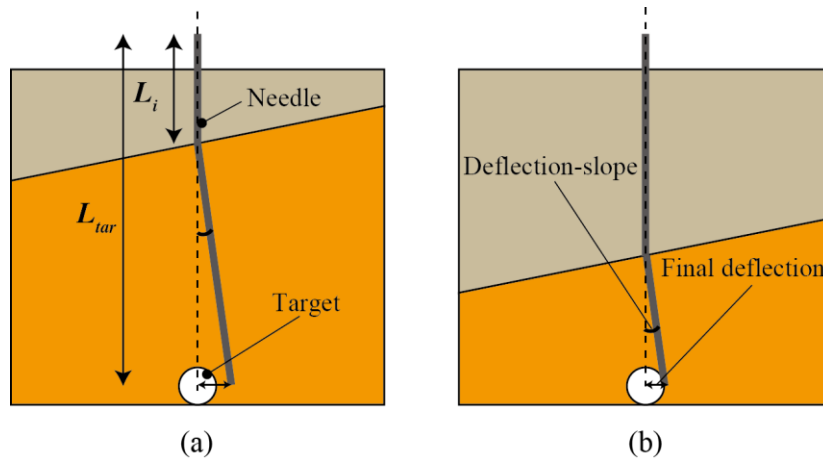


Fig. 4.2 The effect for deflection due to boundary distance: (a) the long distance causing large deflection, and (b) the short distance causing small deflection.

### 4.2.3 Deflection probability

Although there have been various needle deflection models, there are no models for implementing the effect of insertion angle for deflection. As mentioned in chapter 2, the dominant factor for causing the large deflection due to the insertion angle may be initial tissue deformation before puncturing the boundary [4.3]. Meanwhile, the puncture phenomenon are complex and the analysis of the mechanism may be still a challenging problem, because this phenomenon varies, even if the same insertion force and distance are applied to the tissue [4.4]. In addition, the puncture phenomenon may vary when applying axial rotation or vibration to the needle with respect to the insertion angle at each boundary. Thus, it is unrealistic to estimate accurate deflection taken into account the complex phenomena deterministically. Instead, we considered the probability that the deflection occurs due to the insertion angle and tissue properties, which are difficult to be obtained as deterministic parameters. In doing this, the effect of those uncertain factors for deflection were effectively implemented in the insertion path planning.

As shown in Fig. 4.3 (a), deflection has variability, and an acceptable deflection varies depending on the boundary distance ( $L_i$ ) and target size ( $r_{tar}$ ). The deflection slope ( $\varphi_i$ ) may be almost constant after puncturing the surface or boundary, because the main reason for deflection are the insertion angle and the initial tissue deformation as mentioned above. The author defines the probability that the deflection slope ( $\varphi_i$ ) is decreased within the acceptable deflection slope ( $\Phi_i$ ) as *deflection probability*. To determine the *deflection probability*, it is necessary to acquire a probability distribution of deflection occurrence related to arbitrary insertion angles at each tissue layer. By collecting experimental data of deflection-slope under several conditions of the insertion

angle with each tissue type, the probability distribution of deflection occurrences can be generalized and define as *deflection probability distribution*. The *deflection probability* can be expressed as a cumulative distribution function of the *deflection probability distribution* as follows:

$$p(\theta_i) = \int_0^{\phi_i} g(\varphi_i) d\varphi_i \quad (4.3)$$

$$\phi_i = \tan \frac{r_{tar}}{L_{tar} - L_i}$$

where  $p(\theta_i)$  is the *deflection probability*,  $\varphi_i$  is the deflection slope of the insertion angle at  $\theta_i$ ,  $\Phi_i$  is acceptable deflection slope, and  $g(\varphi_i)$  is the *deflection probability distribution* (Fig. 4.3 (b)). We assume that the *deflection probability distribution* is derived from fitting experimental data to a Gaussian distribution model, because it is a common model that can be represented with only two parameters (mean and standard deviation). The *deflection probability distribution* can be represented as follows:

$$g(\varphi_i | \mu_{\theta_i}, \sigma_{\theta_i}) = \frac{1}{\sigma_{\theta_i} \sqrt{2\pi}} e^{-\frac{(\varphi_i - \mu_{\theta_i})^2}{2\sigma_{\theta_i}^2}} \quad (4.4)$$

where  $\mu_{\theta_i}$  and  $\sigma_{\theta_i}$  are the mean and standard deviation of the deflection-slope at the insertion angle at  $\theta_i$ , respectively. By fitting those two parameters at arbitrary insertion angles from the experimental data (see 4.2.4.2), the *deflection probability distribution* can be generalized using the Gaussian distribution model. With the Gaussian distribution model generalized in each layer of a multi-layered tissue, Eq. (4.3) of the *deflection probability* in each tissue can be replaced with Eq. (4.4) as follows:

$$p_{tissue}(\theta_i) = \int_0^{\phi_i} g(\varphi_i | \mu_{\theta_i}, \sigma_{\theta_i}) d\varphi_i \quad (4.5)$$

The *deflection probability* is the likelihood that the value for the occurrence of deflection is within acceptable ranges. In short, the probability approaches approximately 100% when the insertion angle approaches  $0^\circ$ . Since the score of the objective function should be small as each insertion angle decreases, we define the effect of *deflection probability*, as an additional weight factor, as follows:

$$w_i^{Prob} = 1 - p_{tissue}(\theta_i) \quad (4.6)$$

Combining the weight factors from Eq. (2) and (6), the objective function of Eq. (1) is defined as follows:

$$f = \sum_{i=1}^n (1 - p_{tissue}(\theta_i)) \cdot \frac{L_{tar} - L_i}{L_{tar}} \cdot \theta_i \quad (4.7)$$

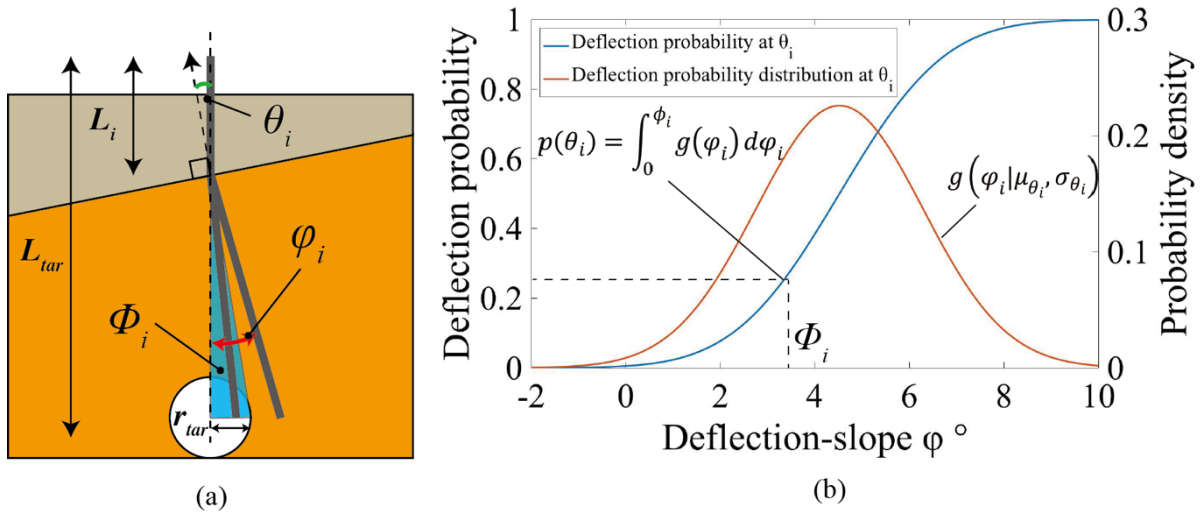


Fig. 4.3 (a) Image of the *deflection probability* that the deflection due to the insertion angle is decreased within the acceptable deflection (b) Example of calculated deflection probability (orange line) and deflection probability distribution (blue line) to deflection slope  $\varphi_i$  in an insertion angle at  $\theta_i$ .

## 4.2.4 Evaluation

### 4.2.4.1 Experimental setup

The author first describes an experiment to fit the *deflection probability*, and then verifies the insertion path planning with the fitted *deflection probability*.

The setup overview used in this experiment is shown in Fig. 4.4. The setup can perform to insert fine needles into multi-layered tissue and to measure needle deflection in the phantom. The setup is composed of two components: 1) a needle insertion unit that has two actuators for translation and rotation about the insertion axis [4.5], and 2) a positioning stage that has three actuators for moving the needle insertion unit. To measure the needle tip position, a Flea2 FireWire 1394b CCD camera (FLIR Inc., Oregon, USA) was attached above the phantom. The needle conditions were same as previous experiments.

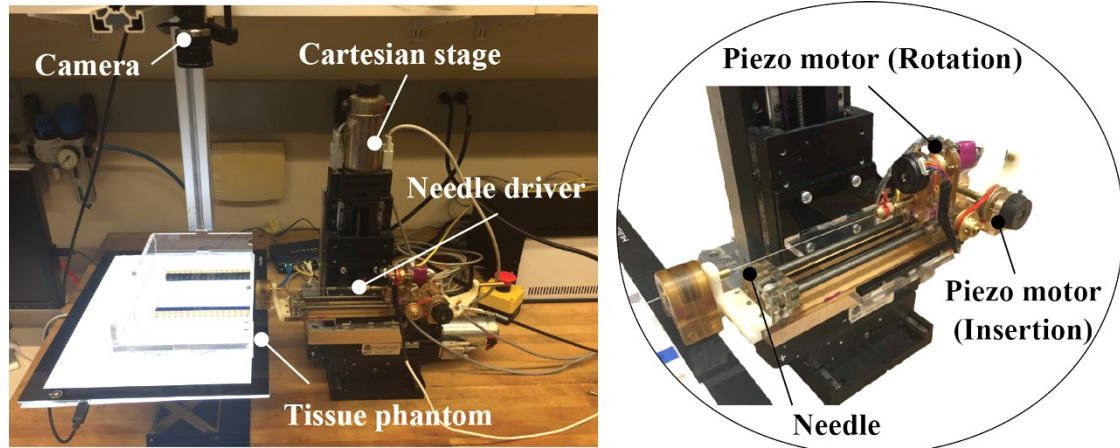


Fig. 4.4 Experimental setup is composed of 2-DOF needle driver [4.5] (insertion and rotation axes), Cartesian stage and tissue phantom.

#### 4.2.4.2 Fitting deflection probability

As mentioned in 4.2.3, experimental deflection-slope data are needed to acquire the *deflection probability distribution* to fit a Gaussian distribution model and obtain the *deflection probability*. In this experiment, the author used Polyvinyl chloride (PVC) and fresh chicken meat as a soft tissue phantom and biological tissue, respectively. The PVC can be manufactured by mixing Super Soft Plastic and softener (M-F manufacturing, Texas, USA), and the stiffness can be adjusted by changing the ratio of plastic to softener. In this experiment, two types PVC phantoms were made as follows: 75% of the plastic volume to 25% of the softener volume ( $E \cong 150$  kPa), 50% of the plastic volume to 50% of the softener volume ( $E \cong 100$  kPa) [4.6]. For mimicking the connective tissue at boundary between each tissues, 0.03-mm thick rubber sheets (McMaster-Carr, Illinois, USA) are placed to the PVC surface by using staples as shown in Fig. 4.5 (a). The PVC phantoms and biological tissues are cut to  $150 \times 250 \times 30$  mm<sup>3</sup> and  $90 \times 120 \times 30$  mm<sup>3</sup>, respectively. Both sides and the back of the biological tissue are fixed with PVC as shown in Fig. 4.5 (b) for fitting to a plastic container ( $150 \times 250 \times 50$  mm<sup>3</sup>). In all experiments, the needle insertion is performed at 100 mm into the tissues. The insertion speed is set at 2 mm/s and rotational speed is set at 10 rpm, applying the bidirectional rotation [4.7]. We perform needle insertion under five-way insertion angles ( $0^\circ$ ,  $10^\circ$ ,  $20^\circ$ ,  $30^\circ$ , or  $40^\circ$ ) for all tissues, by adjusting the set angle of phantom case based on baselines. The deflection-slope is calculated with respect to the arcsine of the insertion distance (100 mm), and the deflection is calculated with the pixel of camera image as shown in Fig. 4.5 (c). Twelve trials are performed for all conditions.

Fig. 4.6 shows the results of the deflection-slope. The result shows that both mean and standard deviation of the deflection-slope increase due to the insertion angle in all tissues. As the result,

the deflection-slope data can be fitted to a Gaussian distribution model as shown in Fig. 4.7. Also, the values of parameters  $\mu$  and  $\sigma$  which represents the Gaussian distribution model are listed in Table 4.1. Both parameters increase non-linearly due to the insertion angle. Therefore, for generalizing parameters  $\mu$  and  $\sigma$  at arbitrary insertion angles in each tissue, second-order and third-order polynomial regression model are applied for fitting  $\mu$  and  $\sigma$ , respectively, as shown below:

$$\begin{aligned} \mu_{\theta_i} &= a_0^\mu + a_1^\mu \theta_i + a_2^\mu \theta_i^2 \\ \sigma_{\theta_i} &= a_0^\sigma + a_1^\sigma \theta_i + a_2^\sigma \theta_i^2 + a_3^\sigma \theta_i^3 \end{aligned} \tag{4.8}$$

Fig. 4.8 and Table 4.1 show the result of fitting the unknown coefficient  $a$  of the polynomial regression model with parameters  $\mu$  and  $\sigma$  listed in Table 4.2. Note that all the determination coefficients ( $R^2$ ) of the regression model are close to 1.0 in all conditions. Those fitted coefficients from Eq. (4.8) are applied to Eq. (4.5).

Table 4.1 Gaussian distribution parameters

Insertion angle °		0	10	20	30	40
PVC50%	$\mu$	0.296	0.835	2.25	2.75	2.83
	$\sigma$	0.241	0.492	0.593	0.655	0.703
PVC75%	$\mu$	0.291	1.12	2.49	2.88	3.28
	$\sigma$	0.273	0.593	0.611	0.694	1.13
Chicken	$\mu$	0.652	2.68	4.12	4.64	5.81
	$\sigma$	0.422	1.40	1.51	1.68	2.64

Table 4.2 Polynomial regression model coefficients

Coefficient		$a_0$	$a_1$	$a_2$	$a_3$
PVC50%	$\mu$	0.133	0.122	-1.31E-03	-
	$\sigma$	0.242	0.0332	-9.91E-04	1.12E-05
PVC75%	$\mu$	0.203	0.130	-1.32E-3	-
	$\sigma$	0.274	0.0566	-3.06E-3	5.46E-5
Chicken	$\mu$	0.747	0.198	-1.88E-3	-
	$\sigma$	0.425	0.165	-8.28E-3	1.38E-4

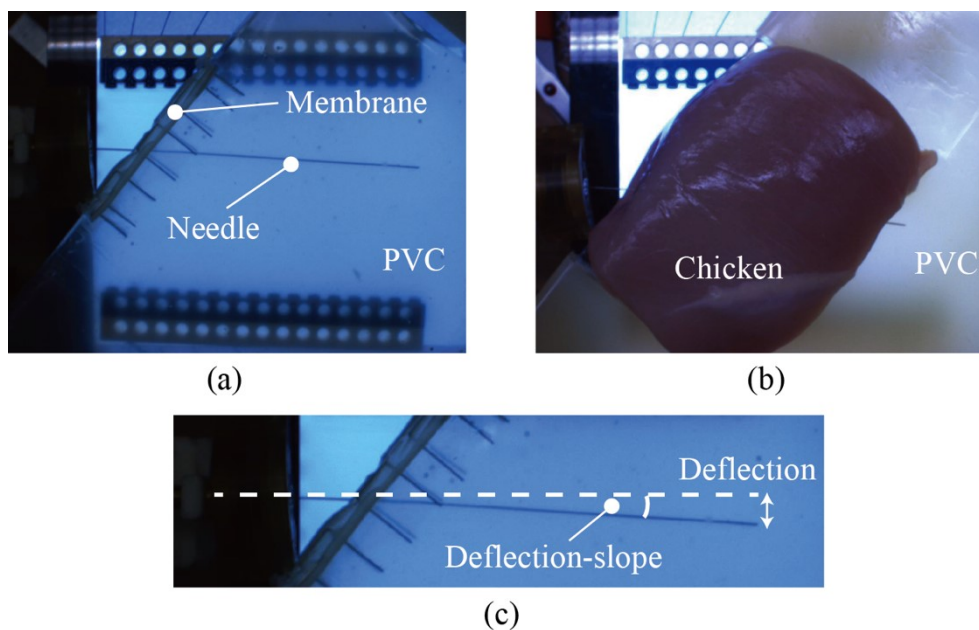


Fig. 4.5 Needle insertion overview: (a) PVC experiment (b) biological tissue (chicken) experiment, and (c) definition of deflection-slope.

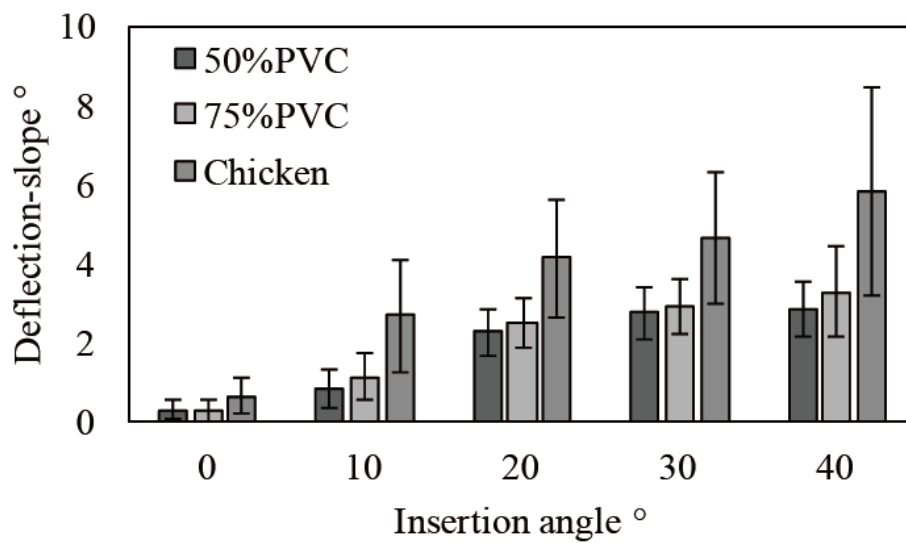


Fig. 4.6 Experimental result of deflection-slope due to insertion angles.

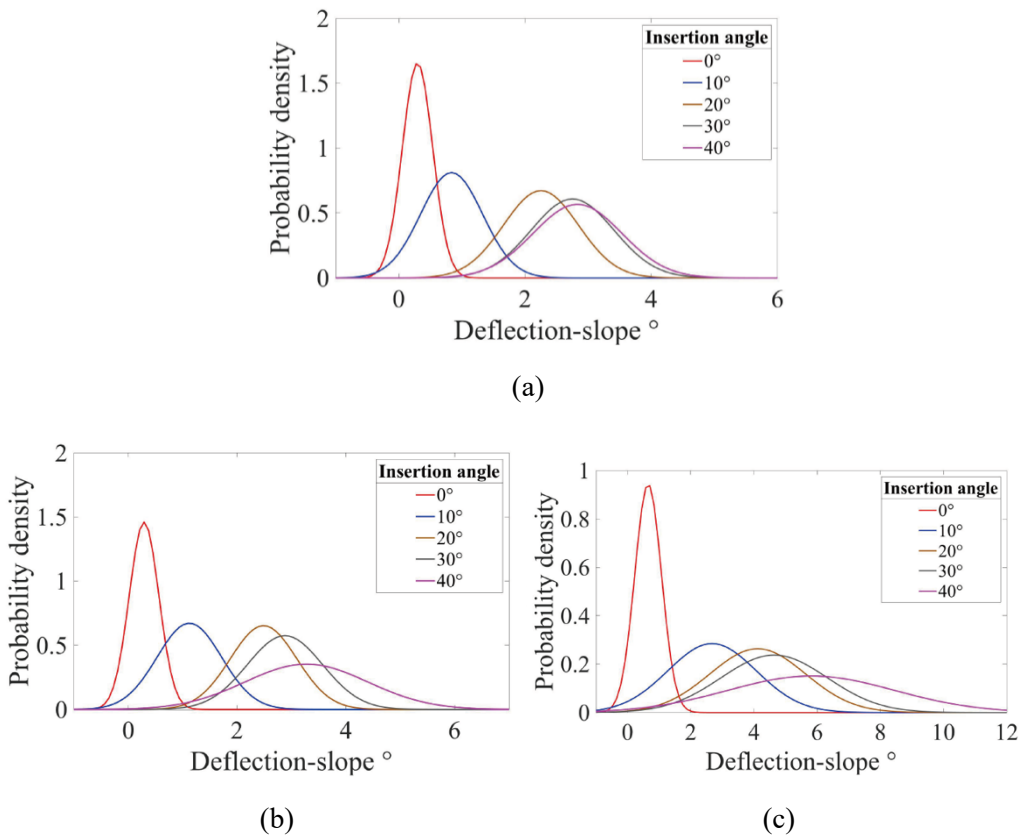


Fig. 4.7 Results of fitting experimental deflection data to the Gaussian model: (a) PVC50%, (b) PVC75%, and (c) chicken.

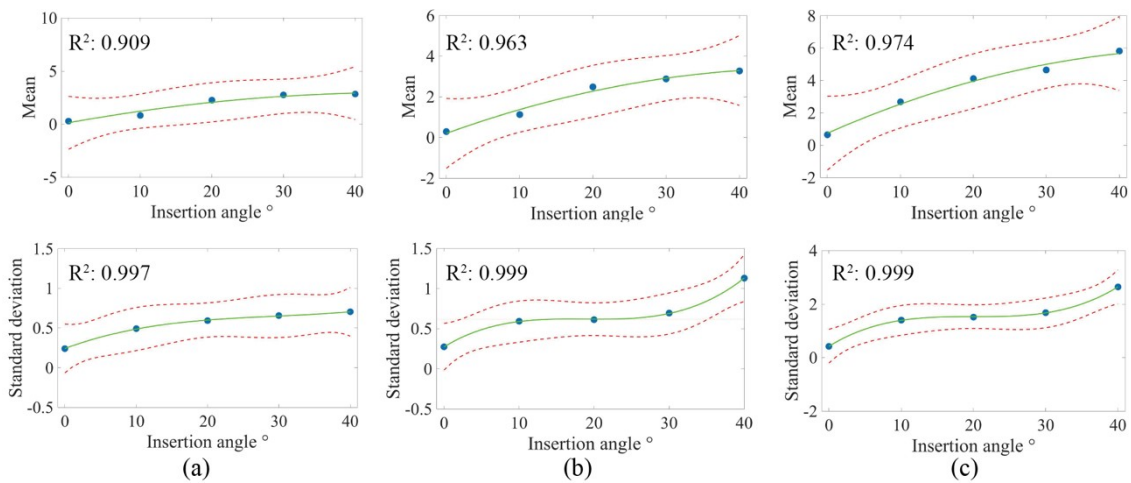


Fig. 4.8 Results of fitting the parameters,  $\mu$  (upper row) and  $\sigma$  (bottom row), of the Gaussian model to the polynomial regression model: (a) PVC50%, (b) PVC75% and (c) Chicken. Blue dots show the parameters obtained by experimental data, green lines show the estimated parameters, and red lines show a confident band of 95%.



### 4.2.4.3 Verification

In order to verify the proposed insertion path plan, some experiments on several of the multi-layered tissues used in 4.2.4.2 are performed. In these experiments, the author conducted two scenarios consisting of two-layered tissue phantoms and two scenarios consisting of three-layered tissue phantoms. The author conducted needle insertions from ten insertion paths. Angles varied under ten conditions (approximately  $-27^\circ$ ,  $-21^\circ$ ,  $-15^\circ$ ,  $-9^\circ$ ,  $-3^\circ$ ,  $3^\circ$ ,  $9^\circ$ ,  $15^\circ$ ,  $21^\circ$ , and  $27^\circ$  based on a insertion target). Each illustration of experimental scenarios is shown in Fig. 4.9. The ten needle insertion paths are randomly chosen among the setup limitations. Each insertion angle is measured with lines of the tissue boundary and insertion path connecting each needle entry position and the target. The objective function score of Eq. (4.1) is calculated for each needle entry position with the calculated insertion angles. For verifying the performance of the proposed weight factor in the objective function score, four-type weight factors are compared: (a) the proposed weight factor ( $w_i = w^{Dist} \times w^{Prob}$ ), (b) implementing only insertion angle ( $w_i = 1$ ), (c) implementing the tissue boundary distance ( $w_i = w^{Dist}$ ), and (d) implementing the deflection probability ( $w_i = w^{Prob}$ ). Note that  $p_{tissue}(\theta_i)$  of Eq. (4.5) was calculated with the measured insertion angles, and the insertion path with minimum score correspond to the optimal needle entry position. By comparing the calculated scores and measured needle tip deflections, the performance of insertion path planning can be verified. The target size ( $r_{tar}$ ) was set to  $\pm 2$  mm in this experiment, as mentioned in chapter 1. Six trials were conducted for each entry position for all experimental scenarios. Needle insertion conditions were the same as in section 4.2.4.2.

Fig. 4.10 shows the results of the needle deflection and objective function score with four-way weight factors. Table 4.3 shows the order of the deflection values and scores for all needle entry positions, and the concordance cases of the order are highlighted in all scenarios. The results show similar trend between deflections and scores for all insertion paths, and the insertion path with minimum score had minimum deflection in all scenarios. The concordance case rates of each objective function in Scenario I-IV are below: (a) 70% (7/10), 50% (5/10), 40% (4/10), and 60% (6/10); (b) 60% (6/10), 10% (1/10), 40% (4/10), and 40% (4/10); (c) 70% (7/10), 10% (1/10), 40% (4/10), and 50% (5/10); and (d) 60% (6/10), 50% (5/10), 40% (4/10), and 60% (6/10) (Table 4.3).

Table 4.3 Order of deflections and scores for all entry positions

<i>Scenario I</i>										
Needle entry positions	<i>1</i>	<i>2</i>	<i>3</i>	<i>4</i>	<i>5</i>	<i>6</i>	<i>7</i>	<i>8</i>	<i>9</i>	<i>10</i>
Deflection	10	9	7	6	2	1	3	4	5	8
(a) Proposal	10	9	7	4	2	1	3	5	6	8
(b) $w_i = 1$	10	9	7	5	3	1	2	4	6	8
(c) $w_i = w^{Dist}$	10	9	7	4	2	1	3	5	6	8
(d) $w_i = w^{Prot}$	10	9	7	5	3	1	2	4	6	8
<i>Scenario II</i>										
Needle entry positions	<i>1</i>	<i>2</i>	<i>3</i>	<i>4</i>	<i>5</i>	<i>6</i>	<i>7</i>	<i>8</i>	<i>9</i>	<i>10</i>
Deflection	6	7	5	3	1	2	4	8	10	9
(a) Proposal	8	6	5	3	1	2	4	7	9	10
(b) $w_i = 1$	8	6	4	2	1	3	5	7	9	10
(c) $w_i = w^{Dist}$	8	6	4	2	1	3	5	7	9	10
(d) $w_i = w^{Prot}$	8	6	5	3	1	2	4	7	9	10
<i>Scenario III</i>										
Needle entry positions	<i>1</i>	<i>2</i>	<i>3</i>	<i>4</i>	<i>5</i>	<i>6</i>	<i>7</i>	<i>8</i>	<i>9</i>	<i>10</i>
Deflection	10	8	5	4	3	1	2	6	7	9
(a) Proposal	10	9	7	5	3	1	2	4	6	8
(b) $w_i = 1$	10	9	7	5	3	1	2	4	6	8
(c) $w_i = w^{Dist}$	10	9	7	5	3	1	2	4	6	8
(d) $w_i = w^{Prot}$	10	9	7	5	3	1	2	4	6	8
<i>Scenario IV</i>										
Needle entry positions	<i>1</i>	<i>2</i>	<i>3</i>	<i>4</i>	<i>5</i>	<i>6</i>	<i>7</i>	<i>8</i>	<i>9</i>	<i>10</i>
Deflection	10	9	5	3	2	1	4	6	7	8
(a) Proposal	10	9	6	4	2	1	3	5	7	8
(b) $w_i = 1$	10	8	6	4	2	1	3	5	7	9
(c) $w_i = w^{Dist}$	10	8	6	4	2	1	3	5	7	9
(d) $w_i = w^{Prot}$	10	9	6	4	2	1	3	5	7	8

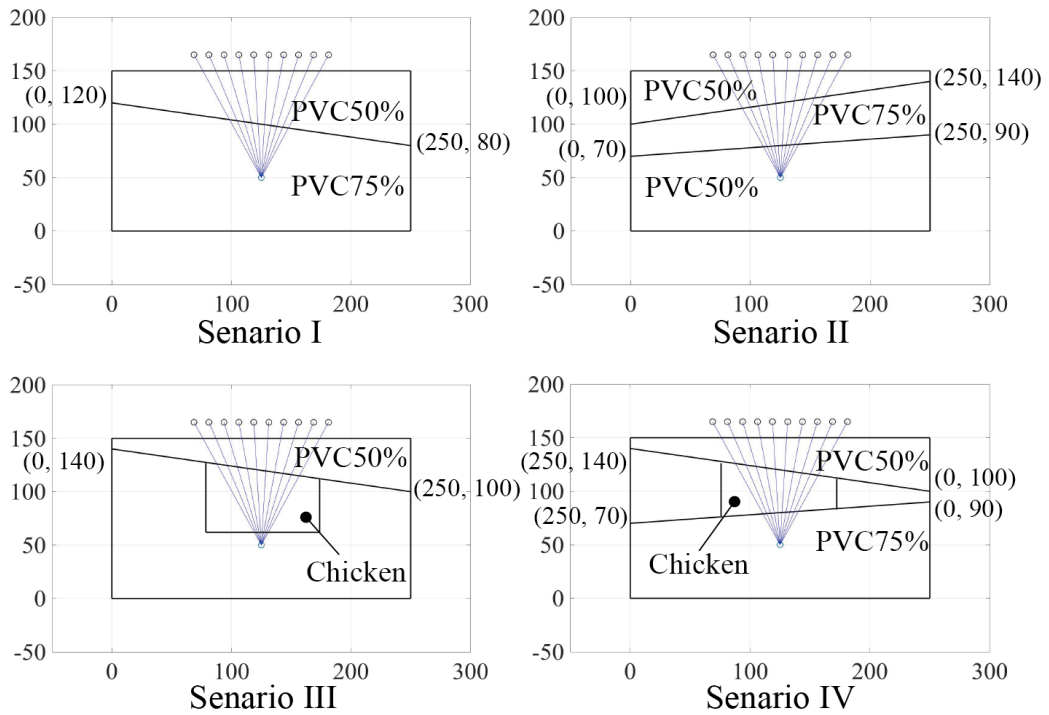


Fig. 4.9 Experimental scenario overview. Targets are set at 125, 50. Both sides of the chicken are fixed with PVC, as in Fig. 4.5 (b).

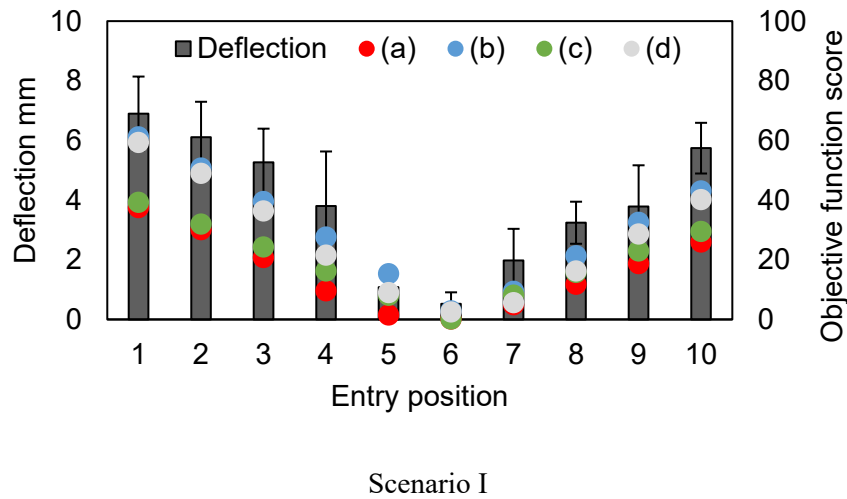


Fig. 4.10 Comparison of scores calculated with the objective function and needle tip deflections for all needle entry positions.

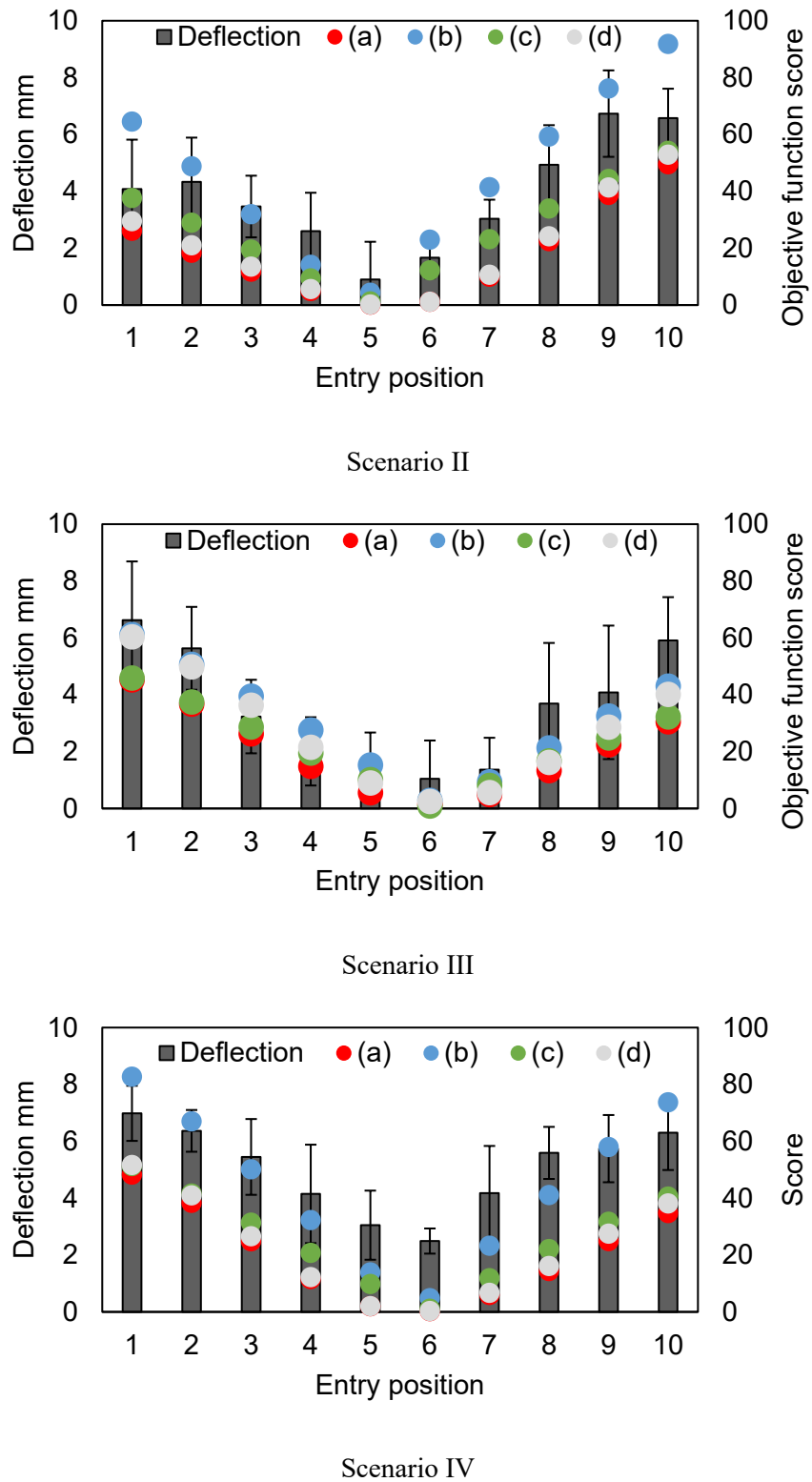


Fig. 4.10 (continued) Comparison of scores calculated with the objective function and needle tip deflections for all needle entry positions.

## 4.2.5 Discussion

The results show that all objective functions can determine the optimal needle entry position in all tested scenarios. On the other hand, focusing on Table 4.3, the concordance rates varied due to the type of weight factor and experimental scenarios. Focusing on scenario I, the concordance rate was increased by using  $w^{Dist}$ , compared to applying only the insertion angle. Focusing on scenario II and IV, the concordance rates were also increased by using  $w^{Prob}$  compared to applying only the insertion angle. Meanwhile, the concordance rates were not increased by using any weight factors in scenario III. As it is considerable that the effect of the weight factor may vary due to the insertion situations, the accuracy of path planning can be increased effectively by integrating the effect of tissue boundary distance and deflection probability in weight factors. Moreover, it is suggested that the sum of the insertion angle is a dominant factor for determining the optimal insertion path.

However, the author found still some mismatching orders between the score and deflection in all scenarios, even applying the proposed weight factor to the objective function score. In the current model, each insertion angle ( $\theta_i$ ) under static conditions was calculated. Actually each insertion angle may vary slightly because of needle deflection during insertion into the previous tissue layer. For increasing the accuracy of the path planning additionally, it is necessary to estimate the actual insertion angle. Moreover, the effect of previous tissue layers is not implemented for obtaining the *deflection probability* in the current model. The *deflection probability* is acquired based on the deflection-slope due to the initial insertion angles at the tissue surface. Looking at the deflection at the tissue boundary, the needle was fixed by a previous tissue layer, but the deflection behavior may have differed due to the previous tissue layer's characteristic [4.8]. Although only final deflections was measured in this experiment, it is desirable to measure the actual trajectory path for observing the effect of the previous tissue layer. In additions, the *deflection probability* may vary due to the insertion velocity, as the puncture event has been affected depending on the insertion velocity [4.4]. In this study, only one-way insertion velocity was set for needle insertion and rotation because the author needed to primarily confirm the performance of insertion path planning with the insertion angle. Thus, as the future work, it is essential to investigate whether the effect of the previous tissue layer and needle insertion conditions are critical for determining *deflection probability*. Moreover, in this study, the author included *deflection probability* the effect of all complexed needle-tissue interactions into one component. The path planning may be further improved if more specific parameters, such as tissue stiffness and non-homogeneity, can be input into *deflection probability* separately.

Locking at the results of optimal insertion positions, all optimal insertion paths were selected

to be almost perpendicular in insertion direction to the tissue surface (entry position: 5 or 6) in all experimental scenarios. As the reason why there are few differences of optimal insertion path between each experimental scenario, it is considerable that the condition of multi-layered tissue phantom is limited. As mentioned above, the sum of insertion angles might be the dominant factor for path planning; Thus, optimal positions in this multi-layered tissue phantom were selected around the central entry positions in all experimental scenarios. Assuming actual environment of lower abdomen, the tissue shape composing the multi-layered tissue is likely convex, but the tissue layer composing the multi-layered tissue was almost flat-shaped. Thus, it is considerable that the optimal insertion path may not be selected perpendicularly to the tissue surface in any cases. Moreover, because PVC phantom and chicken meat composing the multilayered tissue are almost homogeneous, it is necessary to verify the proposed path planning with more realistic models, including a lot of fiber, such as hog meat. With such realistic tissues, the deflection probability is expected to be more effective, because the variance in deflection may be increased due to the tissue characteristics. Therefore, the proposed path planning needs to be verified in a condition mimicking actual tissue properties and anatomical structures.

Focusing on the results of needle deflections for each optimal path, some deflections still remained, especially in scenario IV; nonetheless, these deflections can be reduced, compared to other insertion positions. The deflections may vary depending on the number of tissue layers and the tissue properties. The approach employed in this study was to passively determine the optimal path as a premise for the straight path connecting the initial entry position and target, such that the deflections become inevitable. Meanwhile, the deflection may be more decreased by selecting the initial insertion angle to be able to cancel out the effect of deflection in each layered tissue actively. In order to implement this, it is necessary to consider deflection directions and the deflection probability, and to estimate the deflection probability, including the effect of the previous tissue layer, as mentioned above.

## 4.3 Path planning system based on CT images

In the previous section, preoperative insertion path planning was introduced based on the insertion angles. For practical application of insertion path planning, it is necessary to develop a system for automatically calculating the insertion angle and determining the optimal insertion path on CT images. In this section, a multilayered tissue boundary detection technique was developed in the lower abdomen and the insertion angle was calculated along the insertion path, based on the boundary detection.

### 4.3.1 System overview

Fig. 4.11 shows an overview of the proposed system. First, the doctors manually determine the target on a CT image and the area where the needle can be inserted. The needle may be unable to pass through some areas because of the position of the target. For example, it is desirable to avoid areas in which blood vessels or nerves concentrate. In such cases, the region of interest (ROI) should be set manually to avoid these areas, considering the patient's safety. In the ROI, the multilayered tissue boundary is detected and the insertion angle is calculated accordingly. This improves calculation cost efficiency as it helps avoid needless calculations. The ROI is a triangular shaped area connecting the target and two points outside the body surface, and multiple ROIs can be set as shown in Fig. 4.12. Candidates for the insertion path are generated in the selected ROI, as shown in Fig. 4.13. Each insertion path candidate is processed to allow for subsequent boundary detection and angle calculation described in the next section.

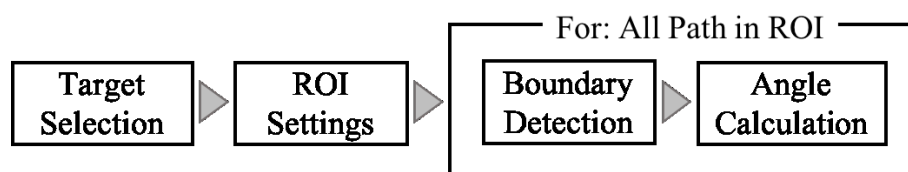


Fig. 4.11 Flow chart depicting the insertion angle calculation.

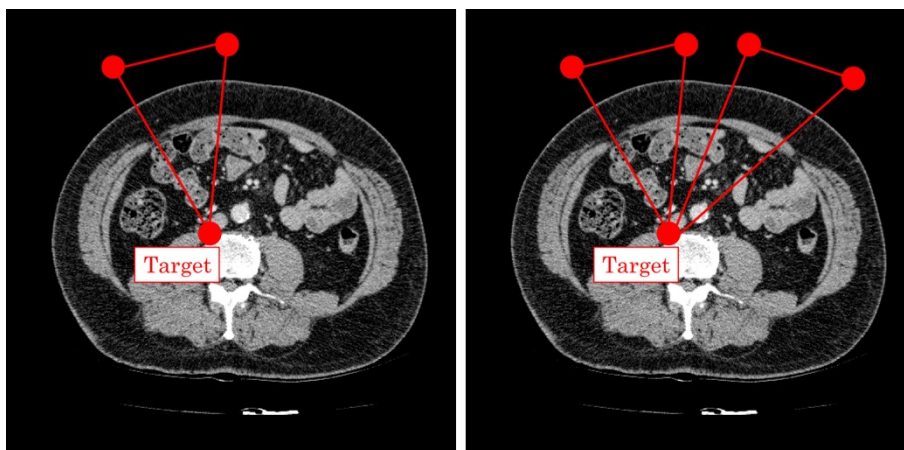


Fig. 4.12 Region of interest (ROI) setting overview: single ROI (left), multiple ROIs (right).

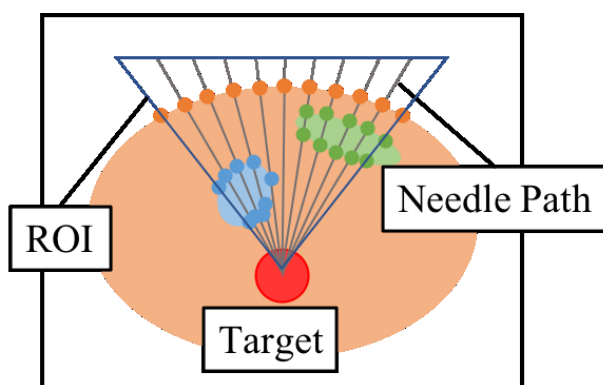


Fig. 4.13 Candidates for needle insertion path in region of interest (ROI)

### 4.3.2 Boundary detection

The tissue boundary in multilayered tissues must be detected to calculate the insertion angles at each tissue boundary. In particular, it is necessary to detect the boundary of the skin, muscle, and bowel while focusing on the lower abdomen. Some researchers have reported boundary detection methods in multilayered tissues. Malcolm et al. [4.9] detected the boundary of the amygdala and hippocampus with the label space technique. Shimizu et al. [4.10] detected multiple abdominal organs with the EM algorithm and level set method. However, those studies did not focus on the lower abdomen, including the bowels. Thus, it may be difficult to apply those methods to bowel boundary detection because of the complex shape of the bowel. Therefore, the aim in this section was to develop a detection method for multilayered tissue boundaries that does not depend on the tissue shape.

As shown in Fig. 4.13, candidates for the insertion path are generated in the ROI. Hence, by



detecting boundary points along each insertion path, and connecting those boundary points, multilayered tissue boundaries in the ROI can be generated. The detailed flow of boundary detection is shown in Fig. 4.14. First, to reduce the effect of noise in the CT image, the median filter was applied to the CT image for preprocessing. Next, graphs of the brightness value and change in brightness along the insertion path were generated (Fig. 4.15). The change in brightness was calculated by differentiating the brightness values on the candidate insertion path. The peak change in brightness must be detected to determine the tissue boundary point on the insertion path. It was difficult to determine the static threshold value because the peak value was significantly different depending on the brightness value distributions on the candidate insertion paths. Hence, the discrimination analysis method was applied to determine the threshold value dynamically. All boundary points in the ROI are detected by applying the process to all insertion path candidates.

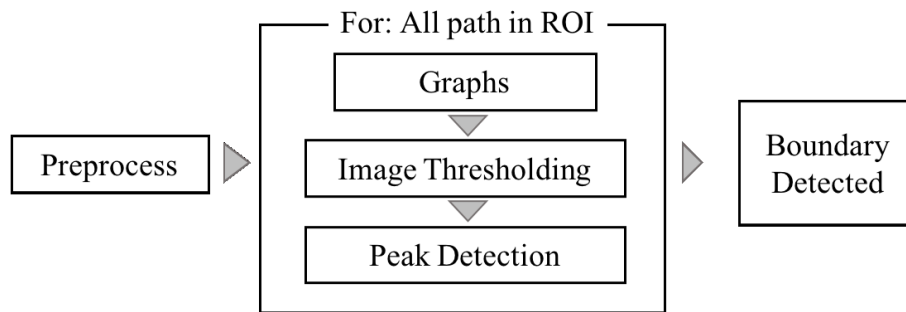


Fig. 4.14 Boundary detection system flow

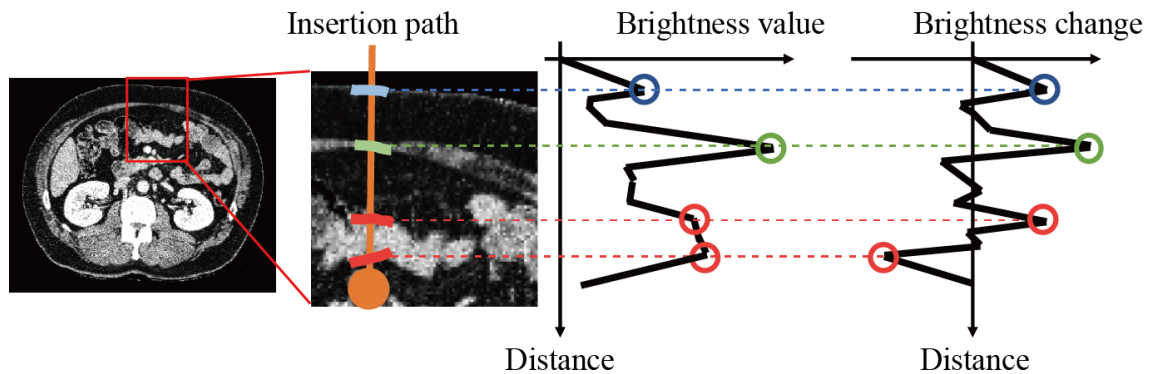


Fig. 4.15 Graphs of brightness value and change in brightness along the insertion path

### 4.3.3 Insertion angle calculation

After boundary detection of the multilayered tissue, the insertion angle on each boundary was calculated by calculating the normal vector at the cross point of the insertion path and tissue boundary. The approximate curve was then obtained from the detected boundary points since each

point is simply an aggregation of pixels. The least-squares polynomial approximation method was applied in this study. The order of approximation may be different depending on each tissue shape. By dividing the ROI into small regions, the approximation curve was obtained under fixing the order. For small regions, the region, including the previous and next  $n$ th insertion path candidate, was set based on the calculated insertion path. After dividing the ROI into small regions, an 8-connected-component label was applied to the detected boundary points to classify each tissue boundary (skin, muscle, or bowel), and the approximation curve was fitted to each classified tissue boundary point. At the cross points of each approximation curve and insertion path, the insertion angles were calculated with the dot product of the normal vector and the insertion direction vector. The flow of this system is shown in Fig. 4.16.

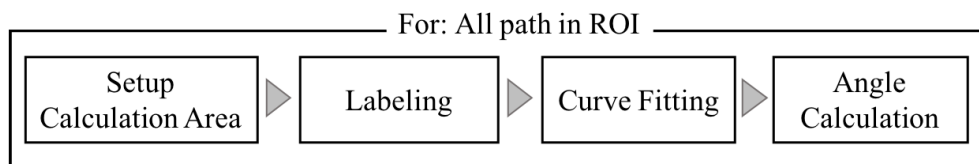


Fig. 4.16 Angle calculation system flow chart

## 4.3.4 Verification

### 4.3.4.1 Experimental setup

The accuracy of the detected multilayered boundary and the error of the insertion angle were evaluated to verify the proposed method. Six CT images of a male and female lower abdomen were used. The window settings were a window width of 350 and window length of 40, which are recommended values for imaging of the lower abdomen. The assumed target tumor size was a radius of 5 mm. The assumed tissues on the insertion path were skin, muscle, and bowel. In addition, the deviation of the ROI in detecting the approximate curve was  $n = 40$ , and the degree of the approximate curve was fixed at 3.

### 4.3.4.2 Tissue boundary detection

A verification test was carried out as follows to evaluate the accuracy of the boundary detection. First, we manually chose an appropriate ROI for each image. Next, the boundaries were detected by manual operation and the proposed method in the selected ROI. The manual operation was performed by visual observation of the CT images on display. Finally, each boundary was

estimated by the least-squares method as mentioned above. The approximate curves derived by the manual operation and proposed method were compared using the dynamic time warping algorithm, which is suitable for evaluating the coincidence of continuous data such as boundary shape [4.11]. Although pixels are compared by a mixing matrix in the field of image processing, it is difficult to properly evaluate the boundary shape using a mixing matrix. Fig. 4.17 compares the dynamic time warping value of each tissue, showing that the boundary of the skin and muscle could be detected or approximated with relatively high accuracy. Meanwhile, the boundary of the bowel could not be accurately detected compared to those of the skin and muscle.

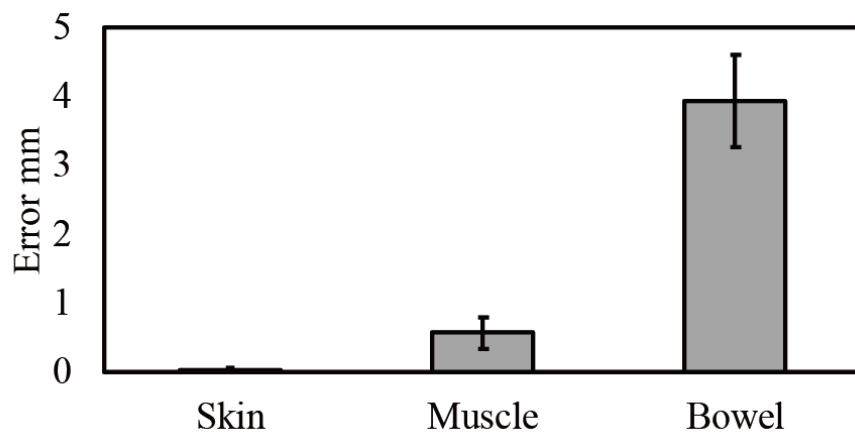


Fig. 4.17 Result of boundary detection using dynamic time warping.

#### 4.3.4.3 Insertion angle calculation

The verification test was performed to evaluate the error of the insertion angle based on the above-described boundary detection method. First, the insertion path was randomly selected in the ROI. The insertion angle of each tissue boundary was then calculated by manual operation and the proposed method. The trials were performed 12 times per CT image. The acceptable angle error was determined using Eq. (4.9) when the size of the assumed target was a radius of 5 mm. This formula describes the maximum angle error allowed to puncture the target at a point located distance  $L$  from the target, considering that the greater the distance from the target, the greater the effect of angle error on the accuracy.

$$\Delta\theta \leq \tan^{-1}\left(\frac{5.0}{L}\right) \cdot \frac{\pi}{180} \quad (4.9)$$

Fig. 4.18 shows the results of the calculated insertion angle. Table 4.4 shows the proportion of tolerance and average error of each tissue. As the figure shows, the insertion angle of skin and muscle could be calculated within relatively acceptable errors. However, the bowel insertion angle

could not be accurately calculated compared to that of the skin and muscle.

Table 4.4 Result of insertion angle evaluation

Tissue type	Proportion of acceptable error %	Average error °
Skin	100.0	0.68
Muscle	95.0	0.99
Bowel	75.7	5.3

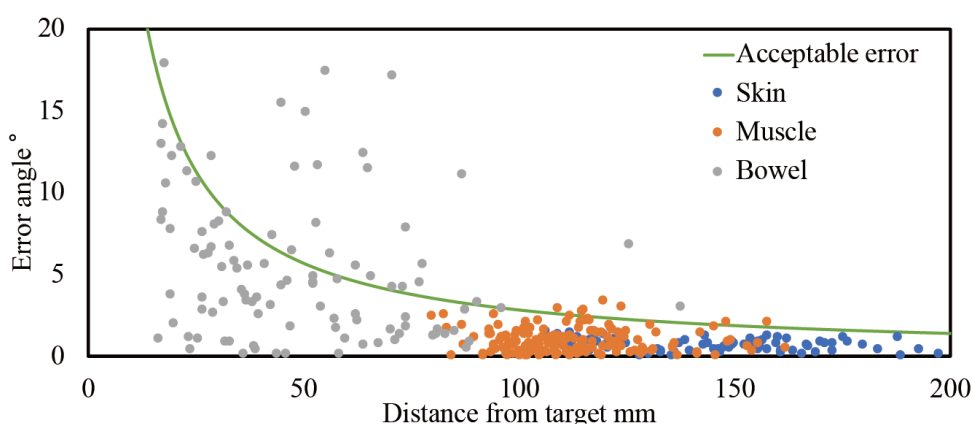


Fig. 4.18 Result of insertion angle error with respect to distance  $L$  from the target

### 4.3.5 Discussion

Some unacceptable insertion angle errors were observed in detecting bowel boundaries. The increased error may be attributed to two factors. First, the shape of the bowel is more complex than those of other tissues. Fig. 4.19 shows an example of an unsuccessful bowel boundary detection; the insertion path and boundary were mostly found to be parallel. Therefore, the system detected only the start and end points of the boundary, resulting in a discontinuous boundary detection. Fig. 4.19 shows that the divided boundaries should be classified as the same boundary. Future studies are required to establish a method that appropriately approximates divided boundaries. In addition, boundaries were not correctly detected in areas of tissue adhesion. As shown in Fig. 4.20, when muscle and bowel were adhered, the desired boundaries could not be detected. Due to tissue overlap in the lower abdomen, a method that does not depend on a threshold process, but on the magnitude of the peak along each insertion path, is needed. Although there was no influence on the error, it was confirmed that the shape that must be approximated as the third or higher order of approximated curve is included in the small region set for curve

approximation as shown in Fig. 4.21. In this study, curve approximation was performed by fixing to a cubic function, but it is necessary to respond by changing the degree with each shape or by changing the width of the small region with each shape.

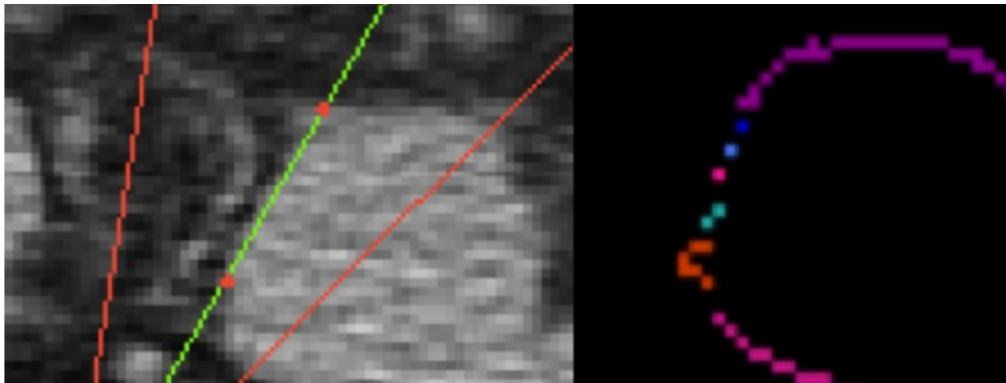


Fig. 4.19 Unsuccessful situations causing divided boundaries

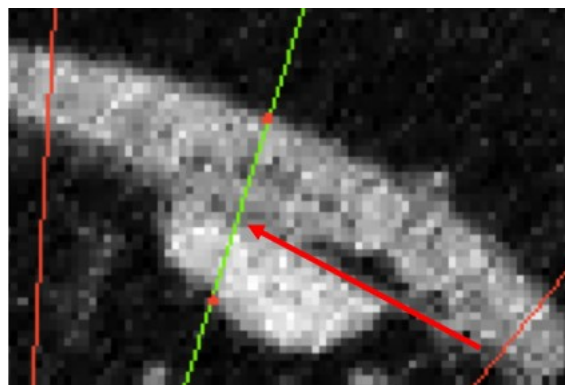


Fig. 4.20 Adhesion of muscle and bowel

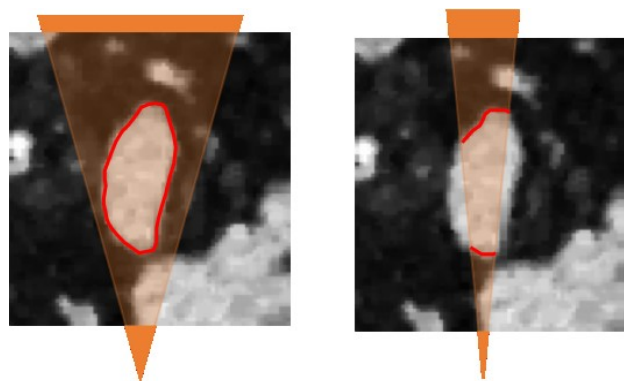


Fig. 4.21 Higher order of a polynomial (left) ideal separation (right)

## 4.4 Summary

In this chapter, a preoperative insertion path plan was proposed for minimizing needle deflection based on the insertion angle at each tissue boundary. By improving the accuracy of path planning, the boundary distance to a target and the probability of needle deflection at the boundary were implemented into the objective function as weight factors. To validate the model, experiments, involving four scenarios of two- and three-layered tissues, were performed. The results showed that the proposed model is capable of determining the optimal insertion path in all scenarios.

In addition, in order to apply the concept of insertion path planning in clinical settings, a system for detecting tissue boundary and calculating the insertion angle at each tissue boundary in CT images was developed. The boundary points were detected with change in brightness along each insertion path in CT images, and then the tissue boundary was generated by connecting the boundary points on all insertion path candidates. The experimental results showed average insertion angle errors of 0.68, 0.99, and 5.3 degrees in the skin, muscle, and bowel, respectively.

# Chapter 5: CT-guided needle insertion robot

## 5.1 Chapter introduction

In Chapters 3 and 4, the needle insertion control planning and insertion path planning for minimizing needle deflection were described. In this chapter, a CT-guided needle insertion robot system is proposed for implementing the proposed control and path planning in clinical situations.

This chapter aims to describe the robot design for conducting the required insertion motions, such as rotation and vibration, and the accurate positioning of needles based on CT images.

This chapter shows the requirements and overall design of the proposed robot system. The detailed designs of the needle insertion unit and method of registration between the CT and robot system were also described. The requirements were set assuming a lower abdomen operation of the CT-guided needle insertion therapy. Based on the requirements, a configuration for a multi-jointed arm attached to an end-effector with the function for needle insertion was applied. Additionally, registration between the robot and the CT image was necessary for the coordinate transform as the robot moves. With the registration method between the robot and CT image, a marker for accurately conducting the registration was consequently developed.

Figures and sentences were used by referring to the publication of the author in this chapter [5.1].

## 5.2 Requirements

### 5.2.1 Usage of the robot system

Procedures of the CT-guided needle insertion therapy with the robotic systems can be divided mainly into two phases.

1. Search and identification of the targets (tumor) in the CT images.
2. Insertion of needles into the targets from the appropriate position and angle based on the CT images.

Regarding 1) the search of targets in the CT images, image processing technologies based on

statistical information was required. A number of related researches exist due to the developing machine learning technologies.

However, those technologies are still developing and slightly deviate from the purpose of this study which is to develop the insertion planning to minimize the needle deflection. Therefore, this study focused on the development of a prototype robotic system for conducting 2) needle insertion from the appropriate position and angle based on CT images. The search and identification of the targets were manually conducted by doctors in this prototype.

## 5.2.2 CT scan

CT scans are widely used in hospitals all over the world. In this robotic system, CT scan was used due to the image modalities in terms of image clarity in the lower abdomen. The CT scan used in this study is an Aquilion LB (Canon Medical Systems, Tochigi, Japan) shown in Fig. 5.1. The specifications of the CT scan are listed in Table 5.1.



Fig. 5.1 CT scan used to needle insertion robot: Aquilion LB [5.2]

Table 5.1 Specification of CT scan

Items	Specifications
Gantry opening size	900 mm
Imaging area	700 mm
Minimum slice thickness	0.5 mm
Maximum reconstruction images	22 images/sec



### 5.2.3 Requirements for the needle insertion robot

In Chapters 3 and 4, the needle insertion control and path planning for minimizing the needle deflection in lower abdominal insertion were proposed. To implement the proposals in actual clinical situations, robot systems were developed to satisfy the requirements for the CT-guided needle insertion robot are described below.

1. Needle insertion with the combination of rotation and vibration

As mentioned in Chapter 3, the needle deflection can be decreased by conducting the insertion with the combination of vibration and rotation. Although there are several needle insertion robots implementing either rotation or vibration, only a few robots use both motions. Hence, structural mechanism design is required for simultaneous application of vibration and rotation motions to the needle.

2. Accurate positioning for initial insertion position

As introduced in Chapter 4, selection of the initial entry position to the targets is vital for a decrease in needle deflection. The robot needs to accurately move the needle to the appropriate positions on the body surface. It is assumed that the robot is controlled based on the CT images. The CT images resolution used in this study is approximately 1 mm/pixel, which is varying depending on the field-of-view setting. Therefore, the required accuracy for positioning is under 1 mm to control the robot over the accuracy of the CT images.

3. Operation inside the CT scan

- 3.1. The clearance between the robot and gantry

Limited space is available for the robot movement and operation inside the gantry. Hence, it is necessary to retain a clearance between the robot and gantry to avoid interferences. Moreover, the robot needs arbitrary positions on the lower abdomen. Fig. 5.2 shows the adequate space for robot movement inside the gantry. The size of the lower abdomen was assumed as the maximum value for Japanese people referring to the human body database [5.3]. Therefore, a compact size design of the robot end-effector is required for the main movements inside the gantry.

- 3.2. The decrease of metal artifacts on CT images

As mentioned above, the CT scan produces the images through X-ray transmission. Meanwhile, image noises are produced when the including substances of X-ray

transmission ratios drastically differ, such as a metal and plastic in an imaging plane. The noise is called metal artifact. Fig. 5.3 shows the effect of metal artifact in the CT images. If loud noises occur in the CT images, it would be difficult for doctors to search for tumors and to judge the condition of the patient during the insertion. Hence, a robot end-effector included in the CT imaging area needs to be designed for minimal noise.

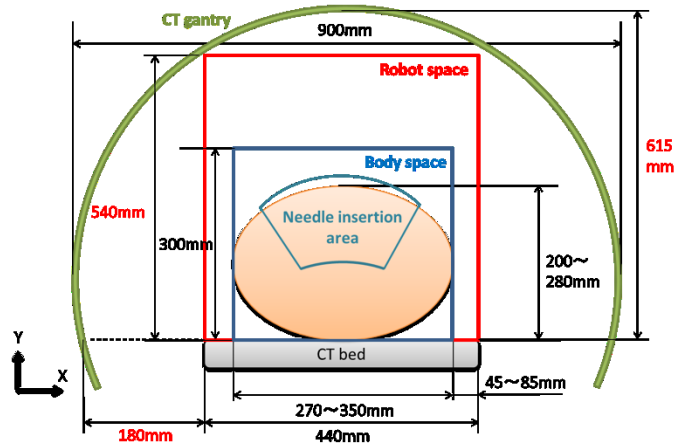
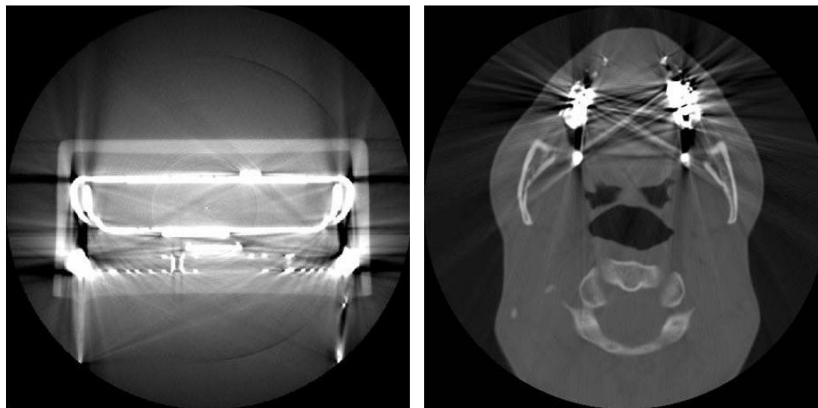


Fig. 5.2 Clearances between CT gantry and patient body



(a) CT image of an electrical device.

(b) CT image of a human jaw bone.

Fig. 5.3 Sample of metal artifacts on CT images [5.4]

## 5.3 Overall design

### 5.3.1 Total configuration

The proposed needle insertion robot is operated from a remote place, such as a CT console room, to avoid radiation exposure for doctors, as shown in Fig. 5.4. Fig. 5.5 shows the total configuration of the proposed needle insertion robot. The needle insertion robot is mainly composed of 1) needle insertion unit, 2) positioning arm, and 3) registration marker. The positioning arm moves the needle insertion unit attached to its end-effector based on the input information from the operators. The needle insertion unit performs the needle insertion motion. The registration marker attached to the needle insertion unit registers the coordinate transformation between the CT images and positioning arm. The details of the 1) needle insertion unit, and 3) registration marker, will be described in the next chapter.

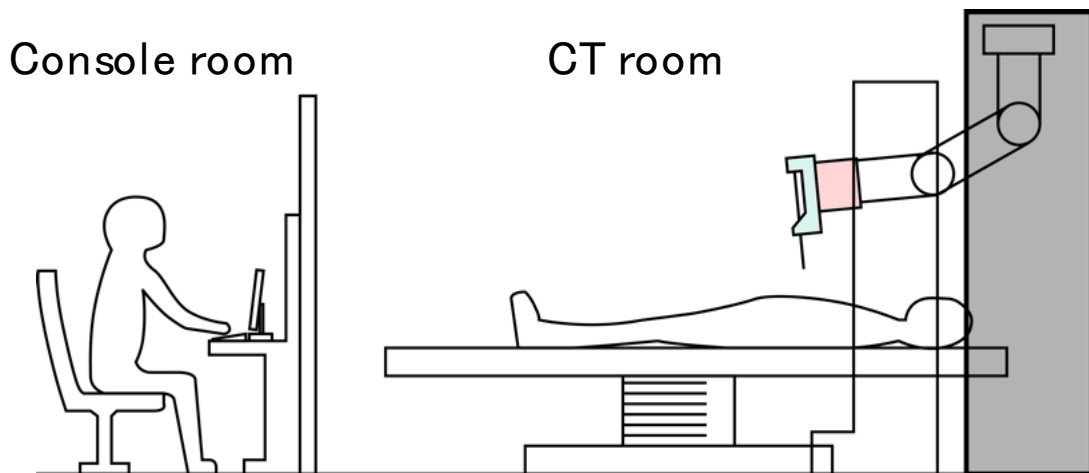


Fig. 5.4 General layout of the needle insertion robot system

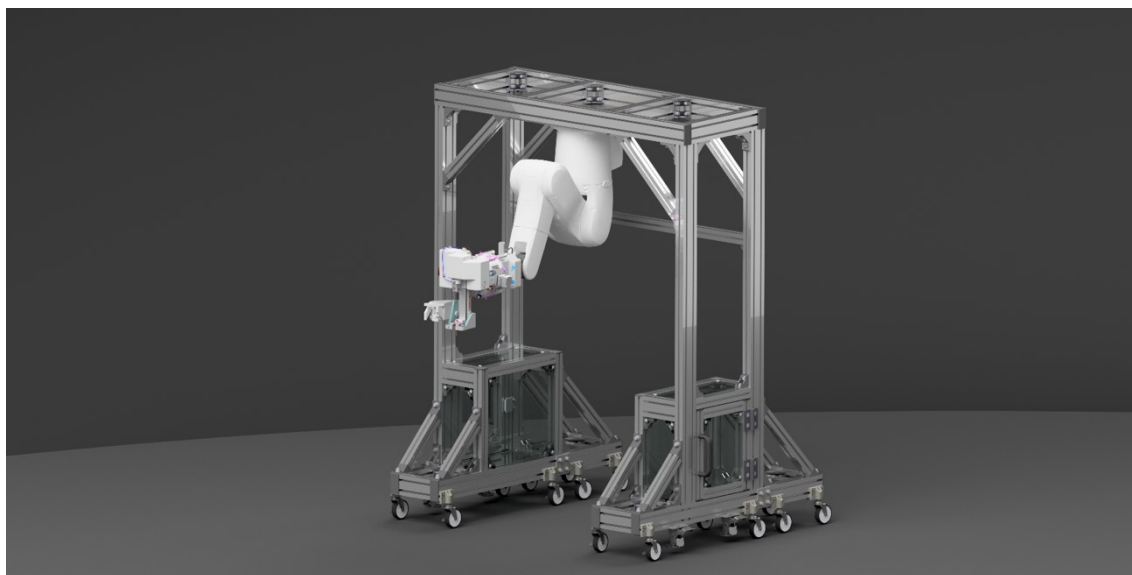


Fig. 5.5 Overview of needle insertion robot composed of 1) needle insertion robot, 2) positioning arm, and 3) registration marker

### 5.3.2 Positioning arm

The positioning arm is configured using a 6-DoF multi-joint robot arm and a gate-type basement. The positioning arm can be set in front of and behind the CT scan as shown in Fig. 5.6. To move the needle insertion unit to its arbitrary position and angle on the lower abdomen for conducting the proposed insertion path planning, 6-DoF is required for the joints positioning. Moreover, in terms of compensating the reliability of positioning accuracy, a commercial robot arm is used in the needle insertion robot. The 6-DoF multi-joint arm used in this study is VS-068 (Denso wave, Japan) as shown in Fig. 5.7. The specifications are listed in Table 5.2.

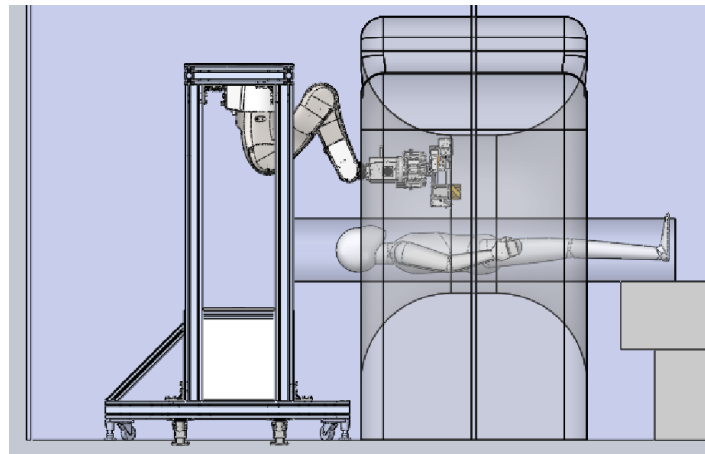


Fig. 5.6 Setting positions of the positioning arm



Fig. 5.7 6-DoF robot arm used in this study (VS-068) [5.5]

Table 5.2 Specifications of robot arm

Items	Specifications
Degree of Freedom (DoF)	6
Position tracking method	Absolute encoder
Motor	AC servo motor (with brake)
Arm length	680 mm
Maximum load	7 kg
Repeat-positioning accuracy	$\pm 0.02$ mm
Weight	49 kg

## 5.4 Needle insertion unit

### 5.4.1 Overall design

The needle insertion unit requires the ability to perform insertion motions by applying the combination of rotation and vibration motions to the needle captured with the needle insertion unit, and designing the material and size for CT compatibility. Fig. 5.8 shows an overview of the needle insertion unit. The needle insertion unit has 3-DoF which are the insertion axis, rotation axis, and vibration axis. The insertion motion is achieved by upward and downward movements of the mounting base attached to the needle with a ball screw (KR1501, THK, Tokyo, Japan) and controlled by a DC servo motor (SGMMV\_A3E, Yasukawa, Tokyo, Japan). The axial rotation motion is achieved by rotating the shaft capturing the needle with a stepping motor (PKP225D15, Oriental motor, Tokyo, Japan) connecting gears. The vibration motion is achieved by connecting the shaft to the piezo actuator (Physik Instrument, Palmbach, German). Additionally, the 6-axis force/torque sensor (ATI, Texas, USA) for collecting the insertion forces is attached between the shaft and part capturing the needle. The specifications of the actuators and sensor are listed in Table 5.3.

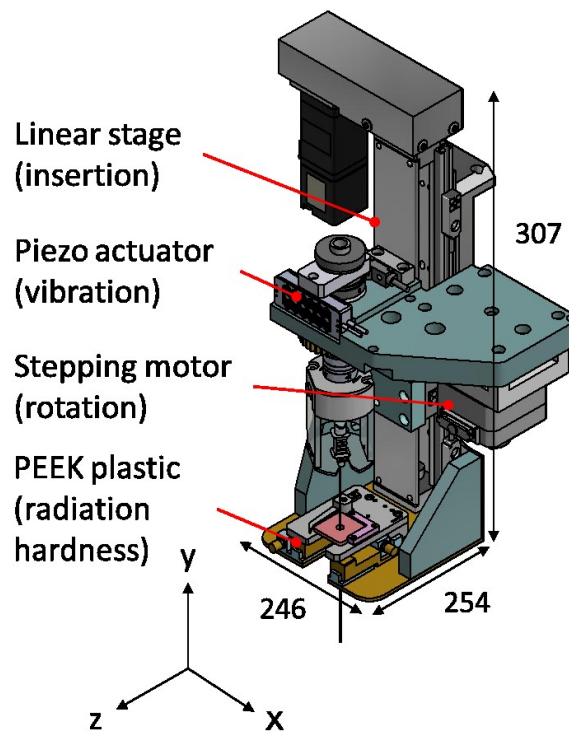


Fig. 5.8 Overview of needle insertion unit

Table 5.3 Specifications of actuator and sensors in needle insertion unit

## (a) Ball screw for insertion motion (KR15, THK, Japan)

Items	Specifications
Dynamic load rating	1930 N
Static load rating	3450 N
Positioning accuracy	0.02 mm
Stroke	156.4 mm
Weight	0.34 kg

## (b) Stepping motor for rotation motion (PKP225D15A2-R2EL, Oriental motor, Japan)

Items	Specifications
Maximum torque	0.19 Nm
Resolution	1.8 °
Accuracy	± 0.05 °
Weight	0.21 kg

## (c) Piezo actuator for vibration motion (P-602.3SL, Physik Instrument, German)

Items	Specifications
Open-loop travel, -20 to +120 V	300 μm
Open-loop resolution	0.3 nm
Unloaded resonant frequency	450 Hz
Push force capacity	100 N
Weight	0.02 kg

## (d) Six-axis force/torque sensor (nano17-SI-25-0.25, ATI, USA)

Items	Specifications	
Range	$F_x, F_y$	25 N
	$F_z$	35 N
	$T_x, T_y$	250 Nmm
	$T_z$	250 Nmm
Resolution	$F_x, F_y$	1/320 N
	$F_z$	1/320 N
	$T_x, T_y$	1/64 Nmm
	$T_z$	1/64 Nmm

## 5.4.2 Mechanism of insertion with rotation and vibration

In this section, the detailed mechanism for applying the simultaneous rotation and vibration motion to the needle is described. As shown in Fig. 5.9, the piezo actuator for the vibration, and stepping motor for the rotation are separately fixed at the mounting base. The stepping motor is then indirectly connected to the piezo actuator. Connecting the rotation motor structure directly to the piezo actuator can result in inaccurate movements of the piezo actuator due to the weights of parts mounted to it which may exceed the load rating. Fig. 5.10 shows the cross-section of the components for applying vibration and rotation simultaneously. The piezo actuator is connected to the shaft with a beam and collar. The beam has a hole for the insertion of the shaft and is held with bearings and collars. The shaft is connected to the collar with screws. By moving the beam connected to the piezo actuator, the shaft can move up and down while accepting the axial shaft rotation. As shown in Fig. 5.9, the stepping motor is connected to the shaft with gears. The gear is in line to the shaft with a hole for shaft insertion. The hole is shaped as a triangle to match the shaft shape as shown in Fig. 5.11. Moreover, the hole area is slightly bigger than that of the shaft to have clearance between both components. With this, the shaft can move up and down while applying the rotational motion to the shaft via gears.

Additionally, the needle guidance is attached to the base of the needle insertion unit as shown in Fig. 5.12. The guidance has a pinhole (diameter: 0.6 mm) that allows the extra-fine needle to pass through. Attaching the guidance minimizes the needle deflection before puncturing the skin since the needle tip is fairly fixed near the skin. Without the guidance, deflection during puncturing the skin may occur since the needle is fixed at the base. Moreover, attachment of the guidance can also absorb eccentricity of the needle when applying the rotation and vibration. The diameter is experimentally determined for adjusting the outer of the 25G needle. With extremely minimal clearance between the guidance hole and needle, the effect of deflection may be minimized, however, the friction between the guidance and needle may occur which can decrease the performance of vibration and rotation.



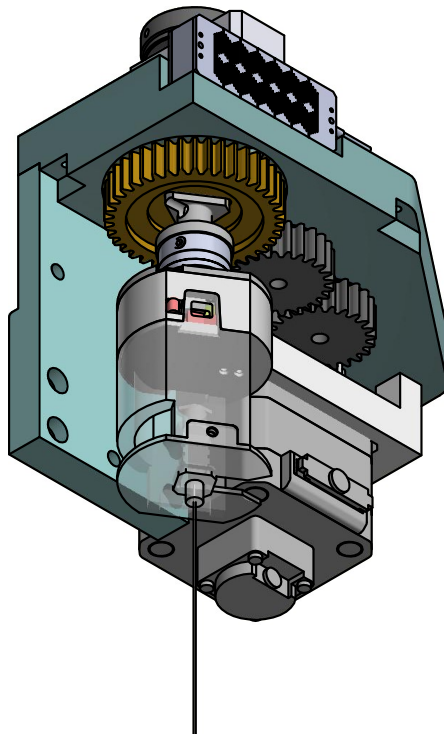


Fig. 5.9 Detailed design of mounting base attached to the piezo actuator and stepping motor

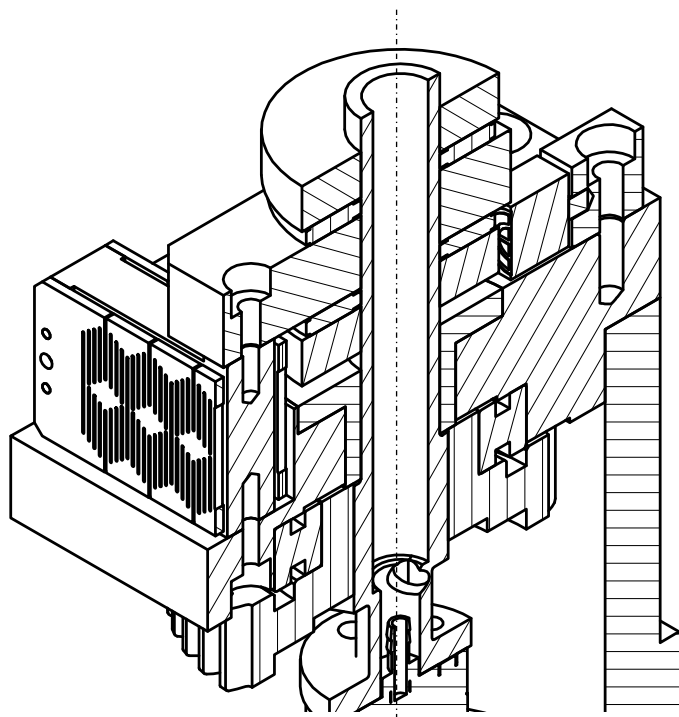


Fig. 5.10 Cross-section of components for applying rotation and vibration

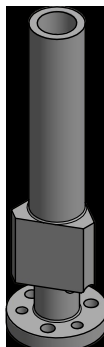


Fig. 5.11 Shape of shaft and gear for accepting the rotation and vibration

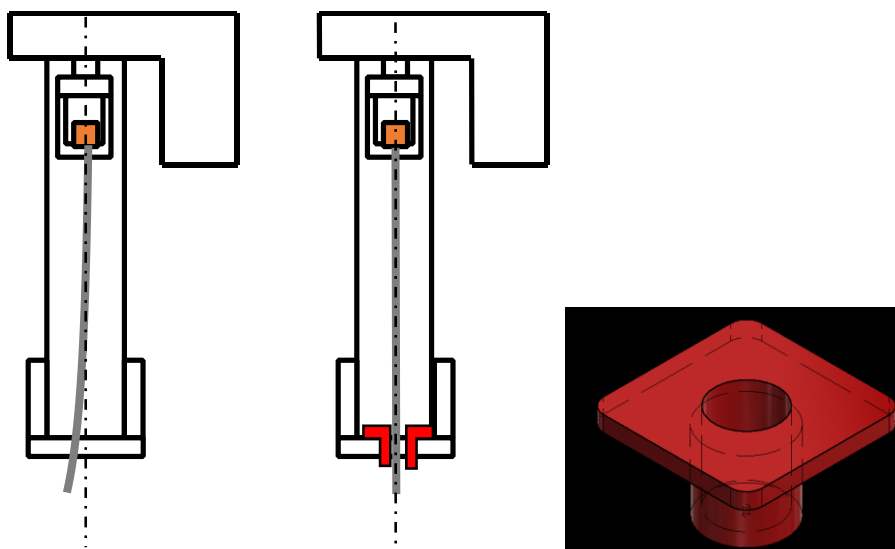


Fig. 5.12 Needle guidance for decreasing needle deflection before punctuation

### 5.4.3 Material and size for CT compatibility

As stated in the previous chapter, the metal artifact occurs when including metal substance in the CT imaging area. It is then necessary to use a non-ferrous material for the needle insertion unit as much as possible. In terms of radiation hardness and chemical proof, polyether ether ketone

(PEEK) is used as the main material of the needle insertion unit. PEEK has heat resistance, fatigue resistance, and crash-proof making it useful in space and medical devices. However, it has a relatively higher cost compared to other plastic materials. In terms of safety, it is necessary to confirm the strength of the needle insertion unit during its operation. As nearly all the forces generated from the actuators and body is concentrated on the shaft, a finite element analysis (FEA) experiment was conducted to the shaft made of PEEK. The experimental condition is set assuming maximum force and torque during the insertion with the rotation and vibration following: resistance along the insertion axis due to the ball screw and insertion force of 7.98 N, torque around the insertion axis due to the wind-up tissue of  $0.38 \times 10^{-3}$  Nm, and acceleration due to the piezo actuator of  $27.3 \text{ m/s}^2$ . The results are shown in Fig. 5.13 and Table 5.4. Since the maximum principal stress of the shaft is significantly under the acceptable shear stress, it is confirmed that there is no problem with the usage of PEEK as the material of the needle insertion unit.

As introduced in the previous section, limited space between the gantry and body is available for the movement of the needle insertion unit. The needle length used in the lower abdomen is up to 150 mm. It is then required to design the needle insertion unit with upward and downward movement along the 150 mm needle within the permitted height size. The designed size of the needle insertion unit is shown in Fig. 5.14.

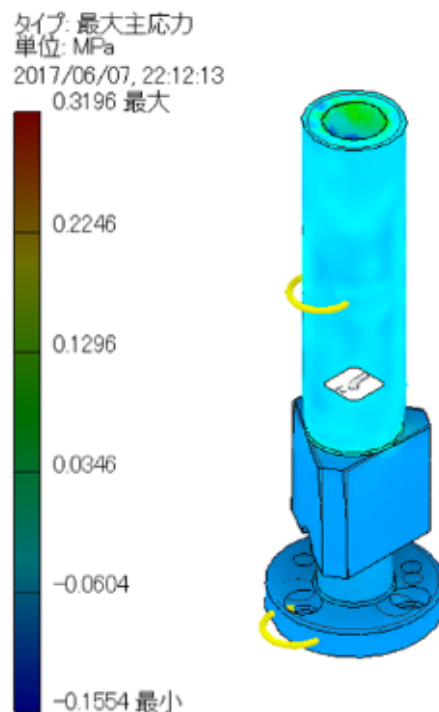


Fig. 5.13 Results of FEA experiments of the shaft

Table 5.4 Results of FEA experiments of the shaft

Items	Values
Maximum prinCBPal stress	0.3198 MPa
Maximum displacement	$25 \times 10^{-4}$ mm
Acceptable shear stress	53 MPa

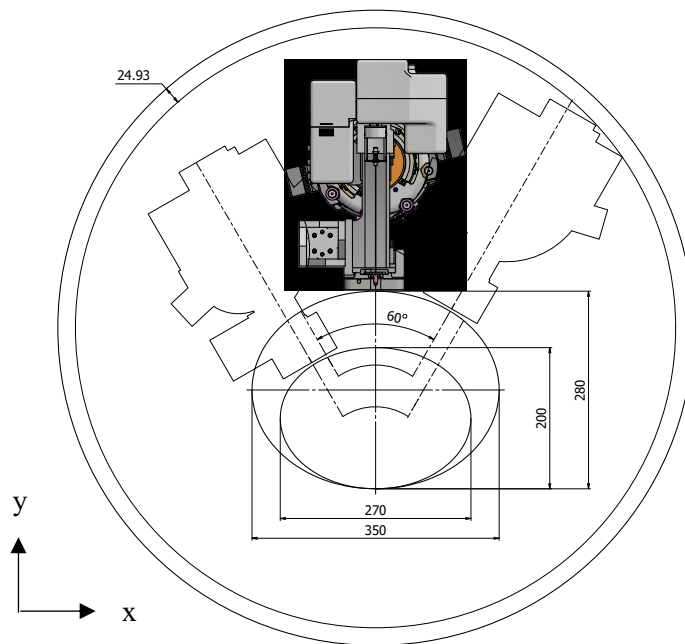


Fig. 5.14 Size of the needle insertion unit designed for avoiding to interfere the gantry and body

## 5.5 Registration method

### 5.5.1 Registration concept

#### 5.5.1.1 System overview

To control the position of the needle insertion unit with the positioning arm based on the CT images, it is necessary to register the coordinates of the robot to that of the CT image. In previous studies of the CT-guided robot system [5.6][5.7], the relative position between the CT image and robot was fixed due to the robot system that was mounted on the CT bed. In this study, for providing broad utilities to the robot system, the robot was not mounted on the bed as shown in Fig. 5.15. Then, the robot system can be placed on the floor arbitrarily near the CT gantry. Meanwhile, as the relative position between the CT image and needle insertion unit was not geometrically established unlike previous studies, it was necessary to acquire the accurate positional relationship of both components, especially between the CT image and needle tip position. Without the accurate positional relationship, the needle may be inserted in an unintentional direction. As general needles are made of ferrous materials and generates metal artifacts on the CT image as mentioned, it may be difficult to acquire accurate positional relation by using the needle on the CT image as a basis of registration. Then, it is necessary to develop the method of rigorous registration between the CT images and needle insertion unit.

Registrations intend to require positional confirmation between the marker base plane (MBP) attached on the needle insertion unit and CT image base plane (CBP). The error of the angle and distance between the MBP and CBP can be obtained by calculating the cross-section shape of the proposed marker from the CT image. This proposal is expected to have high versatility because of performing the registration only through calculating the marker shape on the CT image.

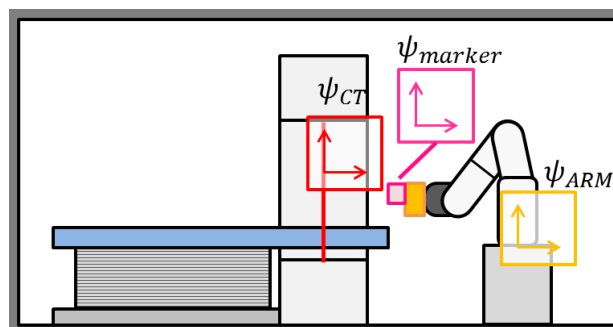


Fig. 5.15 Overview of each coordinate in the CT-guided-needle insertion robot system

### 5.5.1.2 Procedure

The proposed registration is conducted by measuring each side lengths of the cross-section shape of the proposed marker. First, the robot system is placed near the CT scan in the operating room. Next, operators control the positioning arm manually to move the needle insertion unit near CBP roughly for including the marker in the CT image, basically by using a laser light which is implemented in general CT gantries. The geometric quantity of angle and distance between the MBP and CBP is then calculated. Consequently, the positioning arm can move the needle insertion unit to a base position with the calculation result. The base position can be defined as the preferred position such as the center of CT image.

### 5.5.1.3 Requirements of registration marker

As previously described, the author needs to obtain the geometric quantity of the angle and distance between the MBP and CBP. Then, the registration marker needs to be a 3D structure with a cross-section shape applicable in the calculation and to be constructed using the suitable materials for CT image. The yaw and pitch angles and the craniocaudal-axis position are defined in Fig. 5.16. Then, the requirements of registration marker are listed following.

- The 3D geometric structure for calculating the error of 3DOF (yaw, pitch, and craniocaudal direction)
- Non-ferrous material with radiation hardness and drug resistance

As the 3-DOF can satisfy the correction of the error between the MBP and CBP in case of the robot control based on 2D-CT image, the calculation of the rolling angle, and x- and y-axis direction positions was not implemented in this system registration. In terms of image clarity and operability in clinical procedures, the author choose a plastic with high radiation and drug resistance as the marker material.

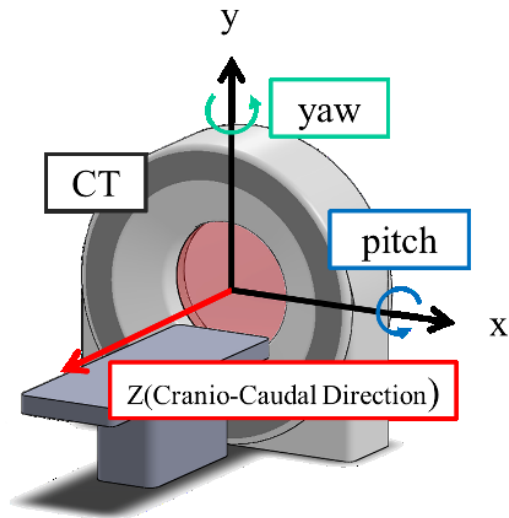


Fig. 5.16 Definition of coordinate of robot to CT image

### 5.5.2 Registration marker design

The registration marker composed of a square built into oblique prisms with inclined rectangular prisms. Fig. 5.17 shows the overview of the registration marker which has the geometrical-shape for satisfying the requirements described before. The marker was constructed of PEEK (poly-ether-ether-ketone) similarly used in the needle insertion unit.



Fig. 5.17 Overview of registration marker

### 5.5.2.1 Property of the oblique prism

The oblique prism structure was applied because of the geometrical superiorities compared with rectangular or spherical shaped objects which are often used for the registration in CT and MRI.

The cross-section was inclined by  $\theta$  degrees around the y-axis (yaw), and  $\varphi$  degrees around the x-axis (pitch) in a rectangular prism as shown in Fig. 5.18 (b). The side lengths of the prism base are defined as  $a$  and  $b$  as shown in Fig. 5.18 (a), and the sides lengths of the cross-section as  $a'$  and  $b'$  as shown in Fig. 5.18 (b). Those relation can be calculated with following formulas.

$$\theta = \cos^{-1} \frac{a}{a'} \quad (5.1)$$

$$\varphi = \cos^{-1} \frac{b}{b'} \quad (5.2)$$

The angles  $\theta$  and  $\varphi$  can be determined by Formula 5.1 and 5.2 with accurately measured side lengths. Meanwhile, slight errors may occur by obtaining CT images using bitmap images where even though  $a'$  is equal to  $a$ , and  $b'$  is equal to  $b$  at the completion of the registration. The errors were amplified by the inverse trigonometric function character, especially when calculating near  $0^\circ$  of  $\theta$  and  $\varphi$ . The ratio of the length of the sides (i.e.  $a'/a$  or  $b'/b$ ) are defined as  $\zeta$ , Formula (5.1) and (5.2) can replace  $f(\zeta) = \cos^{-1}(1/\zeta)$  (see Fig 5.18). Differentiating the  $f(\zeta)$  with  $\zeta$ , a derivate function is obtained. Approaching  $\zeta$  to 1, which means approaching the angle to  $0^\circ$ , the gradient then diverges to infinity.

$$\lim_{\zeta \rightarrow 1+0} f'(\zeta) = \lim_{\zeta \rightarrow 1+0} \frac{1}{\zeta \sqrt{\zeta^2 - 1}} = +\infty \quad (5.3)$$

Therefore, the shape of rectangular prism is not appropriate for the registration even with the theoretically-calculated inclinations. The errors were then assumed to be decreased because  $\zeta$  takes higher values than 1 after complete registration. This is due to the drastic change of the gradient of  $f(\zeta)$  near  $\zeta = 1$  whereas the gradient around  $\zeta = 1.4$  is gentle. The error can be decreased when calculating the angle around  $\zeta = 1.4$  compared to that around  $\zeta = 1$ . Thus, the shape of oblique prism inclined by  $45^\circ$  (around  $\zeta = 1.4$ ) as shown in Fig. 5.20 was suitable and applied.



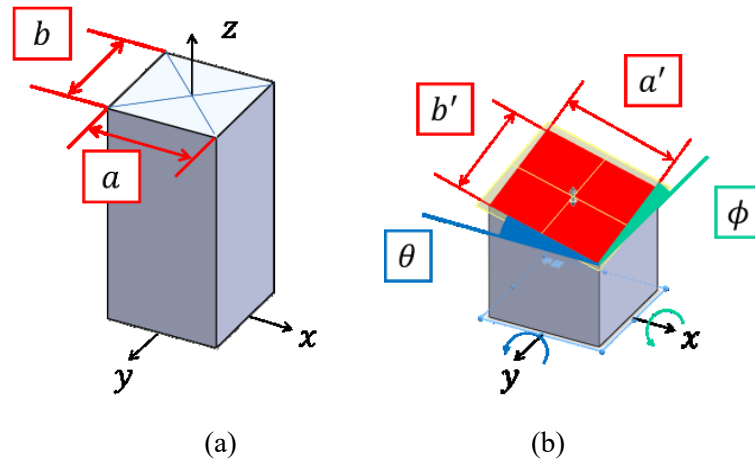


Fig. 5.18 The relationship of side lengths when a rectangular prism is cut by an inclined cross-section.

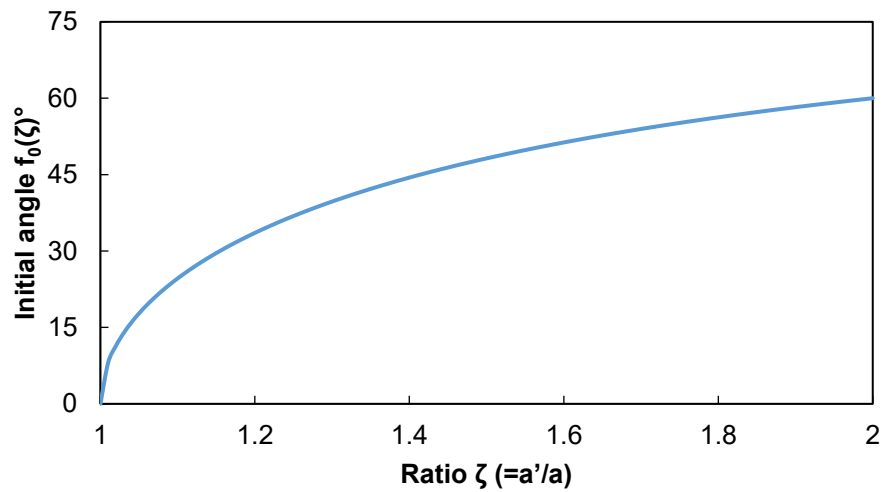


Fig. 5.19 Gradient of the ratio  $\zeta$  of side length change depending on the angle cut by an inclined cross-section to a rectangular prism.

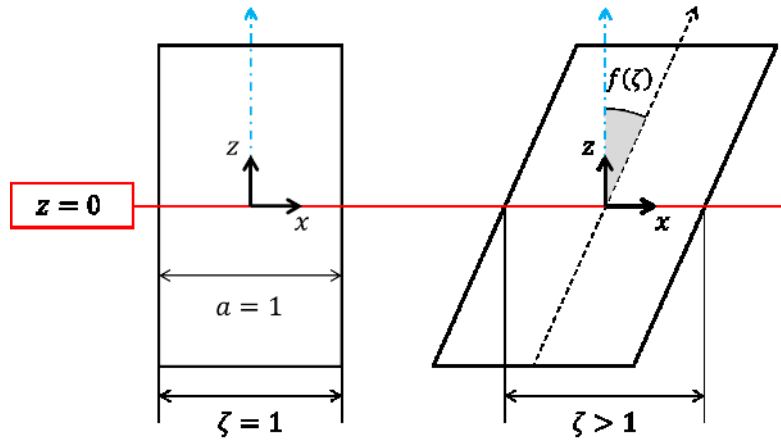


Fig. 5.20 Shape of oblique prism inclined by an angle defined with  $\zeta$

### 5.5.2.2 Calculation procedure of yaw and pitch angle

The inclined angles of the oblique prisms ( $\theta$  and  $\varphi$ ) can be calculated using Formula (5.4) and (5.5) based on Formula (5.1) and (5.2). In this section, the yaw angle calculations will be further explained as the formula used can be applied for both yaw and pitch angle calculations. In the CT coordinate, the oblique prism with a side length of “ $a$ ” and inclined by  $f(\zeta)$  degrees at the viewpoint of the  $y$ -axis shown in Fig. 5.21 was considered. The side length of the cross-section as  $a \cdot \cos(f(\zeta) + \theta)$  was described. Thus, the formula for calculating the yaw and pitch angles of the inclination of the oblique prism follows the formula below, respectively.

$$\theta = \cos^{-1} \frac{a}{a'} - f(\zeta) \quad (5.4)$$

$$\varphi = \cos^{-1} \frac{b}{b'} - f(\zeta) \quad (5.5)$$

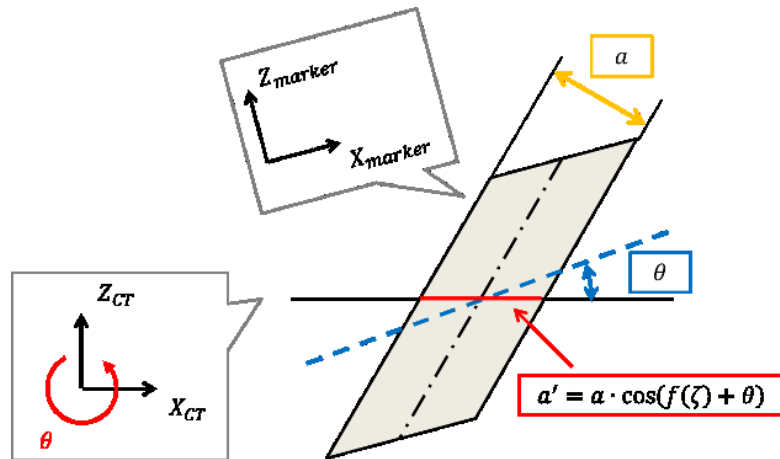


Fig. 5.21 Calculation of angle of oblique prism

### 5.5.2.3 Calculation procedure of craniocaudal distance

The craniocaudal distance (CCD) was calculated after correcting the marker yaw and pitch angles. Oblique prisms enabled the calculation of CCD due to the variation of the position of the cross-section shape on the CT image in proportion as the craniocaudal-axis position. Fig. 5.22 shows the rectangle as it moved from blue to orange on the CT image as the position of cross-section moves from blue to orange in the craniocaudal axial direction ( $Z_{\text{marker}}$ ). With the angle of the oblique prism ( $f(\zeta)$ ),  $\Delta t$  positional change of the cross-section shape on CBP due to  $\Delta z$  movement of the cross-section in the craniocaudal axial direction is described following.

$$\Delta t = \Delta Z \tan f(\zeta) \quad (5.6)$$

Since  $f(\zeta)$  is approaching to  $45^\circ$ ,  $\Delta t$  is also approaching to  $\Delta Z$ . Meanwhile, four oblique prisms were placed symmetrically as shown in Fig. 5.23 due to the cross-section central axes in the CT image needed for the CCD calculation. Focusing on the movement of the rectangles as the marker cross-section shape on CBP, Fig. 5.22 shows the cross-section of the blue oblique prisms move in the x-axis direction only whereas the green ones move in the y-axis direction only on CBP (see Fig. 5.24). With this movement, the central point of the marker cross-section shape can be calculated.

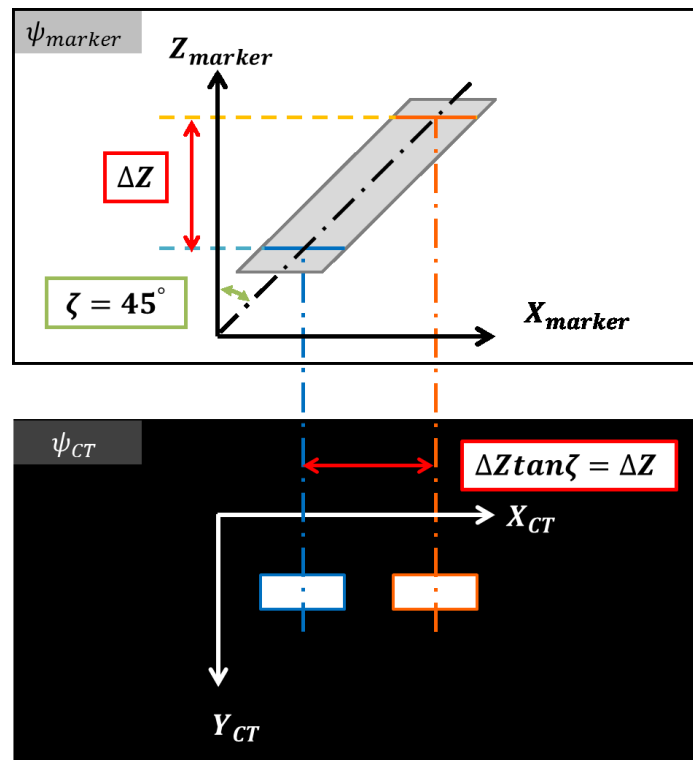


Fig. 5.22 Cross-section appearance depending on the cut position changes in the craniocaudal distance

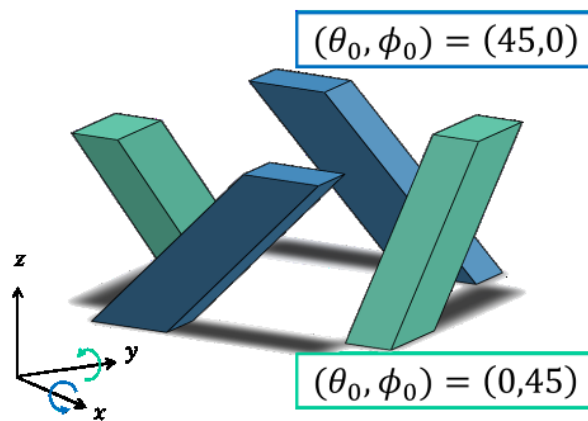


Fig. 5.23 Pairs of oblique disposed oppositely.

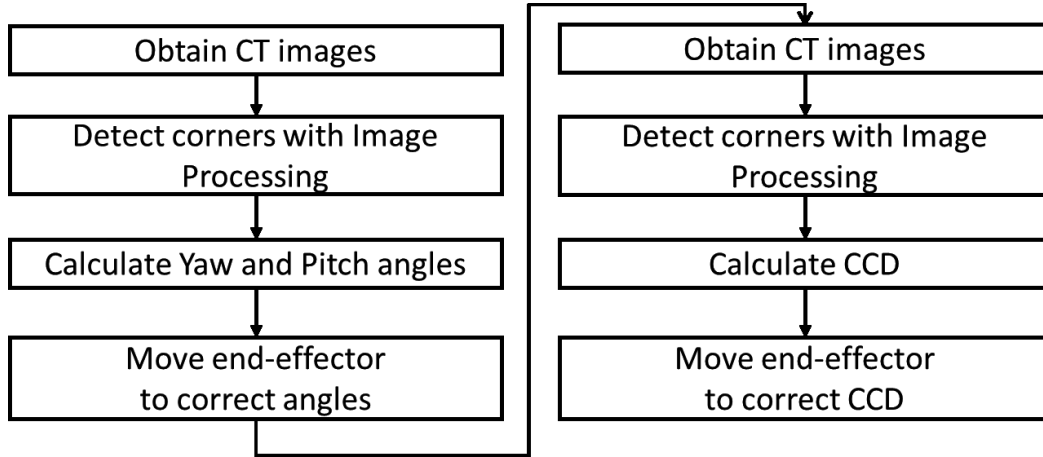


Fig. 5.24 Registration steps with the proposed marker

#### 5.5.2.4 Calculation flow

The yaw angle, pitch angle, and CCD were calculated by the coordinates of the cross-section corner. The intersection point between each line was detected from the grayscale processed CT image. A Canny edge detector and Hough transform were used for the image processing in Fig. 5.25.

With Formula (5.4), the yaw angle,  $\theta$ , and pitch angle,  $\varphi$ , in MBP from CBP are described by the following formulas.

$$\theta = \frac{1}{2} \sum_{i=1}^2 \left( \frac{\pi}{4} - \cos^{-1} \left( \frac{T_0}{T_i} \right) \right) \quad (5.7)$$

$$\varphi = \frac{1}{2} \sum_{i=1}^4 \left( \frac{\pi}{4} - \cos^{-1} \left( \frac{T_0}{T_i} \right) \right) \quad (5.8)$$

CCD was calculated after the angle calculations. If the distance between the CBP and MBP is  $\Delta Z$ , it is equal to  $d_k$  ( $k = 1 \dots 4$ ), the distance between the axis of symmetry of the whole cross-section and that of each rectangle (see Fig. 5.26). For this reason,  $\Delta Z$  is described as the following formula.

$$\Delta Z = \frac{1}{4} \sum_{k=1}^4 d_k \quad (5.9)$$

At the same time, the marker central coordinate in the CT image was calculated. The marker cross-section after the calibration of the yaw and pitch angles are symmetric with respect to the marker center coordinate as shown in Fig. 5.27. The central coordinate was then obtained with the corner coordinates of each cross-section view of the marker in Fig. 5.27.

$$\begin{pmatrix} x_{marker} \\ y_{marker} \end{pmatrix} = \frac{\vec{P}_{ai} + \vec{P}_{bi}}{2} \quad (i = 1, 2, \dots, 8) \quad (5.10)$$

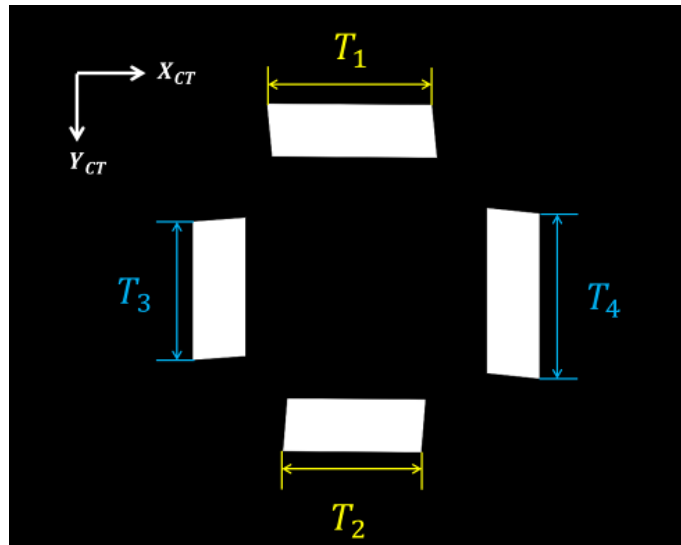


Fig. 5.25 Sample of the cross-section of the marker after image processing by varying the yaw/pitch angle

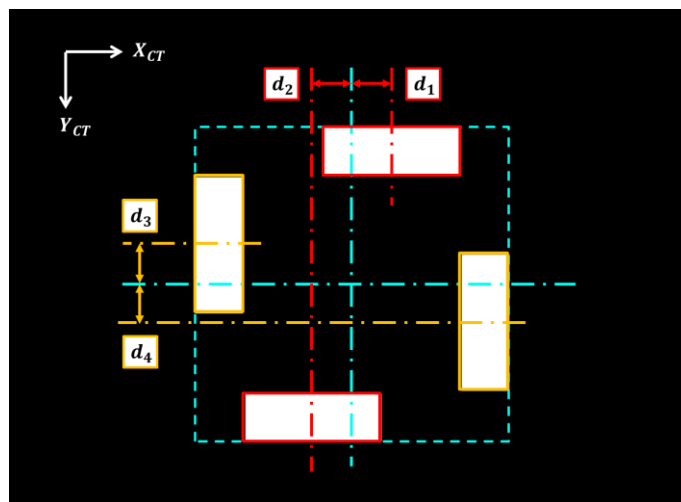


Fig. 5.26 Sample of the cross-section of the marker after image processing by varying the z-axis position after adjusting the yaw and pitch angles.

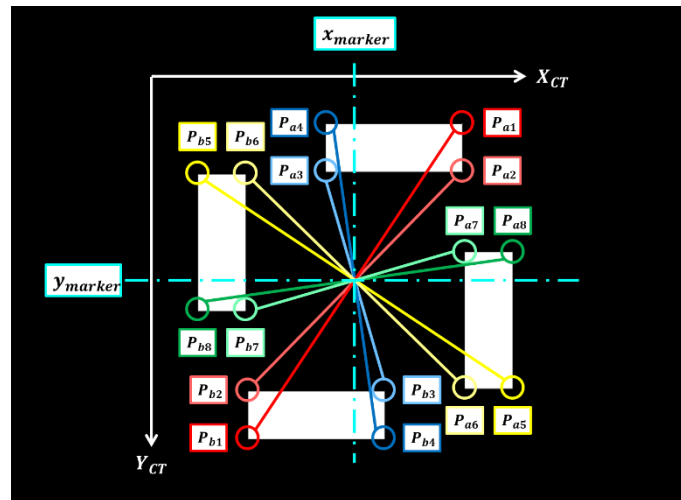


Fig. 5.27 Definition of the central coordinate of the registration marker

### 5.5.3 Verification of registration marker

#### 5.5.3.1 Experimental setup

To evaluate the proposed registration marker, the author obtained CT images including the marker fixed on a CT bed and measured the craniocaudal distance, and yaw and pitch angles. Fig. 5.28 shows the experimental setup composed of the registration marker, an inclined steel for adjusting the marker angles, and a base for supporting the inclined steel. Table 5.5 shows the CT specification and condition used in this experiment. To verify the accuracy under several angle conditions, the marker angles to the CBP were adjusted with high accuracy shaped steels as a grand truth. The author conducted CT shots with 16 continuous slices by changing the yaw angle ( $0^\circ$ ,  $5^\circ$ , and  $10^\circ$ ), and the pitch angle ( $0^\circ$ ,  $5^\circ$ , and  $10^\circ$ ). The angle calculation was conducted with the average value of the slices as results in each condition. The distance of the 16 points ( $-4 - 4$  mm each, and  $0.5$  mm from the center of the marker) with the slices was calculated. Noted that the distance calculation was conducted under the conditions adjusting both yaw and pitch angles at  $0^\circ$ .

Table 5.5 Conditions of CT scan

Model	Aquilion LB
Manufacture	Toshiba Medical System Co. (Tochigi, Japan)
Voltage of X-ray	120 kV
Current of X-ray	300 mA
Slice interval	0.5 mm
View size of reconstruction	$\phi 240.0$ mm

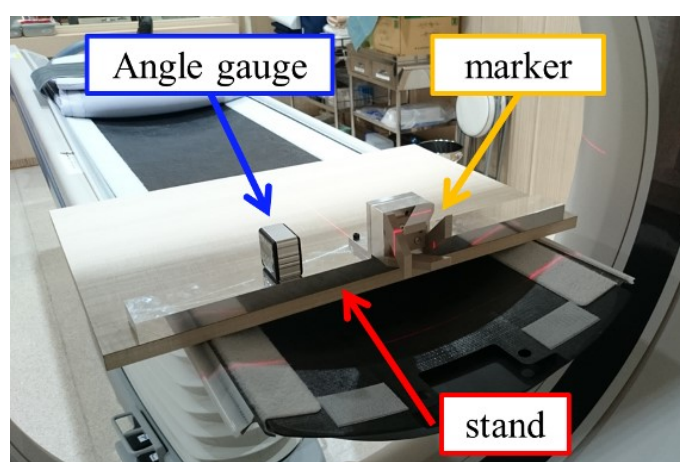
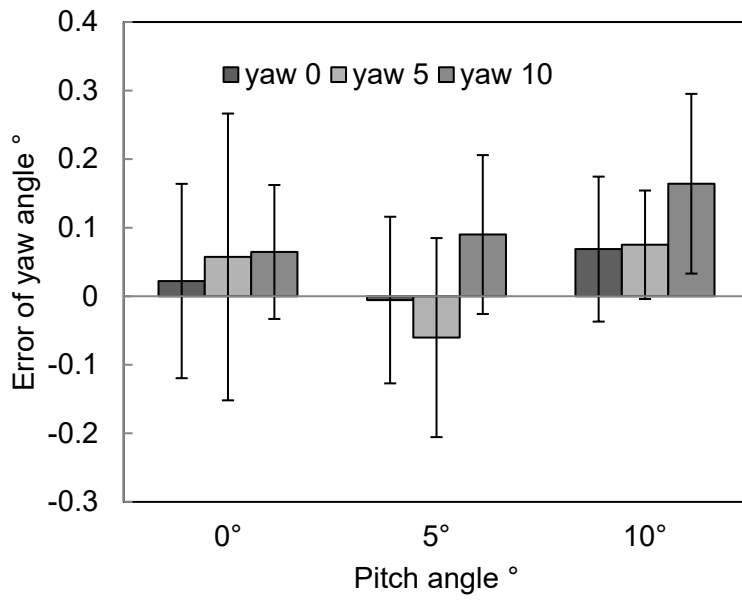


Fig. 5.28 Experimental setup for verifying the registration marker

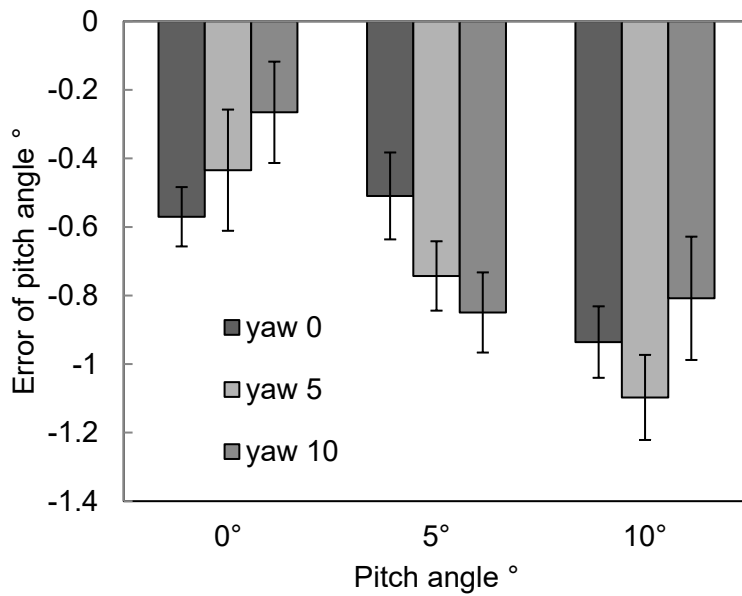
### 5.5.3.2 Results

Fig. 5.29 (a), (b) and (c) show the error of the yaw angle, the pitch angle, and the craniocaudal distance, respectively. Those results show that the average errors of yaw and pitch angles were  $0.053^\circ$  and  $-0.69^\circ$ , respectively. Moreover, an average error of the craniocaudal distance was 0.047 mm.



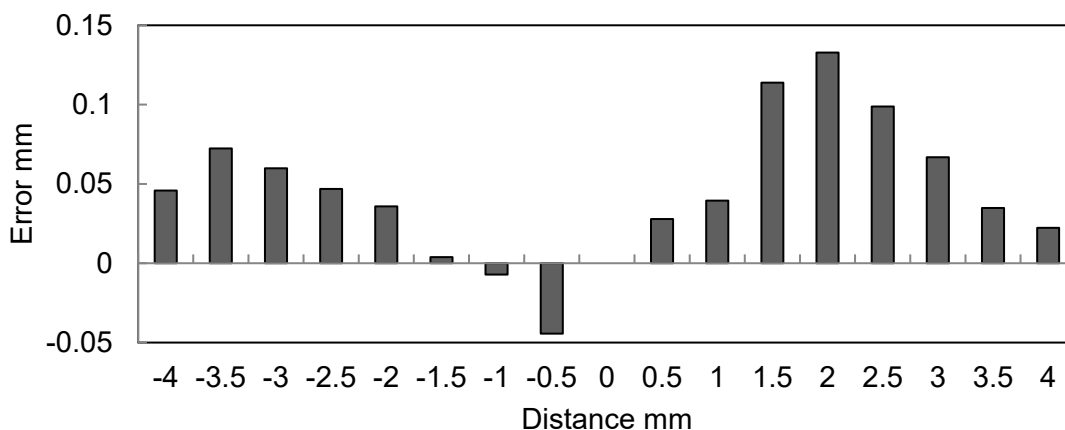


(a)



(b)

Fig. 5.29 Result of errors of (a) yaw angle, (b) pitch angle, and (c) the craniocaudal distance



(c)

Fig. 5.29 (continue) Result of errors of (a) yaw angle, (b) pitch angle, and (c) the craniocaudal distance

### 5.5.3.3 Discussion

Focusing on Fig. 5.29 (a), the error of pitch angle was slightly increased compared to that of the yaw angle. The reason was assumed to be the processing accuracy of the marker and the marker material. Although PEEK plastic was applied in terms of an anti-radiation material, considerations of the sharpness on the CT images are needed. The marker design and calculation method used in this experiment had some problems due to the accuracy under the conditions of the pitch angles and the high craniocaudal distances. In terms of the image resolutions, the marker size may cause calculation accuracy. Meanwhile, with the targeted tumor size of approximately 10 mm in the lower abdomen, the registration accuracy with the proposed marker was sufficient with an insertion robot. For future works, modification of the material, marker size, and processing procedure may be employed for improving the accuracy.

## 5.6 Summary

In this chapter, a CT-guided needle insertion robot system was developed. The robot system was composed of the needle insertion unit, registration marker, and positioning arm. The needle insertion unit performed the insertion motion with simultaneous vibration and rotation. To decrease the noise of the CT images, PEEK was used as the robot material.

Additionally, to move the needle insertion unit based on the CT image, a registration marker was developed for transforming the robot and CT image coordinate. The registration marker, constructed with four oblique prisms, can obtain errors of the angle and position from the CT image with its cross-section shape. The result showed the average errors of the yaw and pitch angles were  $0.053^\circ$  and  $-0.69^\circ$ , respectively. Furthermore, an average error of the craniocaudal distance was obtained to be 0.047 mm. The results showed the sufficient accuracy of the registration marker for the CT-guided insertion robot.



# Chapter 6: Evaluation

## 6.1 Chapter introduction

The proposed insertion control planning and insertion path planning introduced in chapters 3 and 4 integrating the CT-guided needle insertion robot system introduced in chapter 5 are verified through *in vivo* experiment in this chapter.

The objective of this chapter is to evaluate the accuracy of the proposed insertion control planning and insertion path planning in a real environment. Insertion motions generated by the planning are performed with the developed robot system introduced in chapter 5 under CT guidance. As the insertion target, a micro-pig is used in this experiment in terms of similarity of an anatomical structure of human lower-abdomen. In order to evaluate the insertion control planning, needle deflections are measured when applying the insertion motion generated by the insertion control planning compared to when applying the insertion motion without the vibration and rotation. While, in order to evaluate the insertion path planning, needle insertions are performed from various points on lower-abdomen, and actual needle deflections after insertion are compared to the score calculated by the insertion path planning.

## 6.2 *In vivo* experiment

### 6.2.1 Experimental setup

The overview of *in vivo* experiment is shown in Fig. 6.1. This experiment was performed on a female pig (19.6 kg, 10 months old) of specific pathogen free (SPF) using protocols and procedures approved by the Center for Development of Advanced Medical Technology, Jichi Medical University. General anesthesia was delivered through an endotracheal tube. Noted that premedication was performed before introducing the anesthesia. Respiration was controlled with a pump-oxygenator throughout the experiment. Vital signs including blood-pressure, heart rate, O<sub>2</sub> saturation and body temperature were also monitored. This experiment was performed with a CT scanner with a bore of 75 cm (SOMATOM Sensation 16; Siemens, Germany) and the CT-guided needle insertion robot system introduced in chapter 5. The robot was placed in front of the CT gantry across the CT bed, keeping clearances from the CT gantry and the pig placed on the

CT bed.

Ten insertion paths on lower-abdomen were determined randomly avoiding blood vessels on the insertion path with axial continuous CT images. Those insertion paths selected on CT images were shown in Fig. 6.2 and boundary positions and insertion angle of each tissue on the selected insertion path were listed on Tables 6.1 and 6.2, respectively. Noted that the boundary positions and insertion angles are measured manually by physicians. After determining the insertion paths on CT images, the needle insertion unit was moved to the entry position on the body surface. A single axis CT image with 0.6-mm thickness was obtained for confirming the position of needle tip. After moving to the appropriate position, needle insertions with vibration and rotation were performed to each insertion path. As introduced in chapter 4, the combination of bidirectional rotation and vibration was effective for the layered tissue, while the rotation of needle tip direction with respect to bowel surfaces combing vibration was effective for bowels. The author assumed that the integration of insertion control method for the layered tissue and bowel is effective for minimizing the needle deflection in the lower-abdominal insertion. Then, the author performed needle insertions with and without the insertion control planning to each insertion path, and measured the needle deflection after insertion. Epidermis (skin surface) is cut slightly by a surgical knife before insertion because the epidermis of pig is stiff compared to of human, thereby it is difficult to penetrate the skin with fine needles.

During needle insertions, continuous helical axis CT images with 0.6-mm thickness in the scan range of 20 mm were obtained. Needle insertion speed was set at 5 mm/s. The speed of bidirectional rotation and rotating needle tip direction was set at 10 rpm. The vibration amplitude and frequency were set at 0.1 mm and 100 Hz, respectively. Insertion distances were in the range of 60-80 mm depending on the selected insertion path (see Table 6.1).

The needle deflection was defined as the three-dimensional distance between the end point of targeted insertion path and the actual needle tip position after insertion. Identifications of the end point of insertion path, needle tip position and tissue boundary position were conducted by using OsiriX software (Pixmeo SARM, Switzerland). The three-dimensional distance of the needle deflection was calculated with the Pythagorean theorem.

Table 6.1 Tissue boundary positions on the selected insertion path

		Insertion path									
		1	2	3	4	5	6	7	8	9	10
Boundary position mm	Skin	0	0	0	0	0	0	0	0	0	0
	Muscle	14	17.5	19	19.5	7.5	6	21	22	17	13
	Bowel-1	25	24	23	25	18	18	29.5	24.5	25	24
	Bowel-2	40	37	43	35	34.5	31	46	45.5	39	37.5
	Bowel-3	70	46	52.5	67	54.5	48.5	63	62	48	46.5
	Bowel-4	-	-	-	-	-	-	-	-	66	66
	Total	80	70	60	80	65	65	70	70	80	80

Table 6.2 Insertion angles on each tissue boundary on the selected insertion path

		Insertion path									
		1	2	3	4	5	6	7	8	9	10
Insertion angle °	Skin	3.8	2.5	5.7	8.5	1.3	11	-6	-12.5	13	15
	Muscle	10	1	0.6	4	-10	40	-3.5	-5	-1	-34
	Bowel-1	10.5	8.6	1.7	-4	16	23	23	12.5	4	-17
	Bowel-2	14.3	4	20.7	2.1	9.5	15	15	28	18	-17
	Bowel-3	18.5	21	-34	-6	-25	-6.5	-1.5	-12	1.7	-10
	Bowel-4	-	-	-	-	-	-	-	-	-45	4.5

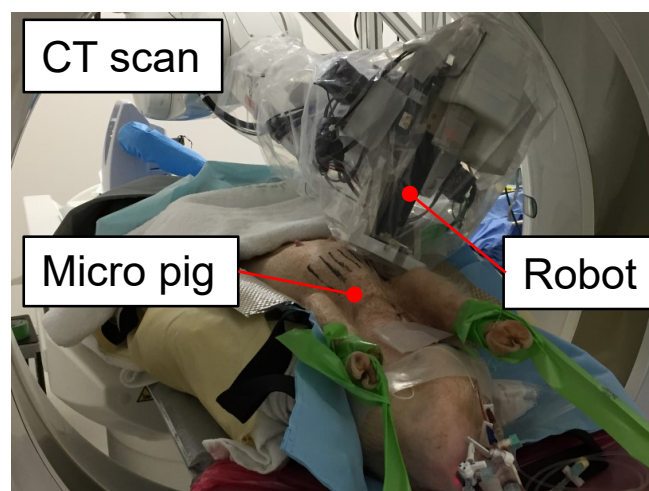


Fig. 6.1 Experiment setup overview

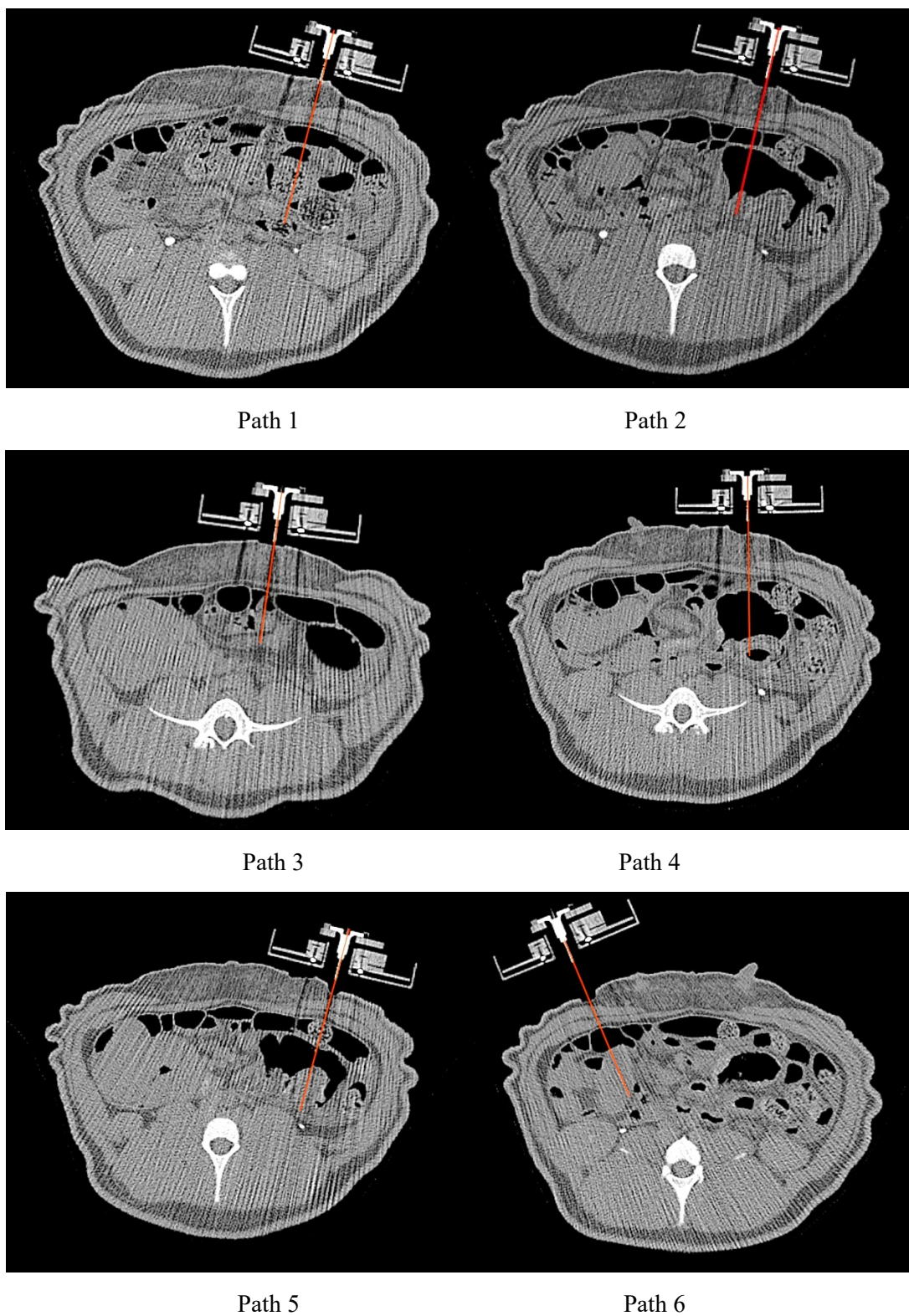
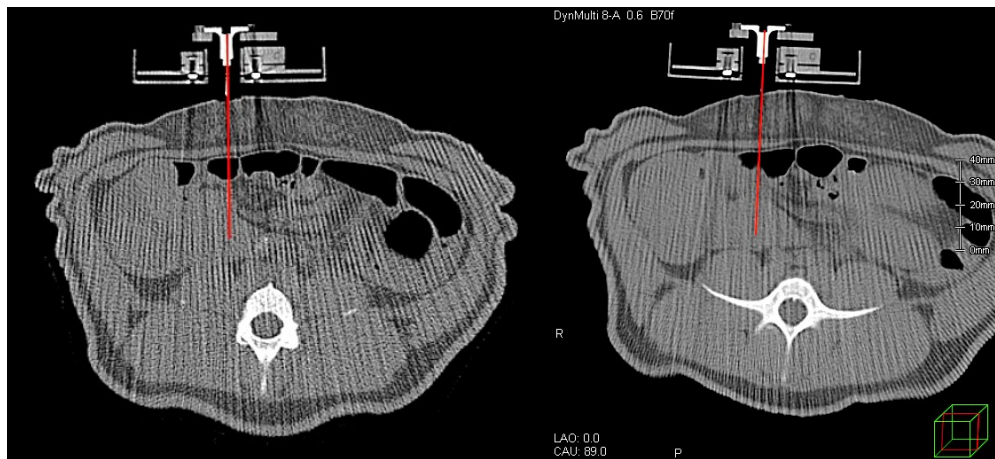


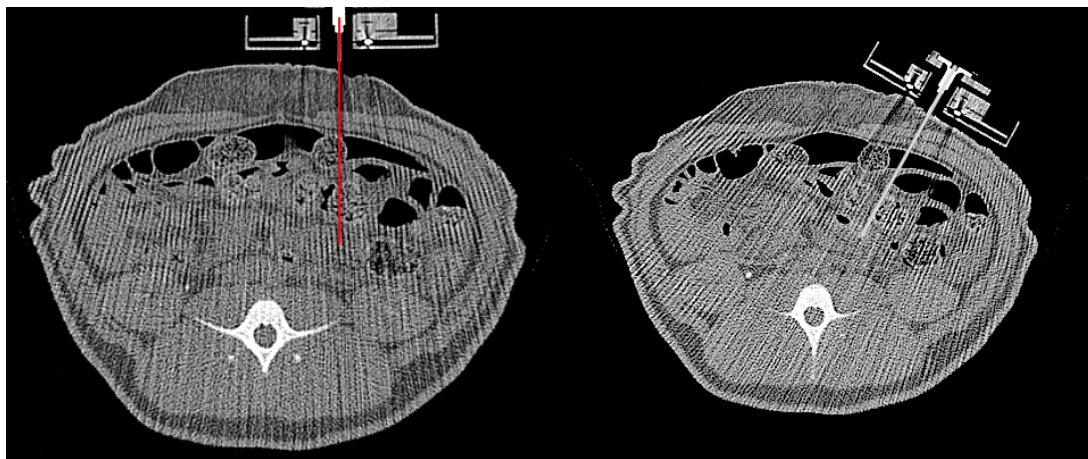
Fig. 6.2 Insertion paths selected in this experiment





Path 7

Path 8



Path 9

Path 10

Fig. 6.2 (continue) Insertion paths selected in this experiment

## 6.2.2 Insertion path planning

As mentioned in chapter 4, the insertion path planning needs the experiment data of needle deflection for fitting parameters of the *deflection probability* of each insertion target. Then, in the insertion path planning of lower-abdomen, it is necessary to collect the experiment data of deflection-slope of fat with skin, muscle and bowels. The soft PVC (50% of the plastic volume to 50% of the softener volume) with thick rubber sheets is used as same in chapter 4 as the insertion target of a fat with skin. The pork rib and porcine small bowel were also used as same in chapter 3 as the insertion targets of muscle and bowel, respectively. The sizes of each insertion target of fat, muscle and bowel are  $100 \times 200 \times 40 \text{ mm}^3$ ,  $100 \times 200 \times 40 \text{ mm}^3$  and  $100 \times 100 \times 2 \text{ mm}^3$ , respectively. The fat and muscle are fixed on a plate which has a hole to allow the needle to pass through. The bowel was cut and opened as a membrane, and the corner of bowel is clumped with plates. In the experiment of fat and muscle, the needle insertion is performed for 100 mm into the targets at an insertion speed of 5 mm/s, bidirectional rotation speed of 10 rpm, and vibration amplitude and frequency of 0.1 mm and 100 Hz. In the experiment of bowel, the needle insertion is performed for 60 mm into the target at an insertion speed of 5 mm/s, and vibration amplitude and frequency of 0.1 mm and 100 Hz. The author performed needle insertions under five-way conditions of insertion angle (0, 10, 20, 30, or 40°) for all insertion targets. The deflection-slope was calculated as same as 4.2.4.2. Twelve trials were performed for all conditions.

Fig. 6.3 shows the result of the deflection-slope of each target. Those results are approximated to a Gaussian distribution and Table 6.3 showed that the values of mean and standard deviation of the Gaussian distribution. As same in Eq. (4.8), the author applied second-order polynomial regression for fitting  $\mu$  and third-order polynomial regression for fitting  $\sigma$  as same as 4.2.4.2.

Table 6.4 shows the result of the unknown coefficient of the polynomial regression equation with the parameters of  $\mu$  and  $\sigma$  listed in Table 6.3. Those fitted coefficient was applied to Eq. (4.5) as the *deflection probability* of each target. By using the *deflection probability* fitted for each target of lower-abdomen (fat with skin, muscle and bowel) and applying the insertion angle and boundary position measured from the CT images to Eq. (4.5), the score of objective function of each insertion path was calculated with Eq. (4.1).

Table 6.3 Gaussian distribution parameters

Insertion angle °		0	10	20	30	40
Skin	$\mu$	0.288	0.735	1.95	2.05	2.52
	$\sigma$	0.222	0.502	0.587	0.666	0.711
Muscle	$\mu$	0.761	2.74	4.91	5.07	5.44
	$\sigma$	0.532	0.711	1.29	1.88	2.29
Bowel	$\mu$	0.459	1.01	1.25	1.26	1.47
	$\sigma$	0.102	0.0573	0.264	0.229	0.357

Table 6.4 Polynomial regression model coefficient

Coefficient		$a_0$	$a_1$	$a_2$	$a_3$
Skin	$\mu$	0.122	0.115	-1.31E-03	-
	$\sigma$	0.238	0.0328	-9.31E-04	1.02E-05
Muscle	$\mu$	0.702	0.266	-3.70E-3	-
	$\sigma$	0.530	-0.00903	-3.29E-3	4.93E-5
Bowel	$\mu$	0.505	0.0492	-6.63E-4	-
	$\sigma$	0.0892	-2.52E-04	-5.18E-4	7.39E-6

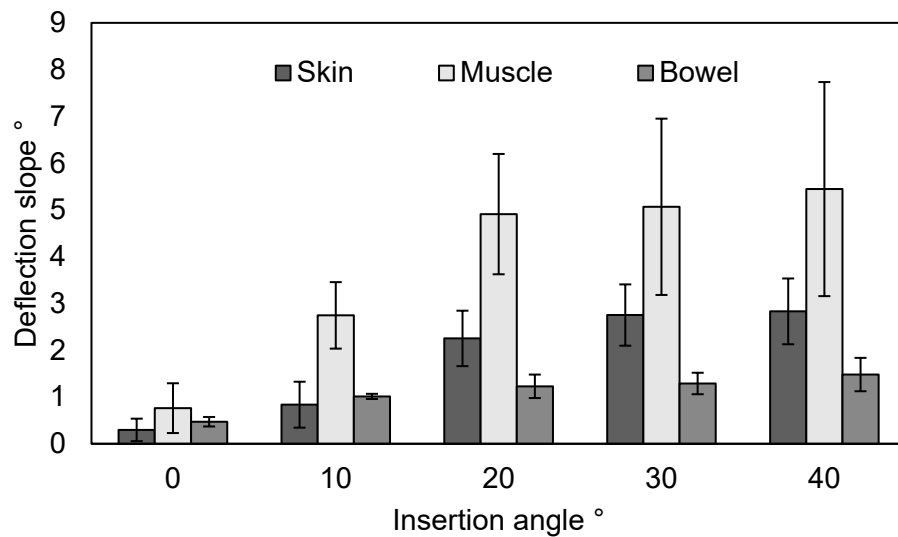


Fig. 6.3 Result of deflection-slope due to insertion angles

### 6.2.3 Results

Fig. 6.4 and Table 6.5 show the result of measured needle deflection in each selected insertion path. Those results show the needle deflection in all insertion path was decreased by applying the insertion control planning. Minimum needle deflection was 1.0 mm at no. 3 of insertion path. Fig. 6.5 shows the result of score of insertion path planning to each insertion path. The result of path planning showed the optimal insertion path is no. 3 of insertion path, which matched the actual insertion path with minimum deflection applying the insertion control planning.

Table 6.5 The result of needle deflection

No. of insertion path	Distance mm	Score of insertion path planning	Needle deflection		
			w/o control	mm with control	Decreasing rate
1	80	8.066	8.0	6.4	0.80
2	70	0.021	2.8	1.5	0.53
3	60	0.011	4.4	1.0	0.23
4	80	6.058	5.8	1.5	0.26
5	65	8.095	2.0	1.8	0.90
6	65	34.785	6.1	5.4	0.89
7	70	1.288	6.3	3.8	0.60
8	70	3.759	5.0	2.0	0.40
9	80	10.734	3.8	3.5	0.92
10	80	13.742	5.8	5.5	0.95

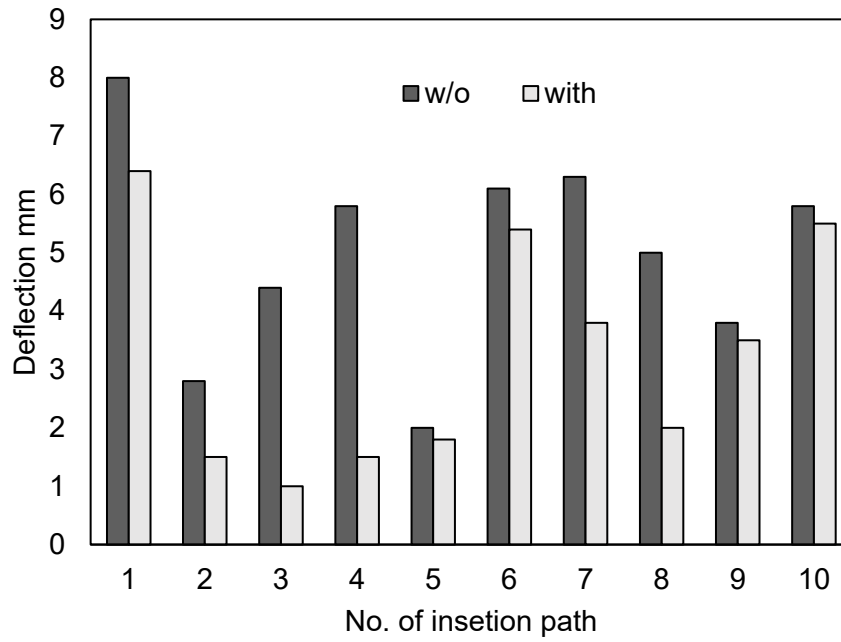


Fig. 6.4 The comparison of needle deflection between without and with insertion control planning

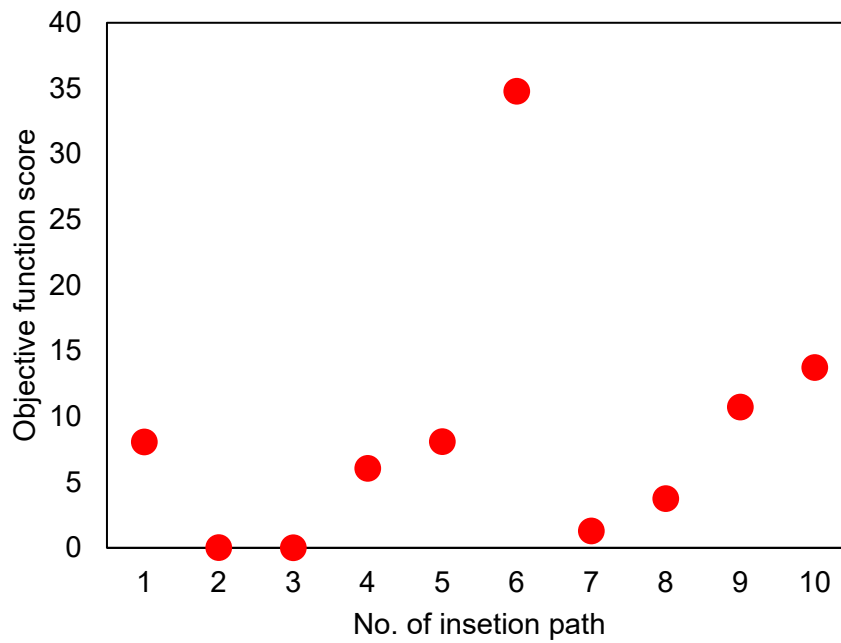


Fig. 6.5 The result of score calculated by objective function of insertion path planning

## 6.2.4 Discussion

Focusing on Fig. 6.4, the needle deflection under the conditions applying the insertion control planning can be decreased compared to the conditions without the insertion control planning in all insertion paths. Especially, the deflection was decreased significantly in no. of 3, 4 and 8 insertion paths (decreasing rates are 23%, 26% and 40%, respectively). While, focusing on the no. of 1, 6, 9 and 10 insertion paths, the needle deflection remained even applying the insertion control planning, although the needle deflections were slightly decreased by applying the insertion control planning. It is assumed that those needle deflections are dominantly due to the insertion angle. Focusing on the sequential CT images of no. 10 insertion path as a sample, the needle tip trajectory was off from the initial insertion path when puncturing the boundaries between the skin and muscle, and between the muscle and first bowel (see Fig. 6.6). Consequently, in order to decrease the needle deflection effectively by applying insertion control planning, it is necessary to select the optimal insertion path at first.

Comparing the measured needle deflection in the conditions under applying insertion control planning (see Fig. 6.4) and the score calculated by the insertion path planning (see Fig. 6.5), the needle deflection was potentially correlated with the score in the most of insertion paths. Meanwhile, focusing on the no. 1 and 7 insertion paths, there were significant difference between the score and measured needle deflection compared to other insertion paths. Focusing on the sequential CT images of no. 1 insertion path, the needle tip was out of the plane when puncturing the second bowel. While, focusing on the sequential CT images of no. 1 insertion path from sagittal direction of insertion path, the needle tip was slipped on the bowel surface (see Figs. 6.7 and 6.8). This may be due to the contents (dense scats) inside the bowel, which may interfere the puncture of bowel. In the case of human, bowel often contains scats which hardness may be depending on the individuals. Then, when planning the insertion path, it is necessary to consider whether the contents are on the insertion path. Also, focusing on the sequential CT images of no. 7 insertion path, the needle tip was slipped on the surface of second bowel, which caused the large deflection (see Fig. 6.9). This was because the positions of bowels were slightly moved due to the layered tissue deformations during insertion, and the insertion angle on the second bowel was changed. As mentioned in 4.2.5, it is important to take the insertion path planning into account of the effect of tissue deformation. Especially, as the bowel is easily deformed due to the hollow organ compared with the layered tissue, it is necessary to consider the effect of tissue deformation for needle deflection. Although the deformation of soft tissue is modeled with various approaches [6.1-6.3], there is no model focusing on the bowel. It is necessary to investigate the interaction relationship between the needle and bowel with some models such as finite element models.

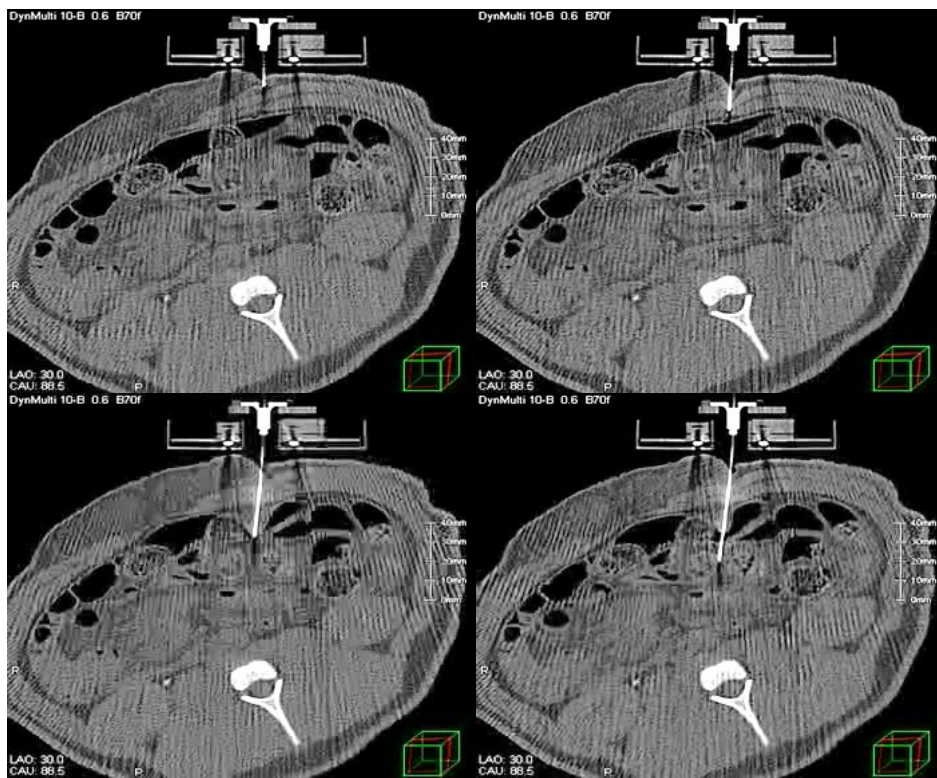


Fig. 6.6 The sequential transversal CT images tracking the needle in No. 10 insertion path

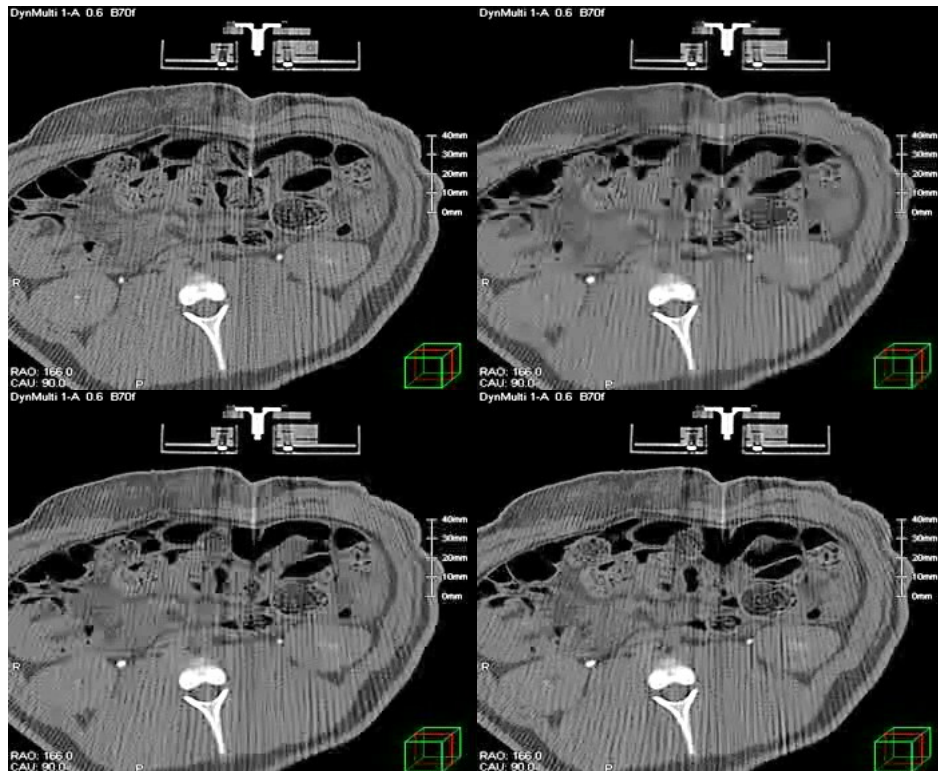


Fig. 6.7 The sequential transversal CT images tracking the needle in No. 1 insertion path



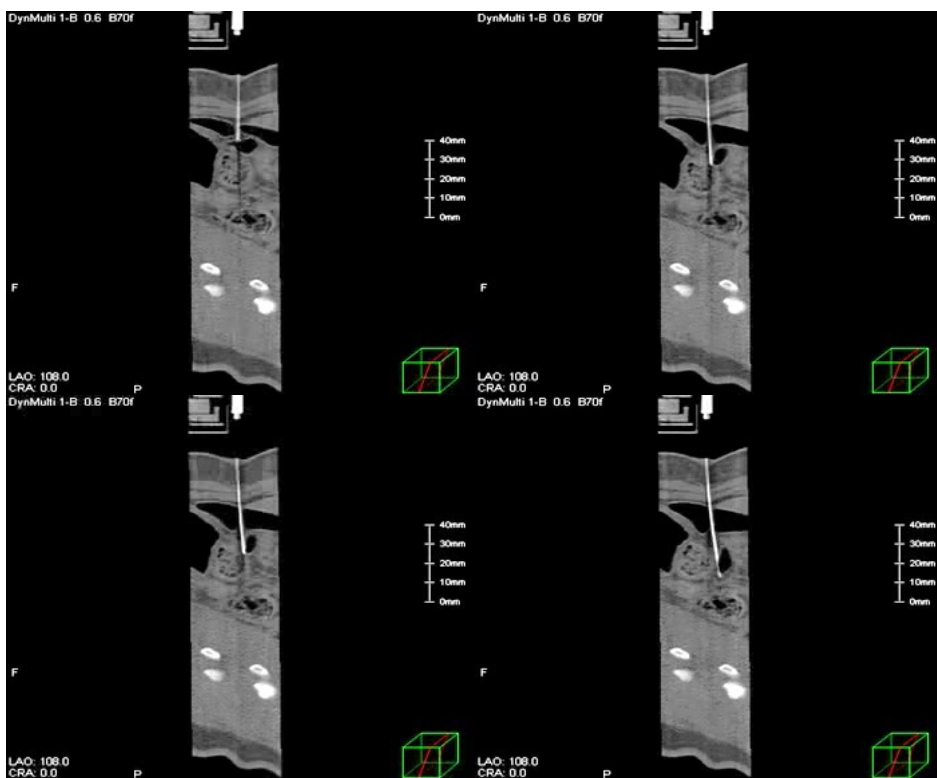


Fig. 6.8 The sequential sagittal CT images tracking the needle in No. 1 insertion path

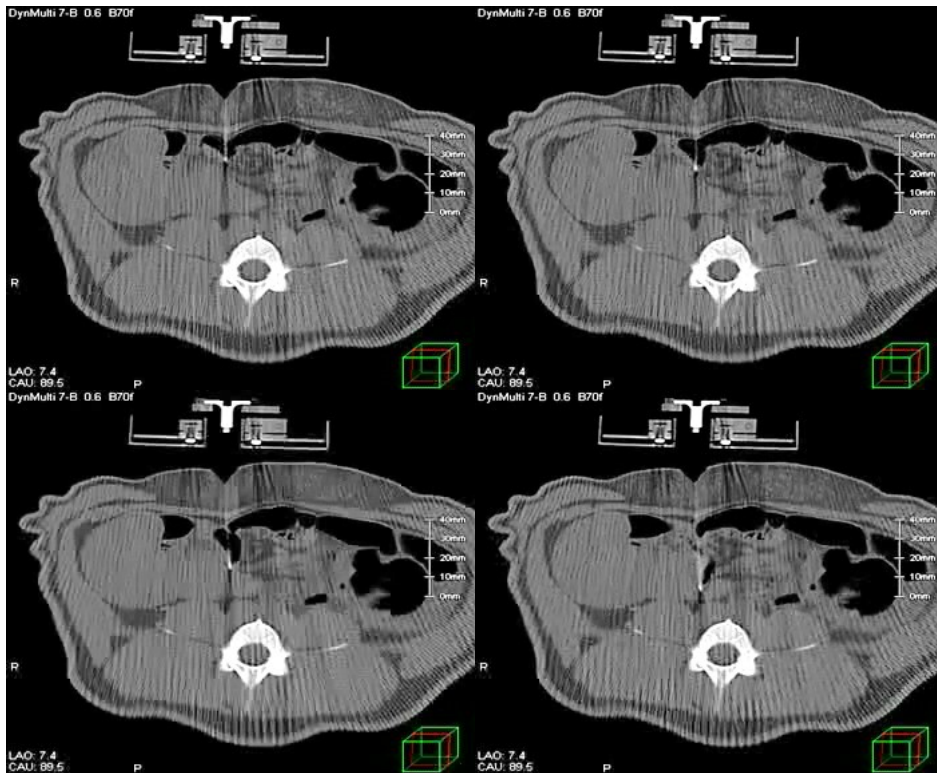


Fig. 6.9 The sequential CT images tracking the needle in No. 7 insertion path



## 6.3 Originality and limitation

### 6.3.1 Insertion control planning

As introduced in chapter 3, the rotation and vibration were reported as the insertion control method for decreasing the deflection of fine needle respectively in previous researches. In this study, the author hypothesize that the needle deflection can be minimized robustly by combing both the vibration and rotation through the experimental analysis in chapter 2. Moreover, the rotational method was optimized for each target composed of lower-abdomen in terms of tissue properties and patient's safety.

The author describes limitations of this insertion control planning following.

(i) Parameter optimization: the insertion control parameters including insertion speed, rotation speed and vibration frequency were selected tentatively through experiments. Meanwhile, it is assumed that the optimum parameters vary depending on the individuals. Especially, it is necessary to further investigate the optimum parameters in terms of tissue damages. The amount of cutting tissue during rotational insertion is related to the number of rotations per insertion distance. Regarding vibration parameters, although the author selected maximum parameter of the current piezo actuator, the insertion force and needle deflection may be further decreased if high-frequency and amplitude can be generated.

(ii) Evaluation of tissue damage: Although the tissue damages of layered tissue was evaluated by measuring the hole area after insertion, it is not sufficient in terms of amount of bleeding. Moreover, bowel damages were not evaluated quantitatively. There may be risk of leading peritonitis if the bacteria inside the bowel leaks through the crack generated by a needle. Therefore, it is necessary to evaluate the effect for patient's safety after insertion with vibration and rotation, such as the amount of bleeding and leak of digestive fluid.

(iii) Effect of tissue deformation: the author didn't focus mainly on the effect of tissue deformation in this study because the tissue deformation during insertion is not large in case of using fine needles compared to using thick needles as mentioned in related works. Meanwhile, through *in vivo* experiments, the author found that the effect of tissue deformation is not negligible in case of fine needle insertion. Especially, during the insertion into the multiple bowels, the uncertain deflection occurred due to the bowel deformation. Moreover, the position of insertion target such as lymph-node may move slightly following other tissue's deformations. Then, it is necessary to evaluate the insertion control planning in terms of tissue movement during insertion.

(iv) Timing of switching the insertion control method: the timing of switching insertion control

methods including the position of applying the bidirectional rotation and rotating needle tip direction is determined preoperatively in this experiment. However, as there was the tissue deformation which moves each boundary position slightly, the timing of switching insertion control method determined before insertion may not match an ideal timing. If the timing is off from ideal positions, the needle deflection may not be minimized completely. Therefore, it is necessary to obtain the timing of puncturing the tissue boundary, and to switch the insertion control method automatically.

### 6.3.2 Insertion path planning

The preoperative insertion path planning for minimizing needle deflection based on the insertion angles on each target boundary is a novel idea. Most of researches focused on the preoperative estimation of needle deflection with mechanical-based or geometric-based model in order to apply it to the needle steering. Moreover, this insertion path planning determined the optimal insertion path based on probabilities of needle deflection occurred, instead of estimating the value of needle deflection. The author assume that it is important and reasonable to show the probability of accurate needle insertion in case of complex situation such as lower-abdominal insertion, compared to estimate the accurate needle trajectory.

The author describes limitations of this insertion path planning following.

(i) Fitting *deflection probability* for each target: the weight factor of *deflection probability* parameters is fitted with the results of *ex vivo* experiments in this experiment. Ideally, the parameters should be fitted by collecting the data through *in vivo* experiments repeatedly. However, it is not reasonable to conduct a lot of *in vivo* experiments. Then, it is necessary to develop the phantom mimicking a real lower-abdomen. As the boundary condition of bowels is quite complex as mentioned especially, it is a key issue how to design the structure of bowel phantom.

(ii) Insertion path planning predicting the deflection: the insertion angle on each tissue boundary used in the insertion path planning is measured on preoperative CT images. However, actual insertion angles without initial insertion angle vary due to the needle deflection and tissue deformation. In order to improve the accuracy of insertion path planning, it is necessary to estimate the actual insertion angle based on the obtained *deflection probability*.

(iv) Three-dimensional insertion path planning: the proposed insertion path planning is designed based on two-dimensional needle deflection. While, as mentioned in discussion section, three-dimensional path planning is necessary since the alignment of bowels is complex, which may occur needle deflections of sagittal direction. In order to expand the insertion path planning

to three-dimensional planning, the three-dimensional data of tissue boundary needs to be obtained. As one approach for generating the data, the tissue boundary detection system introduced in chapter 4 is applied to sequential axial CT images around the target and the tissue boundary data of each CT image are connected.

(iv) Optimization of CT scan: Ideally, the timing of CT scan is twice (before insertion for planning and after insertion for checking needle tip reached into targets). However, assuming a real clinical situation, the CT image should be obtained where the needle deflection may occur for satisfying the safety. As introduced in chapter 2, the amount of needle deflection is related to the insertion force. Then, it is assumed that the abnormal needle deflection can be detected by monitoring the insertion force during insertion. By the robot system alert operators to stop insertion and shot CT image once the needle deflection is detected through monitoring, it will avoid to obtain unnecessary CT images, which leads decreasing the amount of radiation exposure.

### 6.3.3 CT-guided needle insertion robot

Regarding an originality of the proposed CT-guided needle insertion robot system, the robot has the mechanism allowing needle insertions with the combination of vibration and rotation at same time, keeping the size of the robot to be suitable for using into CT gantry. Most of previous CT-guided needle insertion robots can perform just insertion motions or insertion with only rotation. In addition, the author considered that the proposed registration method has the versatility compared to other registration methods of previous CT-guided needle insertion robots. Most of previous registration method between the robot and CT images are based on the geometric relationship of setting position of robots. Meanwhile, the registration method with the geometric relationship between a robot and CT image may be uncertain depending on the accuracy of setting position of robot. While, the proposed registration marker can calibrate all errors including setting error of robot and machining error of each part because those errors are reflected to the shape of cross-section image of the registration marker.

The author describes limitations of this insertion control planning following.

(i) Evaluation for applying the system to clinical tests: the proposed of CT-guided needle insertion robot system is verified in terms of functionality in this study. In order to use this system in clinical situations, it is necessary to consider the safety of this robot. The types of safety the author needs to consider is divided into mechanical safety, electrical safety and software safety. As the mechanical safety, it is necessary to satisfy the requirements of stiffness of hardware and durability of repeated usages as a medical equipment. Also, the durability to radiation exposure due to CT scan needs to be evaluated. As the electrical safety, it is necessary to pass the

requirements of the electromagnetic compatibility (EMC) test and electrical safety test. As the software safety, there is a software system that the real-time data obtaining insertion conditions such as insertion force can be monitored by operators.

(ii) Optimization of the registration marker size: the accuracy of registration marker may be depending on the resolution of cross-section image of the marker. In short, the accuracy is improved by increasing the size of marker. While, the large size marker interferes the human body or CT gantry. Then, the size of marker needs to be optimized in terms of both accuracy and interference.

(iii) Integration of DICOM server and robot system: In order to perform the insertion path planning automatically, the robot system needs to obtain the CT images real-time from DICOM servers stocking the CT images. In the current robot system, the robot control system is separated to the DICOM server so that the author sends the CT image to the PC of robot control system manually via a viewer soft AOC. Then, it is necessary to construct a network connecting the robot control system and DICOM server.

## 6.4 Summary

In this chapter, the author evaluated the proposed insertion control planning and insertion path planning through *in vivo* experiments. The author performed the needle insertion from ten insertion paths, applying the proposed insertion control planning. As the result, by applying the insertion control planning, the needle deflection could be decreased in all insertion paths. In order to evaluate the insertion path planning, the author compared the actual needle deflection and the score calculated by the insertion path planning. As the result, in most of the insertion paths, the score was correlated to the actual needle deflections and the minimum score matched the insertion path with the minimum deflection.

Moreover, the author summarized the originality and limitation of the proposed insertion control planning, insertion path planning and CT-guided needle insertion robot.



# Chapter 7: Conclusion

## 7.1 Summary

In this thesis, the author proposed (a) the insertion control planning and (b) the insertion path planning for minimizing the deflection of fine needles during lower-abdominal insertion, and developed the CT-guided needle insertion robot system for conducting (a) and (b). Those proposals were verified through *ex vivo* and *in vivo* experiments.

The achievement of this thesis is to develop the planning methodology of accurate insertion for lower-abdomen in terms of insertion control and insertion path. The novelty of this thesis is (1) focusing on the lower-abdomen as the insertion target and (2) achieving an accurate insertion with an extra-fine needle under CT-guidance. This thesis was composed of seven chapters. Overviews of each chapter are described following.

In chapter 1, regarding the lymphatic malignancy which is the targeted disease in this study, the author summarized the number of diseased patients, diagnosis method and treatment method, and described the necessity of percutaneous needle insertion. Moreover, by summarizing the research trends of needle insertion robots and methods for achieving the accurate insertion, the author showed the difficulty of lower-abdominal insertion and technological challenges, and described the purpose of this study.

In chapter 2, regarding the mechanical phenomena during needle insertion into each tissue and organ composing lower abdomen (layered tissue including skin, fat and muscle, and bowel), the author summarized the mechanical properties needed to be considered in order to decrease the needle deflection through experimental analysis. At first, the needle insertion was performed in *ex vivo* experiment with porcine rib and bowel in order to observe the behavior of needle deflection and insertion force depending on the tissue properties. Next, the needle is inserted at various angle to the same tissues in order to observe the needle deflection and insertion force depending on tissue geometries.

In chapter 3, based on the experimental analysis of chapter 2, the author proposed insertion control planning to the layered tissue and bowel, respectively. As the requirements of insertion control, it is necessary to consider the equalization of needle tip forces, the reduce of friction force around the needle shaft and the avoidance of winding-up tissues. Then, regarding the insertion for layered tissue, the author proposed the insertion control method with combination of high frequency vibration along insertion direction and bidirectional axial spinning to insertion direction. Regarding the insertion for bowels, the author proposed the combination of the

vibration and the rotation of needle tip angle every time at puncturing bowel walls to cancel the needle deflection.

In chapter 4, the author proposed the preoperative insertion path planning method for determining appropriate needle insertion position and angle to achieve a straight path from skin to tumor. In the chapter 2, it was confirmed that the insertion angle at tissue boundary is key issue to affect the needle deflection. Then, the author made a hypothesis that the amount of needle deflection can be minimized by selecting the path that the sum of insertion angles with respect to each tissue boundary that the needle passes through is minimized. In addition, the effect of insertion angle for the needle deflection varies due to the tissue properties and the tissue boundary positions. Then, weight factors of each insertion angle in the path planning were implemented. As the design of weight factor, the author developed the probability that the needle deflection is within acceptable amount. Moreover, in order to implement the path planning method on CT images, the author developed the image processing method to detect the tissue boundary from CT images and to calculate the insertion angle in each boundary.

In chapter 5, the author described the CT-guided needle insertion robotic systems for implementing the proposed insertion control planning in chapter 3 and insertion path planning in chapter 4. This robotic system is composed of needle insertion unit which enable to implement the insertion with vibration and rotation; robot arm which move the needle insertion unit to appropriate position and angle based on the path planning; and registration marker for conducting coordinate transform between the robot arm and CT image.

In chapter 6, the availability of the proposed insertion control and path planning with the robotic system was evaluated through *in vivo* experiment with micro pig. As the results, by applying the proposed insertion control planning, the needle deflection could be decreased up to 1.0 mm at an insertion point obtained from the proposed insertion path planning. In addition, the limitation of this study was mentioned in terms of insertion control planning, insertion path planning and CT-guided needle insertion robot systems.

In chapter 7, summary of the achievement and remaining tasks of this study were described in this chapter. As the future work, the author described the issues for achieving the robotic system to clinical application.

Thus, in order to minimize the needle deflection for achieving straight insertion path in CT-guided lower-abdominal needle insertion, this thesis proposed novel planning methods of insertion control and insertion path. As the insertion control planning, insertion with the combination of vibration and rotation was proposed. As the insertion path planning, the optimization-based planning model based on the insertion angle was proposed. The effectiveness and validity of the proposed methods were evaluated through *ex vivo* and *in vivo* experiments.



## 7.2 Future direction

The author proposed a novel idea of needle insertion method and robot system. Those knowledges are expected to apply the needle insertion technology for other targets such as lung, liver and prostate. Especially, as a lung biopsy is usually performed under CT image guidance, the proposed approach is also applied directly. Actually, the lower abdomen targeted in this study is really the complexed situation. Then, in other targets which may be simple situations, it is considerable that the proposed approach can be applied easily. Moreover, the author believes that the concept of the proposed methodology is integrated to the needle steering technologies introduced in chapter 1. The concept of my approach is to generate the straight insertion path, while the concept of needle steering is to control the trajectory path. There are pros and cons in both concepts. Then, by integrating those concepts, the accurate insertion to arbitrary tumors will be achieved. Finally, the author believes that the concept will be applied to other medical and surgical instruments and robotic systems, not only needle insertion applications.

Although many surgical and medical robotic system have been widely developed, there has been limited developments of practical systems used in clinical situations currently. In order to enhance the seeds of surgical and medical robotic system to practical applications, the author believes that it is important to not only improve the efficiency of elemental technologies but also to show possibilities that the total robot system can produce clearly. The author believes that technologies of machine learning can be applied further. Actually, in medical fields, the machine learning has been applied to the image processing such as diagnostic imaging system. However, there are few researches implementing the machine learning technologies to the planning and motion of surgical and medical robot system. The author thinks that the surgical and medical robot will be approaching to the autonomous system and a fusion of the machine learning technologies and surgical robot will be essential. The author keeps to contribute the advancement of medical and surgical robotics for helping future medicines.



# References

## Chapter 1

- [1.1] World Health Organization, Cancer statics, <http://www.who.int/news-room/fact-sheets/detail/cancer>
- [1.2] 厚生労働省, 人口動態調査 (がんによる部位別死亡者数), <https://www.mhlw.go.jp/toukei/saikin/hw/jinkou/kakutei17/index.html>
- [1.3] 国立がん研究センター 希少がんセンター, さまざまな希少がんの解説 (悪性リンパ腫), [https://www.ncc.go.jp/jp/rcc/about/malignant\\_lymphoma/index.html](https://www.ncc.go.jp/jp/rcc/about/malignant_lymphoma/index.html)
- [1.4] PubMed Health, Lymphoid, <https://www.ncbi.nlm.nih.gov/pubmedhealth/PMHT0022039/>
- [1.5] 国立がんセンター がん情報サービス, 悪性リンパ 基礎知識, <https://ganjoho.jp/public/cancer/ML/index.html>
- [1.6] 国立がんセンター がん情報サービス, 悪性リンパ 検査, <https://ganjoho.jp/public/cancer/ML/index.html>
- [1.7] NIH National Cancer Institute, Adult Non-Hodgkin Lymphoma Treatment, <https://www.cancer.gov/types/lymphoma/patient/adult-nhl-treatment-pdq>
- [1.8] 国立がんセンター がん情報サービス, 悪性リンパ 治療, <https://ganjoho.jp/public/cancer/ML/treatment.html>
- [1.9] Chemotherapy.com, Lymphoma, [http://www.chemotherapy.com/new\\_to\\_chemo/tumor\\_types/lymphoma/](http://www.chemotherapy.com/new_to_chemo/tumor_types/lymphoma/)
- [1.10] G. Bonadonna and A. Santoro, “ABVD chemotherapy in the treatment of Hodgkin’s disease,” *Cancer Treat. Rev.*, vol. 9, pp. 21–35, 1982.
- [1.11] B. Coiffier *et al.*, “CHOP CHEMOTHERAPY PLUS RITUXIMAB COMPARED WITH CHOP ALONE IN ELDERLY PATIENTS WITH DIFFUSE LARGE-B-CELL LYMPHOMA,” *N. Engl. J. Med.*, vol. 346, no. 4, pp. 235–242, 2002.
- [1.12] American Cancer Society, Immunotherapy for Non-Hodgkin Lymphoma, <https://www.cancer.org/cancer/non-hodgkin-lymphoma/treating/immunotherapy.html>
- [1.13] American Cancer Society, Radiation Therapy for Non-Hodgkin Lymphoma, <https://www.cancer.org/cancer/hodgkin-lymphoma/treating/radiation.html>
- [1.14] Cancer Research UK, Hodgkin lymphoma treatment,

<https://www.cancerresearchuk.org/about-cancer/hodgkin-lymphoma/treatment/stem-cell-bone-marrow-transplants>

- [1.15] I. Mellman, G. Coukos, and G. Dranoff, “Cancer immunotherapy comes of age,” *Nature*, vol. 480, pp. 480–489, 2011.
- [1.16] J. Couzin-Frankel, “Cancer Immunotherapy,” *Science (80-. )*, vol. 342, no. 6165, pp. 1432–1433, 2013.
- [1.17] S. A. Rosenberg, J. C. Yang, and N. P. Restifo, “Cancer immunotherapy: moving beyond current vaccines.,” *Nat. Med.*, vol. 10, no. 9, pp. 909–915, 2004.
- [1.18] J. Tang, L. Pearce, J. O’Donnell-Tormey, and V. M. Hubbard-Lucey, “Trends in the global immuno-oncology landscape,” *Nat. Rev. Drug Discov.*, vol. Advance On, pp. 1–2, 2018.
- [1.19] H. Ueno *et al.*, “Dendritic cell subsets in health and disease,” *Immunol. Rev.*, vol. 219, pp. 118–142, 2007.
- [1.20] C. M. Le Gall, J. Weiden, L. J. Eggermont, and C. G. Figdor, “Dendritic cells in cancer immunotherapy,” *Nat. Mater.*, vol. 17, pp. 474–475, 2018.
- [1.21] K. Palucka and J. Banchereau, “Cancer immunotherapy via dendritic cells,” *Nat. Rev. Cancer*, vol. 12, no. 4, pp. 265–277, 2013.
- [1.22] J. Banchereau and A. K. Palucka, “Dendritic cells as therapeutic vaccines against cancer,” *Nat. Rev. Immunol.*, vol. 5, no. 4, pp. 296–306, 2005.
- [1.23] National Cancer Institute, Immunotherapy to treat cancer, <https://www.cancer.gov/about-cancer/treatment/types/immunotherapy>
- [1.24] D. M. Pardoll, “The blockade of immune checkpoints in cancer immunotherapy,” *Nat. Rev. Cancer*, vol. 12, no. 4, pp. 252–264, 2012.
- [1.25] S. A. Rosenberg, N. P. Restifo, J. C. Yang, R. A. Morgan, and E. Mark, “Adoptive cell transfer: a clinical path to effective cancer immunotherapy,” *Nat. Rev. Cancer*, vol. 8, no. 4, pp. 299–308, 2008.
- [1.26] J. M. Reichert, C. J. Rosensweig, L. B. Faden, and M. C. Dewitz, “Monoclonal antibody successes in the clinic,” *Nat. Biotechnol.*, vol. 23, no. 9, pp. 1073–1078, 2005.
- [1.27] J. A. Berzofsky *et al.*, “Progress on new vaccine strategies for the immunotherapy and prevention of cancer,” *J. Clin. Invest.*, vol. 113, pp. 1515–1525, 2004.
- [1.28] E. Jäger, D. Jäger, and A. Knuth, “Clinical cancer vaccine trials,” *Curr. Opin. Immunol.*, vol. 14, no. 2, pp. 178–182, 2002.
- [1.29] T. Sato *et al.*, “Combination of monocyte-derived dendritic cells and activated T cells which express CD40 ligand: A new approach to cancer immunotherapy,”

- Cancer Immunol. Immunother.*, vol. 53, pp. 53–61, 2004.
- [1.30] K. Hasumi, Y. Aoki, R. Wantanabe, and D. L. Mann, “Clinical response of advanced cancer patients to cellular immunotherapy and intensity-modulated radiation therapy.,” *Oncoimmunology*, vol. 2, no. 10, pp. e26381-1–10, 2013.
- [1.31] HITV LAB, HITV cancer therapy, <http://www.hitvlab.com/hitv-cancer-therapy.html>
- [1.32] K. Ahrar and S. Gupta, *Percutaneous Image-Guided Biopsy*. Springer New York Heidelberg Dordrecht London, 2014.
- [1.33] J. Lee, R. Mueller, L. Dawson, F. Hahn, A. Goldberg, and W. Boland, “Perspective Percutaneous Ethanol Injection for the Treatment of Hepatic Tumors : Indications , Mechanism of Action , Technique , and Efficacy,” *Am. J. Roentgenol.*, vol. 164, no. 1, pp. 215–220, 1995.
- [1.34] Cancer Research UK, Treatment for cancer, <https://www.cancerresearchuk.org/about-cancer/cancer-in-general/treatment/other/radiofrequency-ablation>
- [1.35] A. A. Gage and J. Baust, “Mechanisms of Tissue Injury in Cryosurgery,” *Cryobiology*, vol. 37, no. 3, pp. 171–186, 1998.
- [1.36] Mayo Clinic, Brachytherapy, <https://www.mayoclinic.org/tests-procedures/brachytherapy/about/pac-20385159>
- [1.37] M. Azizian, N. Najmaei, M. Khoshnam, and R. Patel, “Visual servoing in medical robotics: a survey. Part II: tomographic imaging modalities – techniques and applications,” *Int. J. Med. Robot. Comput. Assist. Surg.*, vol. 11, pp. 67–79, 2015.
- [1.38] M. Azizian, N. Najmaei, M. Khoshnam, and R. Patel, “Visual servoing in medical robotics: a survey. Part II: tomographic imaging modalities – techniques and applications,” *Int. J. Med. Robot. Comput. Assist. Surg.*, vol. 11, pp. 67–79, 2015.
- [1.39] National Institute of Biomedical Imaging and Bioengineering, Science education CT, <https://www.nibib.nih.gov/science-education/science-topics/computed-tomography-ct>
- [1.40] J. F. Barrett and N. Keat, “Artifacts in CT: Recognition and Avoidance,” *RadioGraphics*, vol. 24, pp. 1679–1691, 2004.
- [1.41] National Institute of Biomedical Imaging and Bioengineering, Science education MRI, <https://www.nibib.nih.gov/science-education/science-topics/magnetic-resonance-imaging-mri>
- [1.42] National Institute of Biomedical Imaging and Bioengineering, Science

education Ultrasound, <https://www.nibib.nih.gov/science-education/science-topics/ultrasound>

- [1.43] N. Abolhassani, R. Patel, and M. Moallem, “Needle insertion into soft tissue: A survey,” *Med. Eng. Phys.*, vol. 29, no. 4, pp. 413–431, 2007.
- [1.44] C. Yang, Y. Xie, S. Liu, and D. Sun, “Force Modeling, Identification, and Feedback Control of Robot-Assisted Needle Insertion : A Survey of the Literature,” *Sensors*, vol. 18, no. 2, pp. 561-1–38, 2018.
- [1.45] I. Elgezua, Y. Kobayashi, and M. G. Fujie, “Survey on current state-of-the-art in needle insertion robots: Open challenges for application in real surgery,” *Procedia CIRP*, vol. 5, pp. 94–99, 2013.
- [1.46] N. Abolhassani and R. V. Patel, “Deflection of a flexible needle during insertion into soft tissue,” *Proc. Int. Conf. IEEE Eng. Med. Biol.*, pp. 3858–3861, 2006.
- [1.47] H. Kataoka, T. Washio, M. Audette, and K. Mizuhara, “A Model for Relations Between Needle Deflection, Force, and Thickness on Needle Penetration,” *Proc. Int. Conf. Med. Image Comput. Comput. Interv.*, pp. 966–974, 2001.
- [1.48] T. K. Podder *et al.*, “EFFECTS OF TIP GEOMETRY OF SURGICAL NEEDLES : AN ASSESSMENT OF FORCE AND DEFLECTION,” *3rd Eur. Med. Biol. Eng. Conf. EMBEC’05*, vol. 11, no. 1, pp. 1641–1644, 2005.
- [1.49] A. Asadian, M. R. Kermani, and R. V Patel, “An Analytical Model for Deflection of Flexible Needles During Needle Insertion,” *Proc. IEEE/RSJ Int. Conf. Intell. Robot. Syst.*, pp. 2551–2556, 2011.
- [1.50] A. Urrea, F. Casanova, G. A. Orozco, and J. Garcı, “Evaluation of the friction coefficient , the radial stress, and the damage work during needle insertions into agarose gels,” vol. 56, pp. 98–105, 2016.
- [1.51] L. Arendt-Nielsen, H. Egekvist, and P. Bjerring, “Pain following controlled cutaneous insertion of needles with different diameters,” *Somatosens. Mot. Res.*, vol. 23, no. 1–2, pp. 37–43, 2006.
- [1.52] F. Piccinino *et al.*, “Complications following percutaneous liver biopsy,” *J. Hepatol.*, vol. 2, no. 2, pp. 165–173, 1986.
- [1.53] E. H. Smith, “The hazards of fine-needle aspiration biopsy,” *Ultrasound Med. Biol.*, vol. 10, no. 5, pp. 629–34, 1984.
- [1.54] T. Livraghi, B. Damascelli, C. Lombardi, and I. Spagnoli, “Risk in fine-needle abdominal biopsy,” *J. Clin. Ultrasound*, vol. 11, no. 2, pp. 77–81, 1983.
- [1.55] P. A. Schnyder, G. Candardjis, and A. Anderegg, “Peritonitis after thin-needle aspiration biopsy of an abscess,” *Am. J. Roentgenol.*, vol. 137, no. 6, pp. 1271–1272, 1981.

- [1.56] N. Tomiyama *et al.*, “CT-guided needle biopsy of lung lesions: A survey of severe complication based on 9783 biopsies in Japan,” *Eur. J. Radiol.*, vol. 59, no. 1, pp. 60–64, 2006.
- [1.57] A. Oikonomou, F. R. Matzinger, J. M. Seely, C. J. Dennie, and P. J. Macleod, “Ultrathin needle (25 G) aspiration lung biopsy: Diagnostic accuracy and complication rates,” *Eur. Radiol.*, vol. 14, no. 3, pp. 375–382, 2004.
- [1.58] D. C. Howlett, K. J. Drinkwater, D. Lawrence, S. Barter, and T. Nicholson, “Findings of the UK national audit evaluating image-guided or image-assisted liver Biopsy -Part II. Minor and Major Complications and Procedure-related Mortality,” *Radiology*, vol. 266, no. 1, pp. 226–235, 2013.
- [1.59] S. P. Dimairo *et al.*, “Needle Insertion Modeling and Simulation,” *IEEE Trans. Robot.*, vol. 19, no. 5, pp. 864–875, 2003.
- [1.60] R. J. Roesthuis, Y. R. J. Van Veen, A. Jahya, and S. Misra, “Mechanics of needle-tissue interaction,” *IEEE Int. Conf. Intell. Robot. Syst.*, pp. 2557–2563, 2011.
- [1.61] M. G. Harisinghani, *Atlas of Lymph Node Anatomy*. Springer, 2013.
- [1.62] S. M. Chakma *et al.*, “Spectrum of perforation peritonitis,” *J. Clin. Diagnostic Res.*, vol. 7, no. 11, pp. 2518–2520, 2013.
- [1.63] T. Fernandes, M. I. Oliveira, R. Castro, B. Araújo, B. Viamonte, and R. Cunha, “Bowel wall thickening at CT: Simplifying the diagnosis,” *Insights Imaging*, vol. 5, no. 2, pp. 195–208, 2014.
- [1.64] M. M. Ghanei and M. S. Mehraban, “Comparison of the 25, 26 and 27 gauge needles for spinal anesthesia,” *Pakistan J. Biol. Sci.*, vol. 18, no. 6, pp. 290–294, 2015.
- [1.65] H. S. Gill and M. R. Prausnitz, “Does needle size matter?,” *J. Diabetes Sci. Technol.*, vol. 1, no. 5, pp. 725–729, 2007.
- [1.66] T. Fernandes, M. I. Oliveira, R. Castro, B. Araújo, B. Viamonte, and R. Cunha, “Bowel wall thickening at CT: Simplifying the diagnosis,” *Insights Imaging*, vol. 5, no. 2, pp. 195–208, 2014.
- [1.67] D. J. Brenner and E. J. Hall, “Computed Tomography — An Increasing Source of Radiation Exposure,” *N. Engl. J. Med.*, vol. 357, no. 22, pp. 2277–2284, 2007.
- [1.68] M. H. Loser and N. Navab, “A New Robotic System for Visually Controlled Percutaneous Interventions under CT Fluoroscopy,” *Int. Conf. Med. Image Comput. Comput. Interv.*, pp. 887–896, 2000.
- [1.69] N. Shahriari, W. Heerink, T. van Katwijk, E. Hekman, M. Oudkerk, and S. Misra, “Computed tomography (CT)-compatible remote center of motion needle steering robot: Fusing CT images and electromagnetic sensor data,” *Med. Eng.*

- Phys.*, vol. 45, pp. 71–77, 2017.
- [1.70] N. Shahriari, E. Hekman, M. Oudkerk, and S. Misra, “Design and evaluation of a computed tomography (CT)-compatible needle insertion device using an electromagnetic tracking system and CT images,” *Int. J. Comput. Assist. Radiol. Surg.*, vol. 10, no. 11, pp. 1845–1852, 2015.
- [1.71] H. Ishii *et al.*, “Development of a Prototype of Puncturing Robot for CT-guided Intervention,” 2016.
- [1.72] K. Kimura *et al.*, “Needle pose adjustment based on force information with needle puncturing robot,” *Proc. 2017 IEEE/SICE Int. Symp. Syst. Integr.*, pp. 626–631, 2017.
- [1.73] T. Hiraki *et al.*, “Robotic Insertion of Various Ablation Needles Under Computed Tomography Guidance: Accuracy in Animal Experiments,” *Eur. J. Radiol.*, vol. 105, pp. 162–167, 2018.
- [1.74] B. Maurin *et al.*, “A new robotic system for CT-guided percutaneous procedures with haptic feedback,” *Int. Congr. Ser.*, vol. 1268, pp. 515–520, 2004.
- [1.75] B. Maurin *et al.*, “A patient-mounted robotic platform for CT-scan guided procedures,” *IEEE Trans. Biomed. Eng.*, vol. 55, no. 10, pp. 2417–2425, 2008.
- [1.76] K. Masamune *et al.*, “Development of an MRI-compatible needle insertion manipulator for stereotactic neurosurgery,” *Comput. Aided Surg.*, vol. 1, no. 4, pp. 242–248, 1995.
- [1.77] C. J. Walsh, N. C. Hanumara, A. H. Slocum, J.-A. Shepard, and R. Gupta, “A Patient-Mounted, Telerobotic Tool for CT-Guided Percutaneous Interventions,” *J. Med. Device.*, vol. 2, no. 1, pp. 011007-1–10, 2008.
- [1.78] A. Seitel *et al.*, “Development and evaluation of a new image-based user interface for robot-assisted needle placements with the Robopsy system,” *Proc. SPIE*, vol. 7261, p. 72610X-1–9, 2009.
- [1.79] N. Zemiti, I. Bricault, C. Fouard, B. Sanchez, and P. Cinquin, “LPR: A CT and MR-compatible puncture robot to enhance accuracy and safety of image-guided interventions,” *IEEE/ASME Trans. Mechatronics*, vol. 13, no. 3, pp. 306–315, 2008.
- [1.80] I. Bricault *et al.*, “Light puncture robot for CT and MRI interventions,” *IEEE Eng. Med. Biol. Mag.*, vol. 27, no. 3, pp. 42–50, 2008.
- [1.81] E. Taillant, J.-C. Avila-Vilchis, C. Allegrini, I. Bricault, and P. Cinquin, “CT and MR Compatible Light Puncture Robot: Architectural Design and First Experiments,” *Int. Conf. Med. Image Comput. Comput. Interv.*, pp. 145–152, 2004.



- [1.82] N. Hungr, C. Fouard, A. Robert, I. Bricault, and P. Cinquin, "Interventional Radiology Robot for CT and MRI Guided Percutaneous Interventions," *Med. Image Comput. Comput. Interv. -- MICCAI 2011*, vol. 6891, pp. 137–144, 2011.
- [1.83] N. Hungr, I. Bricault, and P. Cinquin, "Design and Validation of a CT- and MRI-Guided Robot for Percutaneous Needle Procedures," *IEEE Trans. Robot.*, vol. 32, no. 4, pp. 973–987, 2016.
- [1.84] F. Y. Wu *et al.*, "AN MRI COIL-MOUNTED MULTI-PROBE ROBOTIC POSITIONER FOR CRYOABLATION," *Proc. ASME 2013 Int. Des. Eng. Tech. Conf. Comput. Inf. Eng. Conf.*, pp. 1–9, 2013.
- [1.85] S. E. Song, J. Tokuda, K. Tuncali, A. Yamada, M. Torabi, and N. Hata, "Design evaluation of a double ring RCM mechanism for robotic needle guidance in MRI-guided liver interventions," *IEEE Int. Conf. Intell. Robot. Syst.*, pp. 4078–4083, 2013.
- [1.86] G. Fichtinger *et al.*, "System for robotically assisted prostate biopsy and therapy with intraoperative CT guidance," *Acad. Radiol.*, vol. 9, no. 1, pp. 60–74, 2002.
- [1.87] D. Stoianovici *et al.*, "AcuBot: A Robot for Radiological Interventions," *IEEE-TR&A Spec. Issue Med. Robot.*, vol. 19, no. 5, pp. 927–930, 2003.
- [1.88] S. Shah *et al.*, "Robotically assisted needle driver: evaluation of safety release, force profiles, and needle spin in a swine abdominal model," *Int. J. Comput. Assist. Radiol. Surg.*, vol. 3, pp. 173–179, 2008.
- [1.89] R. Pollock *et al.*, "Prospects in Percutaneous Ablative Targeting: Comparison of a Computer-Assisted Navigation System and the AcuBot Robotic System," *J. Endourol.*, vol. 24, no. 8, pp. 1269–1272, 2010.
- [1.90] K. Masamune *et al.*, "System for robotically assisted percutaneous procedures with computed tomography guidance," *Comput. Aided Surg.*, vol. 6, no. 6, pp. 370–383, 2001.
- [1.91] J. Kettenbach *et al.*, "Robot-assisted biopsy using ultrasound guidance: Initial results from in vitro tests," *Eur. Radiol.*, vol. 15, pp. 765–771, 2005.
- [1.92] G. Fichtinger *et al.*, "Robotic Assistance for Ultrasound Guided Prostate Brachytherapy," *Int. Conf. Med. Image Comput. Comput. Interv.*, pp. 119–127, 2007.
- [1.93] A. Krieger, G. Metzger, G. Fichtinger, E. Atalar, and L. L. Whitcomb, "A hybrid method for 6-DOF tracking of MRI-compatible robotic interventional devices," *Proc. - IEEE Int. Conf. Robot. Autom.*, no. May, pp. 3844–3849, 2006.
- [1.94] S. Zangos *et al.*, "MR-compatible assistance system for puncture in a high-field system: Device and feasibility of transgluteal biopsies of the prostate gland,"

- Eur. Radiol.*, vol. 17, no. 4, pp. 1118–1124, 2007.
- [1.95] S. Zangos *et al.*, “MR-compatible Assistance System for Biopsy in a High-Field-Strength System: Initial Results in Patients with Suspicious Prostate Lesions,” *Radiology*, vol. 259, no. 3, pp. 903–910, 2011.
- [1.96] D. Stoianovici *et al.*, “MRI-safe robot for endorectal prostate biopsy,” *IEEE/ASME Trans. Mechatronics*, vol. 19, no. 4, pp. 1289–1299, 2014.
- [1.97] R. Monfaredi *et al.*, “Development of a shoulder-mounted robot for MRI-guided needle placement : phantom study,” *Int. J. Comput. Assist. Radiol. Surg.*, 2018.
- [1.98] R. Monfaredi *et al.*, “Shoulder - Mounted Robot for MRI - Guided Arthrography : Accuracy and Mounting Study,” *Proc. 2015 37th Annu. Int. Conf. IEEE Eng. Med. Biol. Soc.*, vol. 1, no. 202, pp. 3643–3646, 2015.
- [1.99] E. Christoforou, I. Seimenis, E. Andreou, E. Eracleous, and N. Tsekos, “A novel, general-purpose, MR-compatible, manually actuated robotic manipulation system for minimally invasive interventions under direct MRI guidance,” *Int. J. Med. Robot. Comput. Assist. Surg.*, vol. 10, no. 1, pp. 22–34, 2014.
- [1.100] N. V. Tsekos, A. Ozcan, and E. Christoforou, “A Prototype Manipulator for Magnetic Resonance-Guided Interventions Inside Standard Cylindrical Magnetic Resonance Imaging Scanners,” *J. Biomech. Eng.*, vol. 127, no. 6, pp. 972–980, 2005.
- [1.101] E. Christoforou, E. Akbudak, A. Ozcan, M. Karanikolas, and N. V. Tsekos, “Performance of interventions with manipulator-driven real-time MR guidance: implementation and initial in vitro tests,” *Magn. Reson. Imaging*, vol. 25, no. 1, pp. 69–77, 2007.
- [1.102] G. Cole, J. Pilitsis, and G. S. Fischer, “Design of a robotic system for MRI-guided deep brain stimulation electrode placement,” *2009 IEEE Int. Conf. Robot. Autom.*, no. May, pp. 4450–4456, 2009.
- [1.103] Y. Wang, G. A. Cole, H. Su, J. G. Pilitsis, and G. S. Fischer, “MRI compatibility evaluation of a piezoelectric actuator system for a neural interventional robot,” *Proc. 31st Annu. Int. Conf. IEEE Eng. Med. Biol. Soc. Eng. Futur. Biomed. EMBC 2009*, pp. 6072–6075, 2009.
- [1.104] G. A. Cole, K. Harrington, H. Su, A. Camilo, J. G. Pilitsis, and G. S. Fischer, “Closed-Loop Actuated Surgical System Utilizing Real-Time In-Situ MRI Guidance,” *Springer Tracts Adv. Robot.*, vol. 79, pp. 785–798, 2014.
- [1.105] G. J. Vrooijink, M. Abayazid, S. Patil, R. Alterovitz, and S. Misra, “Needle path planning and steering in a three-dimensional non-static environment using two-dimensional ultrasound images,” *Int. J. Rob. Res.*, vol. 33, no. 10, pp. 1361–

- 1374, 2014.
- [1.106] C. Rossa, N. Usmani, R. Sloboda, and M. Tavakoli, “A Hand-Held Assistant for Semi-Automated Percutaneous Needle Steering,” *IEEE Trans. Biomed. Eng.*, vol. PP, no. 99, p. 1, 2016.
- [1.107] T. K. Adebar, A. E. Fletcher, and A. M. Okamura, “3-D ultrasound-guided robotic needle steering in biological tissue,” *IEEE Trans. Biomed. Eng.*, vol. 61, no. 12, pp. 2899–2910, 2014.
- [1.108] Y. Kobayashi *et al.*, “Development of an integrated needle insertion system with image guidance and deformation simulation,” *Comput. Med. Imaging Graph.*, vol. 34, no. 1, pp. 9–18, 2010.
- [1.109] M. M. Arnolli, N. C. Hanumara, M. Franken, D. M. Brouwer, and I. A. M. J. Broeders, “An overview of systems for CT- and MRI-guided percutaneous needle placement in the thorax and abdomen,” *Int. J. Med. Robot. Comput. Assist. Surg.*, vol. 11, no. 4, pp. 458–475, 2015.
- [1.110] B. K. B. Reed *et al.*, “Robot-Assisted Needle Steering,” *IEEE Robot. Automation Mag.*, no. December, pp. 35–46, 2011.
- [1.111] C. Rossa and M. Tavakoli, “Issues in closed-loop needle steering,” *Control Eng. Pract.*, vol. 62, pp. 55–69, 2017.
- [1.112] D. Gao, Y. Lei, and H. Zheng, “Needle steering for robot-assisted insertion into soft tissue: A survey,” *Chinese J. Mech. Eng.*, vol. 25, no. 4, pp. 629–638, 2012.
- [1.113] N. J. Van De Berg, D. J. Van Gerwen, J. Dankelman, and J. J. Van Den Dobbela, “Design Choices in Needle Steering - A Review,” *IEEE/ASME Trans. Mechatronics*, vol. 20, no. 5, pp. 2172–2183, 2015.
- [1.114] P. Li, Z. Yang, and S. Jiang, “Needle-tissue interactive mechanism and steering control in image-guided robot-assisted minimally invasive surgery: a review,” *Med. Biol. Eng. Comput.*, vol. 56, no. 6, pp. 931–949, 2018.
- [1.115] S. P. Dimaio and S. E. Salcudean, “Needle steering and motion planning in soft tissues,” *IEEE Trans. Biomed. Eng.*, vol. 52, no. 6, pp. 965–974, 2005.
- [1.116] D. Glozman and M. Shoham, “Image-guided robotic flexible needle steering,” *IEEE Trans. Robot.*, vol. 23, no. 3, pp. 459–467, 2007.
- [1.117] V. G. Mallapragada, N. Sarkar, and T. K. Podder, “Robot-assisted real-time tumor manipulation for breast biopsy,” *IEEE Trans. Robot.*, vol. 25, no. 2, pp. 316–324, 2009.
- [1.118] M. Torabi, K. Hauser, R. Alterovitz, V. Duindam, and K. Goldberg, “Guiding medical needles using single-point tissue manipulation,” *Proc. - IEEE Int. Conf. Robot. Autom.*, pp. 2705–2710, 2009.

- [1.119] R. J. Webster III, N. J. Cowan, G. S. Chirikjian, and a M. Okamura, “Nonholonomic Modelling of Needle Steering,” *Int. J. Rob. Res.*, vol. 25, no. 5–6, pp. 509–525, 2006.
- [1.120] V. Kallem and N. J. Cowan, “Image guidance of flexible tip-steerable needles,” *IEEE Trans. Robot.*, vol. 25, no. 1, pp. 191–196, 2009.
- [1.121] R. Alterovitz, M. Branicky, and K. Goldberg, “Motion Planning Under Uncertainty for Image-guided Medical Needle Steering,” *Int. J. Rob. Res.*, vol. 27, no. 11, pp. 1361–1374, 2008.
- [1.122] R. J. Roesthuis, M. Abayazid, and S. Misra, “Mechanics-based model for predicting in-plane needle deflection with multiple bends,” *Proc. IEEE RAS EMBS Int. Conf. Biomed. Robot. Biomechatronics*, pp. 69–74, 2012.
- [1.123] M. Abayazid, R. J. Roesthuis, R. Reilink, and S. Misra, “Integrating deflection models and image feedback for real-time flexible needle steering,” *IEEE Trans. Robot.*, vol. 29, no. 2, pp. 542–553, 2013.
- [1.124] S. Misra, K. B. Reed, B. W. Schafer, K. T. Ramesh, and A. M. Okamura, “Observations and models for needle-tissue interactions,” *Proc. - IEEE Int. Conf. Robot. Autom.*, pp. 2687–2692, 2009.
- [1.125] E. Dorileo, N. Zemitte, and P. Pognet, “Needle Deflection Prediction Using Adaptive Slope Model,” pp. 2–7, 2015.
- [1.126] H. Lee and J. Kim, “Estimation of flexible needle deflection in layered soft tissues with different elastic moduli,” *Med. Biol. Eng. Comput.*, pp. 729–740, 2014.
- [1.127] P. Moreira and S. Misra, “Biomechanics-Based Curvature Estimation for Ultrasound-guided Flexible Needle Steering in Biological Tissues,” *Ann. Biomed. Eng.*, 2014.
- [1.128] J. Carriere, M. Khadem, C. Rossa, N. Usmani, and R. Sloboda, “Surgeon-in-the-Loop 3-D Needle Steering Through Ultrasound-Guided Feedback Control,” *IEEE Robot. Autom. Lett.*, vol. 3, no. 1, pp. 469–476, 2018.
- [1.129] M. Khadem, C. Rossa, N. Usmani, R. Sloboda, and M. Tavakoli, “Robotics-assisted Needle Steering around Anatomical Obstacles using Notched Steerable Needles,” *IEEE J. Biomed. Heal. Informatics*, vol. PP, no. c, p. 1, 2017.
- [1.130] T. S. Rocha, “A Neural Network Approach for Flexible Needle Tracking in Ultrasound Images Using Kalman Filter,” 2014.
- [1.131] O. Goksel, K. Sapchuk, S. Member, W. J. Morris, and S. E. Salcudean, “Prostate Brachytherapy Training with Simulated Ultrasound and Fluoroscopy Images,” pp. 1–10, 2012.

- [1.132] P. Moreira, S. Patil, R. Alterovitz, and S. Misra, “Needle steering in biological tissue using ultrasound-based online curvature estimation,” *Proc. IEEE Int. Conf. Robot. Autom.*, pp. 4368–4373, 2014.
- [1.133] P. Mignon, P. Poignet, and J. Troccaz, “Automatic Robotic Steering of Flexible Needles from 3D Ultrasound Images in Phantoms and Ex Vivo Biological Tissue,” *Ann. Biomed. Eng.*, vol. 46, no. 9, pp. 1385–1396, 2018.
- [1.134] J. Chevrie, N. Shahriari, M. Babel, and A. Krupa, “Flexible Needle Steering in Moving Biological Tissue With Motion Compensation Using Ultrasound and Force Feedback,” *IEEE Robot. Autom. Lett.*, vol. 3, no. 3, pp. 2338–2345, 2018.
- [1.135] M. Khadem, C. Rossa, R. S. Sloboda, N. Usmani, and M. Tavakoli, “Ultrasound-Guided Model Predictive Control of Needle Steering in Biological Tissue,” *J. Med. Robot. Res.*, vol. 1, no. 1, pp. 1640007-1–17, 2016.
- [1.136] M. Abayazid, P. Moreira, N. Shahriari, S. Patil, R. Alterovitz, and S. Misra, “Ultrasound-guided three-dimensional needle steering in biological tissue with curved surfaces,” *Med. Eng. Phys.*, vol. 37, no. 1, pp. 145–150, 2015.
- [1.137] D. Zhang, Z. Li, K. Chen, J. Xiong, X. Zhang, and L. Wang, “An optical tracker based robot registration and servoing method for ultrasound guided percutaneous renal access,” *Biomed. Eng. Online*, vol. 12, no. 1, p. 47, 2013.
- [1.138] H. Su *et al.*, “Fiber-Optic Force Sensors for MRI-Guided Interventions and Rehabilitation : A Review,” vol. 17, no. 7, pp. 1952–1963, 2017.
- [1.139] S. Elayaperumal, J. H. Bae, B. L. Daniel, and M. R. Cutkosky, “Detection of Membrane Puncture with Haptic Feedback using a Tip-Force Sensing Needle,” no. Iros, pp. 3975–3981, 2014.
- [1.140] Y. L. Park *et al.*, “Real-time estimation of 3-D needle shape and deflection for MRI-guided interventions,” *IEEE/ASME Trans. Mechatronics*, vol. 15, no. 6, pp. 906–915, 2010.
- [1.141] R. J. Roesthuis, M. Kemp, J. J. van den Dobbelsteen, and S. Misra, “Three-Dimensional Needle Shape Reconstruction Using an Array of Fiber Bragg Grating Sensors,” *IEEE/ASME Trans. Mechatronics*, vol. 19, no. 4, pp. 1115–1126, 2013.
- [1.142] X. He, J. Handa, P. Gehlbach, R. Taylor, and I. Iordachita, “A submillimetric 3-DOF force sensing instrument with integrated fiber bragg grating for retinal microsurgery,” *IEEE Trans. Biomed. Eng.*, vol. 61, no. 2, pp. 522–534, 2014.
- [1.143] H. Sadjadi, K. Hashtrudi-Zaad, and G. Fichtinger, “Fusion of electromagnetic trackers to improve needle deflection estimation: Simulation study,” *IEEE Trans. Biomed. Eng.*, vol. 60, no. 10, pp. 2706–2715, 2013.

- [1.144] A. M. Franz, T. Haidegger, W. Birkfellner, K. Cleary, T. M. Peters, and L. Maier-Hein, “Electromagnetic tracking in medicine -A review of technology, validation, and applications,” *IEEE Trans. Med. Imaging*, vol. 33, no. 8, pp. 1702–1725, 2014.

## Chapter 2

- [2.1] D. J. van Gerwen, J. Dankelman, and J. J. van den Dobbelsteen, “Needle–tissue interaction forces – A survey of experimental data,” *Med. Eng. Phys.*, vol. 34, no. 6, pp. 665–680, 2012.
- [2.2] A. M. Okamura, C. Simone, and M. D. O’Leary, “Force modeling for needle insertion into soft tissue,” *IEEE Trans. Biomed. Eng.*, vol. 51, no. 10, pp. 1707–1716, 2004.
- [2.3] S. Jiang, P. Li, Y. Yu, J. Liu, and Z. Yang, “Experimental study of needle–tissue interaction forces: Effect of needle geometries, insertion methods and tissue characteristics,” *J. Biomech.*, vol. 47, no. 13, pp. 3344–3353, 2014.
- [2.4] L. Barbé, B. Bayle, M. De Mathelin, and A. Gangi, “Needle insertions modelling: Identifiability and limitations,” *Biomed. Signal Process. Control*, vol. 2, no. 3, pp. 191–198, 2007.
- [2.5] D. Aulignac, R. Balaniuk, and C. Laugier, “A Haptic Interface for a Virtual Exam of the Human Thigh,” *Proc. IEEE Intemational Conf. Robot. Autom.*, pp. 2452–2457, 2000.
- [2.6] S. Misra, K. J. Macura, K. T. Ramesh, and A. M. Okamura, “The importance of organ geometry and boundary constraints for planning of medical interventions,” *Med. Eng. Phys.*, vol. 31, no. 2, pp. 195–206, 2009.
- [2.7] A. C. Barnett, Y.-S. Lee, and J. Z. Moore, “Fracture Mechanics Model of Needle Cutting Tissue,” *J. Manuf. Sci. Eng.*, vol. 138, no. 1, p. 011005, 2015.
- [2.8] Y. Kobayashi, A. Onishi, T. Hoshi, K. Kawamura, and M. G. Fujie, “Modeling of conditions where a puncture occurs during needle insertion considering probability distribution,” *Proc. IEEE/RSJ Int. Conf. Intell. Robot. Syst.*, pp. 1433–1440, 2008.
- [2.9] M. Heverly, P. Dupont, and J. Triedman, “Trajectory optimization for dynamic needle insertion,” *Proc. 2005 IEEE Int. Conf. Robot. Autom.*, pp. 1646–1651, 2005.
- [2.10] J. T. Hing, A. D. Brooks, and J. P. Desai, “Reality-based needle insertion simulation for haptic feedback in prostate brachytherapy,” *Proc. IEEE Int. Conf. Robot. Autom.*, pp. 619–624, 2006.
- [2.11] T. K. Podder *et al.*, “Effects of velocity modulation during surgical needle insertion,” *Conf. Proc. IEEE Eng. Med. Biol. Soc.*, vol. 6, pp. 5766–5770, 2005.
- [2.12] C. Simone and A. M. Okamura, “Modeling of needle insertion forces for robot-assisted

- percutaneous therapy,” *Proc. 2002 IEEE Int. Conf. Robot. Autom.*, vol. 2, no. May, pp. 2085–2091, 2002.
- [2.13] M. Khadem, C. Rossa, R. S. Sloboda, N. Usmani, and M. Tavakoli, “Mechanics of Tissue Cutting during Needle Insertion in Biological Tissue,” *IEEE Robot. Autom. Lett.*, vol. 1, no. 2, pp. 800–807, 2016.
- [2.14] H. Kataoka, T. Washio, K. Chinzei, K. Mizuhara, C. Simone, and A. M. Okamura, “Measurement of the Tip and Friction Force Acting on a Needle during Penetration,” *Med. Image Comput. Comput. Interv. — MICCAI*, vol. 2488, pp. 216–223, 2002.
- [2.15] Z. Cheng, M. Chauhan, B. L. Davies, D. G. Caldwell, and L. S. Mattos, “Modelling needle forces during insertion into soft tissue,” *Proc. Annu. Int. Conf. IEEE Eng. Med. Biol. Soc.*, pp. 4840–4844, 2015.
- [2.16] A. Asadian, R. V. Patel, and M. R. Kermani, “Dynamics of translational friction in needle-tissue interaction during needle insertion,” *Ann. Biomed. Eng.*, vol. 42, no. 1, pp. 73–85, 2014.
- [2.17] I. Khalaji, M. Hadavand, A. Asadian, R. V. Patel, and M. D. Naish, “Analysis of Needle – Tissue Friction during Vibration-Assisted Needle Insertion,” *Proc. IEEE/RSJ Int. Conf. Intell. Robot. Syst.*, pp. 4099–4104, 2013.
- [2.18] M. Mahvash and P. E. Dupont, “Mechanics of dynamic needle insertion into a biological material,” *IEEE Trans. Biomed. Eng.*, vol. 57, no. 4, pp. 934–943, 2010.
- [2.19] F. Casanova, P. R. Carney, and M. Sarntinoranont, “In vivo evaluation of needle force and friction stress during insertion at varying insertion speed into the brain,” *J. Neurosci. Methods*, vol. 237, pp. 79–89, 2014.
- [2.20] R. J. Roesthuis, Y. R. J. Van Veen, A. Jahya, and S. Misra, “Mechanics of needle-tissue interaction,” *IEEE Int. Conf. Intell. Robot. Syst.*, pp. 2557–2563, 2011.
- [2.21] P. J. Kalarsick, M. A. Kalarsick, C. Goodwin, “Anatomy and Physiology of the Skin,” *J. Dermatology Nurse’s Association*, vol. 3, no. 4, pp. 203-213, 2011
- [2.22] G. Rankin, M. Stokes, D. J. Newham, “Abdominal Muscle Size and Symmetry in Normal Subjects,” *Muscle Nerve*, vol. 34, no. 3, pp.320-326, 2006
- [2.23] D. C. Rubin, J. C. Langer, “Small Intestine: Anatomy and Structural Anomalies,” *Yamada’s Atlas of Gastroenterology*, pp.19-23, 2016
- [2.24] M. M. Arnolli, M. Buijze, M. Franken, K. P. de Jong, D. M. Brouwer, and I. A. M. J. Broeders, “System for CT-guided needle placement in the thorax and abdomen: A design for clinical acceptability, applicability and usability,” *Int. J. Med. Robot. Comput. Assist. Surg.*, vol. 14, no. 1, p. e1877, 2018.

## Chapter 3

- [3.1] R. Tsumura, Y. Takishita, and H. Iwata, “Needle Insertion Control Method for Minimizing Both Deflection and Tissue Damage,” *J. Med. Robot. Res.*, vol. 3, no. 4, pp. 1842005-1–9, 2018.
- [3.2] R. Tsumura, K. Shitashima, and H. Iwata, “Insertion Method for Minimizing Fine Needle Deflection in Bowel Insertion Based on Experimental Analysis,” *IEEE Int. Conf. Intell. Robot. Syst.*, pp. 187–192, 2017.
- [3.3] R. TSUMURA and H. IWATA, “Methods of control for minimizing extra-fine needle deflection with a combination of vibration and rotation in the lower abdomen,” *J. Biomech. Sci. Eng.*, 2017.
- [3.4] T. K. Podder *et al.*, “EFFECTS OF TIP GEOMETRY OF SURGICAL NEEDLES : AN ASSESSMENT OF FORCE AND DEFLECTION,” *3rd Eur. Med. Biol. Eng. Conf. EMBEC’05*, vol. 11, no. 1, pp. 1641–1644, 2005.
- [3.5] L. Arendt-Nielsen, H. Egekvist, and P. Bjerring, “Pain following controlled cutaneous insertion of needles with different diameters,” *Somatosens. Mot. Res.*, vol. 23, no. 1–2, pp. 37–43, 2006.
- [3.6] H. Egekvist, P. Bjerring, and L. Arendt-Nielsen, “Pain and mechanical injury of human skin following needle insertions,” *Eur. J. Pain*, vol. 3, no. 1, pp. 41–49, 1999.
- [3.7] D. S. Minhas, J. a. Engh, M. M. Fenske, and C. N. Riviere, “Modeling of needle steering via duty-cycled spinning,” *Annu. Int. Conf. IEEE Eng. Med. Biol. - Proc.*, pp. 2756–2759, 2007.
- [3.8] N. Abolhassani, R. Patel, and F. Ayazi, “Effects of different insertion methods on reducing needle deflection,” *Proc. 29th Annu. Int. Conf. IEEE Eng. Med. Biol.*, pp. 491–494, 2007.
- [3.9] S. Badaan *et al.*, “Does needle rotation improve lesion targeting?,” *Int. J. Med. Robot. Comput. Assist. Surg.*, vol. 7, pp. 138–147, 2011.
- [3.10] N. Abolhassani, R. Patel, and M. Moallem, “Control of soft tissue deformation during robotic needle insertion.,” *Minim. invasive Ther. Allied Technol.*, vol. 15, no. 3, pp. 165–176, 2006.
- [3.11] K. B. Reed, A. M. Okamura, and N. J. Cowan, “Modeling and control of needles with torsional friction,” *IEEE Trans. Biomed. Eng.*, vol. 56, no. 12, pp. 2905–2916, 2009.
- [3.12] M. A. Meltner, N. J. Ferrier, and B. R. Thomadsen, “Observations on rotating



- needle insertions using a brachytherapy robot.," *Phys. Med. Biol.*, vol. 52, no. 19, pp. 6027–6037, 2007.
- [3.13] H. M. Langevin *et al.*, "Evidence of connective tissue involvement in acupuncture," *FASEB J.*, vol. 16, pp. 872–874, 2002.
- [3.14] M. Mahvash and P. E. Dupont, "Fast needle insertion to minimize tissue deformation and damage," *Proc. - IEEE Int. Conf. Robot. Autom.*, pp. 3097–3102, 2009.
- [3.15] S. P. Dimaio *et al.*, "Needle Insertion Modeling and Simulation," *IEEE Trans. Robot.*, vol. 19, no. 5, pp. 864–875, 2003.
- [3.16] T. Shinei, K. Yuyama, M. Ujihara, and K. Mabuchi, "Reduction of Insertion Force of Medical Devices into Biological Tissues by Vibration," *Japanese J. Med. Electron. Biol. Eng.*, vol. 39, no. 4, pp. 292–296, 2001.
- [3.17] I. Khalaji, M. Hadavand, A. Asadian, R. V. Patel, and M. D. Naish, "Analysis of Needle – Tissue Friction during Vibration-Assisted Needle Insertion," *Proc. IEEE/RSJ Int. Conf. Intell. Robot. Syst.*, pp. 4099–4104, 2013.
- [3.18] T. F. Chan and L. A. Vese, "Active contours without edges," *IEEE Trans. Image Process.*, vol. 10, no. 2, pp. 266–277, 2001.
- [3.19] R. Tsumura, Y. Takishita, Y. Fukushima, and H. Iwata, "Histological Evaluation of Tissue Damage Caused by Rotational Needle Insertion \*," *Proc. Annu. Int. Conf. IEEE Eng. Med. Biol. Soc.*, pp. 5120–5123, 2016.
- [3.20] D. J. van Gerwen, J. Dankelman, and J. J. van den Dobbelsteen, "Needle–tissue interaction forces – A survey of experimental data," *Med. Eng. Phys.*, vol. 34, no. 6, pp. 665–680, 2012.
- [3.21] 八嶋ら, "ゲルの摩擦・潤滑から生体の低摩擦へ", *日本バイオレオロジー学会誌*, 第22巻, 第2号, pp. 10-24, 2008

## Chapter 4

- [4.1] R. Tsumura, J. S. Kim, H. Iwata, and I. Iordachita, "Preoperative Needle Insertion Path Planning for Minimizing Deflection in Multilayered Tissues," vol. 3, no. 3, pp. 2129–2136, 2018.
- [4.2] N. Abolhassani, R. V. Patel, and F. Ayazi, "Minimization of needle deflection in robot-assisted percutaneous therapy," *Int. J. Med. Robot. Comput. Assist. Surg.*, vol. 3, pp. 140–148, 2007.
- [4.3] R. Tsumura and H. Iwata, "Trajectory Planning for Abdominal Fine Needle Insertion

- Based on Insertion Angles,” *IEEE Robot. Autom. Lett.*, vol. 2, no. 2, pp. 1226–1231, 2017.
- [4.4] D. J. van Gerwen, J. Dankelman, and J. J. van den Dobbelsteen, “Needle–tissue interaction forces – A survey of experimental data,” *Med. Eng. Phys.*, vol. 34, no. 6, pp. 665–680, 2012.
- [4.5] R. Seifabadi, I. Iordachita, and G. Fichtinger, “Design of a Teleoperated Needle Steering System for MRI- guided Prostate Interventions,” *Proc. IEEE Int. Conf. Biomed. Robot. Biomechanics*, pp. 793–798, 2012.
- [4.6] N. Hungr, J.-A. Long, V. Beix, and J. Troccaz, “A realistic deformable prostate phantom for multimodal imaging and needle-insertion procedures,” *Med. Phys.*, vol. 39, no. 4, pp. 2031–2041, 2012.
- [4.7] R. Tsumura, Y. Takishita, Y. Fukushima, and H. Iwata, “Histological Evaluation of Tissue Damage Caused by Rotational Needle Insertion \*,” *Proc. Annu. Int. Conf. IEEE Eng. Med. Biol. Soc.*, pp. 5120–5123, 2016.
- [4.8] H. Lee and J. Kim, “Estimation of flexible needle deflection in layered soft tissues with different elastic moduli,” *Med. Biol. Eng. Comput.*, pp. 729–740, 2014.
- [4.9] J. Malcolm, Y. Rathi, M. E. Shenton, and A. Tannenbaum, “Label space: A coupled multi-shape representation,” *Lect. Notes Comput. Sci. (including Subser. Lect. Notes Artif. Intell. Lect. Notes Bioinformatics)*, vol. 5242 LNCS, no. PART 2, pp. 416–424, 2008.
- [4.10] A. Shimizu, R. Ohno, T. Ikegami, H. Kobatake, S. Nawano, and D. Smutek, “Segmentation of multiple organs in non-contrast 3D abdominal CT images,” *Int. J. Comput. Assist. Radiol. Surg.*, vol. 2, no. 3–4, pp. 135–142, 2007.
- [4.11] P. Senin, “Dynamic Time Warping Algorithm Review,” *Tech. Rep.*, vol. University, pp. 1–23, 2008.

## Chapter 5

- [5.1] S. Inoue, R. Tsumura, and H. Iwata, “Development of registration marker for CT-guided needle insertion robot,” *IEEE/ASME Int. Conf. Adv. Intell. Mechatronics, AIM*, pp. 755–760, 2017.
- [5.2] Aquilion LB, Canon Medical Systems, [https://jp.medical.canon/products/computed-tomography/aquilion\\_lb\\_feature](https://jp.medical.canon/products/computed-tomography/aquilion_lb_feature)
- [5.3] AIST/HQL 人体寸法/形状データベース 2003, <https://unit.aist.go.jp/hiri/dhrg/ja/dhdb/fbodyDB/index.html>

- [5.4] J. F. Barrett, N. Keat, “Artifacts in CT: Recognition and Avoidance,” *RadioGraphics*, vol. 24, no. 6, pp.1679-1691, 2004.
- [5.5] VS-068, Denso Wave, <https://www.denso-wave.com/ja/robot/product/five-six/vs068-087.html>
- [5.6] D. Stoianovici *et al.*, “AcuBot: A Robot for Radiological Interventions,” *IEEE-TR&A Spec. Issue Med. Robot.*, vol. 19, no. 5, pp. 927–930, 2003.
- [5.7] A. Melzer *et al.*, “INNOMOTION for percutaneous image-guided interventions,” *IEEE Eng. Med. Biol. Mag.*, vol. 27, no. 3, pp. 66–73, 2008.

## Chapter 6

- [6.1] M. Freutel, H. Schmidt, L. Dürselen, A. Ignatius, and F. Galbusera, “Finite element modeling of soft tissues: Material models, tissue interaction and challenges,” *Clin. Biomech.*, vol. 29, no. 4, pp. 363–372, 2014.
- [6.2] N. Famaey and J. Vander Sloten, “Soft tissue modelling for applications in virtual surgery and surgical robotics.,” *Comput. Methods Biomech. Biomed. Engin.*, vol. 11, no. 4, pp. 351–366, 2008.
- [6.3] Y. Kobayashi *et al.*, “Development of an integrated needle insertion system with image guidance and deformation simulation,” *Comput. Med. Imaging Graph.*, vol. 34, no. 1, pp. 9–18, 2010.



# Research achievements

種 類 別 (By Type)	題名、 発表・発行掲載誌名、 発表・発行年月、 連名者 (申請者含む) (theme, journal name, date & year of publication, name of authors inc. yourself)
論文	<p>○ Needle Insertion Control Method for Minimizing Both Deflection and Tissue Damage, Journal of Medical Robotics Research, 2018.10, vol. 3(4), pp.1842005-1-9, <u>Ryosuke Tsumura</u>, Yusuke Takishita, Hiroyasu Iwata</p> <p>○ Mechanical-based Model for Extra-fine Needle Tip Deflection until Breaching of Tissue Surface, Journal of Medical and Biological Engineering, 2018.10, vol. 38 (5), pp.697-706, <u>Ryosuke Tsumura</u>, Hiroyasu Iwata</p> <p>○ Preoperative Needle Insertion Path Planning for Minimizing Deflection in Multi-layered Tissues, IEEE Robotics and Automation Letters, vol. 3(3), pp.2129-2136, 2018.2, <u>Ryosuke Tsumura</u>, Jin Seob Kim, Hiroyasu Iwata, Iulian Iordachita</p> <p>○ Trajectory Planning for Abdominal Fine Needle Insertion Based on Insertion Angles, IEEE Robotics and Automation Letters, vol. 2(2), pp.1226-1231, 2017.2, <u>Ryosuke Tsumura</u>, Hiroyasu Iwata</p> <p>○ Methods of Control for Minimizing Extra-Thin Needle Deflection with a Combination of Vibration and Rotation in the Lower Abdomen, Journal of Biomechanical Science and Engineering, vol. 12(3), No.16-00468, 2017.1, <u>Ryosuke Tsumura</u>, Hiroyasu Iwata</p>
講演 (査読有)	<p>○ Multi-layered Tissue Boundary Detection System for CT-guided Needle Insertion Path Planning, Proceedings of 2018 IEEE International Conference on Robotics and Biomimetics (ROBIO 2018), 2018.12, Ryutaro Matsumoto, <u>Ryosuke Tsumura</u>, Hiroyasu Iwata (accept)</p> <p>○ Preoperative Needle Insertion Path Planning for Minimizing Deflection in Multi-layered Tissues, Proceedings of 2018 IEEE International Conference on Robotics and Automation (ICRA2018), pp.2129-2136, 2018.5, <u>Ryosuke Tsumura</u>, Jin Seob Kim, Hiroyasu Iwata, Iulian Iordachita</p> <p>○ Insertion Method for Minimizing Fine Needle Deflection in Bowel Insertion Based on Experimental Analysis, Proceedings of 2017 IEEE/RSJ International Conference on Intelligent Robots and Systems (IROS 2017), pp. 187-192, 2017.9, <u>Ryosuke Tsumura</u>, Kai Shitashima, Hiroyasu Iwata</p> <p>○ Development of Registration Marker for CT-guided Needle Insertion Robot, Proceedings of 2017 IEEE International Conference on Advanced Intelligent Mechatronics (AIM 2017), pp. 755-760, 2017.7, Shun Inoue, <u>Ryosuke Tsumura</u>, Hiroyasu Iwata</p>

種 類 別 By Type	題名、 発表・発行掲載誌名、 発表・発行年月、 連名者 (申請者含む) (theme, journal name, date & year of publication, name of authors inc. yourself)
<p>講演 (査読有) ○</p>	<p>Histological Evaluation of Tissue Damage due to Needle Insertion with Axial Rotation, Proceedings of 38th Annual International Conference of the IEEE Engineering in Medicine and Biology Society (EMBC2016), pp.5120-5123, 2016.8, <u>Ryosuke Tsumura</u>, Yusuke Takishita, Yuta Fukushima, Hiroyasu Iwata</p> <p>下腹部への CT ガイド下穿刺支援ロボット ー振動・回転動作を併用した極細針のたわみ抑制手法の構築ー, 第 20 回ロボティクスシンポジウム講演論文集, 2015.3, <u>津村 遼介</u>, 石川 牧子, 渡辺貴文, 岩田 浩康</p>
<p>講演 (査読無)</p>	<p>Development of CT-guided Needle Insertion Robot for Lower Abdomen, The 13th IEEE Transdisciplinary-Oriented Workshop for Emerging Researchers, Session A-27, Japan, 2016.11, <u>Ryosuke Tsumura</u>, Hiroyasu Iwata</p> <p>Experimental Analysis of Needle Tip Deflection until Breaching Tissue Surface, 38th Annual International Conference of the IEEE Engineering in Medicine and Biology Society (EMBC2016), 2016.8, <u>Ryosuke Tsumura</u>, Hiroyasu Iwata</p> <p>子宮内連続超音波画像と CNN による分類確度分布を用いた胎児身体部位座標推定手法の提案, 第 19 回計測自動制御学会システムインテグレーション部門講演会講演論文集, 2018.12, 内藤 雄貴, <u>津村 遼介</u>, 岩田 浩康 (発表予定)</p> <p>穿刺支援ロボットにおける針たわみ検知手法構築, 第 19 回計測自動制御学会システムインテグレーション部門講演会講演論文集, 2018.12, 井上 峻, <u>津村 遼介</u>, 岩田 浩康 (発表予定)</p> <p>心エコー診断ロボットのビジュアルサーボ技術, 第 27 回日本コンピュータ外科学会, 2018.11, 山野 元, 渡辺 貴文, <u>津村 遼介</u>, 内藤 雄貴, 岩田 浩康 (発表予定)</p> <p>下腹部における CT 画像を規範とした 3 次元穿刺パスプランニングシステムの開発, 第 27 回日本コンピュータ外科学会, 2018.11, 松本 隆太郎, <u>津村 遼介</u>, 岩田 浩康 (発表予定)</p> <p>たわみ確率モデルを用いた穿刺パスプランニングの構築, 第 27 回日本コンピュータ外科学会, 2018.11, 松本 隆太郎, <u>津村 遼介</u>, 岩田 浩康 (発表予定)</p> <p>超音波妊婦検査支援ロボットの開発, 日本機械学会ロボティクス・メカトロニクス講演会 2018, 2A2-A15, 2018.6, <u>津村 遼介</u>, 熊切 淳太郎, 内藤 雄貴, 岩田 浩康</p>

種 類 別 By Type	題名、 発表・発行掲載誌名、 発表・発行年月、 連名者 (申請者含む) (theme, journal name, date & year of publication, name of authors inc. yourself)
講演 (査読無)	<p>心エコー診断ロボットのビジュアルサーボ技術, 日本機械学会ロボティクス・メカトロニクス講演会 2018, 1P2-D04, 2018.6, 山野 元, 渡辺 貴文, <u>津村 遼介</u>, 内藤 雄貴, 岩田 浩康</p> <p>超音波検査支援ロボットを用いた自動妊婦健診サービスの研究, 第 18 回計測自動制御学会システムインテグレーション部門講演会講演論文集, 2B4-05, 2017.12, 竹内 里奈, 宮西 将生, <u>津村 遼介</u>, 内藤 雄貴, 岩田 浩康</p> <p>下腹部を対象とした CT ガイド下穿刺制御戦略, 第 18 回計測自動制御学会システムインテグレーション部門講演会講演論文集, 2B4-05, 2017.12, 澤田 将太, <u>津村 遼介</u>, 岩田 浩康</p> <p>組織損傷の低減を両立する穿刺制御手法の構築, 第 18 回計測自動制御学会システムインテグレーション部門講演会講演論文集, 2B4-04, 2017.12, 瀧下 雄介, <u>津村 遼介</u>, 岩田 浩康</p> <p>多層組織における穿刺パスプランニングの構築, 第 18 回計測自動制御学会システムインテグレーション部門講演会講演論文集, 2B4-03, 2017.12, <u>津村 遼介</u>, Iulian Iordachita, Jin Seob Kim, 岩田 浩康</p> <p>組織損傷とたわみの低減を両立する穿刺制御手法の構築, 第 26 回日本コンピュータ外科学会, 2017.10, <u>津村 遼介</u>, 瀧下 雄介, 岩田 浩康</p> <p>CT ガイド下穿刺支援ロボットのためのレジストレーションシステム -四方斜立角柱構造を有したマーカーのデザイン-, 日本機械学会ロボティクス・メカトロニクス講演会 2017, 2017.6, 井上 峻, <u>津村 遼介</u>, 岩田 浩康</p> <p>妊婦超音波検査支援ロボットの開発 -体表面へのプローブの垂直接触性と接触安全性を両立する受動機構の提案-, 日本機械学会ロボティクス・メカトロニクス講演会 2017, 2017.6, 内藤 雄貴, <u>津村 遼介</u>, 竹内 里奈, 宮西 将生, 岩田 浩康</p> <p>組織表面穿刺における極細針のたわみ推定モデル, 第 17 回計測自動制御学会システムインテグレーション部門講演会講演論文集, 1E2-5, 2016.12, <u>津村 遼介</u>, 岩田 浩康</p> <p>極細針を用いた腸管穿刺におけるたわみの実験分析, 第 17 回計測自動制御学会システムインテグレーション部門講演会講演論文集, 3K4-1, 2016.12, 下島 海, <u>津村 遼介</u>, 岩田 浩康</p> <p>妊婦超音波健診における三次元データベース生成手法の提案, 第 17 回計測自動制御学会システムインテグレーション部門講演会講演論文集, 1E2-3, 2016.12, 竹内 里奈, <u>津村 遼介</u>, 岩田 浩康</p>

種 類 別 By Type	題名、 発表・発行掲載誌名、 発表・発行年月、 連名者（申請者含む） (theme, journal name, date & year of publication, name of authors inc. yourself)
<p>講演 (査読無)</p> <p>その他 (講演) (査読有)</p>	<p>下腹部穿刺における極細針を用いた穿刺パスプランニングの構築, 第25回日本コンピュータ外科学会, 2016.11, <u>津村 遼介</u>, 下島 海, 福嶋 勇太, 岩田 浩康</p> <p>回転・振動を付与した穿刺による組織損傷の組織学的分析, 日本機械学会ロボティクス・メカトロニクス講演会 2016, 2016.6, 瀧下 雄介, <u>津村 遼介</u>, 福嶋 勇太, 岩田 浩康</p> <p>極細針を用いた下腹部穿刺の針変形における針先端形状の影響の比較評価, 第15回計測自動制御学会システムインテグレーション部門講演会講演論文集, 2M3-3, 2014.12, <u>津村 遼介</u>, 石川 牧子, 渡辺 貴文, 岩田 浩康</p> <p>極細針を用いた CT ガイド下穿刺支援ロボットの開発 -複合組織における針変形の抑制-, 日本機械学会ロボティクス・メカトロニクス講演会 2014 講演会講演論文集, 3P1-D03, 2014.5, <u>津村 遼介</u>, 石川 牧子, 岩田 浩康</p> <p>Inverse Innovation: Ripple Railway Model to Acquire Local Industries Based on User's Viewpoint in Thailand, Proceedings of 2017 IEEE 13th International Symposium on Autonomous Decentralized System (ISADS), pp.281-286, 2017.3, Satoshi Funabashi, Ryuya Sato, Tamon Miyake, <u>Ryosuke Tsumura</u>, Kinji Mori</p> <p>Ankle-Foot Coupling using Rubber Cushion to Allow Multi-Axis Movement for SACH Foot, Cybathlon Symposium, 2016.10, Naomi Okamura, <u>Ryosuke Tsumura</u>, Akira Kato,</p> <p>A Multi-Axis Rubber Coupling Created using Natural Rubber as an Ankle Joint Adapter for the Standard SACH Foot, 38th Annual International Conference of the IEEE Engineering in Medicine and Biology Society (EMBC2016), 2016.8, Naomi Okamura, <u>Ryosuke Tsumura</u>, Tomohiro Hoshina, Akira Kato, Teruki Shibata, and Shigeki Sugano</p> <p>Objective evaluation of oral presentation skills using Inertial Measurement Units, Proceedings of 37th Annual International Conference of the IEEE Engineering in Medicine and Biology Society (EMBC2015), pp.3117-3120, 2015.8, Salvatore Sessa, Weisheng Kong, Di Zhang, Sarah Cosentino, Udara Manwadu, Motoji Kawasaki, Thomas Thuruthel Gerge, Tomohiro Suzuki, <u>Ryosuke Tsumura</u>, Atsuo Takanishi</p> <p>Ankle-Foot Coupling with Rubber Cushion for Walking on Uneven Terrain, LIMBS Summit, 2015.6, Akira Kato, <u>Ryosuke Tsumura</u>, Tomohiro Hoshina, Naomi Okamura</p> <p>Novel Social Innovation Concept Based on the Viewpoint of the Infrastructure User, Proceedings of IEEE Twelfth International Symposium on Autonomous Decentralized Systems, pp.295-300, 2015.3, Masato Adachi, Gonzalo D. Aguirre, Takafumi Sasaki, <u>Ryosuke Tsumura</u>, Tomoya Koshi, Kinji Mori</p>



種 類 別 By Type	題名、 発表・発行掲載誌名、 発表・発行年月、 連名者 (申請者含む) (theme, journal name, date & year of publication, name of authors inc. yourself)
その他 (記事)	早稲田理工 PLUS 2015 (朝日新聞出版) "特集：日本を支える発想・技術・取り組み"
その他 (特許)	特願 2017-243071 「穿刺経路設定装置、穿刺制御量設定装置及び穿刺システム」, 平成 29.12.19, 蓮見賢一郎, 岩田浩康, <u>津村遼介</u>
その他 (研究費)	<p>特願 2017-93319 「レジストレーションマーカー及びレジストレーションマーカーの活用プログラム」, 平成 29.5.9, 蓮見賢一郎, 岩田浩康, 井上峻, <u>津村遼介</u></p> <p>特願 2017- 「超音波プローブ移動装置」, 岩田浩康, 内藤雄貴, <u>津村遼介</u></p>
その他 (受賞)	<p>一般財団法人 丸文財団 交流研究助成 2019.01 - 現在</p> <p>公益財団法人 NEC C&amp;C 財団 国際会議論文発表者助成金 2018.04</p> <p>日本学術振興会特別研究員 DC2 研究奨励費 2018.04 - 現在</p>
その他 (受賞)	<p>博士課程教育リーディングプログラム 「実体情報学博士プログラム」 奨励金 2014.04 - 2018.03</p> <p>日本機械学会若手優秀講演フェロー賞, 日本機械学会ロボティクス・メカトロニクス講演会 2017, 2018.2 (共著者として)</p> <p>SI2017 優秀講演賞, 第 18 回計測自動制御学会システムインテグレーション部門講演会講演, 2018.2 (共著者として)</p> <p>2nd place design competition award, LIMBS Summit, 2015.6 (共著者として)</p> <p>計測自動制御学会 SI 部門若手奨励賞, 第 20 回ロボティクスシンポジウム講演, 2015.3</p> <p>SI2014 優秀講演賞, 第 15 回計測自動制御学会システムインテグレーション部門講演会講演, 2014.12</p>
その他 (招待講演等)	<p>実体情報学博士プログラム第 5 回シンポジウム 2017 にて登壇発表 2017.12.04</p> <p>第 2 回ロボット研究機構シンポジウムの企画運営の責任者 2017.3.7</p> <p>「さがみロボット産業特区」 ロボット展のパネルディスカッションにて登壇発表 2017.2.21</p> <p>博士課程教育リーディングプログラムフォーラム 2015(Program for leading Graduate Schools Forum 2015) の学生フォーラムにて登壇発表 2015.10.24-25</p> <p>実体情報学博士プログラム第 3 回シンポジウム 2015 にて登壇発表 2015.10.29</p>



# Acknowledgement to Graduate Program of *Embodiment Informatics*

著者は文部科学省の事業の一つである博士課程教育リーディングプログラム「実体情報学博士プログラム (Embodiment Informatics)」に所属している。

## – What I learned from the program

5年間のリーディングプログラムを通じて、私は多岐にわたる沢山の経験をさせてもらった (図1)。経験の軸はワークショップ、異分野共同研究、留学の大きく3つに大別できる。そしてそれぞれの経験を通じて3つの力を身につけ、研鑽できたと考える。

ワークショップでは、私は発展途上国における鉄道インフラのコンセプト提案を行った。そこでは何のために、誰のために鉄道インフラを構築するのか、実際にベトナムやタイで起きている社会問題を題材に、現地調査を踏まえて徹底的に考える訓練を行った。これは自身の研究において、課題設定をどうするか見極める力に繋がったと考える。

異分野共同研究では、発展途上国のための義足開発を行った。これは経済的に貧しいかつ依然として義足の需要が高い国であるカンボジアを対象に、安価で高機能な義足を開発する学生主導で立ち上げたプロジェクトである。メンバー内に義足や発展途上国に精通している学生がいなかったことから、それぞれの専門家と会い、議論を重ねていくことで良いものを作っていく経験ができた。これは自身の研究において、病院や企業と連携して研究を進める際に必要な周りを巻き込む力の研鑽に繋がったと考える。

最後に留学では、手術ロボットの研究が盛んなジョンズホプキンス大学に半年間、滞在した。滞在した研究室には様々なバックグラウンドを人がいて、自身の研究に関して議論する機会も沢山あり、色々な側面から自分の研究を見直すことができた。そしてそこでの研究を通じて、自分の研究に確率モデルという情報技術の要素を取り入れることができた。この経験から、異分野のアイデアを自分のものとして吸収する力を身につけることができたと考える。



Fig. 1 Opportunities in the program for 5 years

## - What is Embodiment Informatics?

「実体情報学」という言葉はまだ完全に定義されていない。昨今の技術革新において、「機械」と「情報」の融合の重要性は常に指摘されているが、具体的な融合の応用例やその融合効果は示されていない。「実体情報学」とは「機械」と「情報」の融合の方法論を意味すると考える。そこで私は、自身の研究を通じて、一つの「実体情報学」の在り方を以下に述べる。

実体情報学とは"Methodology to create a system for sustainable growth"（持続的成長の可能なシステム・体系の創出）を学ぶ学問と定義する。ここでのシステム・体系とは、相互に影響を及ぼし合う要素から構成されるまとまりを指す。昨今の製品において「機械」と「情報」は密接な関係にあることは自明である。製品を「人」と例えるなら、製品を構成する機械技術を「身体」、情報技術を「脳」と私は捉えている。そして人は持っている身体能力を鑑み、目の前の問題を解決しようとする。例えば、目の前に重い荷物があり、所定の箇所まで一人で移動しなければならないが、一度に運べるほどの筋力を持っていないとする。その時に人間は、荷物を小分けにして一度に運ぶ重さを軽くして複数回往復して運ぶことを考えるだろう。しかし、トレーニングを行い、持っている筋力そのものをあげることができれば、頭を使わずとも一度で荷物を運び切ることができるかもしれない。一方、思考力を高めれば、持っている筋力を最大限に発揮できるような身体の使い方や疲れにくい輸送経路を考えつくことができるかもしれない。筋力か思考力どちらか一方を集中的に鍛えることで課題は達成できる。しかし一方で、筋力の限界を思考力で補い、思考力の限界を筋力で補うように、筋力と思考力を相補的に鍛えることで効率的かつ効果的に課題を達成できると考える。同じ思考力でも、筋力の違いによってできることは変わってくる。逆もまた然りである。筋力と思考力の鍛錬の循環を回すことで1 + 1が3にも4にもなると考える。

自身の研究においてもこの考え方を適用できると考えている。例えば、3章で示した回転と振動を併用した穿刺手法は「身体」にあたり、4章で示した穿刺パンプランニングは「脳」にあたる。実際に、回転と振動を併用した穿刺制御手法のみでは穿刺角度によるたわみの問題には対処できなかった。しかし穿刺角度を考慮した穿刺パンプランニングを構築する、つまり「身体」の使い方を考えてあげることで、たわみの問題は解決に向かった。もちろん穿刺中の組織変形など、まだ課題は残されている。残された課題に対しても、穿刺制御手法を工夫することで問題は更に解決に向かうと思われる。もしかしら穿刺パンプランニング自体を少し工夫すれば解決するかもしれない。このように「身体」と「脳」を持続的に成長させる循環を創ることによって問題は効率的かつ効果的に解決でき、この方法論こそが「実体情報学」であると考え。そしてこのシステムを創るために必要な力こそが、先に述べたプログラムで培えた3つの力だと考える。

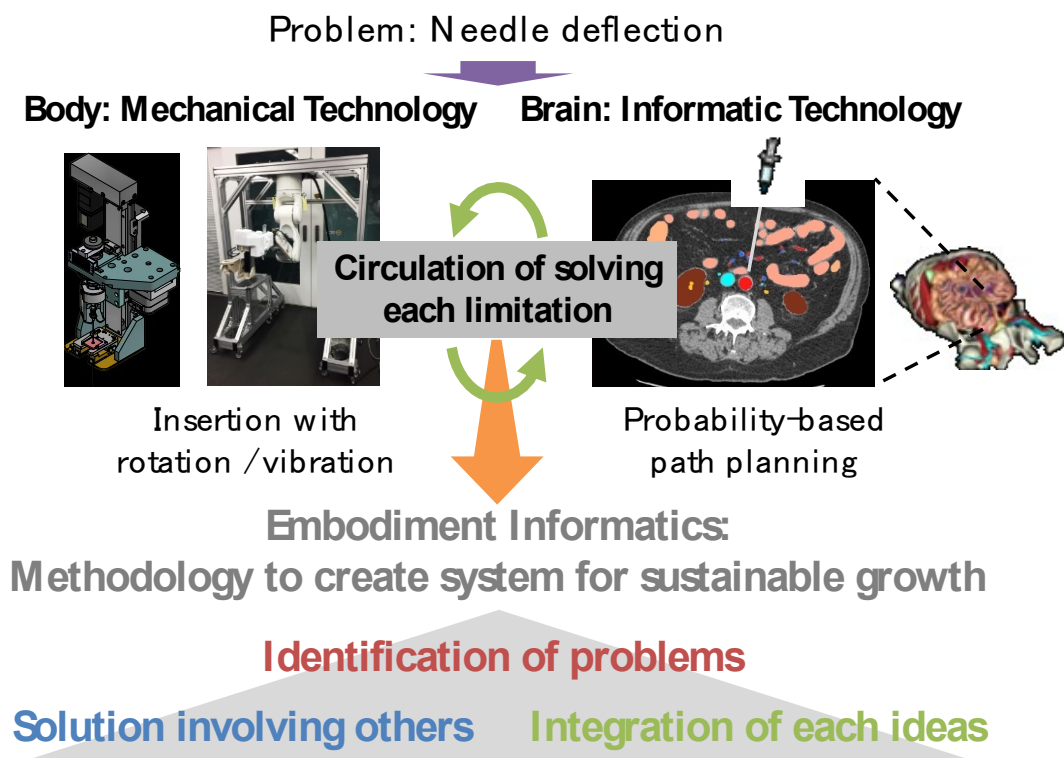


Fig. 2 The concept showing Embodiment Informatics